



Institut für Geowissenschaften
Mathematisch-Naturwissenschaftlichen Fakultät
Universität Potsdam

SEISMOTECTONIC SEGMENTATION,
PALEOEARTHQUAKES AND STYLE OF DEFORMATION
ALONG THE NORTHERN PAMIR THRUST SYSTEM,
SOUTH KYRGYZSTAN

DISSERTATION

von

Magda Patyniak, MSc

zur Erlangung des akademischen Grades

DOKTOR RERUM NATURALIUM

»DR. RER. NAT.«

im Fachbereich der Geowissenschaften

eingereicht an der
Mathematisch-Naturwissenschaftlichen Fakultät
der Universität Potsdam

Potsdam, im Juni 2022

Unless otherwise indicated, this work is licensed under a Creative Commons License Attribution 4.0 International.
This does not apply to quoted content and works based on other permissions.
To view a copy of this licence visit:
<https://creativecommons.org/licenses/by/4.0>

Advisors

Prof. Manfred R. Strecker,
Prof. J Ramón Arrowsmith,

PhD Universität Potsdam, Germany
Arizona State University, USA

Published online on the
Publication Server of the University of Potsdam:
<https://doi.org/10.25932/publishup-57714>
<https://nbn-resolving.org/urn:nbn:de:kobv:517-opus4-577141>

Erklärung zur Eigenständigkeit

Hiermit erkläre ich, dass ich die Dissertation “Seismotectonic Segmentation, Paleoearthquakes and Style of Deformation along the Northern Pamir Thrust System, South Kyrgyzstan.” selbstständig verfasst und keine anderen, als die von mir angegebenen Quellen und Hilfsmittel genutzt habe.

Die Stellen der Dissertation, die anderen Quellen entnommen wurden, sind durch Angaben der Herkunft kenntlich gemacht.

Bereits in einer Fachzeitschrift publizierte Teile der Dissertation sind eindeutig gekennzeichnet.

Ich erkläre weiterhin, dass die Dissertation bisher nicht in dieser oder anderer Form in einem anderen Prüfungsverfahren vorgelegt wurde.

Potsdam, 14. Juni 2022

Magda Patyniak, MSc

When you teach a child that a bird is named bird, the child will never see a bird again

- Krishnamurti

ALLGEMEINEVERSTÄNDLICHE ZUSAMMENFASSUNG

Das Pamir-Gebirge in Zentralasien wächst aufgrund der indisch-eurasischen Plattenbewegungen, was mit wiederholten großen Erdbeben assoziiert ist. Historische Erdbeben und deren Bruchstufen im Gelände sind hier komplex und nicht vollständig verstanden. In dieser Dissertation verwende ich verschiedene Verfahren, um die Erdbebenmuster entlang der Pamir-Frontüberschiebung (PFT) zu bestimmen, welche eine der wichtigsten aktiven Erdbebenzonen in dieser Plattenkollisionszone darstellt.

Im ersten Teil präsentiere ich Ergebnisse aus paläoseismologischen Ausgrabungen, die Hinweise auf fünf oder möglicherweise sechs große Erdbeben in den letzten 16.000 Jahren liefern. Diese Ereignisse wiederholen sich durchschnittlich alle ca. 1.900 Jahre und können eine Stärke von bis zu Magnitude (M_w) 7,4 erreichen. Des Weiteren zeigen meine Untersuchungen, dass sich die PFT in den letzten ~ 5.000 Jahren mit einer Geschwindigkeit von $4,1 \pm 1,5$ mm/Jahr bewegt hat, was sich von den heutigen Schätzungen der Verkürzungsrate auf der Grundlage geodätischer Daten unterscheidet.

Im zweiten Teil der Dissertation präsentiere ich neue Erkenntnisse über einen rezenten Oberflächenbruch, welcher im Jahr 2008 durch das Nura Erdbeben entlang der PFT verursacht wurde. Mit Hilfe von neuen Feldbeobachtungen und hochaufgelösten digitalen Oberflächenmodellen konnte ein Versatz entlang sekundärer Oberflächenstrukturen nachgewiesen werden. Um die dafür verantwortlichen Prozesse zu erklären, wird die Aktivität einer in der Tiefe verborgenen Verwerfung angenommen welche nicht an die Oberfläche kommt, diese jedoch fortlaufend verformt.

Die Diskrepanz zwischen den geodätisch und geologisch abgeleiteten Geschwindigkeiten entlang der PFT auf der einen, und die komplexe Bruchausbreitung entlang benachbarter Strukturen während des Nura Erdbebens auf der anderen Seite deuten auf ein wechselwirkendes System hin. Die Verteilung der aktiven Deformation entlang des nördlichen Pamir scheint weitreichender als bisher angenommen, und impliziert im zentralen Bereich der PFT eine fortschreitende strukturelle Reife der Erdbebenzone mit einem steigenden Potenzial für größere Erdbeben.

Die umfangreichen Forschungsarbeiten meiner Dissertation tragen nicht nur zum Verständnis des Erdbebenverhaltens entlang der PFT, sondern auch zum Allgemeinverständnis von ähnlichen segmentierten Erdbebenzonen in aktiven Plattenkollisionsgebieten bei. Gleichzeitig zeigen meine Ergebnisse, wie wichtig die Kombination verschiedener methodischer Ansätze in den Geowissenschaften ist, insbesondere in strukturell komplexen Gebieten wie dem nördlichen Pamir. Aus GNSS abgeleitete gegenwärtige Deformationsraten sowie Langzeitdeformationsraten hergeleitet aus oberflächlichen geologischen Archiven lassen die Komplexität von Kollisionszonen nicht immer erkennen. In der Bewertung kann es dann zu ungenauen und sogar falschen Schlussfolgerungen hinsichtlich des Grades der Deformation, sowie der seismischen Risikoeinschätzung in tektonisch aktiven Regionen führen. Die Ergebnisse dieser Dissertation dokumentieren diese Komplexität auf verschiedenen Zeitskalen und erlauben dann ähnliche Schlussfolgerungen für Gebiete, in denen zum Beispiel urbane Bebauung, Landschaftserosion oder dichte Vegetation die Hinweise auf eine Erdbebengeschichte ganz oder teilweise verbirgt.

ABSTRACT

The Pamir Frontal Thrust (PFT) located in the Trans Alai range in Central Asia is the principal active fault of the intracontinental India-Eurasia convergence zone and constitutes the northernmost boundary of the Pamir orogen at the NW edge of this collision zone. Frequent seismic activity and ongoing crustal shortening reflect the northward propagation of the Pamir into the intermontane Alai Valley. Quaternary deposits are being deformed and uplifted by the advancing thrust front of the Trans Alai range. The Alai Valley separates the Pamir range front from the Tien Shan mountains in the north; the Alai Valley is the vestige of a formerly contiguous basin that linked the Tadjik Depression in the west with the Tarim Basin in the east. GNSS measurements across the Central Pamir document a shortening rate of ~ 25 mm/yr, with a dramatic decrease of ~ 10 - 15 mm over a short distance across the northernmost Trans Alai range. This suggests that almost half of the shortening in the greater Pamir – Tien Shan collision zone is absorbed along the PFT. The short-term (geodetic) and long-term (geologic) shortening rates across the northern Pamir appear to be at odds with an apparent slip-rate discrepancy along the frontal fault system of the Pamir. Moreover, the present-day seismicity and historical records have not revealed great $M_w > 7$ earthquakes that might be expected with such a significant slip accommodation. In contrast, recent and historic earthquakes exhibit complex rupture patterns within and across seismotectonic segments bounding the Pamir mountain front, challenging our understanding of fault interaction and the seismogenic potential of this area, and leaving the relationships between seismicity and the geometry of the thrust front not well understood.

In this dissertation I employ different approaches to assess the seismogenic behavior along the PFT. Firstly, I provide paleoseismic data from five trenches across the central PFT segment (cPFT) and compute a segment-wide earthquake chronology over the past 16 kyr. This novel dataset provides important insights into the recurrence, magnitude, and rupture extent of past earthquakes along the cPFT. I interpret five, possibly six paleoearthquakes that have ruptured the Pamir mountain front since ~ 7 ka and 16 ka, respectively. My results indicate that at least three major earthquakes ruptured the full-segment length and possibly crossed segment boundaries with a recurrence interval of ~ 1.9 kyr and potential magnitudes of up to $M_w 7.4$. Importantly, I did not find evidence for great (i.e., $M_w \geq 8$) earthquakes.

Secondly, I combine my paleoseismic results with morphometric analyses to establish a segment-wide distribution of the cumulative vertical separation along offset fluvial terraces and I model a long-term slip rate for the cPFT. My investigations reveal discrepancies between the extents of slip and rupture during apparent partial segment ruptures in the western half of the cPFT. Combined with significantly higher fault scarp offsets in this sector of the cPFT, the observations indicate a more mature fault section with a potential for future fault linkage. I estimate an average rate of horizontal motion for the cPFT of 4.1 ± 1.5 mm/yr during the past ~ 5 kyr, which does not fully match the GNSS-derived present-day shortening rate of ~ 10 mm/yr. This suggests a complex distribution of strain accumulation and potential slip partitioning between the cPFT and additional faults and folds within the Pamir that may be associated with a partially locked regional décollement.

The third part of the thesis provides new insights regarding the surface rupture of the 2008 $M_w 6.6$ Nura earthquake that ruptured along the eastern PFT sector. I explore this rupture in the context of its structural complexity by combining extensive field observations with high-resolution digital surface models. I provide a map of the rupture extent, net slip measurements, and updated regional geological observations. Based on this data I propose a tectonic model in this area associated with secondary flexural-slip faulting along steeply dipping bedding of folded Paleogene

sedimentary strata that is related to deformation along a deeper blind thrust. Here, the strain release seems to be transferred from the PFT towards older inherited basement structures within the area of advanced Pamir-Tien Shan collision zone.

The extensive research of my dissertation results in a paleoseismic database of the past 16 ~kyr, which contributes to the understanding of the seismogenic behavior of the PFT, but also to that of segmented thrust-fault systems in active collisional settings. My observations underscore the importance of combining different methodological approaches in the geosciences, especially in structurally complex tectonic settings like the northern Pamir. Discrepancy between GNSS-derived present-day deformation rates and those from different geological archives in the central part, as well as the widespread distribution of the deformation due to earthquake triggered strain transfer in the eastern part reveals the complexity of this collision zone and calls for future studies involving multi-temporal and interdisciplinary approaches.

ZUSAMMENFASSUNG

Die Pamir-Frontüberschiebung (PFT) des Trans-Alai-Gebirges in Zentralasien ist die wichtigste aktive Verwerfung der intrakontinentalen indisch-eurasischen Konvergenzzone und bildet die nördlichste Grenze des Pamir-Orogens am NW-Rand dieser Kollisionszone. Die intensive Seismizität und die fortschreitende Krustenverkürzung spiegeln die nach Norden gerichtete Verlagerung des Pamir in das intermontane Alai-Tal wider. Quartäre Ablagerungen werden durch die vorstoßende Überschiebungsfrent des Trans-Alai-Gebirges sukzessive deformiert und angehoben. Das Alai-Tal trennt das Pamir-Gebirge vom Südrand des Tien Shan-Gebirges und verkörpert die Überreste eines ehemals zusammenhängenden Beckens, welches früher die Tadjik-Senke im Westen mit dem Tarim-Becken im Osten verband. GNSS-Messungen südlich der PFT im Bereich des Zentralpamirs dokumentieren eine Verkürzungsrate von 25 mm/Jahr, welche über eine kurze Strecke zur nördlichen Front des Trans-Alai-Gebirges hin drastisch um 10-15 mm abnimmt. Dies lässt darauf schließen, dass fast die Hälfte der Einengung entlang der PFT absorbiert wird, welche sich in der Kollisionszone zwischen dem Pamir und dem Tien Shan befindet. Eine offensichtliche Abweichung zwischen den kurzfristigen (geodätischen) und langfristigen (geologischen) Verkürzungsraten im nördlichen Pamir weist auf eine Diskrepanz in den Versatzraten entlang des nördlichen frontalen Verwerfungssystems hin. Darüber hinaus weisen weder die heutige Seismizität noch die historischen Aufzeichnungen auf große Erdbeben der Stärke $M_w > 7$ hin, wie sie bei einer solch signifikanten Verschiebung zu erwarten wären. Stattdessen zeigen rezente und historische Erdbeben komplexe Bruchmuster innerhalb und quer zu seismotektonisch definierten Segmenten, die die Pamir-Gebirgsfront begrenzen, was unser Verständnis der Verwerfungsinteraktion und des seismogenen Potenzials dieses Gebiets herausfordert. Die Wechselwirkungen zwischen Seismizität und der Geometrie der Überschiebungsfrent sind somit nicht gut verstanden.

In dieser Dissertation verwende ich verschiedene Verfahren, um das seismogene Verhalten entlang der PFT zu bestimmen. Dazu werden zunächst paläoseismische Daten aus fünf Schürftgräben entlang des zentralen Segmentes der PFT (cPFT) erhoben und eine segmentweite Erdbebenchronologie zusammengestellt. Dieser neue Datensatz liefert wichtige Erkenntnisse über die Häufigkeit, die Stärke und das Bruchausmaß vergangener Erdbeben entlang der cPFT. Darauf basierend wurden fünf bzw. sechs Paläoerdbeben interpretiert, die sich entlang der nördlichen Pamir-Gebirgsfront in den letzten ~ 7 ka bzw. ~ 16 ka ereigneten. Meine Ergebnisse deuten darauf hin, dass davon mindestens drei große Erdbeben die gesamte Länge des zentralen Segments durchbrochen haben und der Bruch möglicherweise sogar die Segmentgrenzen überschritten hat, mit einem Wiederholungsintervall von $\sim 1,9$ kyr und potenziellen Magnituden von bis zu $M_w 7,4$. Entscheidend an dieser Stelle ist, dass ich keine Hinweise auf sehr große (d.h. $M_w \geq 8$) Erdbeben gefunden habe.

Meine paläoseismischen Ergebnisse werden anschließend mit morphometrischen Analysen entlang des zentralen PFT-Segmentes verknüpft, um eine segmentweite Verteilung der kumulativ versetzten Geländestufe entlang fluvialer Terrassen zu ermitteln. Aus dieser Verteilung wird eine langzeitliche Versatzrate für die cPFT modelliert. In der westlichen Hälfte der cPFT zeigen meine Untersuchungen deutliche Unstimmigkeiten zwischen dem Versatz und der Ausdehnung des Oberflächenbruchs auf. In Anbetracht der deutlich höheren Geländestufen im westlichen Bereich deuten die Beobachtungen auf einen reiferen Verwerfungsabschnitt hin. Somit besteht Potenzial für zukünftige Verbindung der Segmente und potenziell starke Erdbeben.

Mit meinen Daten konnte ich eine mittlere horizontale Bewegungsrate von $4,1 \pm 1,5$ mm/Jahr während der letzten ~ 5 kyr für die cPFT ermitteln, welche nicht vollständig mit der von GNSS abgeleiteten heutigen Verkürzungsrate von ~ 10 mm/Jahr übereinstimmt. Dies deutet auf eine komplexe Verteilung des Spannungsaufbaus und eine potenzielle Aufteilung dieser Spannungen zwischen der cPFT und den übrigen Verwerfungen und Falten innerhalb des Pamirs hin, welche möglicherweise mit einem teilweise blockierten regionalen Décollement einhergehen.

Der letzte Teil der Arbeit liefert neue Erkenntnisse über den Oberflächenbruch des Nura-Erdbebens der Stärke 6,6 (M_w) aus dem Jahr 2008, das sich entlang der östlichen PFT ereignete. Ich untersuche diesen Bruch im Hinblick auf seine strukturelle Komplexität, indem ich umfangreiche Feldbeobachtungen mit hochauflösenden digitalen Oberflächenmodellen verknüpfe. Ich erstelle eine Karte der Bruchausdehnung, des gemessenen Gesamtversatzes und aktualisiere regionale geologische Beobachtungen. Auf der Grundlage dieser Daten entwickle ich für dieses Gebiet Szenarien für ein tektonisches Modell, das mit Biegegleitfalten in mesozoischen und känozoischen Sedimentschichten im Zusammenhang steht. Ich zeige, dass diese Formen mit älteren, kumulativ versetzten seismogenen Strukturen übereinzustimmen scheinen und auf eine wiederkehrende, langfristige Deformationgeschichte entlang dieses Sektors der nördlichen Pamir-Gebirgsfront hinweisen.

Die umfangreichen Forschungsarbeiten meiner Dissertation resultieren in einer paleoseismischen Datenbasis der letzten $\sim 16,000$ Jahre, welche zum Verständnis des seismogenen Verhaltens der PFT, aber auch zu dem von segmentierten Überschiebungssystemen in aktiven Kollisionsgebieten beitragen. Meine Beobachtungen unterstreichen, wie wichtig die Kombination verschiedener methodischer Ansätze in den Geowissenschaften ist, insbesondere in strukturell komplexen tektonischen Gebieten wie dem nördlichen Pamir. Die Diskrepanz zwischen den von GNSS abgeleiteten heutigen Deformationsraten und denen aus verschiedenen geologischen Archiven im zentralen Teil, und die weite Verbreitung der Deformation durch erdbebenbedingten Dehnungstransfer im östlichen Teil offenbart die Komplexität dieser Kollisionszone und erfordert künftige Studien mit multitemporalen und interdisziplinären Ansätzen.

ACKNOWLEDGEMENTS

My deep gratitude goes to my supervisor, Manfred Strecker. Thank you for your continuous support and guidance, and for sharing your great experience and knowledge with me. But also thank you, for your patience, and the confidence and trust you showed me at any time that helped me to keep going, despite the life-changing events that unexpectedly intervened. I would like to give my sincere thanks to my second supervisor, J Ramón Arrowsmith. Thank you for your endless engagement and inspiring passion for the geosciences. The experiences I have had through your help at ASU, in various conferences and field trips, as well as those I have had with your work group, are priceless, and I am immensely grateful to have had the opportunity to. I would like to thank both of you for your shared experiences in the field, the detailed discussions, and all the reviews and insightful comments that contributed to the development of this dissertation. It has been an immensely stimulating experience working with both of you over the course of my PhD, and I look forward to more fruitful collaborations.

I would like to take this opportunity to say a special thank you to my former supervisor and personal role model Angela Landgraf, without whom I would not have taken this path of doctoral studies in the first place, but without whom I would not have come this far either. Thank you for taking me to the beautiful realm of Kyrgyzstan during my master's thesis, where my view of life was fundamentally changed by the experiences I gained there. You are an inspiring person for me, both scientifically and personally, and because of you I had the necessary strength and self-esteem, as well as the endurance to realize my scientific path, and to achieve greater goals.

The fieldwork for this dissertation would not have been possible without the Institute of Seismology at the National Academy of Science of Kyrgyzstan and Kanatbek Abdrakhmatov. A special thanks goes to my amazing field team Atyrgul Dzhumabaeva, Sultan Baikulov, Alana M. Williams. It was great to work and spend time with you. Thank you for your perseverance and naturally functioning team work, within a fun and warm family atmosphere.

A great thank you goes also to many in the academic realm. Firstly, I would like to thank my mentor Sabrina Metzger, for the helpful discussions and feedback, scientific or otherwise. Thank you also to others who still are or at some point spent time at the Institute of Geoscience for great discussions, providing helpful suggestions and sharing their experiences and knowledge with me: Frank Krüger, Ed Sobel, Jonathan Weiss, Heiko Pingel, Julius Jara, Victoria Georgieva, and Simon Riedl. A warm thank you to my office mates Lélia Libon, Alessia Borghini and Iris van der Veen for sharing some good times. Great thanks to Tanja Klaka-Tauscher.

An immense thanks goes to my special close friends Anna, Ben and Taylor, who I met at the Institute and who have become an important part of my life. Thank you for always being there for me, for always strengthening me and for the many great moments together over all the years. Thanks to my partner, Manu, for your beautiful soul and existence. Your support has been like magic. Finally, a lot of love goes to my parents, my granny and my sister for giving me the space to go my way, not just scientifically, and for your constant love and support, no matter what.

This dissertation is part of the CaTeNA-project within the Client II program of and funded by the Federal Ministry of Education and Research (BMBF; Sub-project grant 03G0878E to Manfred Strecker). Part of this work was supported by the Volkswagen Foundation grant AZ 86860 to O. Korup, A. Landgraf, and A. Dzhumabaeva, the Deutsche Forschungsgemeinschaft (D.F.G.) granted to M. Strecker, an INTAS grant by the EC to M. Strecker and K. Haselton, the U.S. National Science Foundation grant EAR-9805319 to R. Arrowsmith, and the German Science Foundation project STU 525/2-2 awarded to K. Stübner.

CONTENTS

ALLGEMEINEVERSTÄNDLICHE ZUSAMMENFASSUNG	vii
ABSTRACT	ix
ZUSAMMENFASSUNG	xi
ACKNOWLEDGEMENTS	xiii
LIST OF FIGURES	xvii
LIST OF TABLES	xix
LIST OF ABBREVIATIONS	xxi
1. Introduction	1
1.1. Background.....	3
1.2. Study area and key research questions	4
1.3. The structure of this thesis.....	7
1.4. Publication and author contribution	8
2. The Pamir Orogen	9
2.1 Geodynamic and tectonic setting.....	9
2.2 The Northern Pamir	12
2.2.1 Structural framework of the Pamir Thrust System	12
2.2.2 Geological overview.....	14
2.2.3 Deformation and seismic activity along the Pamir Thrust System.....	16
3. Methods	18
3.1. Preparation and field campaigns	18
3.1.1. Field characterization along the central Pamir Frontal Thrust	18
3.1.2. Nura region.....	20
3.2. Remote sensing-based geologic mapping of fault zones and Quaternary deposits.....	20
3.3. Digital surface models.....	20
3.4. Vertical separation measurements	22
3.5. Paleoseismic trenching.....	23
3.6. Geochronology	25
3.6.1. Radiocarbon dating – ¹⁴ C dating.....	25
3.6.2. Infrared-stimulated luminescence dating.....	26
3.7. Chronological analysis.....	28
3.7.1. OxCal-based earthquake-age modeling.....	28
4. Results I: Geology and geomorphology along the central Pamir Frontal Thrust	30
4.1. Structural style and geomorphology of the central Pamir Frontal Thrust segment	30
4.2. Vertical separation along the cPFT	32
4.3. Excavation sites	34
4.4. Description of stratigraphy and structural context exposed in the excavations.....	39
4.5. Summary	42

5. Results II: Paleoseismology along the central segment of the PFT	43
5.1. Paleearthquake chronologies from five excavation sites	43
5.1.1. T1 – Achyk-Suu (39.48°N 72.50°E).....	47
5.1.2. T2 – Achyk-Suu (39.48°N 72.51°E).....	50
5.1.3. T3 – Ylaisu (39.48°N 72.52°E)	55
5.1.4. T4 – Komansu (39.50°N 72.65°E).....	59
5.1.5. T5 – Tashkungey (39.52°N 72.77°E).....	62
5.2. Displacement per event.....	66
5.3. Summary	67
6. Results III: Seismogenic behavior along the central Pamir Thrust.....	68
6.1. Paleearthquake correlation and recurrence along the segment.....	68
6.2. Late Quaternary dip-slip rate	71
6.3. Summary	74
7. Results IV: Earthquake geology of the 2008 M_w 6.6 Nura event.....	75
7.1. The 2008 M_w 6.6 Nura earthquake.....	75
7.2. Geological and structural framework.....	77
7.3. The Nura earthquake site.....	80
7.3.1. Morphological and stratigraphic observations.....	81
7.3.2. Digital surface model and data compilation.....	85
7.4. The 2008 Nura earthquake surface rupture	87
7.4.1. Displacement-vector measurements and rupture-trace mapping.....	87
7.4.2. Surface breaks and local geomorphology	89
7.4.3. Description and kinematic interpretation of the surface rupture	89
7.4.4. Vertical separation.....	99
7.5. Possible secondary effects associated with the 2008 Nura surface rupture.....	102
7.6. Stream network analysis	103
7.7. Summary	104
8. Discussion and conclusions	105
8.1. The central Pamir Frontal Thrust.....	105
8.1.1. Paleearthquake allocation and potential obstacles	105
8.1.2. Completeness of the paleo-earthquake chronology along the central PFT	107
8.1.3. Partial versus full-segment ruptures	109
8.1.4. Holocene slip rate versus GNSS shortening rates	112
8.2. The 2008 M_w 6.6 Nura earthquake surface rupture	115
8.2.1. Characteristics of the surface breaks and kinematic interpretation.....	115
8.2.2. Seismogenic behavior of the Irkeshtam fault.....	118
8.2.3. Deformation model of the Nura region in the context of prior investigations	120
8.3. Conclusions	123
Bibliography.....	125
Appendix A: Supplementary material for Chapter 4	141
Appendix B: Supplementary material for Chapter 5	147
Appendix C: Supplementary material for Chapter 7	160

LIST OF FIGURES

Chapter 1

- Figure 1.1** Past earthquakes and the range of earthquake magnitudes 2
Figure 1.2 Overview of seismogenic behavior during ruptures along fault zones 4
Figure 1.3 The Pamir-Tien Shan collision zone..... 5

Chapter 2

- Figure 2.1** Seismotectonic overview of the Pamir orogen 11
Figure 2.2 Cenozoic structures and earthquakes of the Northern Pamir..... 13
Figure 2.3 Geological overview of the N. Pamir, Alai Valley, and S. Tien Shan 15

Chapter 3

- Figure 3.1** The Pamir Frontal Thrust (PFT)..... 19
Figure 3.2 Surface rupture of the 2008 Nura earthquake 19
Figure 3.3 Schematic sketch of aerial platform-based structure from motion (SfM)..... 21
Figure 3.4 Schematic illustration of vertical separation (VS) measurement routine..... 22
Figure 3.5 The Achyk-Suu trenching site. 24
Figure 3.6 Schematic illustration of decay of ¹⁴C concentration with time..... 25
Figure 3.7 Illustration of the two sampling techniques used for IRSL dating..... 27

Chapter 4

- Figure 4.1** Topographic and geologic overview of the central Pamir Frontal Thrust (PFT) 31
Figure 4.2 TanDEM-X based hillshade image with Pamir Frontal Thrust (PFT)..... 32
Figure 4.3 Topographic profiles..... 33
Figure 4.4 Distribution of the modelled vertical separation (VS)..... 33
Figure 4.5 Satellite images and Quaternary geologic map of trenching sites 34
Figure 4.6 Field view of trench T1 36
Figure 4.7 Field view of trench T2 36
Figure 4.8 Field view of trench T3 38
Figure 4.9 Field view of trench T4 38
Figure 4.10 Field view of trench T5..... 39
Figure 4.11 Exemplary principal stratigraphic units along the central Pamir Front Thrust ..40
Figure 4.12 Simplified stratigraphic profiles along the central PFT 41

Chapter 5

- Figure 5.1** Examples of fault zones exposed in the trenches..... 44
Figure 5.2 Photomosaic and interpreted trench log of trench T1, Achyk-Suu 48
Figure 5.3 Schematic summary of the structural and stratigraphic results, trench T1 50
Figure 5.4 Photomosaic and interpreted trench log of trench T2, Achyk-Suu 51
Figure 5.5 Schematic summary of the structural and stratigraphic results, trench T2 55
Figure 5.6. Photomosaic and interpreted trench log of trench T3, Ylaisu..... 56
Figure 5.7 Schematic summary of the structural and stratigraphic results, trench T3. 58
Figure 5.8 Photomosaic and interpreted trench log of trench T4, Komansu 60
Figure 5.9 Schematic summary of the structural and stratigraphic results, trench T4 62
Figure 5.10 Photomosaic and interpreted trench log of trench T5, Tashkungey..... 64
Figure 5.11 Schematic summary of the structural and stratigraphic results, trench T5..... 66

Chapter 6

- Figure 6.1** Compilation of all surface-supturing paleoearthquakes..... 69
Figure 6.2 Site earthquake-timing PDFs combined by multiplication..... 70

Figure 6.3 Per-event dip-slip displacements and Late Quaternary dip-slip rate.....	71
Figure 6.4 Near-field estimates for cumulative dip-slip displacement.....	72
Figure 6.5 Dip-slip rate derived from vertical separation along the central PFT.....	74

Chapter 7

Figure 7.1 Overview of recent seismicity of the eastern part of the N. Pamir range front ...	76
Figure 7.2 Topographic and geologic overview of the eastern Pamir-Tien Shan collision .	78
Figure 7.3 The Nura study site	80
Figure 7.4 Field views of landslide-deposit	83
Figure 7.5 View of Qm ₃ stratigraphy.....	84
Figure 7.6 Different digital surface model (DSM) maps for the Nura site	86
Figure 7.7 Distribution of the vector-survey blocks.....	87
Figure 7.8 Characteristics of the 2008 Nura surface rupture	88
Figure 7.9 Observation zones along the Nura surface rupture.....	90
Figure 7.10 Zone A and northeastern end of zone B.....	92
Figure 7.11 Central part of zone B.....	93
Figure 7.12 Southwestern end of zone B.....	94
Figure 7.13 Northeastern end of zone C	95
Figure 7.14 Zone D	96
Figure 7.15 Zone E.....	97
Figure 7.16 Zone F.....	98
Figure 7.17 Selected topographic profiles along the 2008 Nura surface rupture	99
Figure 7.18 Vertical separation (VS) along the 2008 Nura surface rupture	100
Figure 7.19 Comparison of the scarp-height distribution	101
Figure 7.20 Secondary effects along the 2008 Nura surface rupture	102
Figure 7.21 Stream-channel network and knickpoints in the Irkeshtam fault-zone.....	104

Chapter 8

Figure 8.1 Summary of the paleoearthquake data for the PFT	108
Figure 8.2 Map of the 2008 Nura earthquake surface rupture	116
Figure 8.3 Cross-sectional view of the easter	122

Appendix

Figure A1 Scarp perpendicular topographic profiles along the cPFT	142
Figure B1 Uninterpreted high-resolution photomosaic, trench T1.....	148
Figure B2 Uninterpreted high-resolution photomosaic, trench T2	149
Figure B3 Uninterpreted high-resolution photomosaic, trench T3	150
Figure B4 Uninterpreted photomosaic, trench T4	151
Figure B5 Uninterpreted high-resolution photomosaic, trench T4	152
Figure B6 Per-event dip-slip measurements	159
Figure C1 High-resolution DSM generated from UAV, Nura site.....	165

LIST OF TABLES

Chapter 4

Table 4.1 Infrared Stimulated Luminescence ages, cPFT	41
Table 4.2 Radiocarbon Samples, cPFT	42

Chapter 5

Table 5.1 Radiocarbon Samples, trenches.	45
Table 5.2 Infrared Stimulated Luminescence ages, trenches	46
Table 5.3 T1: Summary of indicators for paleoearthquakes	49
Table 5.4 T2: Summary of for paleoearthquakes.....	52
Table 5.5 T3: Summary of indicators for paleoearthquake.....	57
Table 5.6 T4: Summary of for paleoearthquakes.....	60
Table 5.7 T5: Summary of indicators for paleoearthquakes	65
Table 5.8 Summary of refined paleoearthquake timing.....	67

Chapter 6

Table 6.1 OxCal models for paleoseismic sites.....	70
Table 6.2 Summary of cumulative vertical separation and dip-slip displacement.....	73

Chapter 7

Table 7.1 Infrared Stimulated Luminescence ages (IRSL at 150°C); Nura	82
Table 7.2 Data acquisition summary of individual digital surface model (DSM).....	86

Appendix

Table C1 Measurements for the displacement vector along the Nura surface rupture.....	160
--	-----

LIST OF ABBREVIATIONS

σ	Sigma; standard deviation
<i>cPFT</i>	Central Pamir Frontal Thrust
<i>BP</i>	Years before 1950 A.D.
<i>CMT</i>	Centroid moment tensor
<i>DEM</i>	Digital elevation model
<i>DSM</i>	Digital surface model
<i>DS</i>	Dip slip
<i>dGNSS</i>	Differential GNSS
<i>GCP</i>	Ground control point
<i>GNSS</i>	Global navigation satellite system
<i>InSAR</i>	Interferometric synthetic-aperture radar
<i>IrkF</i>	Irkeshdam Fault
<i>IRSL</i>	Infrared stimulated luminescence
<i>ka</i>	Thousand years before present
<i>kyr</i>	Thousand years
<i>MPT</i>	Main Pamir Thrust
M_0	Seismic moment
M_w	Moment magnitude
<i>PFT_{N/S}</i>	Pamir Frontal Thrust north/south
<i>PTS</i>	Pamir Thrust System
<i>SfM</i>	Structure from Motion
<i>UAV</i>	Unmanned aerial vehicle
<i>UTM</i>	Universal Transverse Mercator coordinate system
<i>VS</i>	Vertical separation
<i>WGS 84</i>	World Geodetic System
<i>TS</i>	Top soil

Chapter 1

Introduction

Next to strongly coupled ocean-continent subduction zones, active collisional mountain belts comprise areas of important global seismic-energy release, ongoing deformation and uplift (e.g., Jackson, 1980; Seeber et al., 1981; Gordon & Stein, 1992; Sanz de Galdeano et al., 1995; Tatar et al., 2004; Lin et al., 2009; Schurr et al., 2014; Dal Zilio et al., 2018). In ocean-continent subduction settings it is commonly observed that large earthquakes are associated with extensive ruptures within, but also beyond seismotectonic segments that characterize the forearc (e.g., Melnick et al., 2009; Jara-Muñoz et al., 2015). In terrestrial collision settings, such as along the Himalayan orogen, similar rupture zones have been interpreted to have been activated during megathrust earthquakes (e.g., Mugnier et al., 2013; Wesnousky et al., 2017; Vassallo et al., 2020; Zhao et al., 2021). In this thesis I will focus on the active tectonics and the seismotectonic characteristics of the northern sector of the Pamir orogen, a major Cenozoic collision zone in Central Asia between the northwestern part of the Indian indenter and Eurasia (Molnar & Tapponnier, 1975; Leith, 1982; Burtman & Molnar, 1993; Strecker et al., 1995; Burtman, 2000; Schmidt et al., 2011; Sobel et al., 2013; Thompson Jobe et al., 2017), where a poorly constrained seismotectonic segmentation of the mountain front exists (Nikonov et al., 1983; Arrowsmith & Strecker, 1999; Strecker et al., 2003; Thompson et al., 2015; Li et al., 2019a). In this context the principal objective of my dissertation is to decipher the multi-temporal seismogenic behavior of the frontal fault of the Pamir Thrust System (PTS) that bounds the Trans-Alai Range of the seismically active northern Pamir collision zone in southern Kyrgyzstan. My approach is based on neotectonic fault-zone mapping, the geomorphic study of tectonically active landforms, remote sensing, and paleoseismology. In this analysis of the active tectonics with regard to the neotectonic character of this area I work on deformation features across different timescales, involving hundreds to thousands of years. For this reason, and before defining my most relevant research questions, I first define the terms *active tectonics*, *neotectonics*, and *paleoseismology*.

According to R. Wallace (1981) the study of *active tectonics* involves the analysis of those tectonic movements that are “*expected to occur within a future time span of concern to society*”. As such, the assessment of active tectonic features in the landscape includes the study of seismogenic features that form an integral part of the field of *neotectonics* – a sub-discipline of structural geology, which is applied to reach a solid mechanistic understanding of ongoing deformation processes at plate boundaries or within the interior of the continents. Although the term *neotectonics* has not been stringently defined, in this thesis it is used in the sense of Stewart & Hancock (1994), who classify neotectonic studies as those that address present-day movements at the surface and the responsible forces in the Earth's crust. In particular, the rates and the geometries of the structures that characterize a currently prevailing regional state of deformation and geodynamic conditions, constitute the focus of Neotectonics studies. Consequently, this type of studies

integrates the analysis of seismogenically triggered structural and geomorphological phenomena in the landscape.

The ultimate goal of *neotectonic* and *active tectonic* studies is thus to identify areas prone to seismogenic deformation, its timing, rates, and associated hazards. The analysis of active faults includes the definition of earthquake location, magnitude, displacement, slip rate and recurrence (e.g., Wallace, 1981; Council et al., 1986; Molnar, 1987; Stewart & Hancock, 1994; Pirazzoli, 2019). These are key parameters to understand the present-day tectonic behavior in the context of the regional tectonic evolution and long-term fault behavior. The determination of deformation features through seismological and geological approaches provides a combination of instrumentally recorded data and information gleaned from tectonic landforms and geological archives (for a review see Burbank & Anderson, 2011). However, to bridge the gap between present-day and long-term deformation characteristics recorded in form of Quaternary tectonic landforms, reliable information beyond decadal timescales (i.e., those that cover periods of instrumental data acquisition) is needed. Unfortunately, such information is often difficult to obtain due to erosion processes that degrade or obliterate fault scarps and tectonic landforms (e.g., Davis, 1899; Mayer, 1986; Grützner et al., 2017). Consequently, such information may be highly selective in its rendition of past processes as it is potentially fragmentary and disparate in time and space. To reveal information about tectonic manifestations in the landscape between instrumental records and Quaternary landscape evolution on timescales of several 10^3 to 10^4 yrs, *paleoseismological* studies have been increasingly applied to reduce this lacuna (e.g., Yeats & Prentice, 1996; Yeats et al., 1997; Burbank & Anderson, 2011). *Paleoseismological* studies rely on sedimentological, geochronological, and structural analysis of exposed fault zones and often provide detailed records of fault activity on centennial to multi-millennial timescales (Figure 1.1) (Wallace, 1981; Crone, 1988; Bull, 2007; McCalpin, 2009).

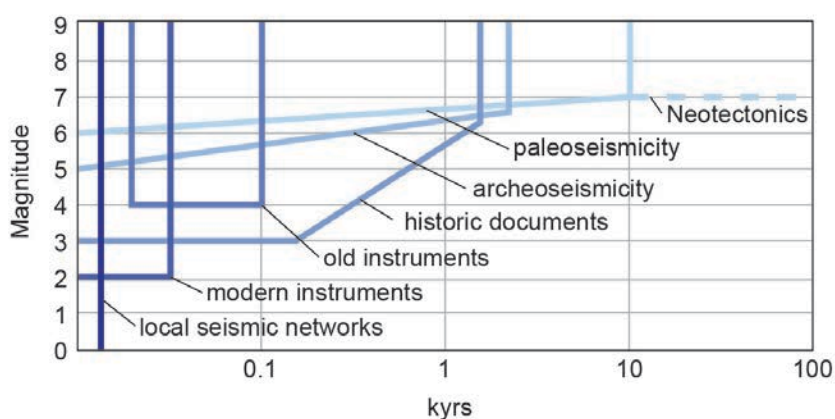


Figure 1.1 Relation between timescales covered by different methods to study past earthquakes and the range of earthquake magnitudes detected. From Caputo & Helly (2008), modified after McCalpin (2009).

1.1. Background

In compressional tectonic environments active orogenic processes are generally accompanied by a high level of seismicity (e.g., Gordon & Stein, 1992; Schulte & Mooney, 2005; Hayes et al., 2020) concentrated along complex thrust and/or reverse-fault systems (e.g., Molnar & Chen, 1983; Yeats et al., 1997). Often difficult to access, these regions represent the most challenging settings to define and characterize seismic source zones and their rupture behavior over time. Reconstructing past surface ruptures in compressional zones is thus often hampered by the nature of reverse and thrust faults, as these structures tend to be more discontinuous and sinuous compared to the linear fault arrays that develop in areas undergoing extension (Arrowsmith & Strecker, 1999; McCalpin & Carver, 2009; Grützner et al., 2017; Ainscoe et al., 2019). Particularly continental collision settings tend to develop spatially and temporally disparate rupture patterns (e.g., Li et al., 2009; Stein et al., 2009), which may lead to significant underestimation of the seismogenic potential of known faults (Rubin, 1996), and uncertainty with respect to unidentified areas of fault slip.

An additional, yet poorly understood aspect of faults in these areas relates to their segmentation and seismogenic behavior during successive ruptures (e.g., DePolo et al., 1991), because geomorphologically and/or geologically defined fault segments along mountain fronts may often interact during major earthquakes (Rubin, 1996; Arrowsmith & Strecker, 1999; Scholz & Gupta, 2000; Davis et al., 2005; Mirabella et al., 2005; Philibosian & Meltzner, 2020). This characteristic of fault-zone behavior is relevant, because individual fault strands within a multi-segment fault system may rupture independently (e.g., Wells & Coppersmith, 1994; Wesnousky, 2006, 2008; Biasi & Wesnousky, 2017) or ruptures may cross segment boundaries during large-magnitude earthquakes. Eventually, individual fault strands may develop into a mature, linked, and potentially more hazardous fault zone (Figure 1.2) (e.g., Ellis & Dunlap, 1988; Scholz & Gupta, 2000; Mirabella et al., 2005; Manighetti et al., 2015).

In addition to geological and paleoseismological observations, slip rate relative to the rate of strain accumulation spanning the entire fault zone is a fundamental parameter for estimating fault activity (e.g., Youngs & Coppersmith, 1985; Anderson et al., 1996). Advances in GNSS (Global Navigation Satellite System) data quality and density provide information on interseismic motion from geodetic observations and help estimate fault activity based on (largely) elastic strain accumulation spanning fault zones (e.g., Youngs & Coppersmith, 1985; Anderson et al., 1996). These measurements, however, only cover decadal timescales (e.g., Abdrakhmatov et al., 1996; Thatcher, 2009; Brooks et al., 2011; Zubovich et al., 2010, 2016; Ischuk et al., 2013; Weiss et al., 2016), whereas studies on active Quaternary faults have repeatedly shown that short-term deformation rates do not always equal long-term rates, resulting in a slip-rate discrepancy (e.g., Gordon & Stein, 1992; Papanikolaou et al., 2005; Oskin et al., 2007; Liu et al., 2011; Gold et al., 2015; Mohadjer et al., 2016; Burgette et al., 2020; Karabacak et al., 2020; Alfaro et al., 2021).

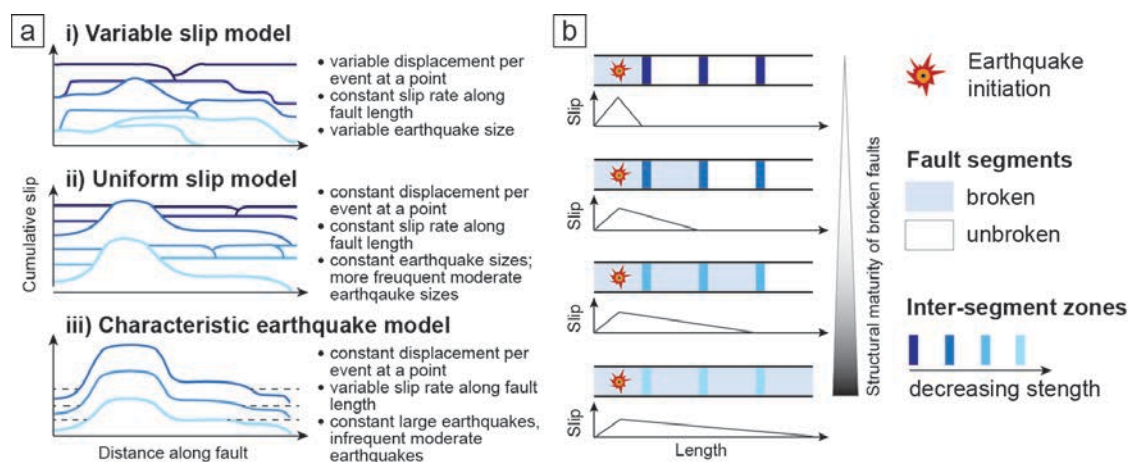


Figure 1.2 Overview of seismogenic behavior during ruptures along fault zones and their segments. (a) Diagrammatic models for variable slip distribution along a fault. Dashed line indicates segment interaction, modified after Schwartz & Coppersmith (1984). (b) Schematic concept of the interplay between segment interaction, fault maturity, and slip-length distribution, modified after Manighetti et al. (2007).

Deciphering such slip-rate discrepancies is crucial for a comprehensive understanding of deformation across complex fault zones. In addition, this information is important to assess whether convergence is absorbed by one main fault that is capable of generating major earthquakes or if it is distributed across several additional structures, some of which may have been deemed irrelevant in terms of their seismogenic potential. Such a dilemma characterizes, for instance, the seismotectonic setting of the 2010-2011 Canterbury earthquakes in New Zealand (e.g., Elliott et al., 2012).

1.2. Study area and key research questions

Seismicity and long-term tectonic processes in the Pamir orogen result from the ongoing collision between Eurasia and India (e.g., Molnar & Tapponnier, 1975; Molnar, 1988; Burtman & Molnar, 1993). Active deformation in the northern Pamir is concentrated along the W-E-oriented northern flank of the orogen and is associated with continental subduction (Figure 1.3) and a heightened level of concentrated crustal seismicity (<25 km) within Central Asia (e.g., Nikonov et al., 1983; Fan et al., 1994; Mechie et al., 2012; Schneider et al., 2013; Schurr et al., 2014; Sippl et al., 2013a). This contrasts with much more spatially and temporally disparate seismogenic deformation in the Tien Shan to the north, implying that slip rates along individual faults could probably be larger here, with possibly shorter return intervals. GNSS profiles across the northern Pamir reveal a significant decrease in horizontal surface motion from the interior of the orogen towards areas north of the PTS over a relatively short distance of ~60 km (Zubovich et al., 2010, 2016; Ischuk et al., 2013; Zhou et al., 2016). This velocity gradient points towards the possibility of localized deformation along the leading edge of the Pamir and the potential for ruptures typical of megathrust events, as seen for instance at the Himalayan thrust front (Bilham et al., 1997;

Berger et al., 2004; Kumar et al., 2006; Bollinger et al., 2014; Mugnier et al., 2017; Lindsey et al., 2018; Bilham, 2019).

The northern Pamir Frontal Thrust fault (PFT) (here defined as PFT_N) within the PTS bounding the Trans-Alai Range is the youngest manifestation of the northward propagation of faulting in the Northern Pamir (Figure 1.3). This region is characterized by well-defined fault scarps that reach several meters in height, and by uplifted and deformed fluvial terraces in the hanging wall of the PFT_N that abruptly terminate at the mountain front (Nikonov et al., 1983; Burtman & Molnar, 1993; Coutand et al., 2002; Mohadjer et al., 2016; Zubovich et al., 2010, 2016). Along the PFT_N, three geologically and geomorphically discrete seismotectonic segments record protracted Quaternary tectonic activity (Arrowsmith & Strecker, 1999; Strecker et al., 2003). Taking into account the empirical relationships between fault length and earthquake magnitude (e.g., Wells & Coppersmith, 1994), the approximate length of 40 km of each of these segments is consistent with the potential occurrence of $M_w \geq 7.0$ earthquakes during thrust-related full-segment ruptures.

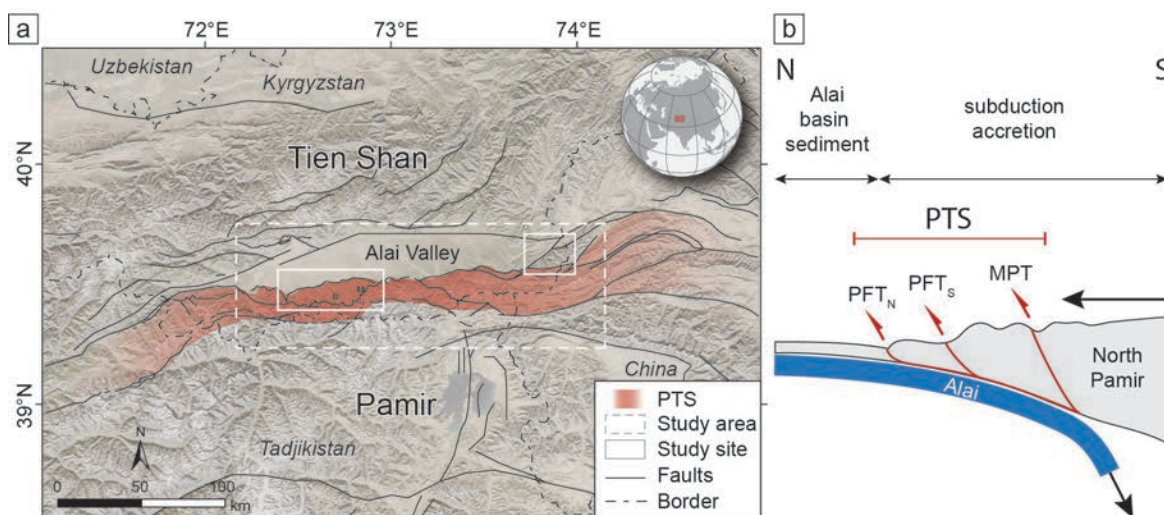


Figure 1.3 (a) The Pamir-Tien Shan collision zone with major Cenozoic faults from the Central Asian Fault database from Mohadjer et al. (2016). PTS = Pamir Thrust System, PFT_{N/S} = Pamir Frontal Thrust North/South, MPT = Main Pamir Thrust. Basemap is World Imagery from Esri. Shaded red area highlights the realm affected by the PTS. Dashed box denotes the study area. Left solid box represents the central PFT and the right box the Nura fieldwork site. (b) Schematic cross-section model of the subduction beneath the Pamir and subduction accretion of the northern Pamir driven by the northward motion of India, modified after Sobel et al. (2013).

An asymmetric distribution of the vertical separation along offset fluvial terraces within the hanging wall of the central segment of the PFT_N (cPFT) (Arrowsmith & Strecker, 1999); rupture propagation between the cPFT and neighboring western transfer zone during the 1978 M_w 6.6 Zaalai earthquake and its aftershock sequence (Nikonov et al., 1983); and widely distributed seismogenic deformation along the eastern segment and within the Trans-Alai Range during the 1974 M_w 7.0 Markansu earthquake (Fan et al., 1994), suggest that mechanical fault interaction between the different segments of the PFT_N has occurred in the recent past (Arrowsmith & Strecker, 1999). Combined with geological evidence of complex transfer zones characterized by a combination of strike- and dip-slip deformation (Nikonov et

al., 1983; Arrowsmith & Strecker, 1999; Pavlis & Das, 2000; Strecker et al., 2003), the different interactions between fault segments in the northern Pamir may be caused by along-strike variations in structural maturity (Figure 1.2) (e.g., Manighetti et al., 2007). Despite tall fault scarps, localized seismicity and geodetically derived indicators for localized deformation, the geodetic (short-term) shortening rates of ~ 10 mm/yr inferred along the PFT_N (Zubovich et al., 2010, 2016; Ischuk et al., 2013; Metzger et al., 2020) are at odds with geological (long-term) shortening rates of $\sim 2\text{--}6$ mm/yr that are constrained from fault scarps in Quaternary deposits (Nikonov et al., 1983; Burtman & Molnar, 1993; Arrowsmith & Strecker, 1999), resulting in an apparent slip-rate discrepancy.

In fact, studies of significant historic earthquakes along the eastern PFT – for instance the 1974 M_w 7.0 Markansu (Nikonov et al., 1983; Fan et al., 1994), 2008 M_w 6.6 Nura (Teshebaeva et al., 2014; Sippl et al., 2014) and the 2016 M_w 6.5 Sary-Tash events (He et al., 2018; Bloch et al., 2021) – show that earthquake-related deformation tends to be more widely distributed within the northern Pamir and is associated with secondary effects such as landsliding and the formation of discontinuous fracture patterns (Nikonov et al., 1983; Arrowsmith & Strecker, 1999). In the eastern sector the earthquakes appear to trigger-fault interaction within and outside the PTS (Teshebaeva et al., 2014; Sippl et al., 2014; Bloch et al., 2021), but often do not reach the surface in spite of strong magnitudes ($M_w > 6.5$) (He et al., 2018). The 2008 M_w 6.6 Nura event is the most recent instrumentally recorded event along the PFT that is associated with a surface rupture. However, this surface rupture was not associated with an exposed, well-developed fault of the PTS, but instead caused an array of linked fractures within the collision zone, possibly associated with the obliquely oriented Irkeshtam Fault (IrkF) adjacent to and north of the PFT (Teshebaeva et al., 2014; Qiao et al., 2015). A local temporary seismic network between August 2008 and July 2010, allowed a detailed evaluation of associated fore-, main-, and aftershocks (Schurr et al., 2014; Sippl et al., 2014), yet, the relations with the Nura main shock and the origin of the observed surface ruptures has remained unresolved.

In summary, the apparent discrepancy between present-day and geological deformation rates, as well as a striking contrast between the level of surface deformation and present character of seismogenic behavior during ruptures along the leading edge of the northern Pamir form the principal motivation for my dissertation. In light of this I have defined the following research questions, which provide the framework of this study:

- What is the seismogenic potential of the PFT_N? What are the expected rupture magnitudes?
- How did ruptures behave along the segments in the past? What does the rupture history say about the seismogenic maturity of the fault and what conclusion can be drawn from this concerning the segmentation thrust faults?
- Are measurements of deformed geomorphic surfaces sufficiently detailed to provide representative statements about deformation rates in this setting?

- Is strain accumulation localized or rather partitioned across several tectonic structures, and what does it imply for the regional tectonic setting?
- What does the surface rupture of the 2008 Nura earthquake reveal about the seismogenic character of Quaternary faults within the continental Pamir-Tien Shan collision zone? And how does it influence the eastern sector of the Pamir Thrust System?

1.3. The structure of this thesis

To address the above questions, I will first provide a brief synthesis of the geodynamic and tectonic characteristics of the Pamir orogen (Chapter 2), which will help to understand the evolution and the current state of the structural setting and the tectonic activity in the northern Pamir. In Chapter 3 I will present detailed information on the different methods applied in this study and evaluate their uncertainties. These introductory chapters are followed by the main part of my dissertation, which is organized into four chapters (Chapters 4-7) and a closing chapter in which I evaluate all of my results in a detailed discussion, followed by a summary of the principal findings and conclusions.

Chapter 4: To accurately characterize the tectonic deformation along the PFT_N, I provide a detailed geologic and geomorphic analysis of the central segment (cPFT) in Chapter 4. I performed systematic fault-scarp profiling to estimate the distribution of cumulative vertical separation along the segment. My investigations confirm the previously indicated asymmetry of the slip profile, but additionally provide new insights into the range of offsets.

Chapter 5: Building on this analysis, I synthesize in Chapter 5 a segment-wide chronological framework of seismogenic faulting along the cPFT by combining geochronological results and paleoseismological observations. Despite ample geological and geodetic evidence for large-scale convergence, I did not find evidence for great $M_w \geq 8.0$ earthquakes. Instead, my results reveal at least three Holocene $M_w \leq 7.4$ earthquakes that probably ruptured the entire length of the cPFT, and possibly crossed segment boundaries. Combined with topographic results from Chapter 4, such a seismogenic character indicates potentially advanced fault maturity and complex segment interaction along the PFT_N.

Chapter 6: Based on the chronological paleoearthquake framework I evaluate in Chapter 6 a deformation rate and rupture-extent characteristics along the cPFT. My estimated Holocene rate of horizontal motion for the cPFT is different from the decadal-scale (i.e., GNSS-derived) shortening rate in this area and suggests more widespread neotectonic activity across the entire PTS, rather than faulting along one major structure. Combined, these findings fundamentally contribute to the seismic hazard evaluation of the Pamir-Alai region, but on a more general level they also help our understanding of seismic behavior of segmented thrust fronts, fault interaction, and slip partitioning in collision zones.

Chapter 7: To investigate the deformation processes and seismogenic behavior along the IrkF, I conducted systematic fracture measurements in the field and offset measurements from a detailed fracture map based on high-resolution digital surface models acquired from unmanned aerial vehicles

(UAV) along the ~8-km-long zone of surface rupture associated with the 2008 Nura earthquake in Chapter 7. Together with a geomorphological and updated geological analysis of the surrounding area I suggest a new deformation model associated with cumulative flexural-slip and bending-moment faulting resulting from deformation of inherited structures within the Pamir-Tien Shan collision zone, which indicates temporally and spatially more distributed deformation along the eastern PTS compared to the central sector. The results of this study not only improve our knowledge about the previously poorly studied area of the frontal sectors of the Pamir orogen, but also serve as an important contribution to the worldwide and unified database of Surface Ruptures due to Earthquakes (SURE), which strengthens the statistics for empirical scaling relationships between earthquake magnitude and fault displacement.

1.4. Publication and author contribution

The majority of the work described in the following chapters has been performed by myself. Results from Chapters 4 to 6 were combined and published in an international peer-reviewed journal. Chapter 7 is in preparation for publication.

Chapters 4, 5 and 6:

Patyniak, M., Landgraf, A., Dzhumabaeva, A., Baikulov, S., Williams, A.M., Weiss, J.R., Hilley, G.E., Preusser, F., Abdrakhmatov, K.E., Arrowsmith, R.J. and Strecker, M.R., 2021. The Pamir Frontal Thrust Fault: Holocene Full-Segment Ruptures and Implications for Complex Segment Interactions in a Continental Collision Zone. *Journal of Geophysical Research: Solid Earth*, 126(12), <https://doi.org/10.1029/2021JB022405>.

M.P, A.L., A. D., S. B., A. W., J R. A., M.S. conducted the field work. F.P. measured the IRSL samples. M.P. created the trench-log inventory and analyzed the data. A.L, J R. A. and M.S assisted with interpretations and editing. J. W. helped integrate geodetic information. All authors discussed the interpretations and commented on the manuscript. M.P. designed the manuscript and all artwork.

Chapter 2

The Pamir Orogen

In this chapter, I describe the geodynamic and tectonic framework of the Pamir orogen to establish the geotectonic and structural context of the study areas in the central and eastern sectors of the Pamir Thrust System, where I analyzed the nature of active deformation processes.

2.1 Geodynamic and tectonic setting

Present-day tectonic activity and deformation across Central Asia results from the ongoing Indo-Eurasian collision (e.g., Molnar & Tapponnier, 1975; Tapponnier & Molnar, 1979; Tapponnier et al., 1986; Burtman & Molnar, 1993; Fan et al., 1994; Ducea et al., 2003; Schwab et al., 2004; Sun et al., 2016). The structurally complex crust of the Central Asian interior has reacted to this Cenozoic collision by reactivating Paleozoic and Mesozoic shear zones and other basement heterogeneities, causing spatiotemporally varying deformation patterns. This includes the active, thick-skinned Laramide-style basement uplifts of the Kyrgyz and Chinese Tien Shan Mountains to the north of the Pamir (e.g., Burtman, 1975; Macaulay et al., 2013, 2014) and thin-skinned deformation zones that exhibit a more systematic, northward-directed deformation regime along the northern Pamir (e.g., Burtman & Molnar, 1993; Strecker et al., 1995; Coutand et al., 2002; Li et al., 2012, 2013, 2019; Sobel et al., 2013).

The Pamir Plateau within the interior of the orogen is the northwestern continuation of the Tibetan Plateau. The Pamir highlands comprise crustal terranes that formed during the Paleozoic and Mesozoic and that were subsequently amalgamated with Eurasia through the successive southward migration of suturing events towards the southern margin of Eurasia (e.g., Tapponnier et al., 1981; Bazhenov & Burtman, 1982; Burtman & Molnar, 1993; Strecker et al., 1995; Robinson et al., 2004; Schwab et al., 2004). Following the Indo-Eurasian collision at ~50 Ma, the suture zones of the Pamir were subsequently bent into a northward convex deformation zone and displaced, while the crust substantially thickened (e.g., Burtman & Molnar, 1993; Ducea et al., 2003; Hacker et al., 2005). Today, the Pamir Plateau region is characterized by a high-elevation (up to ~7000 m), low-relief terrain, with minor Quaternary deformation along strike-slip and normal fault systems (Nöth, 1932; Strecker et al., 1995; Amidon & Hynek, 2010; Schurr et al., 2014; Metzger et al., 2017).

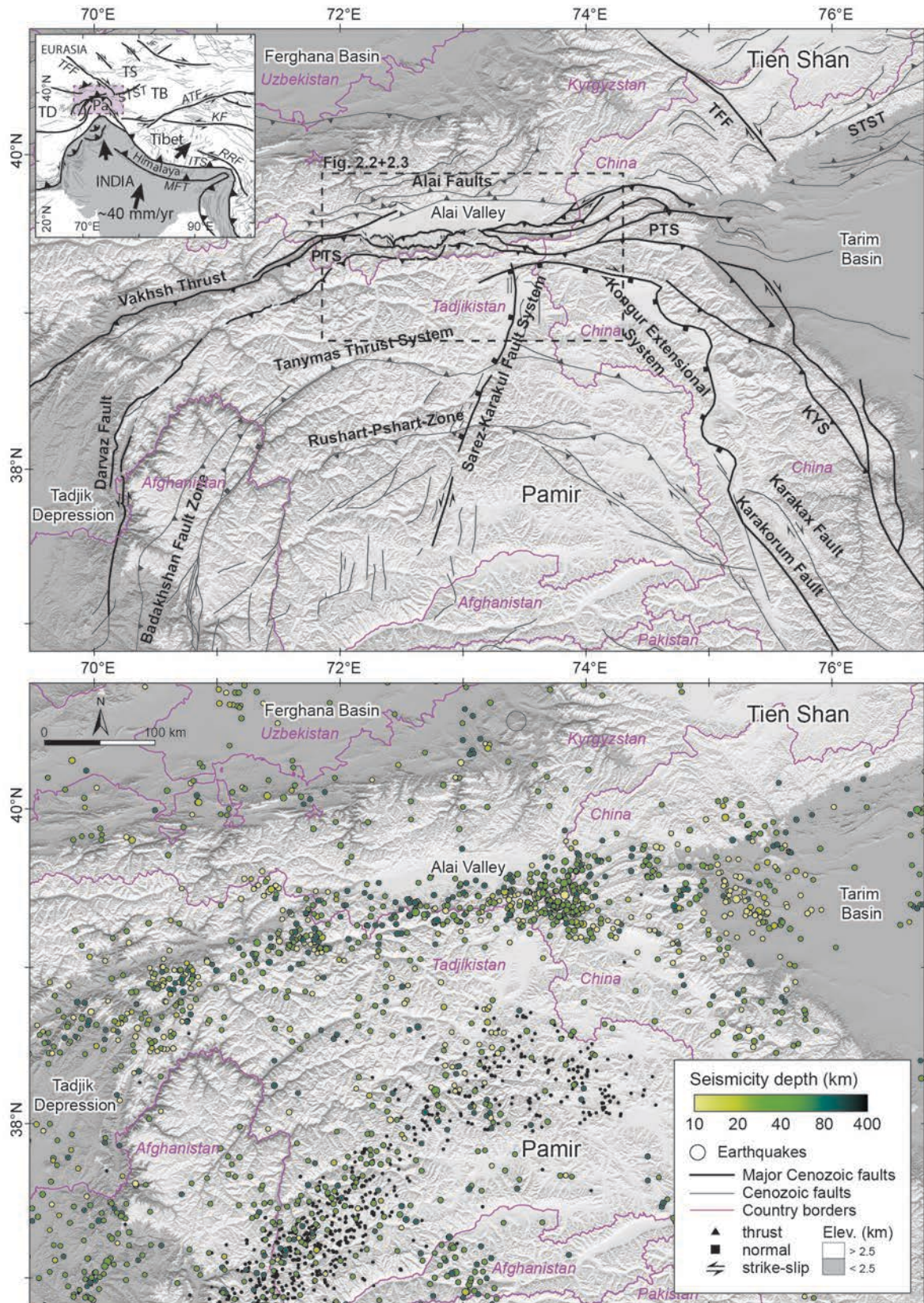


Figure 2.1 Seismotectonic overview of the Pamir orogen at the northwestern continuation of the Indo-Eurasian collision zone (location of the greater study area within the tectonic framework of Central Asia indicated by shaded box in inset). Cenozoic structures outlined in black are modified from the GEM Global Active Fault Database (Styron & Pagani, 2020). Circles indicate crustal seismicity since 1968 from the U.S. Geological Survey seismicity catalog with mixed magnitude types (USGS earthquakes); and from a regional network (Schurr et al., 2014). ATF = Altyn Tagh Fault, ITS = Indus-Tsangpo Suture, JF = Junggar Fault, KF = Kunlun Fault, MFT = Main Frontal Thrust, Pa = Pamir, PTS = Pamir Thrust System, RRF = Red River Fault, STSF = South Tien Shan Fault, TB = Tarim Basin, TD = Tadjik Depression, TFF = Talas Ferghana Fault.

During the Cenozoic (~25-20 Ma), the Pamir indented ~300 km northward with respect to stable Eurasia (Burtman & Molnar, 1993; Sobel & Dumitru, 1997; Cowgill, 2010; Bande et al., 2015; Blayney et al., 2016) as a result of the southward subduction of Eurasian crust beneath the orogen along its northern tip. The northward advance of the orogen is accommodated by the sinistral Darvaz Fault Zone in the west, the Pamir Thrust System (PTS) in the north, and the dextral Karakorum Fault System in the east (Figure 2.1). Combined with the northward migration young thrusts along the PTS, Burtman and Molnar (1994) and Strecker et al. (1995) suggested an *en bloc* northward translation of the Pamir with respect to Eurasia.

The northward advance of these thrust faults has been responsible for the formation and progressive closure of the intermontane Alai Valley and its isolation from the once contiguous Tadjik-Afghan and Tarim sedimentary basins to the west and east, respectively (Figure 2.1) (e.g., Tapponnier et al., 1986; Burtman & Molnar, 1993; Strecker et al., 1995; Robinson et al., 2004; Cowgill, 2010). Today, the Alai Valley separates the northern Pamir front from the Tien Shan Mountains to the north, whereas at its eastern and western flanks the range front has advanced to the southern Tien Shan recording the advanced stage of active continental collision in this region (e.g., Hamburger et al., 1992; Strecker et al., 1995; Pavlis & Das, 2000; Coutand et al., 2002).

Present-day crustal seismicity in the Pamir region is partitioned spatially and limited to well-defined Cenozoic deformation zones, with the highest concentration along an E-W oriented narrow band at the northern Pamir thrust front, and sparser and diffuse seismicity at the eastern and western flanks, respectively. In the Central and Southern Pamir significantly less crustal seismicity is recorded (e.g., Fan et al., 1994; Strecker et al., 1995; Schurr et al., 2014). However, here unusually deep earthquakes and seismic velocity anomalies along a steeply dipping seismogenic zone that reaches depths in excess of ~300 km reflect the subduction of the continental Asian plate (Figure 2.1; e.g., Hamburger et al., 1992; Burtman & Molnar, 1993; Mechie et al., 2012; Sippl et al., 2013a, 2013b; Schurr et al., 2014; Kufner et al., 2016, 2017; Li et al., 2018).

2.2 The Northern Pamir

2.2.1 Structural framework of the Pamir Thrust System

The Northern Pamir range front constitutes the Trans Alai Range, which is bounded by the thrusts of the Pamir Thrust System (PTS) (Nöth, 1932; Nikonov et al., 1983; Arrowsmith & Strecker, 1999; Strecker et al., 2003; Sobel et al., 2013; Thompson et al., 2015; Li et al., 2019). The PTS represents the up-dip expression of the Alai continental subduction zone in form of an accretionary wedge (Hamburger et al., 1992; Burtman & Molnar, 1993; Arrowsmith & Strecker, 1999; Coutand et al., 2002; Strecker et al., 2003; Sobel et al., 2013). The PTS – divided from south to north into the Main Pamir Thrust (MPT) and splays of the Pamir Frontal Thrust (PFT_N and PFT_S) – is dominated by south-dipping thrust faults with strikes varying between N080° to N060°, and local transfer faults (Figure 2.2) (Strecker et al., 1995, 2003; Arrowsmith & Strecker, 1999; Coutand et al., 2002).

Along the eastward continuation of the PTS (east of ~73°20'E), the number of PFT fault splays increases – here defined as PFT_N and PFT_{S1-3} (variously defined in Chinese studies, e.g., Bao & Gao, 2017; Qiao et al., 2017) – north of the southward-diverging MPT (also defined as the Markansu Fault in other studies; e.g., Strecker et al., 1995, 2003; Coutand et al., 2002; Qiao et al., 2017; Xiong et al., 2019) (Figure 2.2). Here the PTS widens northward and merges with the south-vergent fold-and-thrust structures of the southern Tien Shan, where the Tien Shan and Pamir Mountains are effectively in structural contact, separating the Alai and Tarim basins (e.g., Burtman & Molnar, 1993; Thompson et al., 2015; Thompson Jobe et al., 2017; Bufe et al., 2017). At ~74°30'E the PFT thrusts continue eastward by following an apparently sinuous mountain front into a more widely distributed fold-and-thrust province, which eventually merges with the Kashi-Atushi fold-and-thrust system in the northwestern Tarim Basin (Figure 2.1) (e.g., Sobel & Dumitru, 1997; Scharer et al., 2004; Sobel et al., 2011; Li et al., 2013, 2015, 2019; Thompson et al., 2015; Thompson Jobe et al., 2017, 2018).

The south-dipping MPT juxtaposes Pre-Mesozoic and Mesozoic strata, and represents the former frontal thrust that initiated during the late Oligocene to early Miocene (Sobel & Dumitru, 1997; Bershaw et al., 2012; Cao et al., 2013; Sobel et al., 2013), presumably with coeval northward propagation toward the southern Tien Shan. Out-of-sequence thrusting continued along the MPT throughout the Miocene (Coutand et al., 2002), whereas the northern faults seem to have been abandoned and were progressively covered by an up to ~1-km-thick Quaternary conglomeratic fill in the Alai Valley, related to deposition in alluvial fans and glaciofluvial terraces (Coutand et al., 2002; Robinson et al., 2015; Freisleben, 2018).

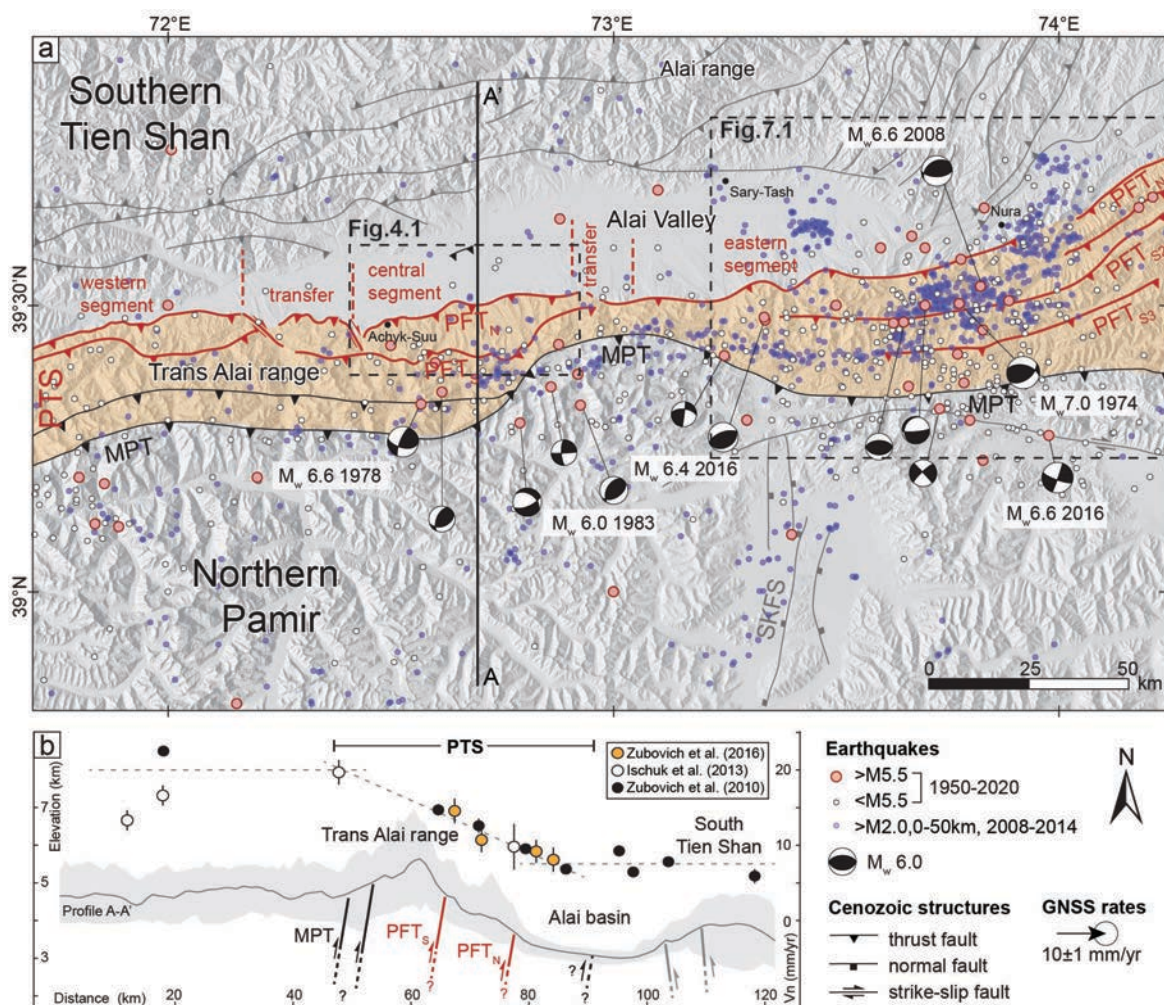


Figure 2.2 Cenozoic structures and earthquakes of the Northern Pamir. (a) Shaded area shows the extent of the Pamir Thrust System (PTS). Note segmentation of the northernmost splay of the PFT (in red), after Strecker et al. (2003). Earthquake epicenters since 1968 in red ($M > 5.5$) and white ($M < 5.5$) from the U.S. Geological Survey seismic catalog with mixed magnitude types ([USGS earthquakes](#)); in blue for the period 2008–2014 from a regional network, indicating for instance, the aftershock sequence from the 2008 M_w 6.6 Nura earthquake (Sippl et al., 2014). Focal mechanisms are from the Global Centroid-Moment-Tensor catalog (Dziewonski et al., 1981; Ekström et al., 2012), Fan et al. (1994), and Sippl et al. (2014). GNSS horizontal surface velocities are relative to stable Eurasia and are color coded according to (b). Hillshade image is based on 30-m resolution NASA Shuttle Radar Topography Mission. Dashed boxes outline study areas from Chapters 4 and 5, and 6, respectively. (b) Northward component of GNSS velocities along A-A' using half-swath width of 80 km. Profile location shown in (a). Thin black line is the mean topography from a 25-km-wide topography swath centered on A-A'. Gray envelope indicates the minimum and maximum swath topography. Vertical exaggeration is ~ 6.4 and the $\sim 30^\circ$ dipping faults are drawn to scale. PTS = Pamir Thrust System, MPT = Main Pamir Thrust, $PFT_{N/S}$ = northern/southern Pamir Frontal Thrust, SKFS = Sarez-Karakul Fault System.

The southern splay of the PFT_S – north of the MPT, still in higher elevation sectors of the Trans Alai range – partly juxtaposes Cretaceous units over Neogene conglomerates, but also cuts into the Neogene strata (Figure 2.2). In contrast, the PFT_S faults within of the eastern PTS continuation form a series of imbricate thrusts of Cretaceous-Paleogene sequences. The hanging wall of the northern splay (PFT_N) delimits the gently northward-sloping alluvial fans of the Alai Valley in the central sector and overthrusts (?) a sequence of folded Silurian-Devonian basement in the eastern sector (Figure 2.2).

Nikonov et al. (1983) pioneered earthquake-geology studies across the northern Pamir. In subsequent studies on the structural and tectono-geomorphic evolution of the Pamir mountain front, Strecker et al. (1995, 2003) and Arrowsmith & Strecker (1999) built on these observations and used the stratigraphic framework for different Quaternary fluvial terrace sequences (Qt₁₋₄) from Nikonov et al. (1983) to suggest that the PFT_N at the Trans-Alai range front comprises three seismotectonic segments – the western, central, and eastern segments – that are inferred to be kinematically linked by dextral transfer faults and oblique thrust faults with semi-independent activity (Figure 2.2).

2.2.2 Geological overview

The long history of numerous geologic and tectonic events combined with ongoing deformation in Central Asia results in a complex and variable stratigraphy in the northern Pamir and adjacent regions. Here, I summarize the major sedimentary units that outcrop in the Northern Pamir, the Alai Valley, and the Southern Tien Shan, with a particular focus on the time span between the late Mesozoic to the present.

The oldest units are Paleozoic low-grade metasediments, constituting the basement of the Alai Valley (Kozlov & Artemov, 1964; Razvalyaev et al., 1964; Burtman, 1975), dominated by Silurian terrigenous strata, 1000 to 2500-m-thick Devonian to middle Carboniferous limestone and marbles, and ≤500-m-thick middle Carboniferous flysch units (Figure 2.3). These strata are intensely deformed and are related to shortening predating the Cenozoic deformation phase (i.e., the Hercynian orogeny). These rocks are the oldest units preserved in the Trans Alai Range and are unconformably overlain by Mesozoic to Quaternary sediments (Burtman, 1975).

The Mesozoic units (Figure 2.3) include ~800 m of Jurassic coarse-grained sandstones and light green to white quartzite pebble conglomerates, interbedded with claystones, including gypsum and coal (Coutand et al., 2002); ~1000 m of early Cretaceous red-colored medium to coarse-grained sandstone interbedded with mudstone (Davidzon et al., 1982); and lower Cretaceous conglomerates, conglomeratic sandstones and siltstones, which grade upward into cross-bedded sandstones (Czassny et al., 1999). These units are overlain by late Cretaceous limestones, marls, claystones, and gypsum (Pojarkova, 1969) deposited during the transgression of the Tethys sea (Hao & Zeng, 1984; Bershaw et al., 2012). The early

Cretaceous deposits constitute 200 to 300-m-thick units within intermediate elevation sectors (~3000 m a.s.l.) of the Trans Alai Range (Arrowsmith & Strecker, 1999).

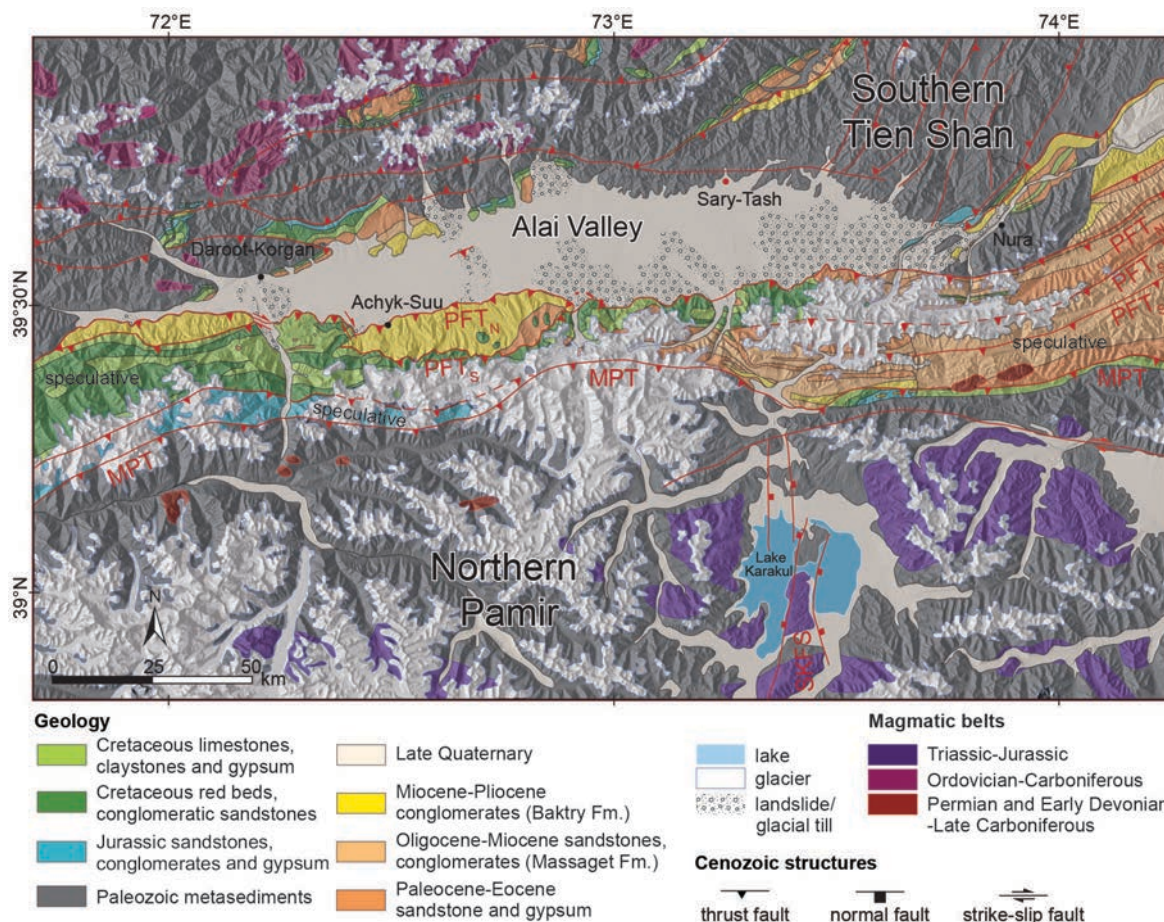


Figure 2.3 Geological overview with major Cenozoic structures of the Northern Pamir, Alai Valley, and Southern Tien Shan. Faults of the Pamir Thrust System are labeled: PFT = Pamir Frontal Thrust, MPT = Main Pamir Thrust. Modified after Kozlov & Artemov (1964), Razvalyaev et al. (1964), Strecker et al. (2003), and Sippl et al. (2014). Data on glacial coverage from RGI Consortium (2017). Basemap is a shaded relief map of a 30-m-SRTM DEM.

Cenozoic sedimentary rocks (Figure 2.3) are represented by Paleocene (~350-m-thick) and Eocene (~400-m-thick) fossiliferous limestones, dolomites, marls, and mudstones containing gypsum. The Eocene strata, however, are only present in the northwestern Alai Valley, north of the axial, westward flowing Kyzylsu River (Coutand et al., 2002). Finally, during the late Oligocene marine environments were superseded by terrestrial sedimentation (Burtman, 2000). Despite these changes, during the Paleogene the Tadjik depression in the west and the Tarim Basin to the east apparently still formed a continuous sedimentary basin via the Alai Valley (Davidzon et al., 1982; Burtman, 2000). The terrestrial environments are represented by the late Oligocene-early Miocene Massaget Formation. In the western Alai Valley this unit is up to 900 m thick and composed of coarsening-upward conglomerates and sandstones interbedded with claystones (Coutand et al., 2002). In the central sector of the Alai Valley the middle Miocene-Pliocene Baktry Formation is ~1300 m thick and comprises massive conglomeratic strata interbedded with thin siltstones. An unconformable contact between the Baktry Formation and

Cretaceous and Paleogene units is exposed in the hanging wall of the western and central sector of the PFT_N (Figure 2.3) (Coutand et al., 2002).

The Quaternary units in the Alai Valley include the early Pleistocene, ~850-m-thick (thinning westward) Sokh Formation, which is composed of gravel to blocky conglomerates and coarse grained sandstones interbedded with siltstone (Coutand et al., 2002). These units are generally covered by coarse middle Pleistocene to Holocene pediment-gravels, glaciofluvial terraces and alluvial-fan gravels, landslide deposits and glacial till (Nikonov et al., 1983; Arrowsmith & Strecker, 1999; Strecker et al., 2003). Burtman and Molnar (1993) interpret the late Neogene and Quaternary units as molasse strata from the northward advancing Pamir Thrust System (PTS).

2.2.3 Deformation and seismic activity along the Pamir Thrust System

Over a relatively short north-south-oriented sector of ~60 km across the PTS (~39°10'–39°50'N) (Figure 2.2), GNSS measurements relative to stable Eurasia (i.e., in an Eurasia-fixed reference frame) document a decrease in present-day NNW-SSE-oriented motion from ~25 mm/yr in the high sectors of the Pamir to ~10 mm/yr north of the Alai Valley (Reigber et al., 2001; Yang et al., 2008; Zubovich et al., 2010, 2016; Ischuk et al., 2013; Metzger et al., 2020). Thus, the northern range front of the Pamir appears to accommodate more than one-third of the ~30–40 mm/yr of total shortening between India and Eurasia (e.g., Molnar & Stock, 2009; Argus et al., 2010; Dal Zilio et al., 2019).

Based on restorations of regional cross sections from seismic reflection data and field observations, Coutand et al. (2002) estimated long-term horizontal shortening rates in the Alai Valley to be less than <1 mm/yr spanning the Neogene (ca. < 25 Ma). Within the PTS, the MPT appears to be virtually inactive, with extremely low Quaternary shortening rates of <1 mm/yr reported from the Chinese sector of the range (Sobel et al., 2011, 2013; Cao et al., 2013; Thompson et al., 2015). The level of current tectonic activity of the southern splay of the PFT (PFT_S) also appears to be rather low (Nikonov et al., 1983; Arrowsmith & Strecker, 1999), whereas Holocene shortening rates reported along the PFT_N, range between ~3.5 and 6 mm/yr (Nikonov et al., 1983; Burtman & Molnar, 1993; Arrowsmith & Strecker, 1999; Li et al., 2012). The PFT_N records recent movement and northward migration associated with a fault-propagation fold linked to displaced late Pleistocene to Holocene alluvial-fan surfaces (Nöth, 1932; Nikonov et al., 1983; Strecker et al., 1995, 2003; Arrowsmith & Strecker, 1999). Hence, the present-day regional convergence seems to be accommodated along the PFT_N (Arrowsmith & Strecker, 1999; Li et al., 2012, 2013; Bufe et al., 2017; Thompson Jobe et al., 2017).

In contrast to adjacent areas to the north and south of the PTS, the elevated strain in this region is reflected by focused crustal seismicity. The present-day high level of seismicity associated with the PTS is concentrated in a narrow, ~15 to 25-km-wide belt north of the MPT, with hypocentral depths in the uppermost 25 km of the crust and along the tectonically active, south-dipping PFT faults (Figure 2.3)

(Fan et al., 1994; Schneider et al., 2013; Sippl et al., 2013b; Schurr et al., 2014). In this region, several earthquakes with $M_w \geq 6.0$ have been recorded. These include the 1974 M_w 7.0 Markansu, the 1978 M_w 6.6 Zaalai, the 2008 M_w 6.6 Nura, and the 2016 M_w 6.4 Sary Tash events (Figure 2.3). The earthquake focal mechanisms indicate dextrally oblique reverse slip, and thrust-dominated faulting with depths ranging from 2 to 17 km (Fan et al., 1994; Ekström et al., 2012; Sippl et al., 2014). Interestingly, despite the large-scale convergence and impressive heights of the fault scarps in Quaternary deposits along the central sector of the Pamir mountain front, no instrumental or historical records have documented events $M > 7.0$ in this region. However, an asymmetric vertical offset distribution along the central segment of the PTF (cPFT) combined with the distribution of paleoseismic dislocations and the rupture patterns of the 1978 M_w 6.6 Zaalai earthquake in the west indicate mechanical interaction between the central, western transfer, and western segments during earthquake ruptures (Nikonov et al., 1983; Fan et al., 1994; Arrowsmith & Strecker, 1999). Deformation in the eastern segment appears to have shifted southward and earthquake-related deformation seems to be more widely distributed and reflected by secondary effects (i.e., landsliding), as demonstrated by the effects of the 1974 M_w 7.0 Markansu earthquake (Jackson et al., 1979; Fan et al., 1994; Arrowsmith & Strecker, 1999; Strecker et al., 2003).

Nikonov et al. (1983) identified voluminous mass-movement deposits in the Alai piedmont, which have been analyzed in more recent studies (e.g., Robinson et al., 2015; Reznichenko et al., 2017) that inferred that these deposits were related to seismogenically triggered collapse of parts of the Trans-Alai mountain front. Based on a compilation of 50 paleo-earthquake-related indicators, Nikonov (1988) estimated a possible maximum magnitude of $\sim M$ 7.6 and an average recurrence time of ~ 1.4 kyr for major earthquakes along the PFT.

Chapter 3

Methods

3.1. Preparation and field campaigns

For the identification of field sites and its accessibility, Google Earth satellite imagery were used, with a focus on the geomorphological fault-scarp expression of the central Pamir Frontal Thrust segment (cPFT) and the Irkeshtam Fault (IrkF) associated with the 2008 Nura earthquake. For the cPFT, these observations were built on prior studies by M. Strecker and JR. Arrowsmith (Arrowsmith & Strecker, 1999; Strecker et al., 2003) and a reconnaissance trip by A. Landgraf and Ch. Haberland within the framework of the Tien Shan-Pamir Monitoring Program (TIPTIMON) funded by the German Federal Ministry of Education and Research. Based on these preliminary evaluations two field campaigns were carried out within the framework of this dissertation in 2017 and 2018, respectively. This dissertation was part of the CaTeNA-project (Climatic and Tectonic Natural Hazards in Central Asia) within the Client II program of and funded by the German Federal Ministry of Education and Research.

3.1.1. Field characterization along the central Pamir Frontal Thrust

Field campaigns in 2017 and 2018 focused on the central Pamir Frontal Thrust segment (cPFT), located in the southern part of the Alai Valley. A total of five sites were selected to perform photogrammetric surveys, mapping, and to open paleoseismic trenches (Figure 3.1). From west to east, trenches were excavated at Achyk-Suu (T1 and T2; opened in 2017), Ylaisu (T3; opened in 2018), Komansu (T4; opened in 1999, revisited in 2017) and Tashkungey (T5; opened in 2018). These sites are separated from each other by 1, 2, 10, and 12 km, respectively. The names of the locations correspond to the principal rivers adjacent to the excavation sites. In addition, samples were taken to date offset terraces. The field observations for the cPFT study in 2017 and 2018 were conducted with assistance from Angela Landgraf, Atyrgul Dzhumabaeva, Sultan Baikulov, Roland Freisleben, Alana M. Williams, J Ramón Arrowsmith and Manfred Strecker. J Ramón Arrowsmith provided unpublished data from field work conducted with George Hilley during a field campaign in 1999 with assistance from Isabelle Coutand, Birka Czassny, Rasmus Thiede, Erin Young, and Manfred Strecker. Atyrgul Dzhumabaeva provided translations and georeferenced information from the study area from Russian literature. Sabrina Metzger and Jonathan Weiss helped me integrate geodetic information from the study area.

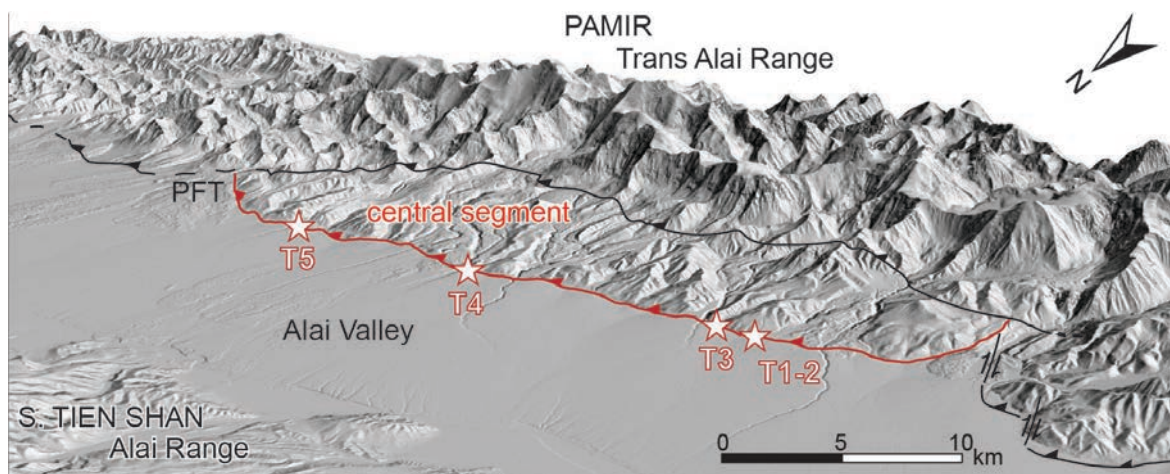


Figure 3.1 The Pamir Frontal Thrust (PFT) along the Trans Alai Range, southern Kyrgyzstan (view SE). The shaded relief map is draped over a 12-m-resolution digital elevation model (TanDEM-X). The central segment of the PFT is outlined in red. Star symbol denotes excavation sites.

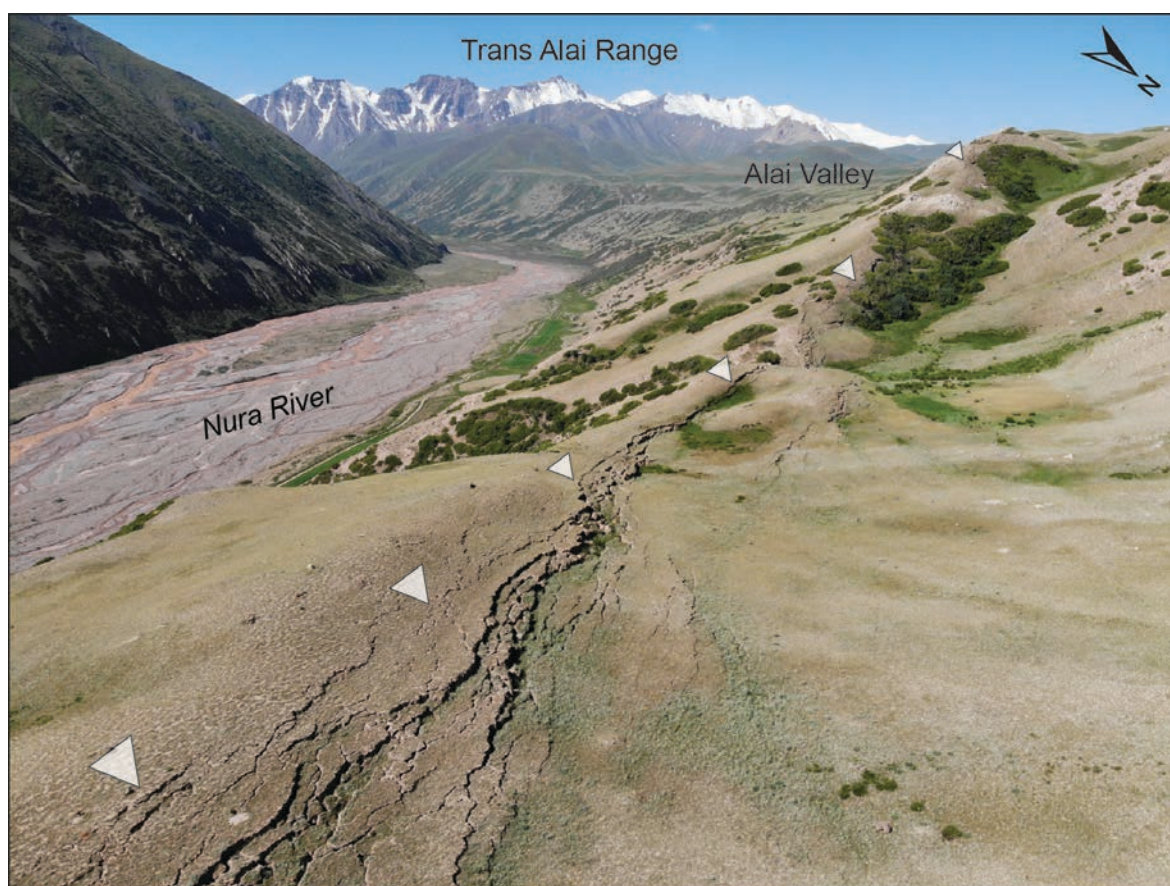


Figure 3.2 Surface rupture of the 2008 Nura earthquake, approximately 5 km southwest of the Nura village, southern Kyrgyzstan (view SW). The surface break extends for ~8 km through Quaternary moraine deposits along the northwestern slope of the Nura River valley.

3.1.2. Nura region

Part of the field campaign in 2018 focused on a photogrammetric survey, photo documentation, mapping, and detailed description of the 2008 M_w 6.6 Nura earthquake surface rupture in the eastern end of the Alai Valley (Figure 3.2). In the surrounding area samples were taken to date mass movements and moraines. The fieldwork was carried out in the area of the Nura village in 2018 with assistance from Atyrgul Dzhumabaeva, Sultan Baikulov, Alana M. Williams, J Ramon Arrowsmith, and Manfred Strecker. Alana Williams and J Ramón Arrowsmith acquired aerial photographs used in this study using unmanned aerial vehicles. Roland Freisleben helped me to generate digital surface models. I conducted the data compilation, modelling, mapping, analysis, interpretations, and writing.

3.2. Remote sensing-based geologic mapping of fault zones and Quaternary deposits

Historical and instrumental seismic data helps to delineate areas that are likely to harbor active faults, i.e. those that are likely to rupture sometime in the future (Wallace, 1981). In order to determine the exact location of such a fault, these areas must be studied in more detail with regard to offset geomorphic features, with the emphasis on Quaternary deposits. In alluvial environments displaced features typically include terrace risers, alluvial fans, channel walls, stream channels, ridges and debris flows (e.g., Burbank & Anderson, 2011).

Remote sensing imagery used in this dissertation includes aerial photographs from unmanned aerial vehicles (UAV), satellite images from high-resolution World Imagery basemap in ArcMap™, Google Earth and PLANET, and digital surface models (DSM) generated from UAV (see below) and 12-m-resolution TanDEM-X digital elevation model (DEM) with a vertical accuracy of ~2 m (Krieger et al., 2007; Rizzoli et al., 2017). For both study areas analyzed in this dissertation existing geological and structural maps were updated to emphasize the Quaternary geology and the distribution of active faults. To do so, field observations and mapping carried out in this study and from previous publications (e.g., Kyrgyz Geodetic and Cartographic Agency, 1978; Nikonov et al., 1983; Arrowsmith & Strecker, 1999; Coutand et al., 2002; Strecker et al., 2003) were combined, and remotely mapped with help of above mentioned basemaps.

3.3. Digital surface models

Digital surface models (DSM) were generated from each study site by acquiring low-altitude (between 35–120 m) aerial photographs during field campaigns using an unmanned aerial vehicle (UAV)

(Figure 3.3). UAV drone models included the DJI Phantom 4 Pro and Mavic Pro carrying cameras with built-in global navigation satellite system (GNSS) with 10 m accuracy and a photo pixel resolution of 5472 x 3648 px and 4000 x 3000 px, respectively. To reduce the positional error of the resulting models, ground-control points (GCP) were placed throughout the survey areas with ~DIN-A0-sized blue tarp targets. The target positions were measured using a

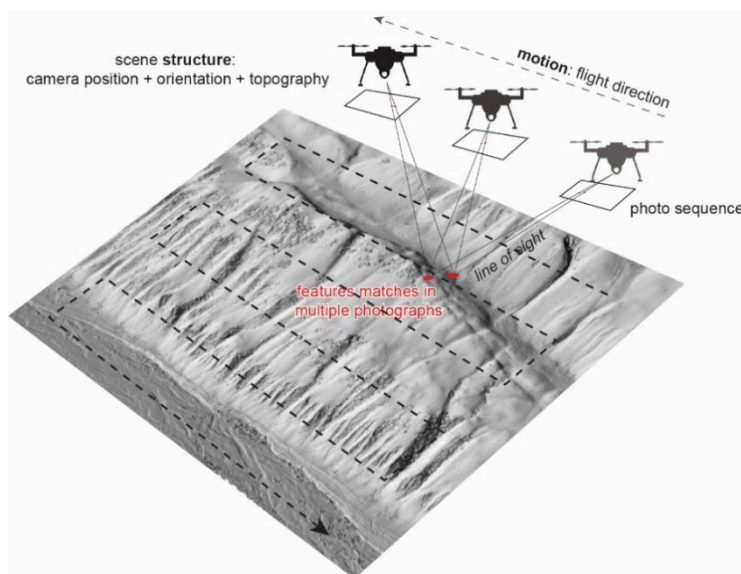


Figure 3.3 Schematic sketch of aerial platform-based structure from motion (SfM) method to produce high-resolution digital surface models (DSM) (modified after Johnson et al., 2014).

kinematic differential GNSS (dGNSS) system with a Leica Viva GS10 Base and Rover system, a CS15 field controller, and AS10 Multi-GNSS Triple-Frequency Compact Antenna. All positions were recorded in absolute coordinates by placing them into the World Geodetic System 1984 (WGS 84) based Universal Transverse Mercator (UTM) grid zone 43N coordinate system (EPSG:32643). The collected raw data was then imported and translated using LEICA Geo Office.

The photogrammetric modeling software Agisoft PhotoScan Pro (v.1.2.1 and v.1.4.3) was used to generate high-resolution point clouds and DSMs (available at OpenTopography; see following chapters for associated links) performing image-based modeling by feature recognition and photo alignment using the Structure-from-Motion (SfM) algorithm (e.g., Bemis et al., 2014; Johnson et al., 2014). After adding the photographs into PhotoScan the DSM workflow included (1) manual removal of take-off, landing or blurred photographs; (2) photo alignment and sparse point-cloud generation; (3) manual marker placement on GCP targets in individual photographs and assignment of the measured dGNSS spatial control data, followed by (4) camera optimization, and (5) high-quality dense point-cloud generation. The final DSM models were compiled with the PhotoScan DEM generation tool, resulting in a resolution between 4 and 10 cm/px. The DSMs were used to produce slope, shaded relief (hillshade), curvature, and aspect maps with the open source Geospatial Data Abstraction Library (GDAL) and to compute a local relief model with ArcMap® and toolbox from Novák (2016). The calculated maps were then used to perform (1) vertical separation measurements (Chapters 4 and 7), (2) mapping of surface offsets displaced by the 2008 Nura earthquake (Chapter 7), and (3) relief and stream channel analysis (Chapter 7).

The accuracy of the DSMs relies on a range of factors during acquisition, including: camera settings, lens type, and resolution; flight stability, flight geometry, photo overlap, and flight altitude; placement,

quantity of GCPs, and dGNSS measurement accuracy; shadows and vegetation at the ground surface. In order to minimize the uncertainty, it was ensured to apply the best practices of which the data-acquisition team was able to control: well-distributed GCP grid, at least 3 GCP targets per ~ 1 km², varying flight altitudes, at least 30% photo overlap, flights during mid-day when winds were slower and the sun angle high.

3.4. Vertical separation measurements

Topographic fault-scarp profiles oriented perpendicular to the fault scarp were extracted from TanDEM-X and the DSMs generated in this study to estimate the vertical separation (VS) of cumulative fault scarps and single-event surface breaks (the 2008 Nura surface rupture), respectively. Here, the VS should not be confused with the fault throw (vertical fault slip), which requires the knowledge of near-surface fault dip and accounts non-parallel far-field slopes (e.g., Thompson et al., 2002; Johnson et al., 2018).

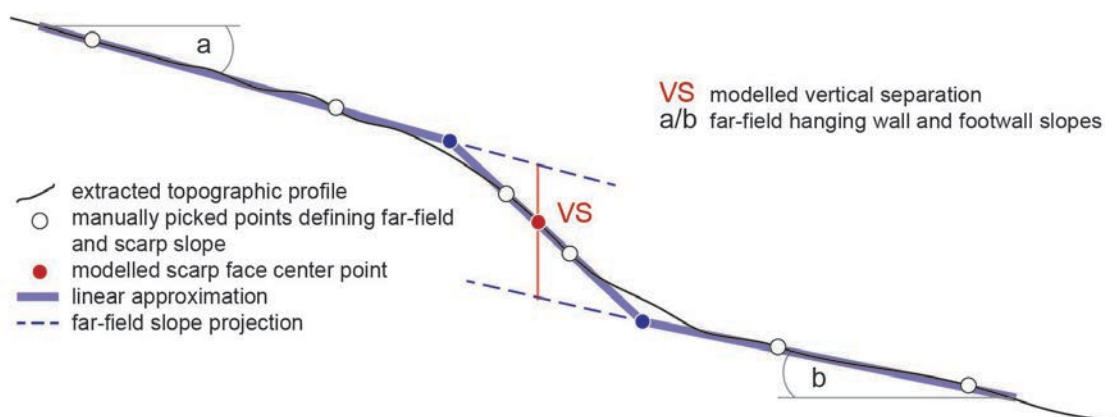


Figure 3.4 Schematic illustration of vertical separation (VS) measurement routine.

For cumulative fault scarp measurements profile locations were manually chosen and drawn on hillshade maps in ArcMap based on the best geomorphic preservation and sparse vegetation to avoid unnecessary noise. Profile lengths range up to 800 m. The VS was modelled following the method of Walker et al. (2015) and using a MATLAB script kindly provided by John Elliott (last update January 2019). This script applies a method for scarp-fit and vertical separation modelling from Monte Carlo sampling through linear regression of geographic points of upper and lower fan slopes, and their intersection with the fault where the scarp gradient is steepest (Figure 3.4). For each profile the extent of the footwall, hanging wall, and fault-scarp face surfaces and the scarp midpoint were manually picked during the script processing. The precision of modeled VS is mainly limited to the TanDEM-X quality and resolution. During linear regression uncertainties in modelled slope angles arise from (1) natural undulations in the ground surface, and/or erroneous DSM generation, and/or presence of vegetation, and (2) from

unquantifiable “user error” while subjectively picking the profile sections during the algorithm execution. These uncertainties in turn propagate to the calculation of the VS. During the modelling of the VS the algorithm assumes a “perfect” pick; thus, the resulting uncertainties are very small and were therefore rounded up to the next decimal when used further.

For VS measurement along the 2008 Nura surface rupture profile locations were generated systematically every 50 m along strike to avoid user-induced bias. Compared to cumulative scarps, the offsets here are small (minimum of tens of centimeter) and often spread across complex surface rupture patterns (i.e., multiple fault splays along one profile). For the VS modelling here, I used a MATLAB script from DuRoss et al. (2019), which follows the same principle of linear approximation of manually picked footwall, hanging wall and scarp face, but allows multiple VS-measurements along one profile and multiple iterations for each individual offset, and provides minimum and maximum VS-values (including the above described uncertainties).

3.5. Paleoseismic trenching

To obtain a detailed record of past earthquakes, their timing, and associated displacements, trenches were excavated across faults with the goal of identifying and documenting the number of earthquake-related event horizons within the subsurface stratigraphic sequence. Remote mapping and preliminary field surveys helped guiding the selection of the excavation sites for this study. Precise locations were selected where the fault scarp (1) appeared unaffected by severe surface erosion that could compromise the subsurface layers (e.g., active stream channels, ponding, agricultural activity or other anthropogenic influence); (2) where all displacement was likely concentrated on a single (in the ideal case) narrow zone; and (3) where the vegetation cover was sparse. The trenches were excavated perpendicular to the fault scarp using a hydraulic excavator, provided and operated by a local worker. In order to achieve the most complete record possible along dip-slip faults the trenches have to be sufficiently deep. During the excavation, care was taken to expose the boundary of the oldest unit (without colluvial wedges) along the fault. In my study area this resulted in trenches up to 3.5 m deep, at least 2.5 m wide and up to 25 m long.

After excavation the trench walls were further sculptured to be vertical and cleaned with scrapers and brushes. Coarse-gravel exposures were smoothed and cleaned from dust with a leaf blower. On the cleaned walls a 1x1 m reference grid was constructed, and the grid points were measured by dGNSS (Figure 3.5). The trench walls were then photographed to reproduce an image-based, seamless and ortho-rectified (combined with dGNSS) photomosaic (see Reitman et al., 2015; Patyniak et al., 2017). Interpreted stratigraphic units, earthquake-related structures, and geochronologic sample locations were flagged and logged onto graph paper.



Figure 3.5 The Achyk-Suu trenching site, a) excavation; b) single-slot trench across a 7-m-high thrust-fault scarp; c) reference-grid measurement with dGNSS; d) view of trench interior.

The principal indicators of ground-rupturing events along dip-slip faults are single or stacked deformed colluvial deposits adjacent to the fault zone. The colluvial material accumulates in a lens-shaped drape over the lower portion of the scarp and is usually thickest at the toe where the slope change is greatest. In my study area, I infer that these colluvial deposits formed as a result of coseismic or immediate postseismic collapse of the overhanging scarp tip followed by subsequent interseismic debris and wash-dominated fault-scarp degradation, which buried the fault tip (e.g., Meghraoui et al., 1988; McCalpin & Carver, 2009; Rockwell et al., 2013; Patyniak et al., 2017). In a subsequent surface rupture, the lens is cut as the rupture drives the hanging wall through and over the deposit and ground surface. The resulting remnant has a wedge shape but is not to be confused with postrupture “colluvial-wedge” formation seen for instance in normal faulting settings (e.g., McCalpin, 2009).

Following this assignment, each colluvial deposit represents one rupturing event of the bounding fault, and helps determining the number of events and amount of coseismic displacement. However, the evolution of such indicators in thrust- and reverse-faulting environments is more complex compared to settings dominated by normal faulting, and the depositional geometry is often affected by different processes during repeated faulting, especially if ruptures occur along the same fault zone. These processes include (1) deformation of the preserved colluvial deposits due to thrusting; (2) “bulldozing” of the fault tip especially along faults with dips $<20^\circ$; and (3) truncation at the upslope limits of the deposits by fault-zone migration or splaying (e.g., McCalpin & Carver, 2009) and were carefully evaluated before further displacement calculations were made and/or considered.

3.6. Geochronology

In order to establish a paleoearthquake chronology (i.e., bracketing the age of paleoseismic evidence), the ages of offset markers along faults (i.e., river-terrace surfaces), and other geomorphic features (i.e., landslide deposits, moraines), radiocarbon and luminescence dating methods were used in this study.

3.6.1. Radiocarbon dating – ^{14}C dating

The radiocarbon dating method uses organic material deposited in sedimentary horizons and it relies on the radioactive decay of ^{14}C (Figure 3.6; half-life 5730 years) to nitrogen ^{14}N (Libby, 1961). Radiocarbon is constantly produced by the interaction of cosmic rays with nitrogen and oxygen in the atmosphere (Kamen, 1963), and oxidizes in the air to form carbon dioxide. Through constant cycling between the atmosphere and biosphere, plants and living organisms assimilate ^{14}C from atmospheric CO_2 . As the exchange is terminated, the ^{14}C content starts to decay systematically (given as ratio of ^{14}C to stable ^{12}C), thus indicating the time span since the organism died (Trumbore, 2000). The content of ^{14}C in the atmosphere varies through time due to natural changes in the production rate, and in the distribution of carbon between ocean, biosphere, and atmosphere (e.g., Stuiver et al., 1991), and more recently through anthropogenic influences (i.e., fossil-fuel burning and atomic weapon testing) (Trumbore, 2000).

To correct the variations and determine calendar ages (calibrated ^{14}C ; BP = years before 1950 A.D.) from conventional ^{14}C ages, a calibration software with established correction factors is used (see below). The radiocarbon dating method is applicable to organic matter that formed within the last 50 to 60 kyrs, however, the reliability of age determination decreases for specimens older than ~ 45 ka (Trumbore, 2000).

The accuracy of the radiocarbon dating method relies mainly on the accuracy of the calibration scale, on the time interval of sample formation, the measuring uncertainties, but most importantly on the reliability of the sample itself (Trumbore, 2000). Terrestrial gastropods, for instance, are often debated whether their ages are reliable, due to potential incorporation of ^{14}C -deficient (or “dead”) carbon from surrounding limestone into the shell (Goodfriend & Stipp, 1983). Although newer studies have shown that even in carbonate terrains this does not have to be the case (Pigati et al., 2004, 2010), it is recommended to cross correlate the snail ages with independently derived ages of plant specimens. In

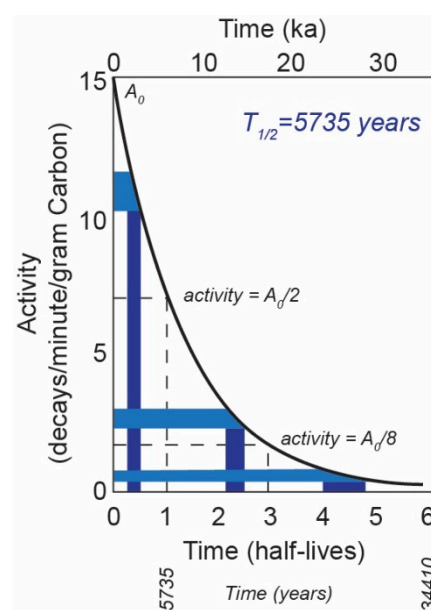


Figure 3.6 Schematic illustration of decay of ^{14}C concentration with time. Shaded bars indicate the uncertainty in activities to uncertainties in age through time. Modified after Olsson (1968) and Burbank & Anderson (2011)

addition to the problem of additional ^{14}C incorporation and/or incomplete closure of the exchange system, further uncertainties may arise during sampling. Radiocarbon samples from organic-rich sediments generally provide a minimum depositional age for a given unit, assuming that soil development and charcoal incorporation postdate the deposition. However, uncertainties may also arise due to cross contamination from both young and old carbon. Younger material can be incorporated into older sedimentary units by bioturbation (burrowing organisms and roots) or during excavation and trench wall cleaning (McCalpin, 2009). In areas with thrust faults older material may come from reworked old deposits or detrital (i.e., recycled) charcoal eroded from the hanging wall and/or adjacent source areas.

For measurements of trench sediments, single specimens of macroscopic charcoal and terrestrial gastropods were collected. Where these materials were not present, bulk-soil samples from dark organic-rich stratigraphic horizons were collected. If possible, these samples were further pretreated by manually picking charcoal fragments under a microscope. To minimize the possibility of erroneous age estimations, great care was taken while sampling and it was attempted to apply several dating methods per stratigraphic unit, respectively. In my study area, where vegetation is limited to grass cover, I assume that inherited ages related to events, when the plant cover may have burned, are negligible. Individual cases of potentially distorted ages are discussed in more detail in the corresponding chapters. All samples were dated with low-energy ^{14}C accelerator mass spectrometry at the Poznan Radiocarbon Laboratory (Poland) and the University of California Irvine Keck-CCAMS facility.

3.6.2. Infrared-stimulated luminescence dating

The luminescence dating method is based on a dosimetry technique, applicable in a variety of terrestrial stratigraphic settings and to sediments ages up to 100–200 kyrs (e.g., Forman et al., 2000; Rhodes, 2011; Forman, 2015). The luminescence dating relies on optically stimulating mineral grains with light of a respective wavelength to evaluate the time that has elapsed since the grain was last exposed to daylight (Huntley et al., 1985; Aitken, 1998; Forman et al., 2000; Duller, 2004; Preusser et al., 2008; Rhodes, 2011; Forman, 2015). Within sediments, environmental-ionizing radiation from naturally occurring radionuclides within minerals (internal dose) and surrounding (external dose) materials move electrons from lower to higher energy levels. These energized electrons become meta-stably trapped within crystal lattice defects of mineral grains, resulting in luminescence-signal accumulation. During exposure to light absorbed optical energy causes detrapping, which erases the luminescence signal (bleached) until it eventually gets completely removed (zeroed). Thus, when subsequently buried and re-exposed to natural radiation, absorbed energy ($1\text{ J kg}^{-1} = 1\text{ Gy}$ [Gray]) gets newly stored, and its accumulated amount since zeroing (paleodose or equivalent dose, D_e) can be measured. Dividing the paleodose by the dose rate (estimated separately) allows sample-age estimation (e.g., Forman et al., 2000; Preusser et al., 2008; Duller, 2008; Burbank & Anderson, 2011):

$$Age (ka) = \frac{\text{Equivalent dose (Gy)}}{\text{Dose rate (Gy/ka)}} \quad (3.1)$$

During my field campaigns predominately silty-sand units were sampled for luminescence dating, using two different sampling approaches following the methods of Gray et al. (2015): (1) homogenous units with small grain sizes were sampled by horizontally driving aluminum tubes with a diameter of 5 cm (or 2-cm thick PVC in 1999) into cleaned, vertical stratigraphic sections; these were retrieved and light-tight closed; and (2) heterogeneous units including pebbles were sampled at night with a low intensity red LED headlamp by sieving, approximately 500 g of sand fraction (250 – 500 μm) were isolated from the bulk sample and filled into double-bagged 4-mil-black conductive bags (Figure 3.7). Afterwards, additional ~500 g of material from the surrounding area were sampled for dose-rate estimation through low-level gamma-spectrometry.

An accurate age estimate with meaningful uncertainty values from luminescence dating primarily relies on sufficiently bleached samples before burial. During optical stimulation sediments get zeroed after less than 1 hour of exposure, so that any preexisting luminescence signal in the grains resets (Aitken, 1998). Deposits used to date landscape or offset features in my study are loess or retransported loess deposits as well as lacustrine silts transported as suspended sediments from the upper part of the water column. Therefore, based on longer-lasting transport processes, these samples can be considered to have been optically well reset. However, many sediments considered in my trenching studies are related to fluvial, colluvial and alluvial processes, where partial bleaching (not complete resetting due to fast transport or no exposure to light) or incorporation of older mineral grains is a common source of error (Forman, 2015). Furthermore, similar to other studies in active mountain belts (Preusser et al., 2006), the quartz grains in my study area show a low luminescence sensitivity.



Figure 3.7 Illustration of the two sampling techniques used for IRSL dating. (a) Sampling tools: aluminum tubes and lids for hammering. (b) Sampling with aluminum tubes during the day. (c) Sampling locations after sampling at night into conductive bags.

To minimize the uncertainties following measures were taken: during sampling (1) locations in the trench exposure were carefully chosen, so that sediments were not collected from collapsed, thus poorly exposed, or unambiguous areas; and (2) if possible, radiocarbon samples were additionally collected to provide age cross-checks. During sample measurements, (3) feldspar grains were used instead of quartz,

which have a higher luminescence sensitivity (e.g., Rhodes, 2011) and were measured by using infrared stimulated luminescence (IRSL) signals, and (4) the single aliquot technique was applied, which to a certain degree allows to isolate partially bleached or out-of-sequence grains (Duller, 2008; Preusser et al., 2008; Forman, 2015). One major disadvantage of feldspar in luminescence dating is the effect of anomalous fading due to higher dose-saturation levels (Wintle, 1973; Spooner, 1994), which results in age underestimation and thus needs to be accordingly corrected (e.g., Huntley & Lamothe, 2001; Auclair et al., 2003; Lamothe et al., 2003; Kars & Wallinga, 2009).

Samples collected in 1999 were processed in the same year by S. Forman at the Luminescence Dating Research Laboratory at the University of Illinois, Chicago. All samples collected after 1999 were processed at the Institute of Earth and Environmental Science (University of Freiburg, Germany) and associated gamma spectrometric analyses were conducted by Detlev Degering at VKTA Rossendorf, Germany. For additional information on sample preparation and measurement protocol for IRSL dating see Appendix B1.

3.7. Chronological analysis

In order to model slip rates and integrate paleoearthquake timing of different sites along a fault, chronologies with representative precision and accuracy need to be provided. A good geochronological record in turn requires combination of information from multiple sources, including absolute and relative ages, as well as cross-correlations between data sets. To put such data into a common reference frame, I used the radiocarbon calibration and analysis software OxCal (v.4.4) (Bronk Ramsey, 1995, 2001) using the IntCal 20 calibration curve (Reimer et al., 2020). OxCal provides calendar-year correction of radiocarbon ages and age modeling of events using Bayesian analysis of sequences of ages that pre- and post-date these (Bronk Ramsey, 2008, 2009, 2017b). Bayesian analysis is a statistical method, which provides probability statements for unknown parameters. In paleoseismic studies, age-relevant parameters such as laboratory uncertainties and stratigraphic relationships, together with their likelihood (PDF; probability density function) are used to refine chronological data and model undated events (e.g., Lienkaemper & Ramsey, 2009). Resulting possible solutions are modelled through Markov Chain Monte Carlo sampling (Bronk Ramsey, 2008).

3.7.1. OxCal-based earthquake-age modeling

To evaluate earthquake timing and associated uncertainties at each paleoseismic trench site, I followed the modeling approach for paleoseismic data developed by Lienkaemper & Ramsey (2009). For the paleoearthquake models I used depositional models (simple *Sequence*; Bronk Ramsey, 2008), which are

independent of depth, i.e., undated events (paleoearthquakes) are not influenced by burial depth (DuRoss et al., 2011).

Individual depositional layers were modeled with the *Phase* function, which does not require chronological ordering within the layering. If available within a layer, both radiocarbon and luminescence age data were used to model age distributions with the *R_Date* function (for radiocarbon calibration based on a calibration curve) and *C_date* function (as calendar date in years before present), respectively. When samples from different sources were used to determine the age of a stratigraphic unit (i.e., from the hanging wall and footwall in trench exposures, and associated terrace surfaces outside the trench), I used the *Combine* function that combines the number of PDFs which all provide independent information on the same unit.

Within my trench exposures, most earthquake horizons are defined by clear surface displacements with consequent depositional change from soil-development to scarp derived colluvial deposition. The sampling density naturally varies from layer to layer, based on sampling material availability. Consequently, to model PDFs of undated paleoearthquakes, I used the *Boundary* function, which models independently from sample density within the pre- and post-faulting deposits. In contrast to the *Date* function, which assumes that more samples reflect more depositional time, the *Boundary* function does not affect the timing of an earthquake. In some cases, minimum- and maximum-limiting ages of the bracketing layers did not overlap, but were separated by a considerable time gap of several thousands of years (see Discussion). In order to provide a broad, uniform PDF, I bracketed the earthquake (Boundary) with the *Zero_boundary* function, which models a linear rising/falling from/to zero when paired with a *Boundary*.

Chapter 4

Results I: Geology and geomorphology along the central Pamir Frontal Thrust

The present-day deformation along the northern Pamir orogen concentrates at the Pamir Thrust System and is assumed to be localized in a narrow thrust zone bounding the Trans-Alai range front, the Pamir Frontal Thrust. The offset of Quaternary deposits and landforms in the Trans Alai range and Alai Valley region indicates structural segmentation of the mountain front and demonstrates that deformation on regional scale is accommodated along faults active on different temporal scales. This chapter focuses on the examination of the local geology and geomorphology associated with the central sector of the Pamir Frontal Thrust (cPFT). To investigate the structural character of the segment I estimate the offset of associated landforms to present a segment-wide offset distribution, which can help to assess the seismogenic maturity of this fault. To explore the genesis of the offset landforms I investigate their associated stratigraphy, age, and inferred origin to provide a stratigraphic framework for my paleoseismic investigations in the following chapter.

4.1. Structural style and geomorphology of the central Pamir Frontal Thrust segment

The central segment of the Pamir Frontal Thrust (cPFT) is structurally defined by pronounced, segmented, occasionally left-stepping north-vergent thrust faults along the uplifted piedmont of the central Trans Alai mountain front (Figure 4.1). This sector of the thrust system forms along faulted Pleistocene and folded Neogene conglomerates that are overthrust by Paleogene and Cretaceous units at higher elevations of the hanging wall farther to the south (Nikonov et al., 1983).

The delimitation of the cPFT is largely based on the distribution and deformation of the prominent Qt_3 terrace (old nomenclature fgQ3/fgQIII; Nikonov et al., 1983) that is generally preserved in the hanging wall of the cPFT and extends for several km into high-elevation sectors of the Trans-Alai Range (Figure 4.1). The fluvial terrace deposits reflect a former extensive braided-stream environment in the mountain valleys that transitioned into alluvial fans in the piedmont; the deposits constituting these terrace surfaces are in erosional or conformable depositional contact over Qm_2 moraines and join the terminal Qm_3 moraines that presumably formed during the penultimate, Early Holocene (~10 ka) glaciation in this region (Arrowsmith & Strecker, 1999; Strecker et al., 2003). The formation of Qt_3 was followed by faulting and range uplift combined with regional incision (Arrowsmith & Strecker, 1999). Occasional aggradation or lateral erosion allowed the formation of the lower and younger terrace Qt_4 (fgQ4/fgQIV; Nikonov et al., 1983). Arrowsmith & Strecker (1999) report radiocarbon ages for the Qt_3 surface from the Ylaisu (~7.2 ka) and Syrinadjar (~6.4 ka) river terraces (Figure 4.1). My

paleoseismological investigations focused on profiling the fault-zone topography and excavating trenches at five sites along the cPFT (Figure 4.1). The area of investigation covers ~25 km of the total ~35-km-length of the central segment.

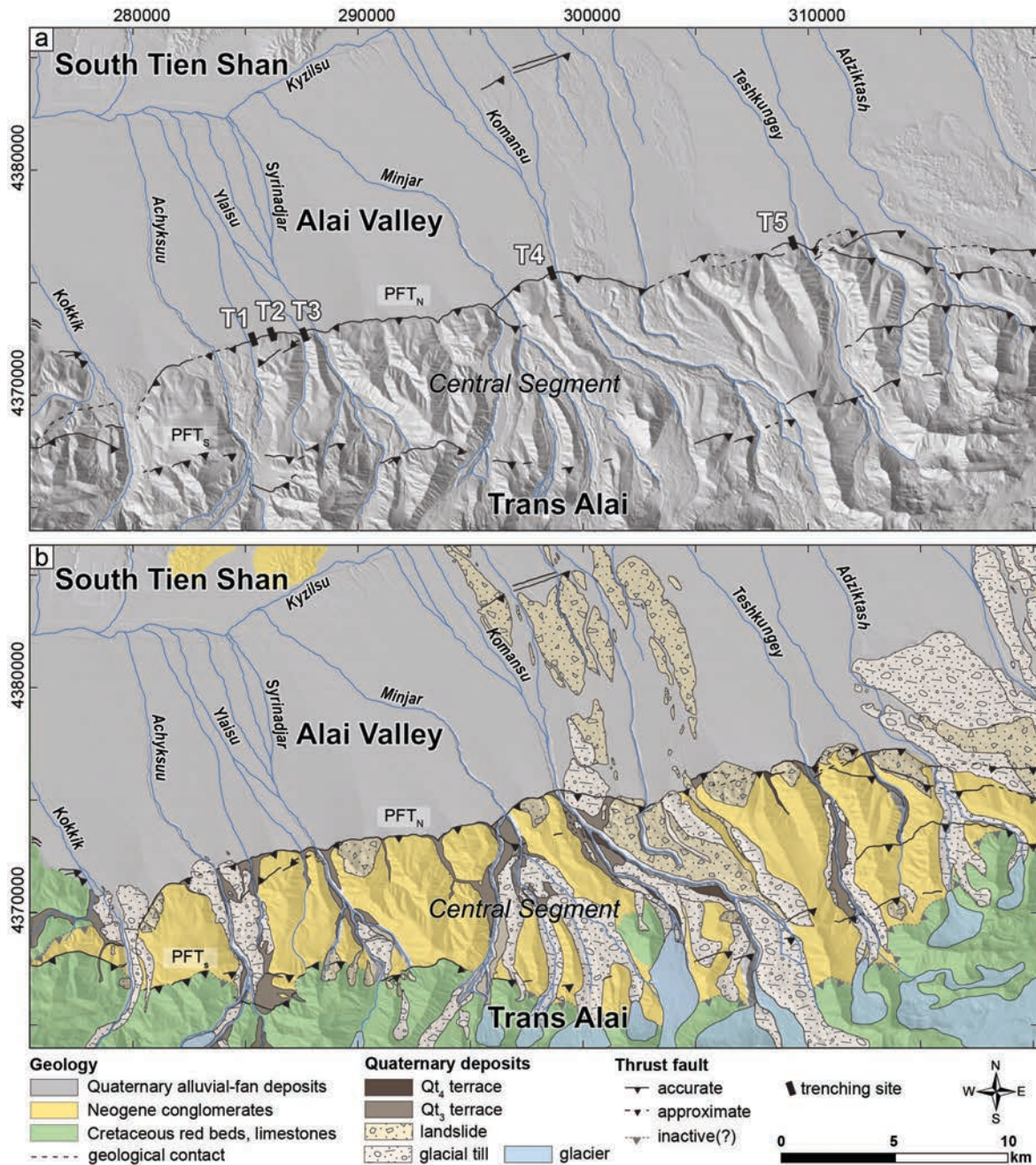


Figure 4.1 Topographic and geologic overview of the central segment of the Pamir Frontal Thrust (PFT) (see Chapter 2, Figure 2.3 for map location). (a) Shaded relief map, derived from the TanDEM-X image, with updated surface fault traces of PFT_N and PFT_S (black lines). Major rivers outlined in light blue. Blue bars indicate locations of trenching sites. (b) Updated geological map modified after Strecker et al. (2003) and 1:200,000 Geological Map sheets J-43-I (Chong-Alai) (Razvalyaev et al., 1964).

4.2. Vertical separation along the cPFT

Total vertical separation (VS; as defined in Yang et al., 2015) was measured from the offset Q_t surface along the cPFT by extracting scarp-perpendicular topographic profiles from the 12-m-resolution TanDEM-X model (Figure 4.2).

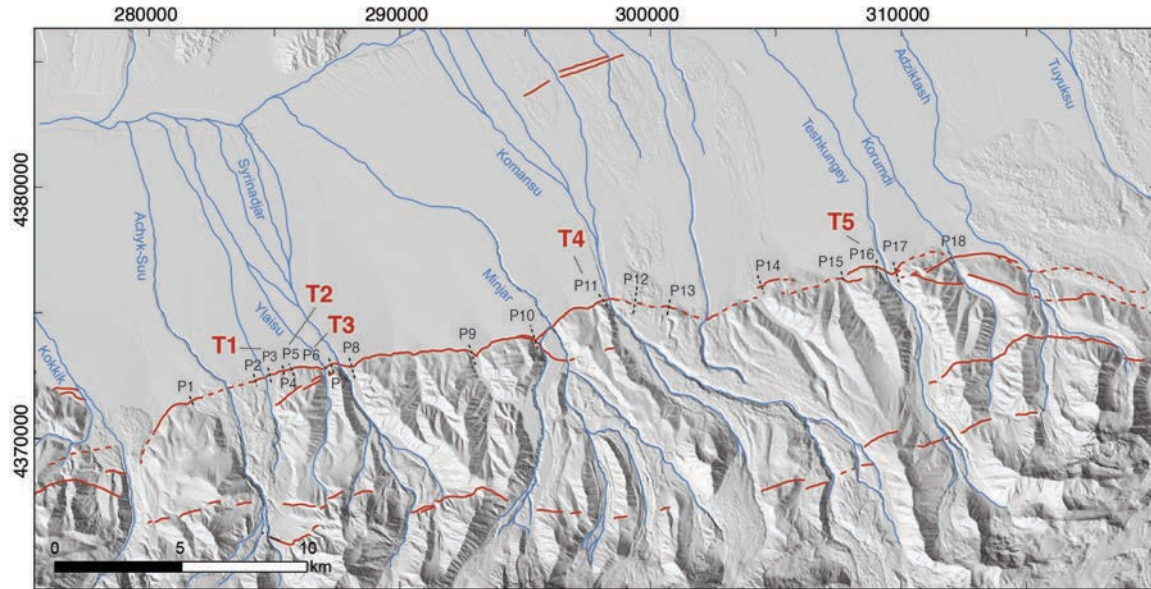


Figure 4.2 TanDEM-X based hillshade image with Pamir Frontal Thrust (PFT) traces (red) and location of scarp perpendicular profiles (dashed black lines); T1 to T5 denote paleoseismic trench locations.

In order to assess the accuracy of the TanDEM-X model, I compared these profiles with profiles extracted from the 0.5-m-resolution digital surface models (DSM) (generated from UAV photography) of the scarp from trenching sites T1, T2, T3 and T5 (see Figure 4.5 for location). The correlation shows that the elevations and slopes from the extracted data do not differ significantly (see profile P3, P5, P6 and P16 in Figure 4.3 and Appendix A, Figure A1), thus I am confident that the TanDEM-X-based profiles are suitable for reliable VS calculations. The resulting far-field cumulative VS along the cPFT ranges from ~ 5 – 16 m, with nearly parallel hanging-wall and footwall slopes at $\sim 2^\circ$ (Figure 4.3, Figure 4.4). The along-strike distribution shows an asymmetry with significantly higher VS (up to double) in the western half of the central segment, consistent with results presented in Arrowsmith & Strecker (1999), with a maximum VS of 16.2 ± 0.2 m at the Syrinadjar river terrace (Profile P8; Figure 4.4 and Appendix A, Figure A1), and an average VS of 9.2 ± 0.3 m.

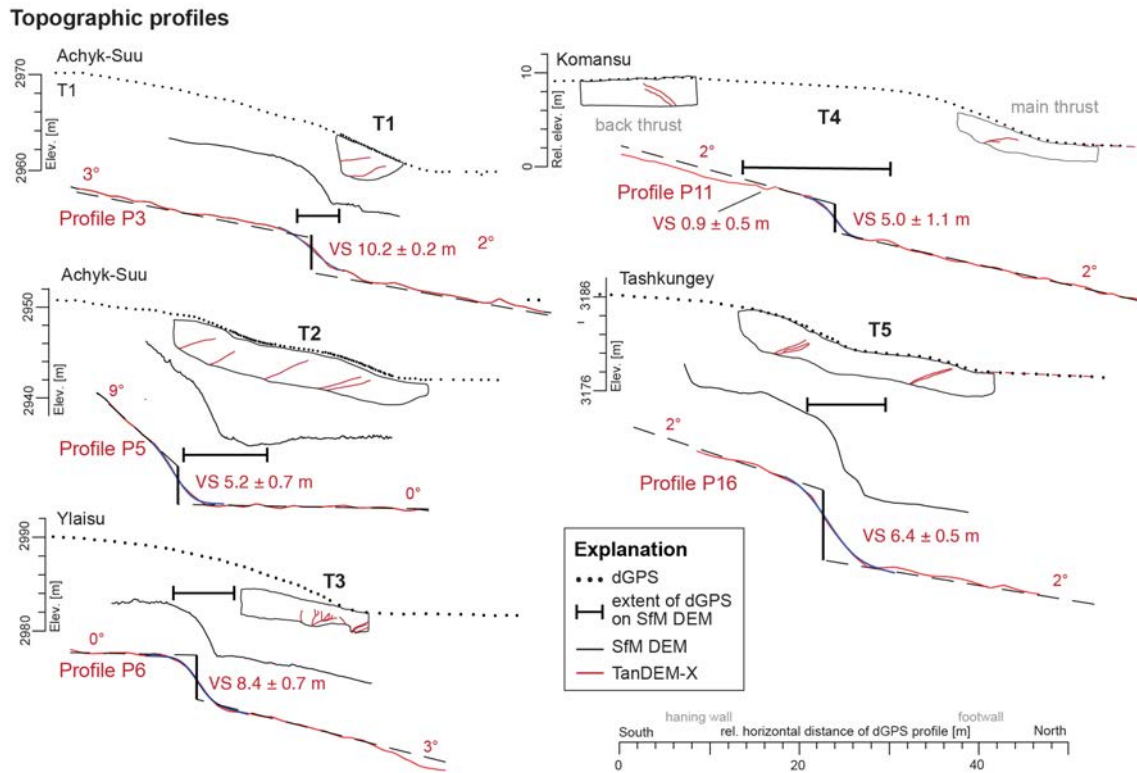


Figure 4.3 Topographic profiles derived from dGPS, and vertically exaggerated TanDEM-X and SfM-DEMs with estimated upper and lower fan surface slope and modelled vertical separation. Cross-section views of the trench show main faults (red lines) with respect to the fault scarp. See Figure 4.2 for profile locations.

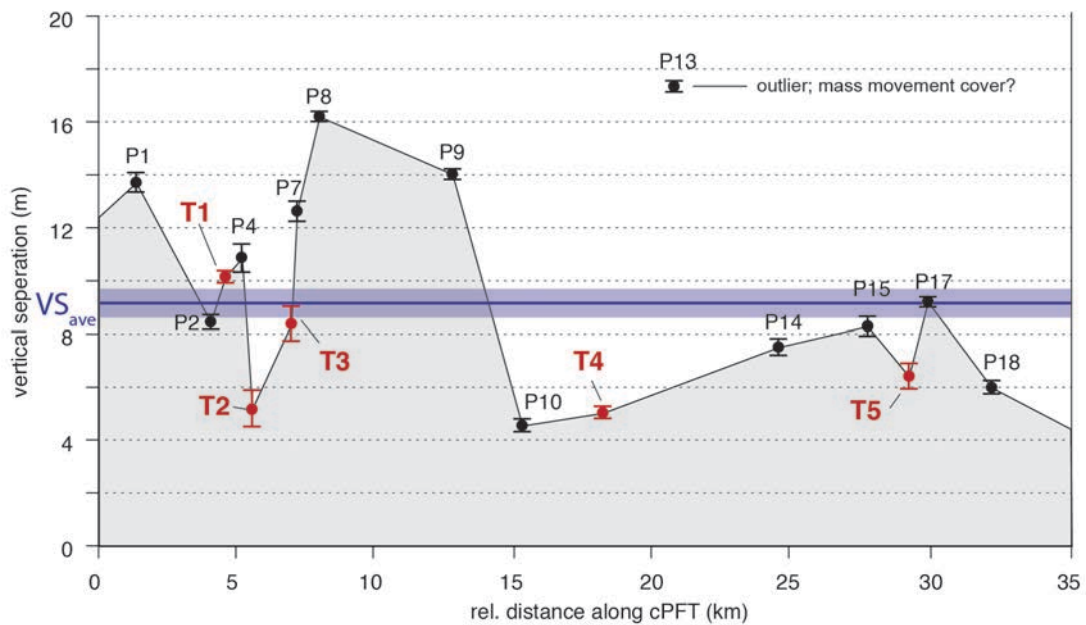


Figure 4.4 Distribution of the modelled vertical separation (VS) from west to east along the central segment of the Pamir Frontal Thrust (cPFT). Shaded area shows average VS. For individual scarp profiles see Appendix A, Figure A1.

4.3. Excavation sites

The trace of the cPFT defines a nearly continuous, north-facing $N080^\circ$ striking fault scarp with maximum slopes between 15° and 20° and heights of up to ~ 15 m cutting through the fluvial and alluvial surfaces. Following the Quaternary geological interpretation and regional correlation by Strecker et al. (2003), the fluvial terraces at the trenching sites correspond to the prominent Qt_3 and Qt_4 terrace deposits (Figure 4.5). The uplifted alluvial-fan and fluvial terrace surfaces along the range front generally have gentle north-facing slopes with dips ranging from $\sim 0^\circ$ to $\sim 4^\circ$ (Figure 4.3), incised by northward-directed river channels, and partly covered by glacial till and landslide deposits (Figure 4.5).

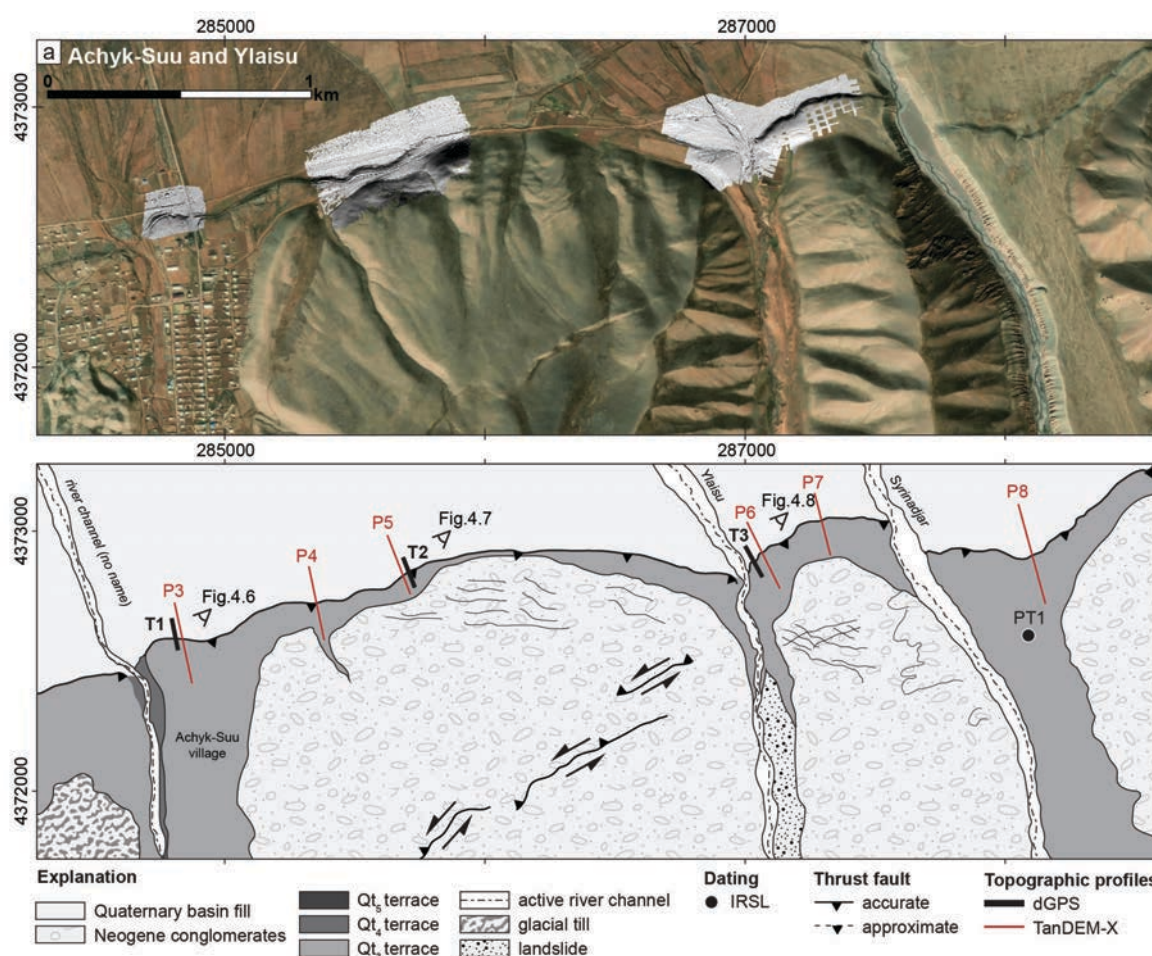


Figure 4.5 Satellite images and Quaternary geologic map of trenching sites showing the relationship between landforms, deposits, and structures near the trenching sites along the central PFT. See Figure 4.1 for site locations. Note how secondary fault traces cut the Neogene units exposed in the hanging wall. World Imagery Map (1 m resolution; Source: Esri; GeoEye IKONOS, AeroGRID, and IGN Spain) is overlain by hillshades from high-resolution DSM generated from UAV imagery (b, d). Black lines indicate the location of the trenches and dGPS topographic profiles, and red lines indicate TanDEM-X-based topographic profiles in (e).

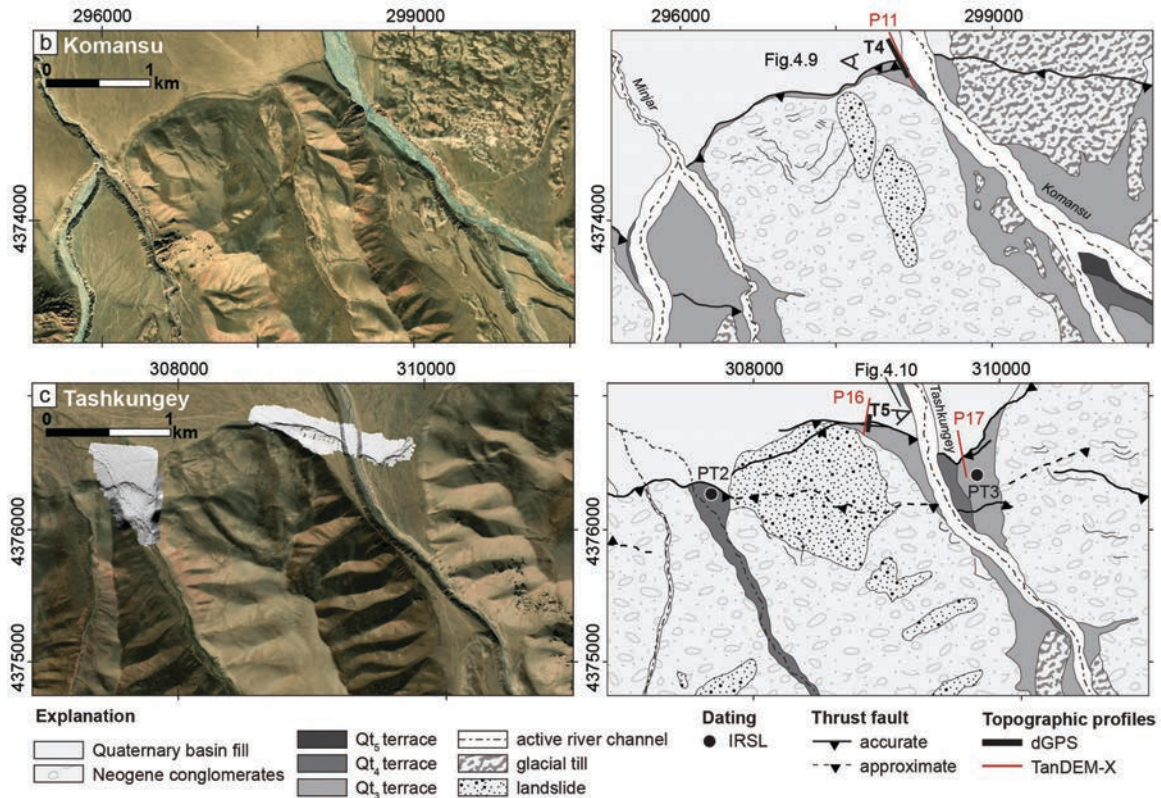


Figure 4.5 (continued)

T1 – Achyk-Suu (39.48°N 72.50°E): The Achyk-Suu excavation site is situated at the westernmost end of the cPFT (Figure 4.5). Trench T1 is part of an abandoned gravel pit that was excavated in the faulted alluvial-fan deposits close to the village of Achyk-Suu (Figure 4.6). The trench consisted of a 7-m-long and up to 3-m-deep east wall across the lower portion of the fault scarp in the eastern part of the pit. The scarp fit-modeling of the 600-m-long topographic profile next to the trench indicates 10.2 ± 0.2 m of vertical separation, with an upper and lower alluvial-fan surface slope of $\sim 3^\circ$ (profile P3; Figure 4.3).

T2 – Achyk-Suu (39.48°N 72.51°E): Trench T2 at the Achyk-Suu site was excavated about 1 km east of trench T1 (Figure 4.5), across a part of the fault with a double scarp morphology (Figure 4.7). Conditions along the single fault scarp with heights of 11 m and steep scarp slopes (i.e., profile P4; see Appendix A, Figure A1) made an excavation logistically challenging. The scarp at the location of choice appeared unaltered and likely recorded the same faulting events as the single scarp. The excavation resulted in a 24-m-long, 3-m-wide, and up to 4-m-deep trench. The scarp-fit modeling of the 250-m-long, topographic profile results in a total vertical separation of 5.2 ± 0.7 m, and an upper and lower fan surface slope of $\sim 9^\circ$ and $\sim 0^\circ$, respectively (profile P5; Figure 4.3).

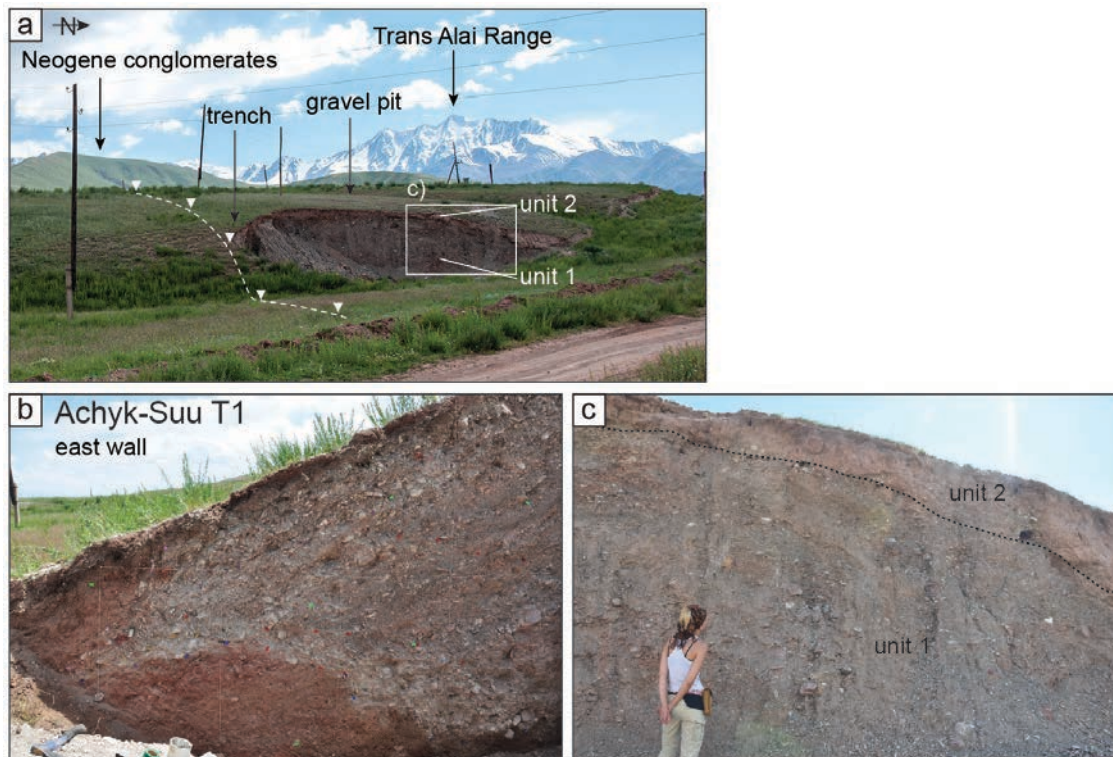


Figure 4.6 (a) Field view of the abandoned gravel pit located at the entrance of the Achyk-Suu village (see location in Figure 4.5). Fault scarp indicated by dashed line. The white box indicated location in (c). (b) View of the east wall exposure of trench T1 after cleaning. (c) West-wall hanging-wall exposure away from the fault zone; note the presence of unit 2 here, which appears to be eroded along the scarp face farther towards the fault zone in (b).

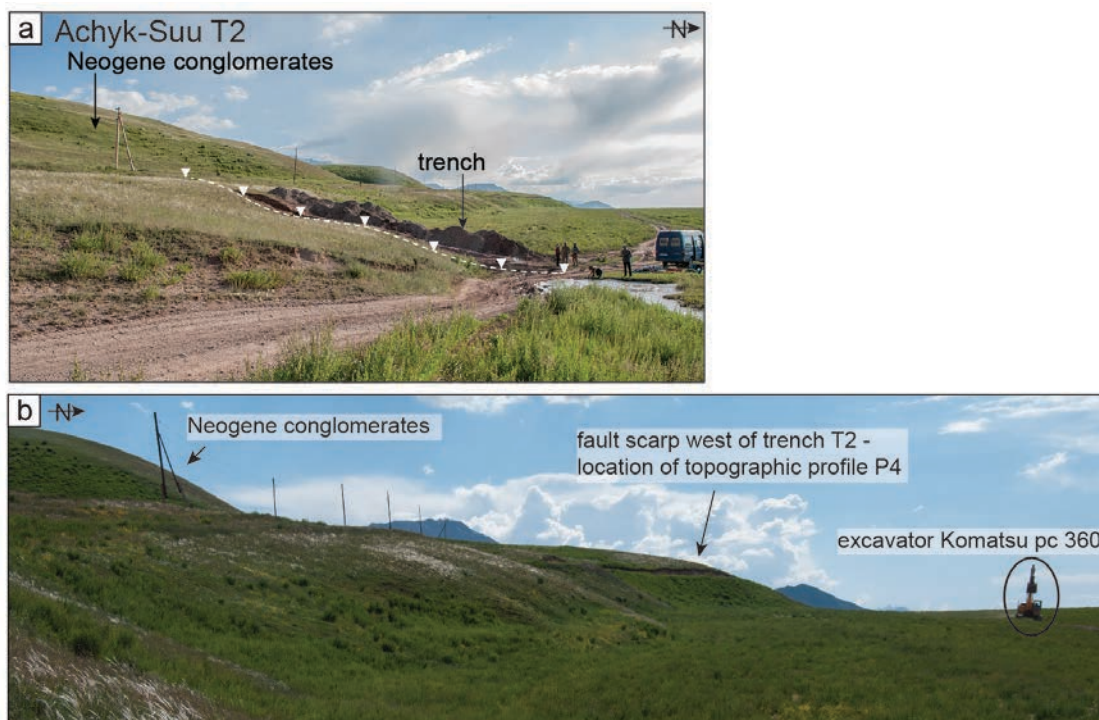


Figure 4.7 (a) Field view of trench T2 at the Achyk-Suu site (see location in Figure 4.5). Fault scarp indicated by dashed line. (b) Field view of the fault scarp west of trench T1; note the transition from a double scarp in (a) to a steep single scarp here. Location of topographic profile P4.

T3 – Ylaisu (39.48°N 72.52°E): During the preliminary geomorphic assessment of potential trenching locations, we discovered a trench cut into the fault scarp at the Ylaisu site (Figure 4.5) that had been excavated for agricultural purposes. The trench position was perpendicular to the fault scarp, and the exposed walls were straight and undamaged when it was decided to clean and to log this exposure. The 11-m-long, 3.5-m-wide and up to 3-m-deep trench is located on a terrace of an alluvial fan east of a ~5-m-deep river channel (Figure 4.8). The scarp-fit modeling of the 300-m-long topographic profile across the scarp revealed a vertical separation of 8.4 ± 0.7 m, and an upper and lower fan surface slope of $\sim 0^\circ$ and $\sim 3^\circ$, respectively (profile P6; Figure 4.3). In the surrounding foothills west of the trench, fault-scarp splays of the cPFT could be observed with opposite thrust vergence that are possibly conjugate with respect to the main scarp at the trench location (Figure 4.5). These structural complexities around Ylaisu suggest a possible oblique-slip component during the ruptures.

T4 – Komansu (39.50°N 72.65°E): The Komansu trench site is located approximately in the central part of the cPFT, on a terrace west of the ~30-m-deep active Komansu river channel (Figure 4.5). In this area, the fault generated a double-scarp morphology, with a main thrust (northern trench) and a back thrust 50 m south (southern trench), which is well developed in the western river cut (Figure 4.9). The scarp-fit modeling of the 600-m-long topographic profile perpendicular to both scarps revealed a vertical separation of 5.0 ± 1.1 m at the main scarp and 0.9 ± 0.5 m at the back scarp, and an upper and lower fan surface slope of $\sim 2^\circ$, respectively (profile P11; Figure 4.3). The T4 trenches were excavated at a lower terrace surface, which is inferred to be correlative with the younger Q_{t4} terrace (~ 4.5 ka) according to the regional correlation developed by Arrowsmith & Strecker (1999) and Strecker et al. (2003) and dating presented here (Figure 4.5).

T5 – Tashkungey (39.52°N 72.77°E): The Tashkungey paleoseismic site is located at the eastern end of the cPFT, on alluvial-fan deposits of Q_{t3} , west of the active ~20-m-deep Tashkungey river channel (Figure 4.5). We chose to excavate across a portion of the fault scarp which has a double-scarp morphology (Figure 4.10). The scarp-fit modeling of the 350-m-long, scarp-perpendicular topographic profile reveals 6.4 ± 0.5 m of total vertical separation, and an upper and lower fan-surface slope of $\sim 2^\circ$, respectively (profile, P16; Figure 4.3). The excavated trench was ~19 m long, ~2.5 m wide, and up to ~3 m deep

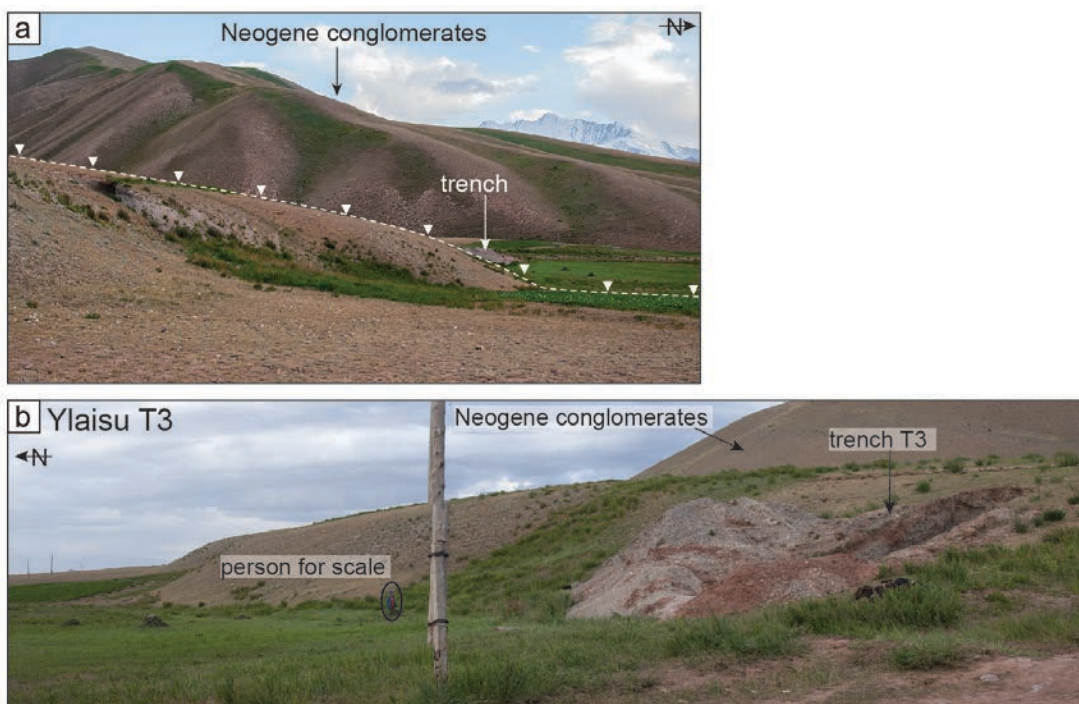


Figure 4.8 a) Field view to the west; fault scarp morphology at the Ylaisu site. Location of topographic profile P6 (see location in Figure 4.5). Fault scarp indicated by dashed line. (b) Field view to the east; trench T3 excavation.

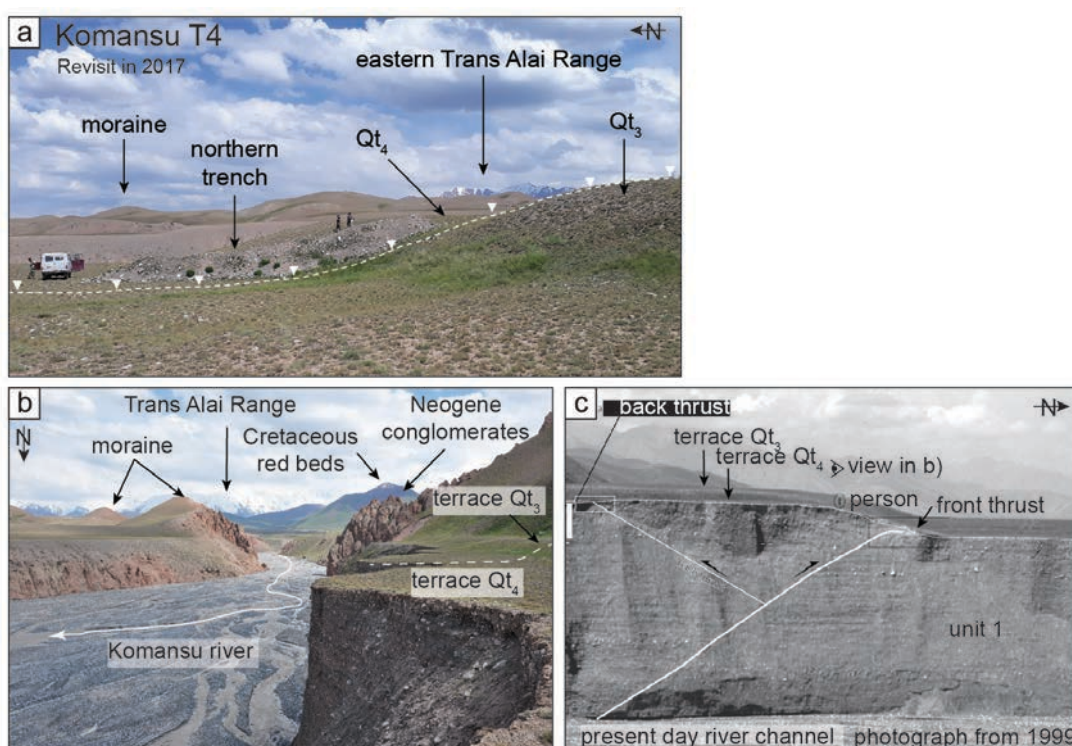


Figure 4.9 a) Field view to the east; fault scarp morphology and northern trench T4 location at the Komansu site (see location in Figure 4.5). Fault scarp indicated by dashed line. (b) View to the south of the Komansu River and its terraces. The dashed line indicates the terrace levels of Qt_4 with respect to Qt_3 . (c) Field view of the western river cut of the Komansu River. White lines indicate extent of the main and back-thrust fault within the fluvial terrace material. Photograph taken from the eastern terrace in 1999.

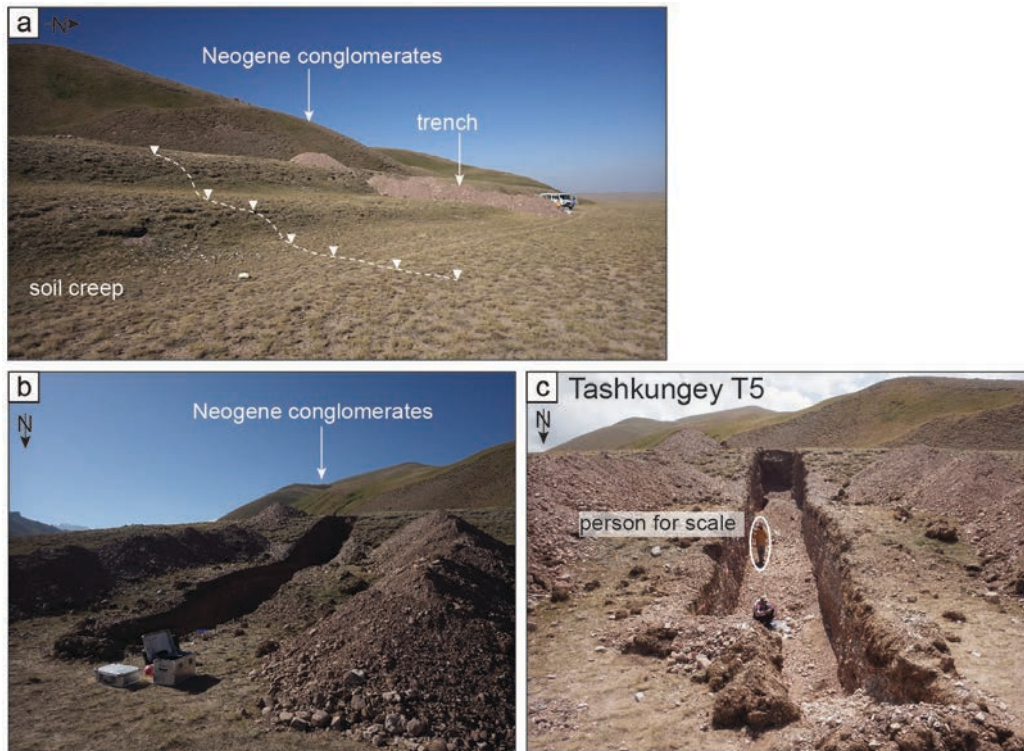


Figure 4.10 a) Field view to the west; fault scarp morphology and trench T5 location at the Tashkungey site (see location in Figure 4.5). Fault scarp indicated by dashed line. (b and c) Field views of the trench excavation.

4.4. Description of stratigraphy and structural context exposed in the excavations

The fault-scarp morphology along the cPFT is dominated by the combined effects of hanging-wall collapse and the formation of pressure-ridges implying gentle thrust fault dip-angles ($<30^\circ$) associated with unconsolidated friable to clayey surface material and moderate dip-slip displacements (Philip et al., 1992).

Considering the unfaulted alluvial-fan portion exposed in the trenches, the associated stratigraphy appears consistent along the cPFT. The characteristic stratigraphic sequence starts with a massive unit visible in the lower 1–3 m of the trench exposures, consisting of laterally discontinuously bedded and subrounded to rounded poorly sorted fluvial gravel (unit 1). At the T1, T2, T4 and T5 locations, and within the upper 20 to 50 cm of unit 1, a well-developed horizon of CaCO_3 -coated gravel indicates a stage I to II soil-development (unit 1b; associated with the Qt_3 surface formation) (Figure 4.11). The fluvial-gravel beds (unit 1) generally dip gently north due to the northward transport direction of the regional depositional system; however, at the fault zones the beds of unit 1 as well as the unit 1/1b transition are folded parallel to the scarp. Unit 1 is capped by unit 2, a compacted layer with moderate thickness (10–50 cm) of fine-grained sediments covering terrace Qt_3 (Figure 4.11). I infer that a change in sedimentation between unit 1 and unit 2 marks the timing of initial floodplain abandonment, regrading, and incision below the Qt_3 surface associated with melting of the Qm_3 glaciers (Strecker et al.,

2003). Thus, the contact between gravel and capping material dates or postdates terrace formation and will be used as a geomorphic marker. The topsoil layer is a thin dark and organic-rich *A-horizon* in the upper 10 to 30 cm below the surface. The vegetation is characterized by grass cover, with root horizons 0.5-1.0 m deep.

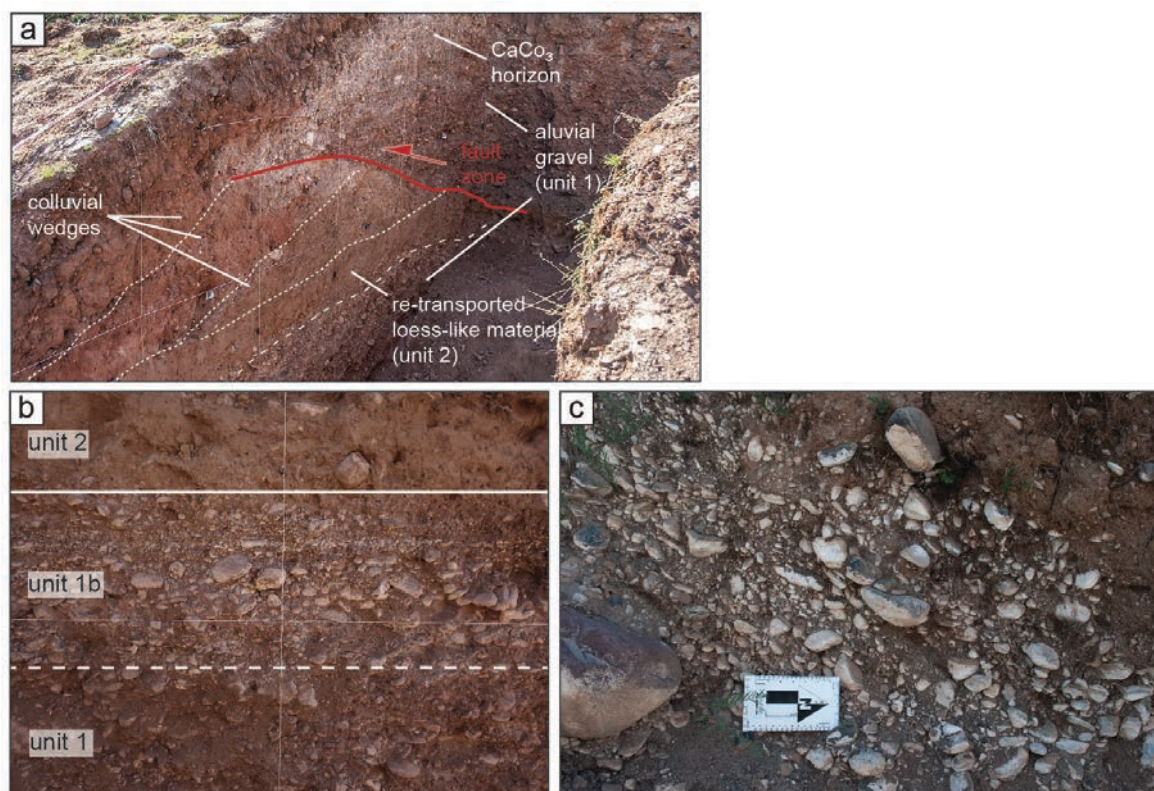


Figure 4.11 (a) Oblique view into trench T2 excavation at the Achyk-Suu site showing exemplary principal stratigraphic units along the central Pamir Front Thrust and paleoseismic interpretations. (b) Principal stratigraphic sequence of unfaulted alluvial-fan deposits; note the subdivision of unit 1. Photograph from trench T5, Tashkungey site. (c) Example of the development of pedogenic CaCO_3 on the underside of clasts in trench exposure (trench T4, Komansu site).

Unit 1 IRSL samples from trench T2 (T2-L4e), T3 (T3-L7, T3-L2, T3-L6) and T5 (T5-L4e) yield consistent ages resulting in a modeled mean age of 20.1 ± 0.6 ka (Table 4.1; Figure 4.12). Footwall IRSL and radiocarbon ages for unit 2 derived from trench T2 (T2-L2e, T2-L5e, T2-Rs4w, T2-Rs1e, T2-Rs2e) coincide with IRSL ages obtained from the terrace Qt_3 capping unit in the hanging walls away from the scarp at Syrinadjar (PT1-Syn) and Tashkungey (PT2-Tsh) (Table 4.1 and Table 4.2; Figure 4.12). Together, these ages result in a modeled mean age of 7.3 ± 0.1 ka, which further agrees with radiocarbon Qt_3 ages reported by Arrowsmith & Strecker (1999) (see above). From an assigned Qt_4 surface from a neighboring valley in the immediate vicinity west of Tashkungey, an age of 4.5 ± 0.2 ka from one IRSL sample (PT2-Tsh2) was obtained (Table 4.1; Figure 4.12). More detailed description of sample location and stratigraphic association within individual trench exposures will be presented in Chapter 5.

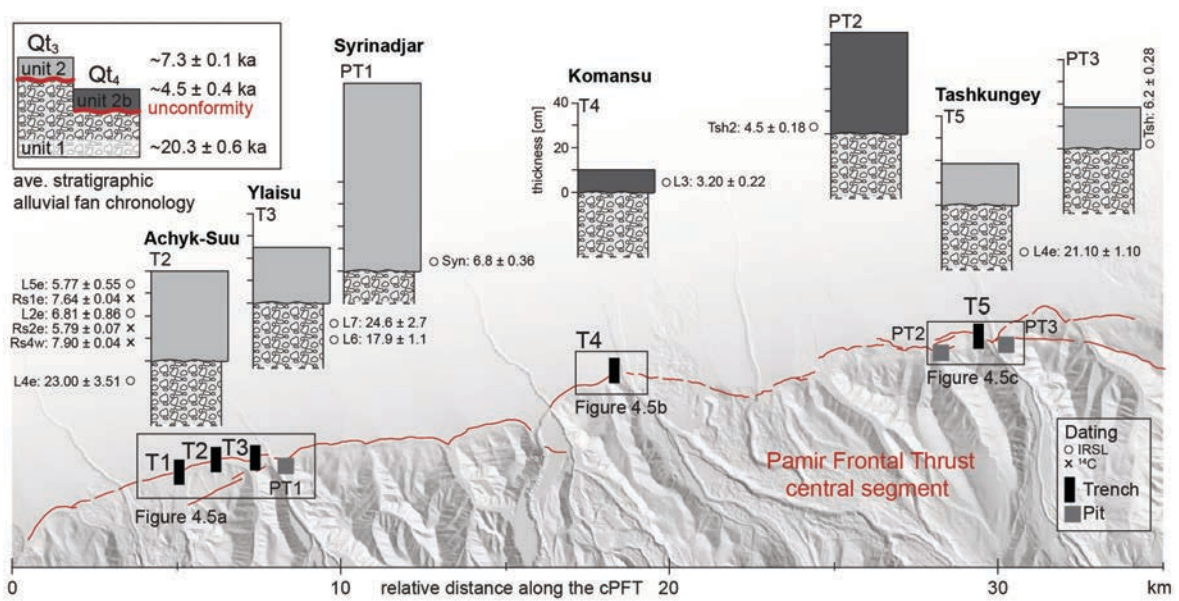


Figure 4.12 Simplified stratigraphic profiles of the upper sectors of the subsurface along the central PFT (red fault trace). The vertical position of the profiles indicates their relative elevation context. Ages (circle = IRSL; cross = radiocarbon) are mean thousands of years cal. BP $\pm 2\sigma$ (Table 4.1 and Table 4.2). Inset shows an age constraint of the terrace chronology and corresponding mean ages $\pm 2\sigma$. Black bars indicate trench location; Gray rectangles indicate pit location.

Table 4.1 Infrared Stimulated Luminescence ages (IRSL at 150°C). Concentration of dose-rate relevant elements (K, Th, and U), water content (W), dose rates (D), observed overdisperssion (OD), equivalent dose (D_e). Samples run at the Institute of Earth and Environmental Sciences (University of Freiburg in Germany).

Location	Sample Name	Sample Type	Depth (cm)	W (%) ^a	K (%)	Th (ppm)	U (ppm)	D (Gy/ka)
Hanging wall/Qt ₄	PT2-Tsh2	tube	58	15 \pm 5	2.29 \pm 0.14	9.99 \pm 0.63	3.19 \pm 0.19	4.09 \pm 0.18
Hanging wall/Qt ₃	PT1-Syn	tube	83	15 \pm 5	1.93 \pm 0.20	7.57 \pm 0.50	2.19 \pm 0.14	3.36 \pm 0.18
Hanging wall/Qt ₃	PT3-Tsh	tube	35	15 \pm 5	2.21 \pm 0.18	9.98 \pm 0.63	3.08 \pm 0.18	3.97 \pm 0.18
Trench T2/Unit 2	T2-L2e	tube	308	15 \pm 5	1.88 \pm 0.19	8.49 \pm 0.48	2.70 \pm 0.15	3.57 \pm 0.17
Trench T2/Unit 2	T2-L5e	tube	88	15 \pm 5	2.23 \pm 0.23	9.69 \pm 0.62	3.13 \pm 0.19	3.97 \pm 0.20
Trench T2/Unit 1	T2-L4e	tube	225	8 \pm 4	2.15 \pm 0.12	6.85 \pm 0.37	1.69 \pm 0.10	3.66 \pm 0.15
Trench T3/Unit 1	T3-L2	tube	95	15 \pm 5	1.93 \pm 0.12	8.40 \pm 0.54	2.79 \pm 0.17	3.69 \pm 0.20
Trench T3/Unit 1	T3-L6	con. bag	215	15 \pm 5	1.65 \pm 0.11	7.57 \pm 0.47	2.17 \pm 0.14	3.26 \pm 0.37
Trench T3/Unit 1	T3-L7	con. bag	92	15 \pm 5	2.04 \pm 0.13	8.47 \pm 0.54	2.85 \pm 0.17	3.86 \pm 0.18
Trench T5/Unit 1	T5-L4e	con. bag	35	15 \pm 5	1.75 \pm 0.11	6.28 \pm 0.41	1.80 \pm 0.12	3.24 \pm 0.16
Grain								
size (μ m)	n ^b	OD	D_e IRSL (Gy) ^c	D_e pIR-150 (Gy)	Age IRSL (kyr) ^d	Age pIR-150 (kyr)		
63-100	40/39	0.22/0.27	18.23 \pm 0.24	22.98 \pm 0.44	4.46 \pm 0.18	5.62 \pm 0.24		
100-150	33/33	0.06/0.06	23.13 \pm 0.25	30.12 \pm 0.36	6.85 \pm 0.36	8.92 \pm 0.47		
100-150	40/39	0.05/0.08	24.68 \pm 0.22	30.63 \pm 0.40	6.21 \pm 0.28	8.02 \pm 0.38		
100-150	13	0.32/0.66	24.05 \pm 2.82	35.29 \pm 3.28	6.81 \pm 0.86	9.99 \pm 1.05		
150-200	10	0.26/0.37	22.91 \pm 1.86	38.31 \pm 4.81	5.77 \pm 0.55	9.64 \pm 1.31		
100-250	20	0.44/0.45	84.11 \pm 12.38	143.44 \pm 24.63	23.0 \pm 3.51	39.22 \pm 6.91		
63-100	40/40	0.19/0.44	68.15 \pm 2.17	168.45 \pm 16.57	21.3 \pm 1.3	52.6 \pm 5.9		
100-150	40/40	0.49/0.83	60.63 \pm 1.41	151.49 \pm 16.10	17.9 \pm 1.1	44.8 \pm 5.3		
150-200	40/40	0.36/0.63	80.70 \pm 8.29	226.62 \pm 14.41	24.6 \pm 2.7	69.1 \pm 5.5		
100-250	40/40	0.16/0.29	68.36 \pm 2.16	179.37 \pm 14.65	21.1 \pm 1.1	55.4 \pm 5.0		

^aWater content was estimated based on present day moisture and grain-size composition.

^bNumber of accepted aliquots passing internal recycling ratio criteria ($\geq 10\%$).

^cMean dose was calculated using either the Central Age Model (CAM) or the Minimum Age Model (MAM), depending on the statistical parameters of D_e distributions, such as overdisperssion, skewness and kurtosis (cf. Galbraith & Roberts, 2012).

^dAges were calculated using ADELEv.2017 (Degering & Degering, 2020), using the results of high-resolution gamma spectrometry (cf. Preusser & Kasper, 2001).

Table 4.2 Radiocarbon samples, laboratory results, and calibrated and modeled ages BP

Location	Sample Name	Lab Accession Number	Ref.	Location	Sample Name	Lab Accession Number	Ref.	Location
Trench T2/Unit 1	S4w	Poz-100595	T2-Rs4w	terr. shell	108	7070 ± 40	7.90 ± 0.04	
Trench T2/Unit 1	S1e	Poz-100593	T2-Rs1e	terr. shell	238	6800 ± 50	7.64 ± 0.04	0.15 mgC
Trench T2/Unit 1	S2e	Poz-100594	T2-Rs2e	terr. shell	234	5030 ± 40	5.79 ± 0.07	0.6 mgC

Samples run at Poznan Radiocarbon Laboratory and AMS Laboratory (Poznan, Poland).

^aSamples run at Keck Carbon Cycle AMS Facility (Earth System Science Dept., UC Irvine, USA).

^b¹⁴C ages (mean) and errors (1σ) calibrated using IntCal Calibration Curve of Reimer et al. (2020) in OxCal v.4.4 (Bronk Ramsey, 2020).

4.5. Summary

Analysis of TanDEM-X digital elevation model data combined with extensive field observations along the central sector of the Pamir Frontal Thrust allowed a qualitative update of the structural and geological map in this region with a better resolution of the PFT trace in the frontal sectors and throughout the Trans Alai range, especially at higher elevations. Measurement of offset Quaternary landforms associated with the cPFT records an asymmetric distribution toward the western end of the central segment with a maximum offset of ~16 m at the Syrnadjar River and an average offset of ~9 m for the entire length of the segment. New radiocarbon and luminescence dating from multiple sites along the segment suggest that the final phase of fluvial deposition at the range front began at ~20 ka. The data furthermore provide an age estimate of 7.3 kyr for the Qt₃ terrace, which appears to be consistent along the cPFT, and a new age estimate of 4.5 kyr for the Qt₄ terrace.

Chapter 5

Results II: Paleoseismology along the central segment of the Pamir Frontal Thrust fault

The previous chapter described the geological and geomorphological character of the areas along the central segment of the Pamir Frontal Thrust (cPFT). Folded Neogene deposits truncated at the range front and uplifted fluvial terraces crossing this structure unambiguously document active deformation in this area. In this chapter, I examine associated paleoseismic evidence for earthquakes from five trenching sites introduced in Chapter 4 to estimate recurrence intervals and displacements along the cPFT. The outcome of this chapter serves as a basis for the assessment of the seismogenic behavior along this segment of the PFT, further elaborated in the subsequent Chapter 6. Since the fieldwork for the paleoseismic survey was carried out with the help of a team, I will use the "we" in the following when talking about jointly conducted activities and observations made in the field.

5.1. Paleoearthquake chronologies from five excavation sites

The excavations along the cPFT expose multiple fault zones, which are represented by 15° to 30° south-dipping narrow (5–20-cm-wide) zones with oriented and broken clasts or wider (up to 1-m-wide) zones with an imbricate fabric of fault splays and injected material between bodies of fault breccia (Figure 5.1). The principal indicators of ground-rupturing events are single or stacked deformed colluvial deposits in the footwall adjacent to the fault zone. The colluvial material accumulates in a lens-shaped drape over the lower portion of the scarp and is usually thickest at the toe where the slope change is greatest, comparable to the modern topsoil (TS) (e.g., T2 and T5; Figure 5.5 and Figure 5.11). I infer that these colluvial deposits formed as a result of coseismic or immediate postseismic collapse of the overhanging scarp tip and subsequent debris-dominated and wash-dominated fault-scarp degradation (see Discussion), which buried the fault tip (e.g., Meghraoui et al., 1988; McCalpin & Carver, 2009; Rockwell et al., 2013; Patyniak et al., 2017).

The scarp-face colluvium consists of poorly-sorted and reworked, matrix-supported deposits of silty sand that vary in color. In some cases, these strata contain gravel or consist of poorly sorted, clast-supported gravel. The colluvial material is often sliced up in fragments within the fault zone. Secondary indicators of faulting include (1) nearly vertical fissures in the gravel deposits, indicated by pronounced CaCO₃ cementation along the fissure trace; (2) fault-induced material deposition against and in front of the scarp face inferred to have been deposited during temporary ponding; (3) offset markers from distinct unit boundaries or internal bedding; (4) deformed channel lenses interbedded within the fluvial deposits; (5) patches of injected sediments along and/or within the fault zone; and (6) fault breccia

injected into the base of the colluvium. Taken together, these features are all characteristics of reverse-fault exposures (McCalpin & Carver, 2009).

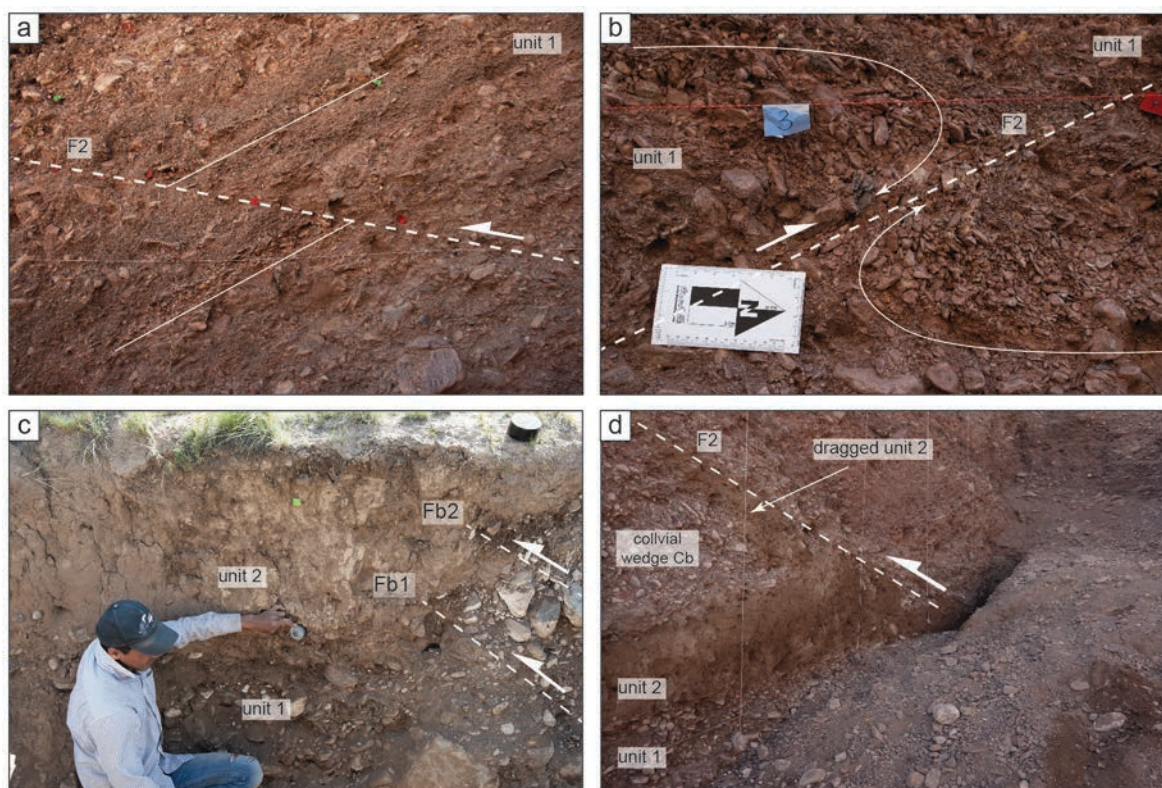


Figure 5.1 Examples of fault zones exposed in the trenches. (a) Trench T1: offset bedding of fluvial deposits along a narrow zone of rotated clasts. (b) Trench T2: imbricate clast fabric along narrow fault zone. (c) Trench T4: migrating thrust fault in the back-thrust trench exposure. (d) Trench T5: major, several-decimeter-wide fault zone with a multiple rupture history. Note the injection of lower (fine sediment) units into the fault zone.

For each excavation site, I provide trench logs and associated photomosaics to display the stratigraphic and structural interpretations I used to infer individual surface-rupturing events. I provide high-resolution photomosaics for each site in Appendix B (Figures B1 to B2). Because of the stratigraphic and age consistency between unit 1 and unit 2 along the cPFT (see Chapter 4.3) and in order to provide a more consistent basis for subsequent modeling of earthquake timing, I will use the estimated mean ages of 20.1 ± 0.6 ka and 7.3 ± 0.1 ka, respectively. After a careful reevaluation of the stratigraphic and chronologic context in the multi-fault trench exposures, I assume coeval activation of these fault zones during some surface rupturing events.

In the following chapters, I summarize all interpreted earthquake evidence along the different fault zones to define event horizons for each earthquake per site. Combined with the available age control (Tables 5.1 and 5.2), I constrain the event timing using OxCal and provide an event catalogue that I later use for paleoearthquake correlation along the cPFT. Additional OxCal modeling information can be found in Appendix B (Codes B1 to B5).

Table 5.1 Radiocarbon samples, laboratory results, and calibrated and modeled ages BP

Trench	Sample Name	Lab Accession Number	Ref. in Paper	Sample Type	Depth (cm)	¹⁴ C age (yr BP)	Calibrated Age ^b (cal kyr BP) [†]	Remark
T1	T2c1e	Poz-104376	T1-R1	charcoal	21	130 ± 30	0.21 ± 0.10	0.13 mgC
	T2c2e	Poz-104378	T1-R2	plant	146	1595 ± 30	1.48 ± 0.04	
	AST2e_b1	Poz-100672	T1-Rb1	bulk soil	18	225 ± 35	0.14 ± 0.08	
	AST2e_b2	Poz-100673	T1-Rb2	bulk soil	15	ill	1.78 ± 0.04	
T2	C1e	Poz-100574	T2-R1e	charcoal	225	3560 ± 35	3.85 ± 0.06	TOC
	C3e	Poz-100582	T2-R3e	charcoal	115	3500 ± 40	3.77 ± 0.06	
	C4e	Poz-100108	T2-R4e	charcoal	40	50 ± 30	0.11 ± 0.08	
	C5e	Poz-99959	T2-R5e	charcoal	30	215 ± 30	0.19 ± 0.10	
	C6e	Poz-100584	T2-R6e	charcoal	210	1495 ± 30	1.38 ± 0.04	
	C7e	Poz-100618	T2-R7e	charcoal	200	1845 ± 35	1.78 ± 0.05	
	C8e	Poz-100619	T2-R8e	charcoal	110	1490 ± 40	1.38 ± 0.05	
	C9e?	Poz-100620	T2-R9e	charcoal	108	840 ± 140	0.80 ± 0.12	
	C10e	Poz-100621	T2-R10e	charcoal	58	1210 ± 30	1.14 ± 0.05	
	C11e	Poz-100623	T2-R11e	charcoal	126	210 ± 50	0.19 ± 0.11	
	C13e	Poz-100624	T2-R13e	charcoal	56	75 ± 30	0.12 ± 0.08	0.5 mgC
	S1e	Poz-100593	T2-Rs1e	terr. shell	238	6800 ± 50	7.64 ± 0.04	0.15 mgC
	S2e	Poz-100594	T2-Rs2e	terr. shell	234	5030 ± 40	5.79 ± 0.07	0.6 mgC
	C1w	Poz-99961	T2-R1w	charcoal	108	1145 ± 30	1.06 ± 0.06	0.15 mgC very small 0.03 mgC 0.08 mgC
	C2w	Poz-100626	T2-R2w	charcoal	114	1195 ± 30	1.12 ± 0.05	
	C5w	Poz-99962	T2-R5w	charcoal	56	1145 ± 30	1.06 ± 0.06	
	C6w	Poz-100627	T2-R6w	charcoal	52	1215 ± 30	1.14 ± 0.05	
	C7w	Poz-100628	T2-R7w	charcoal	24	310 ± 30	0.38 ± 0.05	
	C8w	Poz-100629	T2-R8w	charcoal	108	modern	-	
	C10w	Poz-100671	T2-R10w	charcoal	110	260 ± 60	0.30 ± 0.12	
S4w	Poz-100595	T2-Rs4w	terr. shell	108	7070 ± 40	7.90 ± 0.04		
AST1e_Be1	Poz-104441	T2-Rb1e	bulk soil	23	115 ± 30	0.14 ± 0.08		
AST1e_Be2	Poz-104442	T2-Rb2e	bulk soil	46	modern	-	0.04 mgC	
AST1e_Be3	Poz-104443	T2-Rb3e	bulk soil	105	195 ± 30	0.17 ± 0.09	0.9 mgC	
AST1e_Be4	Poz-104444	T2-Rb4e	bulk soil	30	155 ± 30	0.15 ± 0.09		
AST1w_B1w	Poz-104446	T2-Rb1w	bulk soil	122	1130 ± 30	1.04 ± 0.05		
AST1w_B2w	Poz-104447	T2-Rb2w	bulk soil	48	495 ± 30	0.53 ± 0.02		
AST1w_B3w	Poz-104375	T2-Rb3w	bulk soil	78	575 ± 30	0.59 ± 0.04		
T3	LS-T1-C1w	208768 ^a	T3-R1w	charcoal	185	2795 ± 15	2.90 ± 0.03	
	LS-T1-C2w	208769 ^a	T3-R2w	charcoal	196	2330 ± 15	2.35 ± 0.01	
	LS-T1-C3w	208770 ^a	T3-R3w	charcoal	135	4550 ± 15	5.21 ± 0.09	
	LS-T1-C4w	208771 ^a	T3-R4w	charcoal	140	2455 ± 15	2.57 ± 0.09	
	LS-T1-C5w	208772 ^a	T3-R5w	charcoal	13	330 ± 15	0.38 ± 0.04	
	LS-T1-C1e	208773 ^a	T3-R1e	charcoal	150	3095 ± 15	3.31 ± 0.04	
	LS-T1-C2e	208774 ^a	T3-R2e	charcoal	35	170 ± 20	0.16 ± 0.09	
	LS-T1-B1e	Poz-114567	T3-Rb1e	bulk soil	20	655 ± 30	0.61 ± 0.04	
	LS-T1-B2e	Poz-114568	T3-Rb2e	bulk soil	5	modern	-	
LS-T1-B1w	Poz-114569	T3-Rb1w	bulk soil	30	890 ± 30	0.82 ± 0.05		
T4	8-4-99-9	Beta-134705	T4-R1b	charcoal	55	2480 ± 40	2.57 ± 0.09	
	8-4-99-11	Beta-134706	T4-R2b	charcoal	75	1910 ± 60	1.85 ± 0.07	
T5	TSH-T1-C2e	208775 ^a	T5-R2e	charcoal	52	175 ± 15	0.17 ± 0.09	very small
	TSH-T1-C3e	208776 ^a	T5-R3e	charcoal	60	modern	-	
	TSH-T1-C4e	208777 ^a	T5-R4e	charcoal	110	1085 ± 50	1.01 ± 0.06	
	TSH-T1-C6e	208778 ^a	T5-R6e	charcoal	25	285 ± 15	0.36 ± 0.05	
	TSH-T1-C7e	208779 ^a	T5-R7e	charcoal	50	modern	-	
	TSH-T1-C8e	208780 ^a	T5-R8e	charcoal	30	350 ± 15	0.40 ± 0.05	
	TSH-T1-C9e	208781 ^a	T5-R9e	charcoal	110	1645 ± 15	1.55 ± 0.02	
	TSH-T1-C10e	208782 ^a	T5-R10e	charcoal	35	805 ± 15	0.71 ± 0.01	
	TSH-T1-C11e	208783 ^a	T5-R11e	charcoal	24	260 ± 15	0.30 ± 0.04	
	TSH-T1-C1w	208784 ^a	T5-R1w	charcoal	113	90 ± 15	0.13 ± 0.08	
	TSH-T1-B1e	Poz-114523	T5-Rb1e	bulk soil	88	1975 ± 30	1.93 ± 0.03	
	TSH-T1-B1w	Poz-114565	T5-Rb1w	bulk soil	40	1645 ± 30	1.54 ± 0.05	
TSH-T1-B2w	Poz-114566	T5-Rb2w	bulk soil	44	2590 ± 30	2.73 ± 0.04		

Samples run at Poznan Radiocarbon Laboratory and AMS Laboratory (Poznan, Poland).

^aSamples run at Keck Carbon Cycle AMS Facility (Earth System Science Dept., UC Irvine, USA).

^b¹⁴C ages (mean) and errors (1σ) calibrated using IntCal Calibration Curve of Reimer et al. (2020) in OxCal v.4.4 (Bronk Ramsey, 2020).

Table 5.2 Infrared Stimulated Luminescence ages (IRSL at 150°C).

Loca- tion	Sample Name ^a	Ref. in Paper	Sample Type	Depth (cm)	W (%) ^b	K (%)	Th (ppm)	U (ppm)	D (Gy/ka)	Grain size (µm)	n ^c	OD	D ₀ IRSL (Gy) ^d	D ₀ pIR-150 (Gy)	Age IRSL (kyr) ^e	Age pIR-150 (kyr)
T1	AsTe-3	T1-L3	tube	135	10 ± 5	2.53 ± 0.15	9.71 ± 0.61	2.98 ± 0.18	4.55 ± 0.16	100-150	20	0.4170/68	9.24 ± 0.85	15.96 ± 1.41	2.03 ± 0.20	3.50 ± 0.34
	AsTe-5	T1-L5	tube	60	10 ± 5	2.18 ± 0.22	8.59 ± 0.59	2.65 ± 0.16	4.03 ± 0.21	150-200	20	0.4250/57	6.94 ± 0.44	8.51 ± 0.55	1.72 ± 0.14	2.11 ± 0.18
	AsTe-2	T2-L2e	tube	308	15 ± 5	1.88 ± 0.19	8.49 ± 0.48	2.70 ± 0.15	3.57 ± 0.17	100-150	13	0.3270/66	24.05 ± 2.82	35.29 ± 3.28	6.81 ± 0.86	9.99 ± 1.05
	AsTe-4	T2-L4e	tube	225	8 ± 4	2.15 ± 0.12	6.85 ± 0.37	1.69 ± 0.10	3.66 ± 0.15	100-250	20	0.4470/45	84.11 ± 12.38	143.44 ± 24.63	23.0 ± 3.51	39.22 ± 6.91
	AsTe-5	T2-L5e	tube	88	15 ± 5	2.23 ± 0.23	9.69 ± 0.62	3.13 ± 0.19	3.97 ± 0.20	150-200	10	0.2670/37	22.91 ± 1.86	38.31 ± 4.81	5.77 ± 0.55	9.64 ± 1.31
T2	LS-T1-OSL1	T3-L1	tube	65	15 ± 5	2.05 ± 0.21	9.41 ± 0.57	3.05 ± 0.19	3.94 ± 0.25	63-100	40/40	0.1470/33	10.55 ± 0.40	17.38 ± 1.71	3.15 ± 0.21	5.19 ± 0.56
	LS-T1-OSL2	T3-L2	tube	95	15 ± 5	1.93 ± 0.12	8.40 ± 0.54	2.79 ± 0.17	3.69 ± 0.20	63-100	40/40	0.1900/44	68.15 ± 2.17	166.45 ± 16.57	21.3 ± 1.3	52.6 ± 5.9
	LS-T1-OSL3	T3-L3	tube	23	15 ± 5	1.76 ± 0.18	8.12 ± 0.53	2.65 ± 0.17	2.93 ± 0.17	63-100	40/40	0.2300/49	23.96 ± 0.84	77.23 ± 2.75	8.68 ± 0.50	28.0 ± 1.3
	LS-T1-OSL4	T3-L4	tube	227	15 ± 5	1.63 ± 0.14	7.57 ± 0.49	2.49 ± 0.16	3.34 ± 0.21	63-100	40/40	0.4070/47	11.59 ± 1.08	24.43 ± 2.57	3.62 ± 0.39	7.63 ± 0.90
	LS-T1-OSL5	T3-L5	tube	123	15 ± 5	1.75 ± 0.11	6.28 ± 0.41	1.80 ± 0.12	3.24 ± 0.16	100-150	40/40	0.1670/29	12.16 ± 0.98	29.50 ± 2.89	4.20 ± 0.37	10.2 ± 1.1
	LS-T1-OSL6	T3-L6	con. bag	215	15 ± 5	1.65 ± 0.11	7.57 ± 0.47	2.17 ± 0.14	3.26 ± 0.37	100-150	40/40	0.4890/83	60.63 ± 1.41	151.49 ± 16.10	17.9 ± 1.1	44.8 ± 5.3
	LS-T1-OSL7	T3-L7	con. bag	92	15 ± 5	2.04 ± 0.13	8.47 ± 0.54	2.65 ± 0.17	3.68 ± 0.18	150-200	40/40	0.3670/63	80.70 ± 6.29	226.62 ± 14.41	24.6 ± 2.7	69.1 ± 5.5
T4	KOM 17-1b	T4-L1b	tube	72	10 ± 5	2.57 ± 0.16	11.30 ± 0.71	3.68 ± 0.23	4.70 ± 0.19	150-200	20	0.1970/39	17.33 ± 0.28	21.92 ± 2.08	3.69 ± 0.16	4.66 ± 0.48
	KOM 17-2b	T4-L2b	tube	20	10 ± 5	2.34 ± 0.14	10.49 ± 0.68	3.52 ± 0.20	4.49 ± 0.18	150-200	20	0.2870/74	5.43 ± 0.34	6.07 ± 0.25	1.21 ± 0.09	1.35 ± 0.08
	99KOM-STL2	T4-L3b	tube	50	-	2.77 ± 0.02	9.60 ± 1.28	2.67 ± 0.46	4.34 ± 0.33	4-11	-	-	8.126 ± 0.025	-	1.87 ± 0.14	-
	99KOM-NL2	T4-L2	tube	55	-	2.40 ± 0.02	6.84 ± 1.00	2.66 ± 0.37	3.85 ± 0.29	4-11	-	-	5.505 ± 0.039	-	1.43 ± 0.10	-
	99KOM-NL3	T4-L3	tube	115	-	2.47 ± 0.02	6.48 ± 0.80	1.91 ± 0.30	3.46 ± 0.21	4-11	-	-	11.08 ± 0.021	-	3.20 ± 0.22	-
	99KOM-NL4	T4-L4	tube	85	-	2.64 ± 0.03	6.90 ± 0.87	2.87 ± 0.34	4.02 ± 0.30	4-11	-	-	6.073 ± 0.017	-	1.51 ± 0.10	-
	99KOM-NL5	T4-L5	tube	85	-	1.75 ± 0.02	6.48 ± 0.80	1.91 ± 0.30	2.76 ± 0.18	4-11	-	-	8.636 ± 0.032	-	3.20 ± 0.26	-
T5	99KOM-NL7	T4-L7	tube	115	-	1.54 ± 0.02	5.21 ± 0.69	1.90 ± 0.26	2.45 ± 0.15	4-11	-	-	24.806 ± 0.06	-	10.72 ± 0.72	-
	TSH1-1w	T5-L1w	con. bag	56	15 ± 5	2.05 ± 0.21	9.41 ± 0.57	3.05 ± 0.19	3.94 ± 0.25	100-250	40/40	0.1470/33	7.98 ± 0.35	9.64 ± 0.35	2.03 ± 0.13	2.45 ± 0.15
	TSH1-1e	T5-L1e	con. bag	113	15 ± 5	1.93 ± 0.12	8.40 ± 0.54	2.79 ± 0.17	3.69 ± 0.20	100-250	40/40	0.1900/44	17.65 ± 1.09	22.84 ± 0.86	4.79 ± 0.35	6.19 ± 0.33
	TSH1-2e	T5-L2e	con. bag	55	15 ± 5	1.76 ± 0.18	8.12 ± 0.53	2.65 ± 0.17	2.93 ± 0.17	100-250	40/40	0.2300/49	7.93 ± 0.31	10.35 ± 0.32	2.25 ± 0.14	2.93 ± 0.17
	TSH1-3e	T5-L3e	con. bag	78	15 ± 5	1.63 ± 0.14	7.57 ± 0.49	2.49 ± 0.16	3.34 ± 0.21	100-250	40/40	0.4070/47	14.86 ± 0.70	16.67 ± 1.80	4.45 ± 0.28	5.00 ± 0.58
	TSH1-4e	T5-L4e	con. bag	35	15 ± 5	1.75 ± 0.11	6.28 ± 0.41	1.80 ± 0.12	3.24 ± 0.16	100-250	40/40	0.1670/29	68.36 ± 2.16	179.37 ± 14.65	21.1 ± 1.1	55.4 ± 5.0
TSH1-5e	T5-L5e	con. bag	120	15 ± 5	1.65 ± 0.11	7.57 ± 0.47	2.17 ± 0.14	3.26 ± 0.37	100-250	40/40	0.4970/83	12.33 ± 1.34	17.31 ± 1.93	3.78 ± 0.44	5.30 ± 0.63	
Pit	TSH1-6e	T5-L6e	con. bag	30	15 ± 5	2.04 ± 0.13	8.47 ± 0.54	2.85 ± 0.17	3.88 ± 0.18	100-250	40/40	0.3670/63	11.79 ± 0.31	14.34 ± 0.87	3.06 ± 0.14	3.72 ± 0.27
	SYN18-OSL1	PT1-Syn	tube	83	15 ± 5	1.93 ± 0.20	7.57 ± 0.50	2.19 ± 0.14	3.36 ± 0.18	100-150	33/33	0.0670/06	23.13 ± 0.25	30.12 ± 0.36	6.85 ± 0.36	8.92 ± 0.47
	18TSH2-OSL1	PT2-Tsh2	tube	58	15 ± 5	2.29 ± 0.14	9.99 ± 0.63	3.19 ± 0.19	4.09 ± 0.18	63-100	40/39	0.2270/27	18.23 ± 0.24	22.98 ± 0.44	4.46 ± 0.18	5.62 ± 0.24
	18TSH-OSL1	PT3-Tsh	tube	35	15 ± 5	2.21 ± 0.18	9.99 ± 0.63	3.08 ± 0.18	3.97 ± 0.18	100-150	40/39	0.0570/08	24.68 ± 0.22	30.63 ± 0.40	6.21 ± 0.28	8.02 ± 0.38

^aSamples run at the Institute of Earth and Environmental Sciences (University of Freiburg in Germany), 99KOM Samples run by S. L. Forman at the Luminescence Dating Research Laboratory in 1999 (University of Illinois, Chicago, USA).

^bWater content was estimated based on present day moisture and grain-size composition.

^cNumber of accepted aliquots passing internal recycling ratio criteria (≥10%).

^dMean dose was calculated using either the Central Age Model (CAM) or the Minimum Age Model (MAM), depending on the statistical parameters of D₀ distributions, such as overdispersion, skewness and kurtosis (cf. Galbraith & Roberts, 2012).

^eAges were calculated using ADELEV.2017 (Degering & Degering, 2020), using the results of high-resolution gamma spectrometry (cf. Preusser & Kasper, 2001).

To indicate my confidence regarding each interpreted surface-rupturing paleoearthquake including the age, all observations within the exposed trench walls were assigned a quality ranking, following the approach of Schärer et al. (2007). The quality scheme ranges from 1 to 4 (best to speculative) and is based on an evaluation of strength regarding paleoearthquake evidence of the observed features. A summary of all event indicators and associated earthquakes from each trenching site is listed in Tables 5.3 to 5.7. Finally, I assigned an additional ranking to the OxCal-modeled earthquake age by considering (1) the completeness of bracketing of the earthquake-event horizon, and (2) the uncertainty of the resulting modeled age of the earthquake (Table 5.8). These ratings are used here to systematically and qualitatively assess the results to develop the final interpretation; in the future, they might be useful for additional quantitative analysis (e.g., correlation models, etc.).

5.1.1. T1 – Achyk-Suu (39.48°N 72.50°E)

In trench T1 at the Achyk-Suu site, the exposed hanging wall reveals a ~3 to 4-m-thick unit 1 with ~25° north-dipping bedding of the fluvial gravel covered by a thin topsoil (TS) layer (Figure 5.2). Unit 2 is not exposed in this location. However, farther south along the walls of the quarry in the hanging wall, unit 2 is present where the slope of the scarp flattens out again (Figure 4.6; Chapter 4). Hence, I infer that along the scarp face unit 2 was completely eroded through time.

The footwall consists mainly of a succession of fine-grained sandy deposits (Figure 5.2). The boundary between units 1 and 2 is not exposed. The lowermost unit 3 is made up of grayish, very fine sandy silt and contains a few patches of fine gravel. Unit 3 is overlain by material of a similar, but more heterogeneous composition that is less compacted with a higher clast content (C1) than unit 3. The change from unit 3 to C1 is also marked by a sharp change in color, from grayish to reddish brown. C1 gradually changes color upwards to beige, of softer, homogeneous fine silty sand and fewer clasts (unit 4). The subsequent package C2 can be separated from unit 4 by a clear boundary of a thin basal layer of fine gravel, a distinct change in color from beige to reddish beige, and increased clast content. C2 is covered by gravitationally collapsed and reworked unit 1 material (C3a) overlain by a block of reddish silty sand (C3b). Finally, a lens of organic paleosol material lies between unit C3b and the overlying, less organic-rich top soil TS.

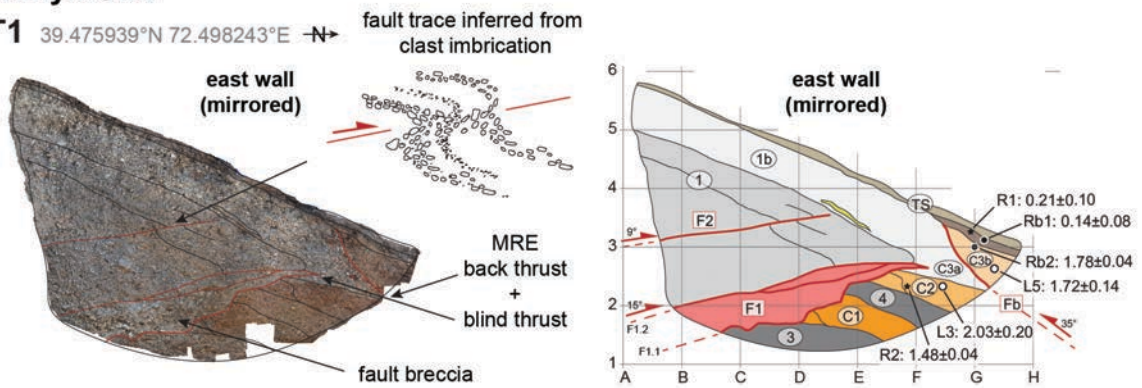
The main fault F1 is a wide zone (~20 cm) of chaotically oriented clasts, with a pronounced, undulating lower contact. The strata of unit 1 are locally disturbed by deformation along fault F2, expressed as a narrow zone of imbricated clast fabric. The upper tip of a back thrust fault Fb is exposed in the northern portion of the trench.

I assume that the steep northward dip of the bedding of unit 1 presumably results from cumulative faulting and folding along F1, a common effect of thrust faulting along shallow faults (<30°) (e.g., McCaillin & Carver, 2009; also compare with following trench logs). I interpret that C1 is scarp-derived

colluvium deposited interseismically after a surface-rupturing event that overthrust parts of units 1 and 2 over unit 3. The part of C1 proximal to the fault was presumably deformed and dragged towards the upper boundary of unit 4 during subsequent faulting, leading to the deposition of more mixed colluvial material during the following interseismic period (C2). However, the evidence for this interpretation is not very strong, which makes this event debatable (see Discussion). During the penultimate event, upthrust strata of unit 1 partially collapsed (C3a) and were displaced downhill over C2. I suggest that the overlying material of C3b was originally deposited during the subsequent interseismic period at the scarp toe on top of C3a and later pushed and compacted against C3a during backthrusting along Fb, forming a convex contact between C3a and C3b.

Achyk-Suu

T1 39.475939°N 72.498243°E →



Alluvial fan units

TS	top soil; silty-sand; loose, matrix supported; dark brown; roots; poorly sorted; 25% discontinuous subrounded pebbles; gradual basal contact
4	fine sand and silt; less compacted, holey; reddish light-beige; well sorted; 3% subrounded pebbles; clear basal contact
3	very fine silty-sand; moderately compacted, holey; grayish-brown; well sorted; 2% subrounded pebbles; basal contact not exposed
1b	sub-unit of unit 1; stage I-II pedogenic CaCO ₃ soil development; clasts with CaCO ₃ crusts on their undersides; diffuse and undulating basal contact
1	fluvial gravel; clast supported; reddish-gray silt matrix; alternating bedding and imbrication; overall poorly sorted, locally well sorted lenses; 50% subrounded gravel, max. 20 cm diam.; basal contact not exposed

Colluvial sequences

C3b	very fine sandy-silt; moderately compacted; higher organic content; reddish brown; moderately sorted, local layers of aligned clasts; 10% subangular pebbles; clear basal contact
C3a	reworked unit 1b; loose; reddish gray; poorly sorted; chaotic CaCO ₃ coating orientation; 50% subangular gravel; clear basal contact
C2	fine sandy-silt; less compacted, holey; some caliche; dark reddish brown; moderately sorted; 10% subangular rotten pebbles; clear basal contact of clasts
C1	very fine sandy-silt; compacted, holey; light reddish-brown; poorly sorted; from bottom: 7% to top: 20% subangular pebbles; clear basal contact of clasts

Contacts

	fault; accurate
	fault; approximate
	contact; accurate
	contact; approximate

Symbols

	fault dip and fault vergence
	internal lamination

Dated samples

	Infrared Stimulated Luminescence (IRSL)
	bulk soil
	charcoal
	terrestrial snail
radiocarbon ¹⁴ C (age in cal kyr B.P.)	

Fault zone

	zone of rotated clasts; aligned subparallel to fault
--	--

Figure 5.2 Photomosaic and interpreted trench log with major lithological units, faults, scarp-derived colluvium and locations of geochronologic samples in the east wall (mirrored) of trench T1, Achyk-Suu. See Table 5.3 for reference and summary of stratigraphic and geomorphologic indicators for all interpreted paleoearthquakes. Radiocarbon (¹⁴C) and infra-red stimulated luminescence (IRSL) ages shown in thousands of years (mean ± 2σ) correspond to Tables 5.1 and 5.2, respectively. See Appendix B for high-resolution photomosaics of the trench walls.

Table 5.2 Summary of stratigraphic and geomorphic indicators for paleoearthquakes in trench T1 and assigned ranking for event evidence evaluation.

Trench	Fault Zone	Site Earthquake	Trench Location ^a	Unit	Indicator	Ranking ^b	Ranking Sum
T1	F2	A5	T1-3D	1	offset marker, faulted fluvial bedding	3	6
	F1		T1-34DE	F2	Upper fault termination, sand lens	3	
	F1	A4	T1-2D	C1	Colluvium	1	1
	F1	A3	T1-23E	C2	Colluvium	1	1
	F1	A2	T1-3F	C3a	Colluvial wedge	4	8
	F1		T1-3F	F1	Upper fault termination	4	
	Fb		Ab1	T1-3G	Fb	Convex contact between C3a and C3b, indicator for bulldozing during backthrusting	

^a Location according to trench log documentation Figure 5.2.

^b Ranking quality: 1 = speculative; 2 = indistinct; 3 = slightly visible; 4 = distinct.

T1 EQ Five (A5): The evidence for the oldest rupture observed in T1 is along fault zone F2. F2 terminates at unit 1b and an unfaulted sand lens, indicating that this fault has not been active since the final phase of the fluvial gravel deposition. To bracket the timing for A5, I used the age of unit 1 (20.1 ± 0.6 ka) and the capping unit 2 (7.3 ± 0.1 ka) as maximum and minimum age constraints, respectively. Due to the large age gap between both units, A5 has a modeled age of 14.2 ± 2.6 ka.

T1 EQ Four (A4): The second oldest event ruptured along F1 and is associated with unit C1. We were not able to obtain absolute age control for paleoearthquake A4 and can only state that it is younger than A5. However, OxCal allows to determine relative time constraints by modeling empty uniform phases based on interpreted stratigraphic order (see Code B1). Thus, the age for this paleoearthquake is modeled using relative ages of the stratigraphic sequence of units 3, C1 and 4. For broader bracketing, I used the age of unit 2 (7.3 ± 0.1 ka) as a maximum age (assuming that unit 3 formed subsequently) and the age of unit C2 (see below) capping unit 4 as a minimum age. Consequently, A4 has a modeled age of 4.8 ± 1.0 ka.

T1 EQ Three (A3): Event A3 is associated with unit C2. We use two ages (L3: 2.03 ± 0.20 and R2: 1.78 ± 0.04 ka) obtained from the upper part of C2 as minimum bracketing, assuming these represent the deposition of C2 in the interseismic period. Combined with the relative timing associated with A4, A3 has a modeled age of 2.4 ± 0.5 ka.

T1 EQ Two (A2): The penultimate event is associated with C3a. The timing of A2 is tightly constrained by the age of the underlying unit C2 and the age constraints from the overlying unit C3b (L5: 1.72 ± 0.14 ; Rb2: 1.48 ± 0.04). This bracketing results in a model age for A2 of 1.6 ± 0.1 ka.

T1 EQ One (Ab1; MRE): The most recent event Ab1 ruptured along F1 without breaking the surface and along the back-thrust fault Fb. The timing for the MRE is well constrained by the age of unit C3b as maximum age and radiocarbon ages from the overlying paleosol (R1: 0.21 ± 0.10 ; Rb1: 0.14 ± 0.08 ka) as minimum bracketing. Combined, the bracketing yields a model age for the MRE Ab1 of 0.8 ± 0.4 ka.

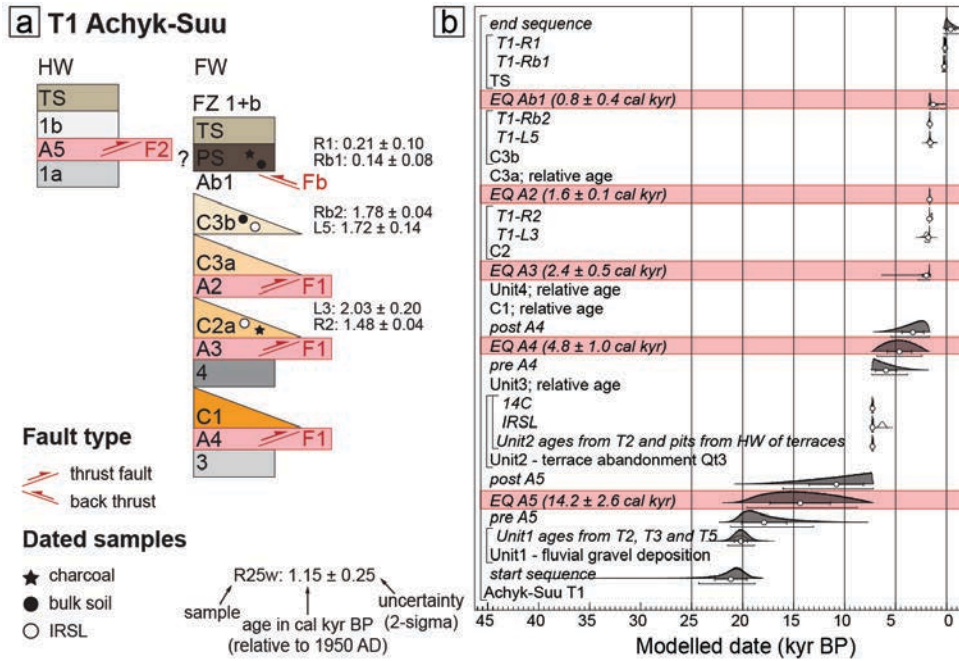


Figure 5.3 Trench T1, Achyk-Suu. (a) Schematic summary of the structural and stratigraphic results. Colors correspond to lithostratigraphic units in the corresponding trench log (Figure 5.2). All collected radiocarbon (^{14}C) and infra-red stimulated luminescence (IRSL) samples are included in the scheme. All modeled unit ages are mean $\pm 2\sigma$ (Table 5.1 and Table 5.2). (b) OxCal models (v4.4.4 Bronk Ramsey (2021); r:5 Atmospheric data from Reimer et al. (2020) of paleoearthquake timing constraints). See Code B1 in Appendix B for the associated OxCal script.

5.1.2. T2 – Achyk-Suu (39.48°N 72.51°E)

The major part of the exposed stratigraphy in trench T2 at the Achyk-Suu site consists of fluvial gravel (unit 1; max. thickness 3 m) overlain by unit 2 (~50 cm). In total, the exposed trench walls revealed four separate fault zones (F1, F2, F3, F4), where fault zones F1 and F4 coincide with the surface traces of the fault scarp (Figure 5.4).

In the footwall, unit 2 is covered by a layer of fine silty sand with internal lamination and varying color between gray and reddish beige (unit 3), which I interpret as pond-related sediments. The character of these sediments is compatible with modern laminated and reddish to beige silts and fine sands that were observed in the footwall during the field campaign. Unit 3 sediments are covered by a more compacted, slightly reworked reddish clayey fine sand (unit 4) with homogeneously distributed CaCO_3 nodules in their upper part. I interpret that this unit developed during a protracted interseismic period with soil formation and I assume that its upper boundary is a paleosurface. Units 3 and 4 are only present in the footwall. Unit 4 is overlain by two sheets of inferred colluvial origin (C2, C3) that can be distinguished from each other and the lower units by a clear change in color and composition (Figure 5.4).

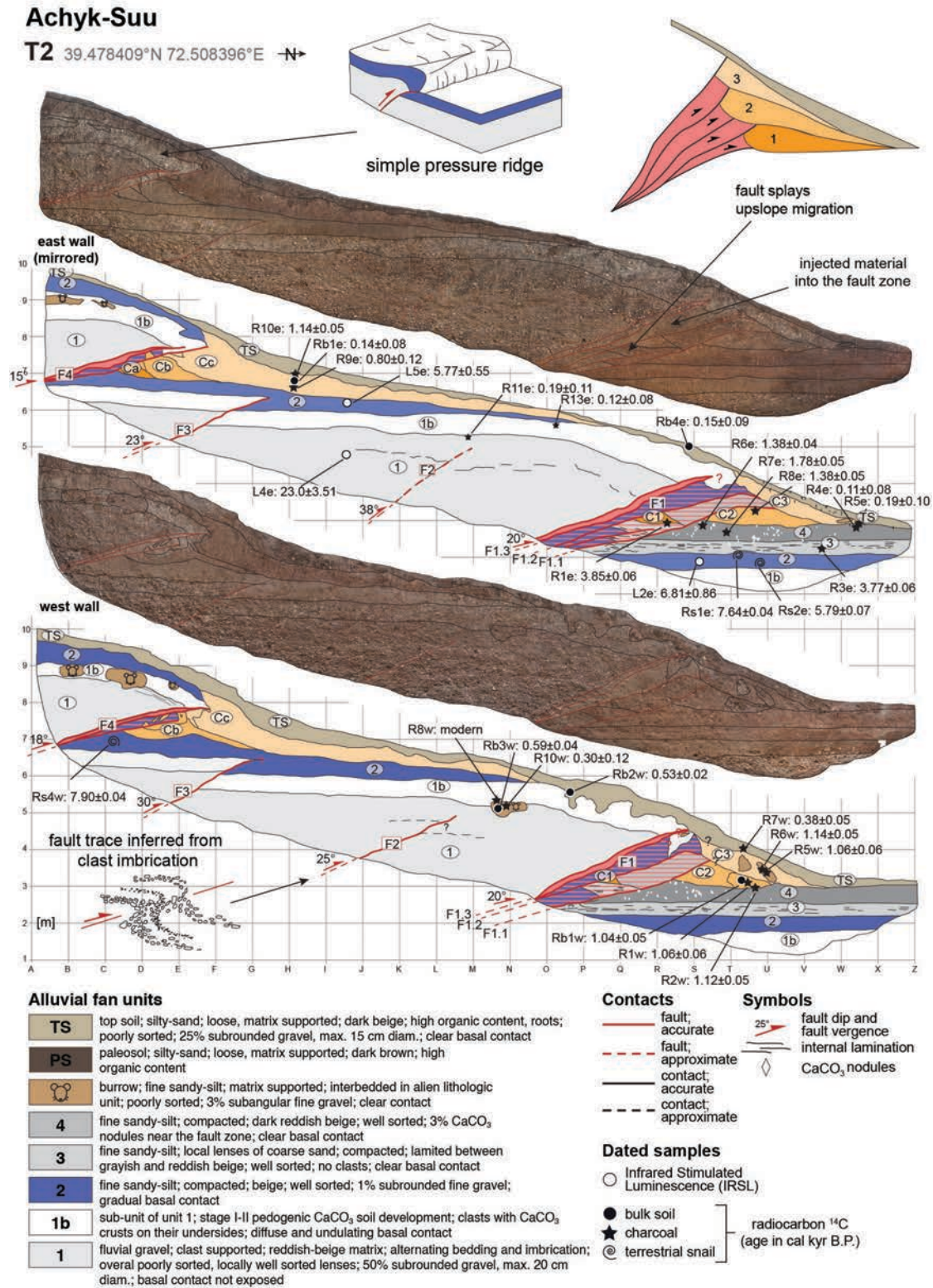


Figure 5.4 Photomosaic and interpreted trench log with major lithological units, faults, scarp-derived colluvium and locations of geochronologic samples in the east wall (mirrored) and west wall of trench T2, Achyk-Suu. See Table 5.4 for reference and summary of stratigraphic and geomorphologic indicators for all interpreted paleoearthquakes. Radiocarbon (¹⁴C) and infra-red stimulated luminescence (IRSL) ages shown in thousands of years (mean ± 2σ) correspond to Table 5.1 and 5.2, respectively. See Appendix B for high-resolution photomosaics of the trench walls.

Colluvial sequences

Cc	clayey fine sandy-silt; moderately compacted, holey; reddish beige, poorly sorted, local layers of aligned clasts; 10% subangular gravel to cobble, clear undulating diffuse basal contact
Cb	reworked unit 2; compacted, holey; beige to reddish beige; moderately sorted; 10% subangular gravel; clear basal contact
Ca	reworked unit 2; compacted, holey; beige; moderately sorted; 1% subangular fine gravel; clear undulating basal contact
C4	clayey fine sandy-silt; moderately compacted, holey; reddish beige, very poorly sorted, lenses of reworked unit 1b material, 25% subangular gravel to cobbles, diffuse basal contact
C3	clayey fine sandy-silt; compacted, holey; beige with reddish patches; moderately sorted; 15% subangular fine gravel; clear undulating basal contact
C2	reworked unit 2; compacted, holey; beige to reddish beige; moderately sorted; 5% subangular gravel; clear basal contact
C1	reworked unit 2; compacted, holey; beige; moderately sorted; 1% subangular fine gravel; clear undulating basal contact

Fault zones





	zone of rotated clasts; aligned subparallel to fault
	upthrust and deformed material of unit 4
	upthrust part of unit 3, internal structure stayed intact
	injected and continuously smeared upwards material of unit 2

Figure 5.4 (continued)

Table 5.3 Summary of stratigraphic and geomorphic indicators for paleoearthquakes in trench T2 and assigned ranking for event evidence evaluation.

Trench	Fault Zone	Site Earthquake	Trench Location ^a	Unit	Indicator	Ranking ^b	Ranking Sum
T2	F2	AS5	T2-W-4K	F2	Trace of rotated clasts	2	4
			T2-E-45LM	F2	Offset marker; offset internal bedding within unit 1	1	
			T2-W-45LM	F2	Offset marker; offset internal bedding within unit 1	1	
	F1	AS4	T2-E-2U	3	Pond sediments	3	18
			T2-W-2U	3	Pond sediments	3	
			T2-E-23P	F1	Upthrust unit 2 material slightly reworked, its upper boundary is dipping slightly northwards: part of old colluvium	1	
	F1	AS4	T2-W-23O	F1	Upthrust unit 2 material slightly reworked, its upper boundary is dipping slightly northwards: part of old colluvium	1	4
			T2-E-6G	F3	Offset marker; faulted unit 1 and unit 2	4	
			T2-W-6G	F3	Offset marker; faulted unit 1 and unit 2	4	
	F4	AS3	T2-E-7D	Ca	Colluvium; injected fault breccia	2	12
			T2-E-3R	C1	Reworked unit 2	2	
			T2-W-3Q	C1	Reworked unit 2	2	
	F4	AS2	T2-E-7E	Cb	Colluvium	4	16
			T2-W-7D	Cb	Colluvium	4	
			T2-E-3T	C2	Colluvium	4	
	F1	AS2	T2-W-3S	C2	Colluvium	4	4
			T2-E-7F	Cc	Colluvium	4	
			T2-W-7G	Cc	Colluvium	4	
	F1	AS1	T2-E-4U	C3	Colluvium	4	38
			T2-W-4T	C3	Colluvium	4	
			T2-E-4T	F1	Upper termination of F1, covered by C3	4	
	F1	AS1	T2-W-4S	F1	Upper termination of F1, covered by C3	4	4
			T2-E-3S	F1.3	Offset marker; upthrust unit parts (unit 2, 3, and 4) with retained stratigraphy	4	
			T2-W-3R	F1.3	Offset marker; upthrust unit parts (unit 2, 3, and 4) with retained stratigraphy	4	
	F4	AS1	T2-E-8E	F4	Upper termination of F4	4	3
			T2-W-8F	F4	Upper termination of F4	4	
			T2-E-8E	Cc	Deformed/bulldozed southern edge of colluvial wedge	3	
	F4	AS1	T2-E-8E	Cc	Deformed/bulldozed southern edge of colluvial wedge	3	3
T2-E-8E			Cc	Deformed/bulldozed southern edge of colluvial wedge	3		

^a Location according to trench log documentation Figure 5.4.^b Ranking quality: 1 = speculative; 2 = indistinct; 3 = slightly visible; 4 = distinct.

In the intermediate sectors of the hanging wall, unit 2 is also overlain by a succession of colluvial sheets (Ca, Cb, Cc). All of these layers can be distinguished from each other by small wedges of injected clast material and a thin trace of clasts at their lower boundary emerging proximal to F4. Ca was only poorly exposed in the east wall. The surface soil (TS) constitutes a layer of mixed sediments from gravity-, debris- and/or wash-dominated degradation or fluvial transport from the adjacent foothills SSE of the trench and is covered by a thin soil A horizon (~10 cm).

Fault zone F1 exhibits a complex structure with several subparallel, internal fault strands (F1.1, F1.2 and F1.3; Figure 5.4), which indicates upslope fault splay migration due to cumulative faulting. Within the fault zone interior, we were able to recognize parts of units 2 and 3 that were dragged upwards retaining their stratigraphic boundary.

The laminated material of unit 3 between F1.1 and F1.2 is overlain by a small, clearly distinguishable wedge-like unit of beige-colored reworked fine material (C1) covered by reddish fine material, presumably from unit 4. The termination of fault strands F1.1 and F1.2 is covered by C2, I therefore conclude that C3 must be related to an event other than C2. The width of the F1 zone increases upward and is made up of more homogenous beige-colored fine material between F1.2 and F1.3, which I infer to be unit 2 material that got liquefied and injected into the fault zone during repeated faulting (e.g., Weber & Cotton, 1981). Faults F2 and F3 cut through the intermediate hanging wall and were active only once, but presumably not related to the same surface-rupturing event. Although F2 can be unambiguously identified in the west wall by a pronounced trace of rotated clasts, F2 is not clearly distinguishable in the east wall.

Fault zone F3 cuts through units 1 and 2 and upthrusts parts of unit 1 above unit 2. Above the upper termination of F3, unit 2 is thicker, which strongly indicates degradation processes that reworked unit 2 material across the small scarp-free face. The undulatory nature of the paleosurface suggests that remnants of a paleo-scarp were covered by subsequent colluvial strata Cb and Cc, which formed after faulting along F4. Similar to F1, F4 exhibits internal deformation, fault splay migration and liquefied fine materials injected between fault-breccia bodies. For instance, one could observe patches of clasts that presumably belonged to the former injected material of unit 1 proximal to the fault that was deformed during subsequent faulting, indicating multiple fault activation.

T2 EQ Five (AS5): The oldest evidence for a paleoearthquake retrieved from the stratigraphic relationships in T2 is associated with fault F2. I infer, similar to earthquake A5 (trench T1), that this fault was active during the final phase of the deposition of unit 1 and before the formation of unit 2. Thus, I bracket the timing for AS5 with the age of unit 1 (20.1 ± 0.6 ka) and of unit 2 (7.3 ± 0.1 ka). The bracketing leads to a modeled age for AS5 of 14.3 ± 2.9 ka.

T2 EQ Four (AS4): From the stratigraphical and chronological context, I infer that AS4 is associated with faulting along three faults (F1, F3 and F4), assuming that faulting along F1 cut through unit 2 and caused the formation of a ponded drainage and deposition of unit 3 at the toe of the lowest scarp related to initial scarp formation. Less strong faulting along F3 and faulting along F4 is associated with Ca also cut into and/or through unit 2. Following these observations, I assume that F3 and F4 were coeval, with F1 during this event. To bracket the age of this event, I used the age of unit 2 (7.3 ± 0.1 ka) to define the maximum age constraint. For the minimum age constraint, I used two radiocarbon samples from the base of unit 3 (R3e: 3.77 ± 0.06 ka; R1e: 3.85 ± 0.06). AS4 can be modeled at 4.7 ± 1.0 ka.

T2 EQ Three (AS3): Subsequent faulting along F4, cut through, and deformed the upslope part of Ca. Subsequent diffusion processes deposited colluvial package Cb. Unit C1 serves as a poor indicator for coeval fault activation along F1.2 and I infer that its position results from upthrusting during subsequent events that ruptured along F1.1 toward its current position. Following this indicator and the visible contact with unit 4, I suggest that unit 4 was deposited after AS3. Consequently, as a maximum age estimate, we use a radiocarbon age (R1e: 3.85 ± 0.06 ka) sampled from below C1 that agrees with the age of unit 3, and three radiocarbon ages (R7e: 1.78 ± 0.05 ka; R6e: 1.38 ± 0.04 ka) from unit 4 as a minimum age constraint. Combined, AS3 is modeled at 3.4 ± 0.4 ka.

T2 EQ Two (AS2): Considering the age control from C2 (R2w: 1.12 ± 0.05 ka; R1w: 1.06 ± 0.06 ka; Rb1w: 1.04 ± 0.05 ka; R8e: 1.38 ± 0.05 ka); Cc (R10e: 1.14 ± 0.04 ka; R9e: 0.8 ± 0.1 ka), I suggest that these colluvial strata are related to one surface rupturing earthquake that reactivated both F1 and F4, respectively. Sample R8e, however, is inconsistent and it may represent reworked material from unit 4 that was displaced towards the upper area of C2 during subsequent faulting along F1.3 (MRE; AS1), where the leading edge of the fault deformed the parts of C2 proximal to the fault during bending subhorizontally. Combined, four radiocarbon samples from C2 and Cc are used as minimum age constraints and the age of the underlying unit 4 (R7e and R6e) serves as a maximum age constraint. Together, AS2 is modeled at 1.2 ± 0.1 ka.

T2 EQ One (AS1, MRE): The most recent event along F1 is linked to the uppermost massive colluvial strata of C3. C3 covers the termination of fault strand F1.2 and F1.3; I therefore conclude that both were activated simultaneously with F1.1 during AS1. Motion along them upthrust older units (unit 2 and C1) and cut through C2 along F1.3. I suggest that this event activated F4 at the same time, however, the faulting probably did not rupture the surface. Instead, faulting cut into the lower part of Cc and shoved material along the fault, which thickened the southern part of Cc. It also appears that this fault motion steepened the paleo-scarp, which allowed the deposition of slumped material at its toe (TS). We obtained two radiocarbon ages from C3 (R5w: 1.06 ± 0.06 ka; R6w: 1.14 ± 0.05 ka); however, these ages coincide with the ages from the underlying unit C2. I suggest that these ages probably rather represent an inherited age from reworked unit C2 material that was later recycled into C3. Following this interpretation, I use the age of C2 and Cc (R10e, R9e) as maximum age constraint and five radiocarbon samples (Rb2w: 0.49 ± 0.03 ka; R7w: 0.38 ± 0.05 ka; R4e: 0.11 ± 0.08 ka; Rb4e: 0.15 ± 0.09 ka; R5e: 0.19 ± 0.10 ka) representing the age of the topsoil (TS) as broader minimum age constraint. Using all of this information, I was able to model AS1 at 0.8 ± 0.2 ka.

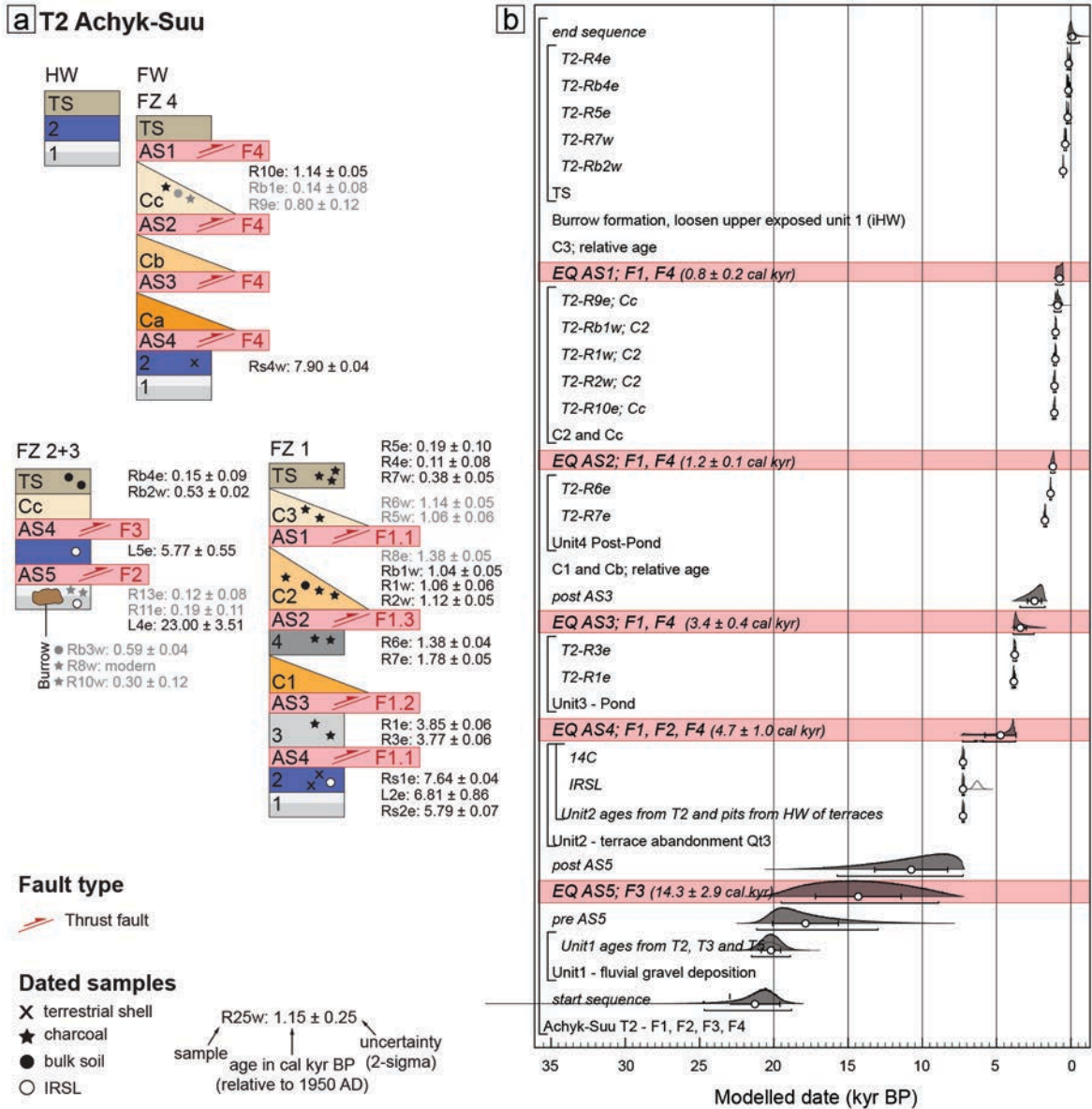


Figure 5.5 Trench T2, Achyk-Suu. (a) Schematic summary of the structural and stratigraphic results. Colors correspond to lithostratigraphic units in the corresponding trench log (Figure 5.4). All collected radiocarbon (^{14}C) and infra-red stimulated luminescence (IRSL) samples are included in the scheme; gray shaded samples are excluded from the OxCal models because of inconsistency in the stratigraphic order and/or disagreement with surrounding samples (see text for explanation). All modeled unit ages are mean $\pm 2\sigma$ (Table 5.1 and Table 5.2). (b) OxCal models (v4.4.4 Bronk Ramsey (2021); r:5 Atmospheric data from Reimer et al. (2020) of paleoearthquake timing constraints). See Code B2 in Appendix B for the associated OxCal script.

5.1.3. T3 – Ylaisu (39.48°N 72.52°E)

In trench T3 at Ylaisu, the exposed hanging wall mainly consists of the massive 2 to 3-m-thick unit 1 with an undulatory and reworked boundary against unit 2 (Figure 5.6). A massive channel-like body (Ch1) composed of sandy, matrix-supported gravel with patches of silty sand lenses and burrows cuts through unit 1. A second, distinctly red and fine silty-sandy deposit (Ch2) is exposed only in the west wall.

Ylaisu

T3 39.47916°N 72.52376°E →N

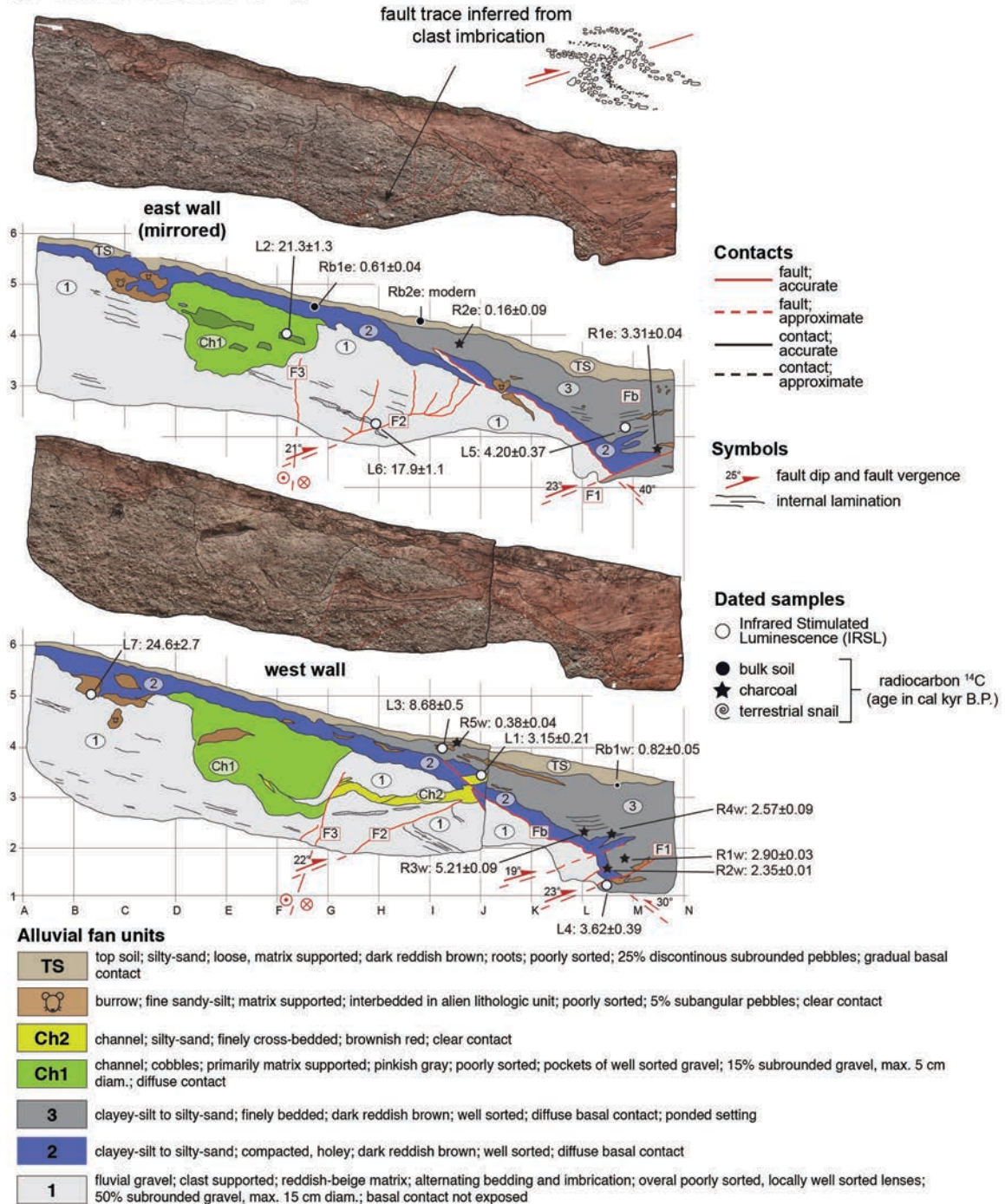


Figure 5.6 Photomosaic and interpreted trench log with major lithological units, faults, scarp-derived colluvium and locations of geochronologic samples in the east wall (mirrored) and west wall of trench T3, Ylaisu. See Table 5.5 for reference and summary of stratigraphic and geomorphologic indicators for all interpreted paleoearthquakes. Radiocarbon (¹⁴C) and infra-red stimulated luminescence (IRSL) ages shown in thousands of years (mean ± 2σ) correspond to Tables 5.1 and 5.2, respectively. See Appendix B for high-resolution photomosaics of the trench walls.

Table 5.4 Summary of stratigraphic and geomorphic indicators for paleoearthquakes in trench T3 and assigned ranking for event evidence evaluation.

Trench	Fault Zone	Site Earthquake	Trench Location ^a	Unit	Indicator	Ranking ^b	Ranking Sum			
T3	F2	YL3	T3-E-2H	1	Offset sandy lens	4	21			
	F2		T3-E-2H	1	Fissure; broken sandy lens	4				
	F2		T3-E-3IJ	1	Fissure; filled with matrix supported gravel. Mixed unit 1 and 2?	3				
	F3		T3-E-4FG	1	Carbonated fault strand (F3); traceable downwards by rotated clasts	2				
	F2		T3-W-3G	Ch2	Deformed channel	4				
	F2		T3-W-3IJ	Ch2	Offset lower boundary of channel, upper termination of F2	4				
				T3-E-3IJ	1	Slightly tilted fissure; folding of hanging wall during faulting along F1		1	5	
				YL2	T3-E	1		Inclined bedding; folding of hanging wall during faulting along F1		2
					T3-E	3		Pond sediments		1
					T3-W	3		Pond sediments		1
		Fb1		T3-E-4IJ	1	Injected unit 1 material into unit 2; backthrusting along Fb	2	21		
		F1		T3-E-1LM	F1	Unit 1 overthrusting unit 2	4			
		F1		T3-E-2LM	3	Deformed internal bedding	2			
		F1		T3-E	1	Inclined bedding; folding of hanging wall during faulting along F1	1			
		F1	YL1	T3-W-3J	Ch2	Offset channel; backthrusting along Fb	4			
		F1		T3-W-1M	F1	Unit 1 overthrusting unit 2	4			
		F1		T3-W-1M	3	Offset burrow	2			
		F1		T3-W-1L	1+2	Faulted unit 1 and 2, upper termination of fault strand; F1 splay	1			
		F1		T3-W	1	Inclined bedding; folding of hanging wall during faulting along F1	1			

^a Location according to trench log documentation Figure 5.6.

^b Ranking quality: 1 = speculative; 2 = indistinct; 3 = slightly visible; 4 = distinct.

Finely laminated reddish silty-sand deposits (unit 3) in front of the scarp indicate sedimentation during ponding after scarp formation, similar to the setting described in T2. We were able to excavate a limited area to deepen the northern part of the trench. This, however, only exposed a shallow part of unit 3 in the footwall (~20 cm) that did not reveal the contact to unit 2, and the upper termination of fault zone F1. The deformation in T3 is expressed at three separate fault zones and one back thrust. The main thrust-fault zone F1 in the north upthrusts unit 1 and cuts into unit 3. The gently north-dipping bedding and frontal bend of unit 1 indicates pressure-ridge formation along the ~23°-dipping F1, reminiscent of features observed during the Al Asnam earthquake (Philip et al., 1992).

Above and south of F1, the back thrust Fb offsets the northern end of Ch2; in the east wall, a thin layer of unit 1 was smeared upwards as indicated by clasts that are aligned subparallel to the inferred fault strand Fb. The south dipping fault zone F2 cuts through unit 1. In the east wall, the top of F2 splays into several, nearly vertical fissures, whereas in the west wall, F2 can be traced along a single strand; both die out before the upper boundary of unit 1. In the east wall, F2 offsets a sandy layer and in the west wall, the lower part of Ch2. Fault zone F3 is nearly vertical, deforms Ch1 and Ch2 in the west wall, and terminates approximately at the same depth as F2. The deformation patterns of F2 and F3 resemble a positive flower structure, suggesting transpressive, coeval deformation with both faults rooting in one structure. However, the evidence for coeval or independent activation is ambiguous.

T3 EQ Three (YL3): The timing of YL3 is not very well constrained. Considering the vicinity of trenches T1, T2 and T3 (distance along cPFT = ~3 km) and comparable event indicators (i.e., fault cuts

through unit 1, terminates before its upper boundary, and no scarp/colluvium), I suggest that YL3 can be correlated with A5 and AS5 from trenches T1 and T2, respectively. The only indication regarding chronology is provided by the deformation of channel Ch1 (L2: 21.3 ± 1.3 ka) by F3, and channel Ch2 (L1: 3.15 ± 0.21 ka) by F2, which provides a maximum age constraint on timing. However, L1 was omitted from the modeling because it is out of stratigraphic order and inconsistent with IRSL ages from unit 1 (L7: 24.6 ± 2.7 ka; L6: 17.9 ± 1.1 ka). Consequently, to bracket the timing, I used the age of unit 1 (20.1 ± 0.6 ka) and of unit 2 (7.3 ± 0.1 ka). Combined, the age for YL3 is modeled at 13.9 ± 2.9 ka.

T3 EQ Two (YL2): Fault zone F1 is not well exposed, preventing a detailed reconstruction of the earthquake history. However, because I infer that YL3 did not produce a significant scarp, a younger event must have occurred to allow ponding at its front and the deposition of unit 3, similar to T2. The age constraints from four radiocarbon ages (R3w: 5.21 ± 0.09 ; R1e: 3.31 ± 0.04 ka; R2w: 2.35 ± 0.01 ka; R1w: 2.90 ± 0.03 ka) and two IRSL ages (L5: 4.20 ± 0.37 ; L4: 3.62 ± 0.39 ka) from unit 3 compare well with those from unit 3 in T2. Thus, I assume the pond formation is associated with the same event at T2 (AS4). Without any further indicators, I use the average age of unit 2 (7.3 ± 0.1 ka) as maximum age and unit 3 as minimum age constraint. Together, these provide a modeled age for YL2 of 6.1 ± 0.6 ka.

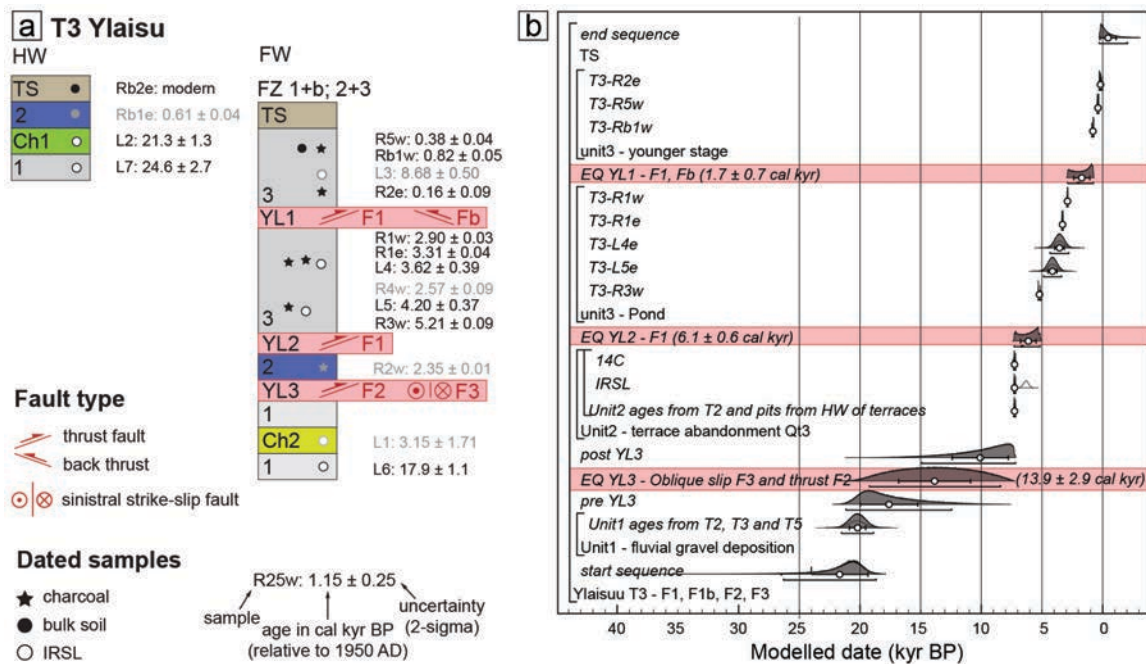


Figure 5.7 Trench T3, Ylaisu. (a) Schematic summary of the structural and stratigraphic results. Colors correspond to lithostratigraphic units in the corresponding trench log (Figure 5.6). All collected radiocarbon (^{14}C) and infrared stimulated luminescence (IRSL) samples are included in the scheme; gray shaded samples are excluded from the OxCal models because of inconsistency in the stratigraphic order and/or disagreement with surrounding samples (see text for explanation). All modeled unit ages are $\pm 2\sigma$ (Table 5.1 and Table 5.2). (b) OxCal models (v4.4.4 Bronk Ramsey (2021); r:5 Atmospheric data from Reimer et al. (2020) of paleoearthquake timing constraints). See Code B3 in Appendix B for the associated OxCal script.

T3 EQ One (YL1; MRE): With respect to the exposed part of deformation features, I interpret that the most recent event ruptured along F1 and coevally backthrust along Fb. Deformed internal layering unconformably overlain by undisturbed strata within unit 3 indicates that the deformation took place during its final deposition. Following this interpretation, I use the older phase of deposition of unit 3 (lower part; see above) as a maximum age constraint and two radiocarbon ages obtained from the upper part of unit 3 (Rb1w: 0.82 ± 0.05 ka; R2e: 0.16 ± 0.09 ka) as minimum age constraints. I omit one IRSL sample (L3: 8.68 ± 0.50) due to apparent partial bleaching (major offset of pIR and IRSL; Table 5.2). This bracketing yields a modeled age for YL1 of 1.7 ± 0.7 ka.

5.1.4. T4 – Komansu (39.50°N 72.65°E)

At the Komansu site the exposed lower stratigraphy is consistent throughout both trench exposures (Figure 5.8). Each footwall consists of undeformed layers of horizontally and discontinuously bedded fluvial gravels with CaCO₃ coatings (unit 1b) overlain by fine silty sand with incorporated pebbles in its lower part (unit 2b). Unit 2b (Qt₄) is less thick than unit 2 defined elsewhere on Qt₃ and has a more diffuse basal contact with unit 1, which could imply less stable depositional conditions and potentially higher seasonal erosional events during deposition. All ages in the northern trench result from IRSL samples collected during the 1999 campaign. In the southern trench, two IRSL samples (L1b, L2b) were collected in 2017 in order to cross-check the reliability of the older samples.

The northern trench exposes a major ~21°-S-dipping main thrust fault F1 and inclined bedding of unit 1b in the hanging wall, as observed in the other trenches. The layering within the gravel is not well developed, but manifest in layers defined by variations in the clast/matrix ratio and the sizes of clasts. F1 manifests as a 10-cm-wide zone with broken and rotated clasts (Figure 5.8). Below, and to the north of the fault, we observe fault breccia inferred to have been injected (C0) into unit 2b during rupture and two colluvial layers (C1, C2) that are preserved with gentle northward inclinations, but with an unambiguous relative age relationship. The composition of the colluvium is distinctly different from that of the fluvial gravel. The lateral pinch-outs of the colluvial layers merge with unit 2b towards the north.

The southern trench exposes a minor ~30°-N-dipping back thrust (Fb), with two fault strands bounding the shear zone (Fb1 and Fb2). We did not find evidence for colluvial material derived from the scarp face. Instead, the south facing scarp, which builds an efficient sediment trap, has been blanketed repeatedly by fine material with north-directed transport from the surface to the south (unit 3 and TS). Unit 3 is absent in the hanging wall of Fb. Structural relation along Fb indicates two separate faulting events and fault migration. The lower fault strand (Fb1) displaces sediments of unit 1b above unit 2b and is buried by unit 3, while the northern fault strand (Fb2) cuts through units 1b and 3, and terminates approximately 20 cm below surface. The exposed stratigraphy is covered by a ~20-cm-thick topsoil layer (TS) that becomes gradually mixed with fines from unit 3 with increasing depth.

Komansu

T4 39.505461°N 72.652224°E →

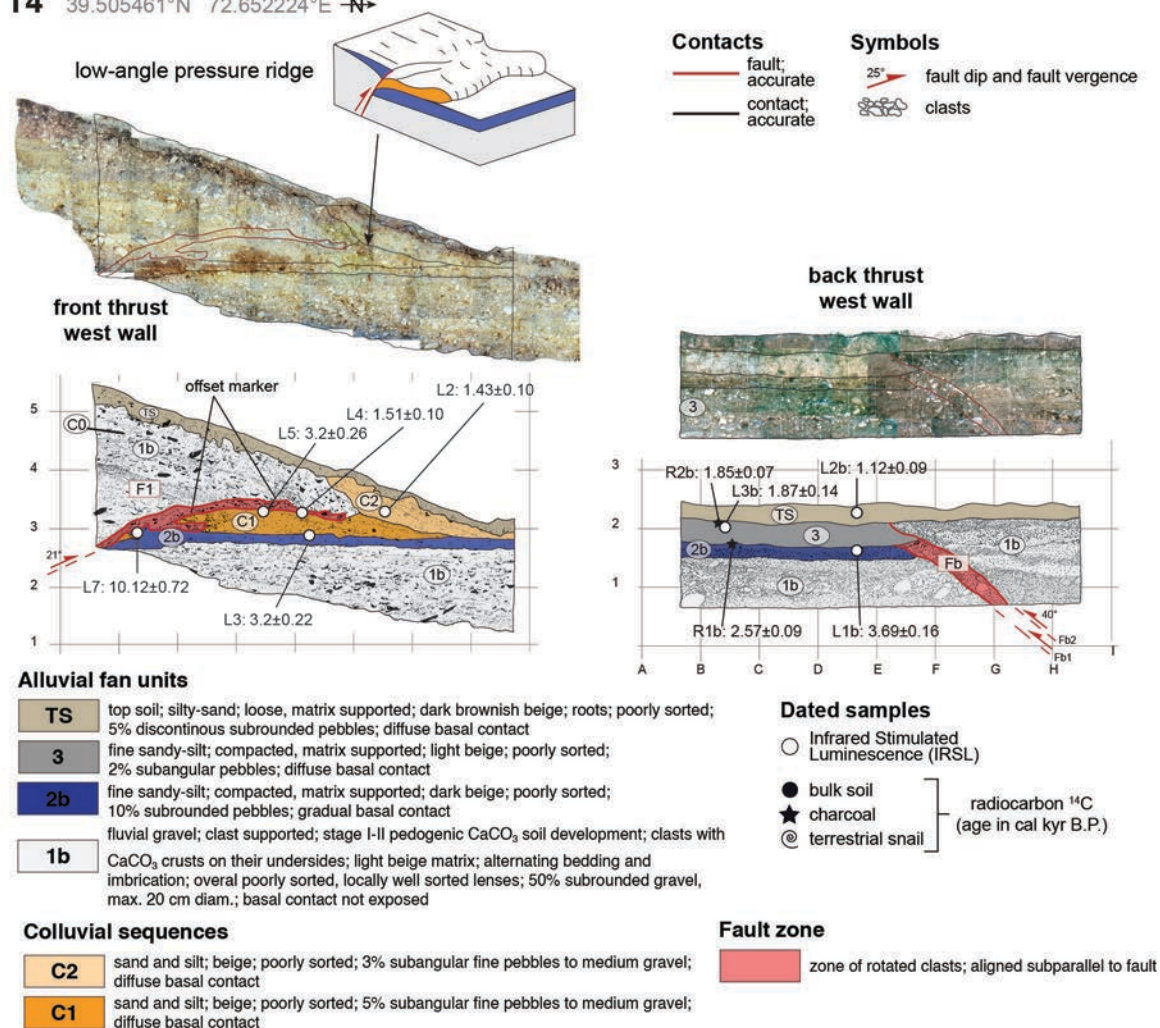


Figure 5.8 Photomosaic and interpreted trench log with major lithological units, faults, scarp-derived colluvium and locations of geochronologic samples in the west wall of the front and back thrust of trench T4, Komansu. See Table 5.6 for reference and summary of stratigraphic and geomorphologic indicators for all interpreted paleoearthquakes. Radiocarbon (¹⁴C) and infra-red stimulated luminescence (IRSL) ages shown in thousands of years (mean ± 2σ) correspond to Tables 5.1 and 5.2, respectively. See Appendix B for high-resolution photomosaics of the trench walls.

Table 5.5 Summary of stratigraphic and geomorphic indicators for paleoearthquakes in trench T4 and assigned ranking for event evidence evaluation

Trench	Fault Zone	Site Earthquake	Trench Location ^a	Unit	Indicator	Ranking ^b	Ranking Sum
T4	F1	KO3	T4-FT-3C	C0	Injected fault breccia	1	1
	F1	KO2	T4-FT-4D	C1+1	Offset marker, offset gravel	2	10
	F1		T4-FT-3E	C1	Colluvium	4	
	Fb1		T4-BT-2E	Fb1	Event horizon; Fault termination capped by horizontal sedimentation of unit 3	4	
	F1	KO1	T4-FT-3G	C2	Colluvium	4	8
	Fb2		T4-BT-2.5E	Fb2	Event horizon; Fault termination capped by horizontal sedimentation of top the soil	4	

^a Location according to trench log documentation Figure 5.8.

^b Ranking quality: 1 = speculative; 2 = indistinct; 3 = slightly visible; 4 = distinct.

T4 EQ Three (KO3): The oldest event ruptured solely along F1 in the northern trench and is indicated by C0 that was presumably injected during faulting and ongoing deposition of unit 2b. IRSL ages sampled stratigraphically above C0 from unit 2b yield 10.12 ± 0.72 ka (L7) and 3.2 ± 0.22 ka (L3) (northern trench), and 3.69 ± 0.16 ka (L1b) and 2.57 ± 0.09 ka (R1b) (southern trench). Assuming that unit 2b represents the cover that constitutes the surface of Qt_4 (4.5 ± 0.2 ka), and because sample L7 is older than unit 2 (7.3 ± 0.1 ka) that corresponds to the older terrace surface Qt_3 , I suggest that L7 is an outlier and omit the age from our model. Consequently, I used the ages of Qt_4 and L1b, and L3 and R1b as the maximum and minimum limiting age for KO2, respectively. These ages yield an age for KO3 of 3.2 ± 0.3 ka.

T4 EQ Two (KO2): The penultimate event is associated with unit C1 in the northern trench, which covers unit 2b and F1 cuts updip past C0, injecting fault breccia at the base of C1. The age control of C1 (L5: 3.2 ± 0.26 ka, L4: 1.51 ± 0.10 ka) and unit 3 (L3b: 1.87 ± 0.14 ka, R2b: 1.85 ± 0.07 ka) from both trenches suggests that during this event, faults F1 and Fb1 were activated. The similarity in ages (≈ 3.2 ka) between L3 (unit 2b) and L5 (C1) implies that L5 may have been recycled during faulting without sufficient bleaching of the material; thus, this sample will be omitted. In contrast, L4 (C1) more likely represents a true depositional age for C1, assuming it got pushed northward and disturbed during the subsequent earthquake (KO1) given its location with respect to L5 and proximity to the inferred portion of the ground surface prior to the earthquake. Following this argument, L3 and L1b serve as maximum limiting ages and L4, L3b and R2b as minimum bracketing ages, which yield a modeled age for KO2 of 2.4 ± 0.2 ka.

T4 EQ One (KO1, MRE): The most recent evidence for earthquake faulting exposed in the northern trench is the steeper F1 strand that cuts off and deforms C1, while its upper end flattened out to a horizontal position. As a result, the hanging wall collapsed partly and the strata were displaced downhill over the preexisting toe of the scarp (top of C1). The overlying colluvial sequence C2 formed presumably during subsequent interseismic scarp diffusion processes. Similarly, for KO2, the age control in both trenches indicates that the MRE rupture activated both faults F1 and Fb2 simultaneously. To bracket KO1, I used the ages of C1 (L4), and unit 3 (L3b and R2b) as maximum age constraint and the IRSL age from C2 (L2: 1.43 ± 0.10 ka) and TS (L2b: 1.12 ± 0.09 ka) in the southern trench as a minimum age constraint. The age for KO1 is modeled at 1.5 ± 0.1 ka.

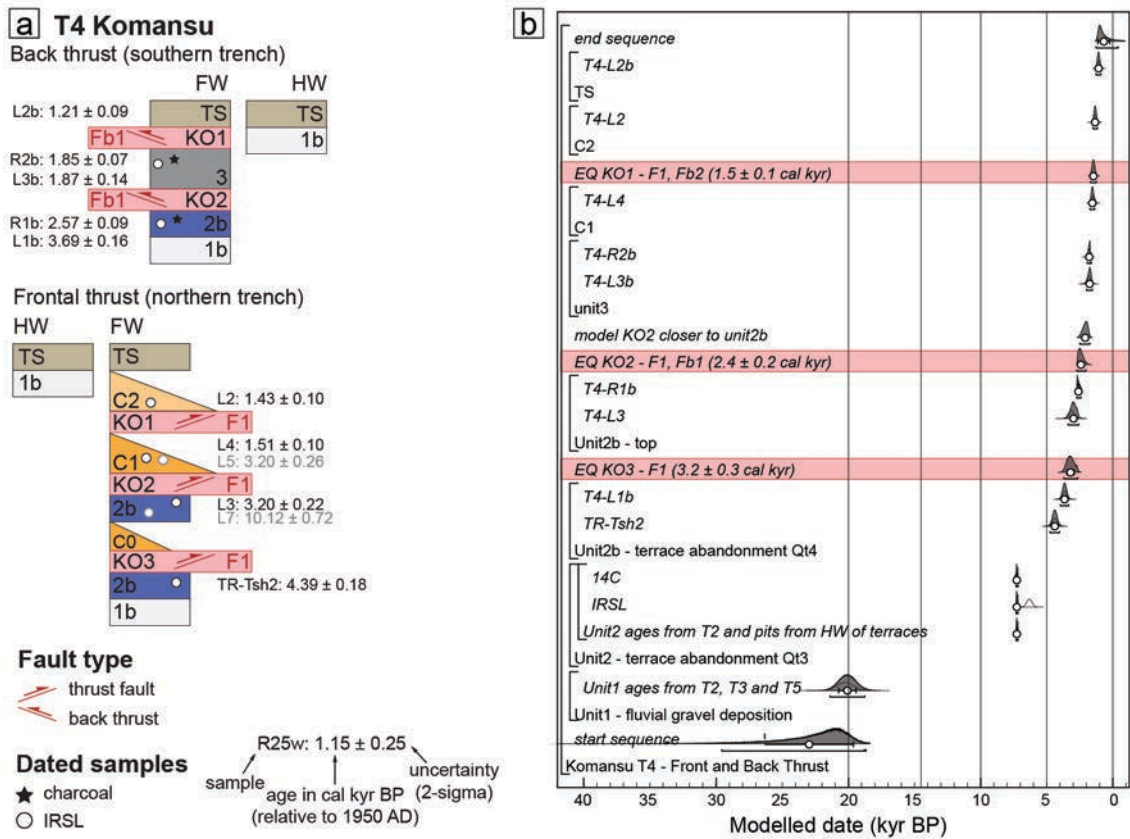


Figure 5.9 Trench T4, Komansu. (a) Schematic summary of the structural and stratigraphic results. Colors correspond to lithostratigraphic units in the corresponding trench log (Figure 5.8). All collected radiocarbon (^{14}C) and infra-red stimulated luminescence (IRSL) samples are included in the scheme; gray shaded samples are excluded from the OxCal models because of inconsistency in the stratigraphic order and/or disagreement with surrounding samples (see text for explanation). All modeled unit ages are mean $\pm 2\sigma$ (Table 5.1 and Table 5.2). (b) OxCal models (v4.4.4 Bronk Ramsey (2021); r:5 Atmospheric data from Reimer et al. (2020)) of paleoearthquake timing constraints. See Code B1 in Appendix B for the associated OxCal script.

5.1.5. T5 – Tashkungey (39.52°N 72.77°E)

At the Tashkungey site, the trench T5 excavation exposed up to 3 m of fluvial gravel terrace deposits of the bottom (unit 1) capped by a thin (10-20 cm) layer of presumably reworked and partly eroded remnants of unit 2 (fine silty sand) in both trench walls, and is stratigraphically and chronologically consistent with the other trenches (~ 21 ka). The boundary between unit 1 and unit 2 is not sharp. Instead, interspersed subangular clasts are incorporated into the silty sand matrix at the basal contact of unit 2. This indicates that the upper contact of unit 1b was reworked during the deposition of unit 2. The main stratigraphic sequence is faulted along two separate fault zones (F1, F2), which coincide with the surface position of the scarps. Near to and north of each fault zone, unit 2 is overlain by a succession of scarp-derived colluvial deposits C1-C3, and Ca-Cc, respectively. The organic-rich silty to sandy

modern soil A horizon of the modern soil reaches a thickness of up to 30 cm at the scarp toes and is only poorly developed in an area of unfaulted intermediate hanging-wall deposits.

Both fault zones show a clear 10 to 20-cm-wide zone of rotated clasts subparallel to the fault dip. Fault zone F1-related deformed colluvial packages comprise loess-like deposits similar to unit 2. Unit 2 and colluvial units C1 and C2 are only distinguishable by fault breccia injected into the base of the colluvium at F1. C3 is more mixed, shows a clear change in color from beige to reddish beige, and includes more organic material. Colluvium related to fault zone F2 is massive and structurally and stratigraphically complex. Ca consists of well-sorted silty sand. Its base is derived from a remnant of injected fault breccia (similar as at F1) that was dragged and faulted during subsequent faulting along F2. A major faulting event deformed a large wedge-shaped block with a maximum thickness of up to ~ 80 cm and composed of poorly sorted gravel with chaotic orientation of pedogenic carbonate coatings and reworked matrix-supported pebbles at its tip (Cb). This unit is overlain by a lens of organic-rich paleosol, developed in a matrix-supported, poorly sorted gravel (PS). The youngest colluvium (Cc) constitutes strata of poorly sorted gravel that fines upward and merges laterally into more organic-rich fine material toward its northern tip. I suggest that internal structural disorder in Cc is a result of possible bioturbation or cryoturbation. Considering the stratigraphic and chronologic relationship across the trench, I infer that C1, C2 and C3 formed coevally with Ca, Cb, and Cc after simultaneous fault activation during rupturing events.

T5 EQ Three (TS3): The oldest earthquake that caused rupture along F1 and F2 led to subsequent deposition of C1 and Ca, respectively. We collected five radiocarbon samples from both units. Unfortunately, the resulting ages (R3e: modern; R2e: 0.17 ± 0.09 ka; R9e: 1.55 ± 0.02 ka; R1w: 0.13 ± 0.08 ka; R4e: 1.01 ± 0.06 ka) are neither in the expected chronologic order nor do they fit the stratigraphic order, and were therefore omitted in the modeling (see Discussion for more detailed explanation). Two IRSL ages (L1e: 4.79 ± 0.35 ka; L3e: 4.45 ± 0.28 ka) from unit C1 provide a more realistic age, assuming that the underlying unit 2 formed at $\sim 6-7$ ka. We were not able to obtain absolute age control for unit 2 in the trench; however, the terrace-surface age obtained from a pit (PT3) within the hanging wall east of the river (see Chapter 4 for location) is consistent with the ages of unit 2 along the cPFT. Thus, I am confident in using the age for unit 2 (7.3 ± 0.1 ka) as a maximum age and use our IRSL ages (L1e and L3e) as a minimum age constraint. Combined, this information yields an age for TS3 of 5.4 ± 0.8 ka.

T5 EQ Two (TS2): The penultimate earthquake ruptured along F1 and F2 deforms C1 and Ca, respectively, and was followed by inferred hanging-wall collapse at F2 depositing Cb and slow subsequent deposition of the northern tip of Cb and C2. We obtained three IRSL ages (L2e: 2.25 ± 0.14 ka; L6e: 3.06 ± 0.14 ka; L5e: 3.78 ± 0.44 ka) and one radiocarbon age (Rb2w: 2.73 ± 0.04 ka) from both colluvial packages. The age constraints provide a good stratigraphic and chronologic order, and serve as minimum age constraints. Combined with the age of unit C1 (L1e, L3e) as a maximum age constraint, TS2 is modeled at 3.7 ± 0.4 ka.

Tashkungey

T5 39.520219°N 72.777639°E -N→

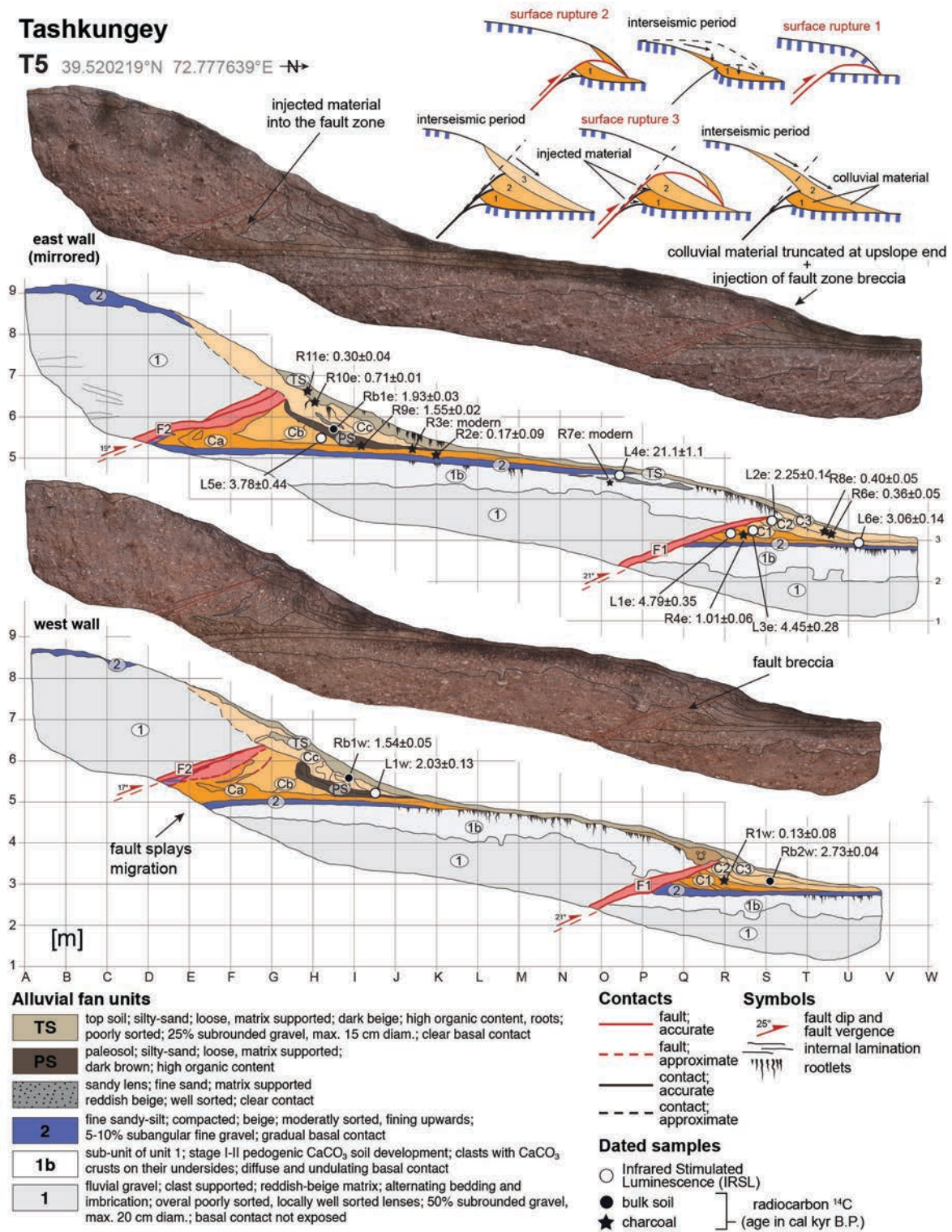


Figure 5.10 Photomosaic and interpreted trench log with major lithological units, faults, scarp-derived colluvium and locations of geochronologic samples in the east wall (mirrored) and west wall of trench T5, Tashkungey. See Table 5.7 for reference and summary of stratigraphic and geomorphologic indicators for all interpreted paleoearthquakes. Radiocarbon (¹⁴C) and infra-red stimulated luminescence (IRSL) ages shown in thousands of years (mean ± 2σ) correspond to Table 5.1 and 5.2, respectively. See Appendix B for high-resolution photomosaics of the trench walls.

Colluvial Wedges

Cc	fine sand; moderately compacted; dark reddish beige, poorly sorted; 20-30% subrounded gravel to cobble, diffuse basal contact	C3	fine sand; moderately compacted; dark beige, poorly sorted, lenses of reworked unit 1b material, 15% subangular gravel to cobbles, diffuse basal contact
Cb	gravel; clast supported; reddish beige silty matrix; poorly sorted; 50% subangular gravel; clear basal contact	C2	clayey fine sandy-silt; compacted, holey; beige; injected fault breccia in southern end; moderately sorted; 3% subangular fine gravel; diffuse basal contact
Ca	clayey fine sandy-silt; compacted, holey; beige; injected fault breccia in southern end; moderately sorted; 10% subangular gravel; diffuse basal contact	C1	clayey fine sandy-silt; compacted, holey; beige; injected fault breccia in southern end; moderately sorted; 10% subangular gravel; diffuse basal contact

Figure 5.10 (continued)

Table 5.6 Summary of stratigraphic and geomorphic indicators for paleoearthquakes in trench T4 and assigned ranking for event evidence evaluation.

Trench	Fault Zone	Site Earthquake	Trench Location ^a	Unit	Indicator	Ranking ^b	Ranking Sum
T5	F1	TS3	T5-E-3R	C1	Colluvium with injected fault breccia of unit 1	4	13
	F1		T5-W-3R	C1	Colluvium with injected fault breccia of unit 1	4	
	F2		T5-E-56EF	Ca	Wedge shaped colluvium of unit 1	3	
	F2		T5-W-56G	Ca	Lens of former colluvium of unit 1	2	
	F1	TS2	T5-E-34ST	C2	Colluvium with injected fault breccia of unit 1	4	16
	F1		T5-W-34ST	C2	Colluvium with injected fault breccia of unit 1	4	
	F2		T5-E-56H	Cb	Massive colluvial wedge with chaotic unit 1 material and reworked unit 2 material	4	
	F2		T5-W-56I	Cb	Massive colluvial wedge with chaotic unit 1 material and reworked unit 2 material	4	
	F1	TS1	T5-E-34T	C3	Colluvium with injected fault breccia of unit 1	4	47
	F1		T5-E-34T	F1	Upper fault termination	4	
	F1		T5-W-34T	C3	Colluvium with injected fault breccia of unit 1	4	
	F1		T5-W-34T	F1	Upper fault termination	4	
	F2		T5-E-56GH	Cb	Fault proximal deformation and overturning of Cb material	3	
	F2		T5-E-6G	Ca	Injection of Ca material upwards and subparallel to fault F2	3	
	F2		T5-E-5E	Ca	Deformation of former colluvium	2	
	F2		T5-E-5E	F2	Injection of unit 2 material into the fault zone	2	
	F2		T5-E-67H	F2	Upper fault zone termination	3	
	F2		T5-E-6I	Cc	Colluvial wedge capping paleosol	4	
	F2		T5-W-56HI	Cb	Fault proximal deformation and overturning of Cb material	3	
	F2		T5-W-6I	Ca	Injection of Ca material upwards and subparallel to fault F2	3	
F2	T5-W-5F	F2	Injection of unit 2 material into the fault zone	2			
F2	T5-W-6I	F2	Upper fault zone termination	3			
F2	T5-W-6J	Cc	Colluvial wedge capping paleosol	3			

^a Location according to trench log documentation Figure 5.^b Ranking quality: 1 = speculative; 2 = indistinct; 3 = slightly visible; 4 = distinct.

T5 EQ One (TS1; MRE): The most recent event ruptured along F1 and F2 and is associated with units C3 and Cc, respectively. Cc covers a layer of paleosol (PS) that presumably developed after the deposition of Cb (further distinguishing this and the prior earthquake). Injection and upward-dragged Ca material south of Cb and subparallel to F2 indicates that the Cb and PS units were truncated and deformed during this younger rupture. The inferred strong deformation during the faulting event could further explain the chaotic gravel orientation in the main body of Cb. Following this interpretation, I use one IRSL (L1w: 2.03 ± 0.13 ka) and two radiocarbon ages (Rb1e: 1.93 ± 0.03 ka; R9e: 1.55 ± 0.02 ka) from PS that broadly agree with each other, as maximum age constraints. For a minimum age bracket, I used the age of one radiocarbon bulk-soil sample (Rb1w: 1.54 ± 0.05 ka) associated with Cc. Two radiocarbon samples (R8e: 0.40 ± 0.05 ka; R6e: 0.36 ± 0.14 ka) obtained from C3 were omitted due to their unrealistically young ages (see Discussion). Combined, this bracketing yields an age for the most recent event TSa at 1.5 ± 0.1 ka.

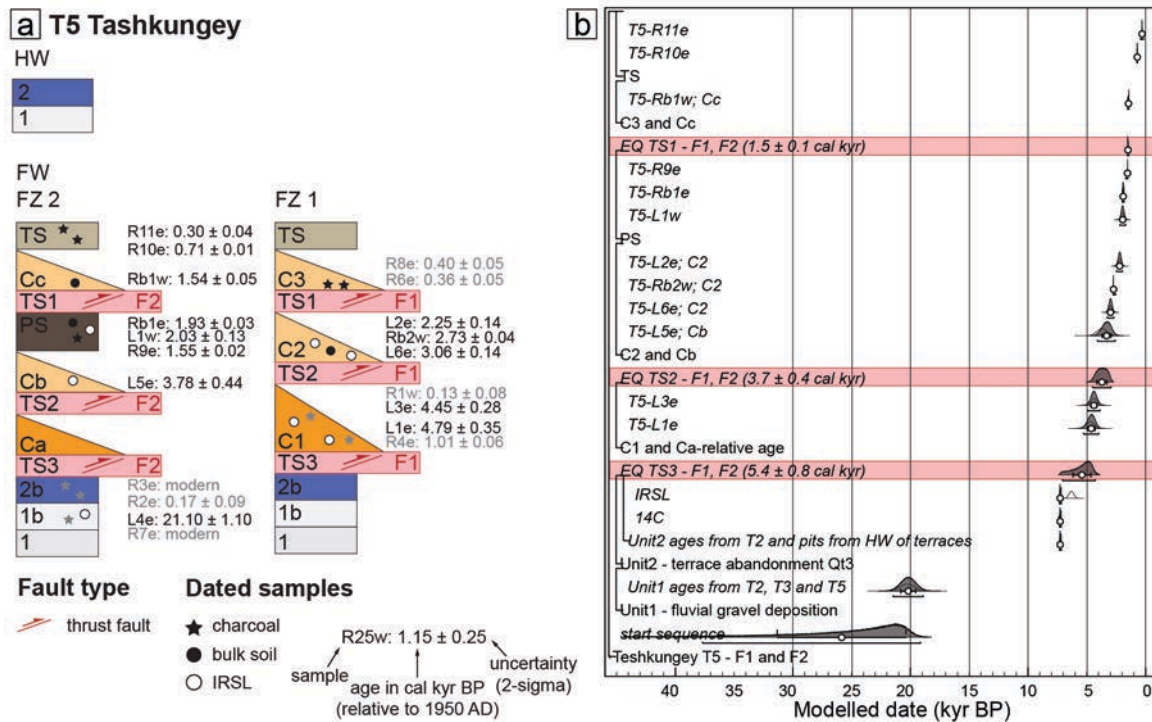


Figure 5.11 Trench T5, Tashkungey. (a) Schematic summary of the structural and stratigraphic results. Colors correspond to lithostratigraphic units in the corresponding trench log (Figure 5.10). All collected radiocarbon (^{14}C) and infra-red stimulated luminescence (IRSL) samples are included in the scheme; gray shaded samples are excluded from the OxCal models because of inconsistency in the stratigraphic order and/or disagreement with surrounding samples (see text for explanation). All modeled unit ages are mean $\pm 2\sigma$ (Table 5.1 and Table 5.2). (b) OxCal models (v4.4.4 Bronk Ramsey (2021); r:5 Atmospheric data from Reimer et al. (2020) of paleoearthquake timing constraints. See Code A1 in Appendix A for the associated OxCal script.

5.2. Displacement per event

The dip-slip displacement of stratigraphic horizons that are inferred to have been offset during a single rupture, and the upslope thicknesses of colluvial deposits on both trench walls (if unambiguously related to surface ruptures) were measured at all trench exposures where possible to reconstruct per-event dip-slip displacements (T1-T5; Figure B1 in Appendix B). As shown in my paleoseismic observations, I expect that several earthquakes ruptured along multiple fault strands within single trench exposures coevally, implying partitioning of the total dip-slip displacement. Additionally, reconstruction of the effects from cumulative and coeval faulting may be very ambiguous. Consequently, I will use my estimates to provide approximate (minimum) ranges of dip-slip magnitudes during the earthquake history preserved in the trenches.

Dip-slip displacements measured from offset stratigraphic horizons presumably related to only one rupturing event range from 0.4 to 1.1 m. From colluvial deposits, I estimate an approximate dip-slip range of 0.6 to 2.8 m, assuming that the maximum preserved fault-proximal colluvial thickness represents

about one-half of the initial coseismic dip-slip along the fault (Personius & Mahan, 2005; McCalpin & Carver, 2009). In case of simultaneous multi-fault activation during one rupture, total per-event dip-slip displacement estimates reach up to 4.9 ± 0.7 m (Table 5.8).

Table 5.7 Summary of refined paleoearthquake timing, timing quality, interseismic recurrence intervals from five trenches along the central PFT, including measured and accordingly calculated per-event displacements and potential surface rupture length from empirical relationships.

Trench	Fault Zone ^a	Site EQ name	Modeled EQ age (ka) Mean $\mu \pm 1\sigma$	EQ Indicator Quality ^b	EQ Timing Quality ^c	Interseismic Recurrence ^d (kyr)	Event Horizon ^e	Mean Per-Event Displacem. (PED) ^f (m) $\pm 15\%$	Surface Rupture Length (SRL) ^g [km]
T1	Fb	Ab1	0.8 ± 0.4	2	1	0.8 ± 0.4	offset	0.5 ± 0.1	24
	F1	A2	1.6 ± 0.1	8	2	0.8 ± 0.5	cd	1.0 ± 0.2	28
	F1	A3	2.4 ± 0.5	1	1	2.4 ± 1.1	cd	1.1 ± 0.2	29
	F1	A4	4.8 ± 1.0	1	1	9.4 ± 2.8	cd	1.8 ± 0.3	33
	F2	A5	14.2 ± 2.6	6	1	-	offset	0.4 ± 0.1	22
T2	F1+F4	AS1	0.8 ± 0.2	38	1	0.4 ± 0.2	cd+offset	2.2 ± 0.3	35
	F1+F4	AS2	1.2 ± 0.1	16	3	2.2 ± 0.4	cd+offset	4.9 ± 0.7	43
	F1+F4	AS3	3.4 ± 0.4	12	2	1.3 ± 1.1	cd	2.8 ± 0.4	37
	F1+F2+F4	AS4	4.7 ± 1.0	18	2	9.6 ± 3.1	cd	$1.0 \pm ?$	28
	F3	AS5	14.3 ± 2.9	4	2	-	offset	0.6 ± 0.2	25
T3	F1+Fb	YL1	1.7 ± 0.7	21	1	4.4 ± 0.9	offset	1.0 ± 0.1	28
	F1	YL2	6.1 ± 0.6	5	2	7.8 ± 3.0	-	-	-
	F2+F3	YL3	13.9 ± 2.9	21	1	-	offset	0.2 ± 0.1	19
T4	F1+Fb2	KO1	1.5 ± 0.1	8	3	0.9 ± 0.2	cd+offset	2.1 ± 0.3	34
	F1+Fb1	KO2	2.4 ± 0.2	10	3	0.8 ± 0.2	cd+offset	3.3 ± 0.5	38
	F1	KO3	3.2 ± 0.3	1	2	-	cd	-	-
T5	F1+F2	TS1	1.5 ± 0.1	47	3	2.2 ± 0.4	cd	1.8 ± 0.3	33
	F1+F2	TS2	3.7 ± 0.4	16	2	1.7 ± 0.9	cd	3.5 ± 0.5	39
	F1+F2	TS3	5.4 ± 0.8	13	2	-	cd	4.6 ± 0.7	42

^aFor fault zone location, see associated trench log, respectively.

^bSummarized ranking of stratigraphic evidence per event.

^cNormalized modeled earthquake timing quality: based on bracketing and resulting timing uncertainty 1σ ; 0 = poor, 1 = moderate, 2 = good, 3 = excellent.

^dClosed interval preceding the earthquake.

^eOffset = one event dip-slip offset; cd = colluvial deposits, uncertainty assumed to be 15%.

^fFor cd, twice the mean max-thickness of colluvial deposit.

^gCalculated with $\log(\text{SRL})=1.45+0.26*\log(\text{PED})$ for reverse faults from Wells & Coppersmith (1994).

5.3. Summary

Paleoseismic investigations from five trenching sites along the central sector of the Pamir Frontal Thrust revealed earthquake histories with evidence for multiple ruptures in the past 14 kyr, with the most recent event rupturing the surface at ~ 0.8 ka BP at the western end of the segment. The resulting chronological paleoearthquake framework shows overlap of rupture timing across several trenching sites. Estimated per-event dip-slips range from 0.5 m to 4.9 m, suggesting a possible surface-rupture length of up to ~ 40 km during past surface rupturing events.

Chapter 6

Results III: Seismogenic behavior along the central Pamir Thrust.

The earthquake histories from five different sites along the central sector of the Pamir Frontal Thrust (cPFT) described in the last chapter demonstrate overlap of modeled earthquake timing in several cases, suggesting segment activation during some of the events described. This chapter focuses on a segment-wide correlation of the examined paleoearthquakes to infer surface-rupture lengths and extent of segment activation during ruptures along the cPFT, which will help to evaluate the seismogenic potential of this sector of the Pamir Frontal Thrust. By combining these outcomes with offset data from Chapter 4, I present slip-rate estimates for the cPFT that will allow an estimation of its contribution to the seismogenic activity of the entire Pamir Thrust System at the central northern front of the Pamir orogen.

6.1. Paleoearthquake correlation and recurrence along the segment

My modeled timing of single earthquakes is consistent for several events across all trenching sites. Considering the proximity of these sites to each other, and taking into account the logic of Biasi & Weldon (2009) and the scaling relationships of Wells & Coppersmith (1994), potential minimum surface-rupture lengths based on average dip-slip displacements (Table 5.8) support the assumption that several identified paleoearthquakes likely extended from one site to another along the cPFT. The graphical paleoearthquake PDF correlation across multiple trenching sites suggests six earthquakes (E6-E1, oldest to youngest) ruptured the surface along the cPFT since ~14 ka (Figure 6.1). To justify this interpretation of the correlation, I use the earthquake evidence and timing quality metric (i.e., poor, moderate, good, and excellent) based on the bracketing and resulting modeled uncertainty of the timing of the event (Table 5.8; Chapter 5).

The oldest earthquake E6 (~12–16 ka) was constrained based on the correlation of earthquakes with moderate timing quality from trenches T1 (A5), T2 (AS5), and T3 (YL3), all concentrated at the western end of the cPFT (Table 5.8 Figure 6.1). I did not find evidence for this rupture in trenches T4 and T5. Earthquake E5 (~4–6 ka) was constrained based on four poorly overlapping PDFs, with one poor, and three good timing-quality rankings from trenches T1 (A4), T2 (AS4), T3 (YL2), and T5 (TS3), respectively. The intermediate Komansu site (T4) did not show evidence for a rupture at this time. Earthquake E4 (~3–4 ka) resulted from the correlation of earthquakes with good timing quality identified at trenches T2 (AS3), T4 (KO3) and T5 (TS2). Both trenches (T1 and T3), which are in close vicinity to T2 did not reveal clear evidence for a correlative surface rupture (Table 5.8 Figure 6.1). Earthquake E3 (~2–3 ka) is based on correlation of one earthquake with poor timing quality from trench T1 (A3) and one with very good timing quality from trench T4 (KO2). None of the other sites revealed

evidence for this event. The penultimate earthquake E2 (~1–2 ka) ruptured all of the trenching sites: T1 (A2), T2 (AS2), T3 (YL1), T4 (KO1), and T5 (TS1). The most recent earthquake (MRE; E1 at <1 ka) is only evident in trenches T1 (Ab1) and T2 (AS1) at the western end of the cPFT (Table 5.8 Figure 6.1).

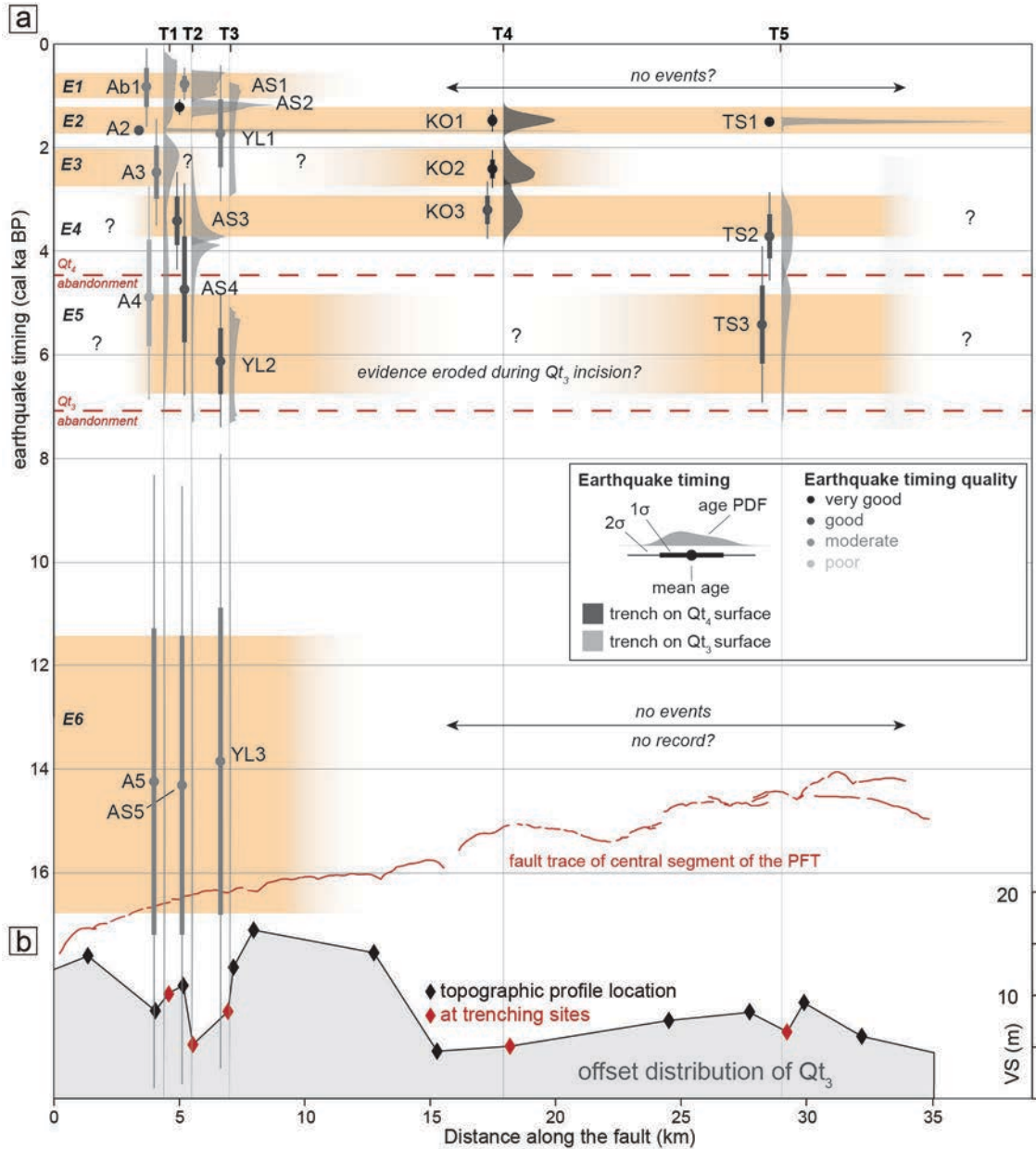


Figure 6.1 (a) Compilation of age and location results for all surface-supturing paleoearthquakes identified at the five trenching sites along the central PFT and best-fit graphical correlation. (a) Individual earthquake age PDFs (grey-shaded) were modeled in OxCal (see Chapter 5). Graphical correlation (light-orange-shaded) at 1σ of the modeled site earthquake PDFs show possible rupture propagation along the segment (segment earthquakes E_x). Earthquakes E2, E4, and E5 indicate a possible full-segment rupture, whereas events E1, E3, and E6 are partial-segment ruptures in the western end of the central PFT. Red line in the lower part of the figure indicates the cPFT fault trace. (b) Shaded area plots cumulative vertical separation along the central PFT, based on topographic profiles across the scarp extracted from TanDEM-X data (black diamonds indicate location; red diamonds indicate trenching sites). For details see Chapter 4.

Based on this correlation, I have produced a segment-wide earthquake chronology following the approach of Personius et al. (2012) and the method established by Biasi & Weldon (2009) and DuRoss et al. (2011). I evaluated and integrated multiple paleoseismic ages into a single refined-age model by applying the product method (direct multiplication of the discretized PDFs), which yields better-defined earthquake ages. Applying this method to this interpretation resulted in refined earthquake ages for the segment (with $\pm 2\sigma$) of $E6 = 14.3 \pm 2.2$ ka, $E4 = 3.4 \pm 0.2$ ka, $E3 = 2.4 \pm 0.2$ ka, $E2 = 1.5 \pm 0.1$ ka, and $E1 = 0.8 \pm 0.2$ ka (Figure 6.2). Due to poor overlap of the site PDFs in the case of $E5$, we used the simple-sum mean, which resulted in $E5 = 5.3 \pm 1.1$ ka with a significantly higher uncertainty. The new segment-wide earthquake chronology reveals a stepwise decrease in recurrence intervals from past to present (Table 6.1), which contrasts the irregular recurrence intervals in site-specific earthquake chronologies (Table 5.8).

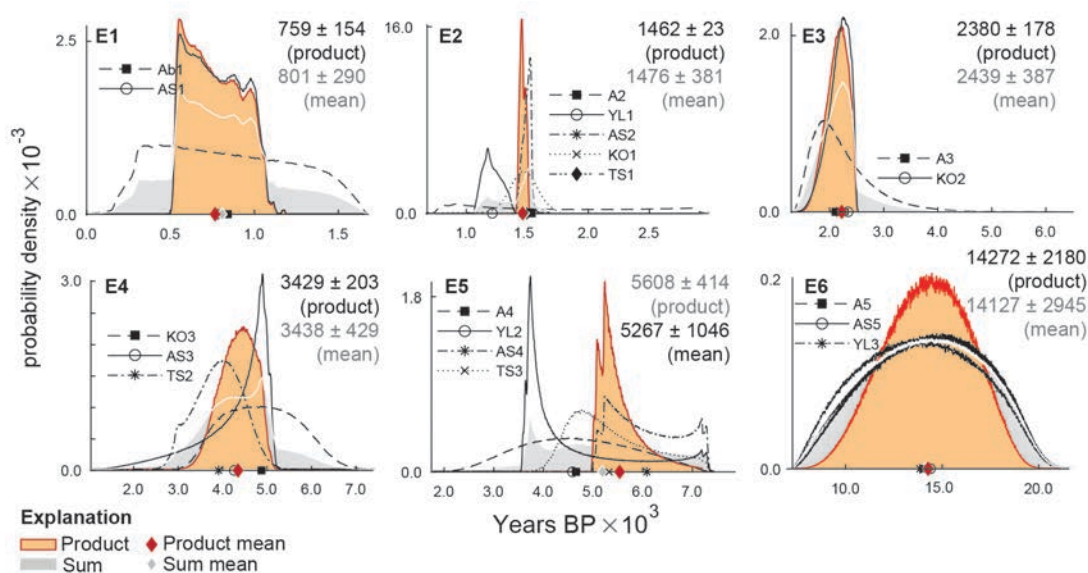


Figure 6.2 Site earthquake-timing PDFs combined by multiplication from graphical correlation in Figure 6.1. Plots of combined PDFs for six segment earthquakes (E1 through E6). Black lines = single site PDFs; white line = summed PDF; red line = resulting product PDF (segment earthquake). Resulting timing is in cal BP $\pm 2\sigma$.

Table 6.1 OxCal age models for paleoseismic sites and refined segment earthquake ages for the central PFT

Trenching Site from West to East along the cPFT ^a (ka, 2σ)					Segment EQ #	Segment EQ age ^b (ka, 2σ)	Interseismic Recurrence ^c (kyr)	
T1	T2	T3	T4	T5			cPFT	Partial Activation
0.8 ± 0.4	0.8 ± 0.2	-	-	-	E1	0.8 ± 0.2	0.7 ± 0.2	-
1.6 ± 0.1	1.2 ± 0.1	1.7 ± 0.7	1.5 ± 0.1	1.5 ± 0.1	E2	1.5 ± 0.1	0.9 ± 0.2	2.0 ± 0.2
2.4 ± 0.5	-	-	2.4 ± 0.2	-	E3	2.4 ± 0.2	1.0 ± 0.3	-
-	3.4 ± 0.4	-	3.2 ± 0.3	3.7 ± 0.4	E4	3.4 ± 0.2	1.8 ± 1.1	1.8 ± 1.1
4.8 ± 1.0	4.7 ± 1.0	6.1 ± 0.6	evidence eroded?	5.6 ± 0.8	E5	5.3 ± 1.1	9.0 ± 2.4	-
14.2 ± 2.6	14.3 ± 2.9	13.9 ± 2.9	evidence eroded?	-	E6	14.3 ± 2.2	-	-

Note. Orange highlights the paleoevents that ruptured the full segment length, which are the base for the calculation of the interseismic recurrence of “full activation”. Coloring emphasizes relationships.

^a Sequence of paleoearthquakes correlateable in their timing from all trenches along the cPFT.

^b Refined earthquake timing through multiplication of overlapping site PDFs.

^c Recurrence interval for major earthquakes that activated the entire segment during rupture. Closed recurrence ($E_{\text{older}}-E_{\text{younger}}$) and absolute error.

6.2. Late Quaternary dip-slip rate

The dip-slip rate v is calculated from the division of accumulated offset x by the age t of a corresponding geological unit ($v = x/t$ with $\Delta v/v = v \Delta x/x + \Delta t/t$). The cumulative dip-slip calculated from single segment event related dip-slips in the trenches is significantly lower than would be expected if compared to the associated VS measured from the offset surface along the cPFT (Figure 6.3), highlighting the ambiguity of dip-slip reconstructions in thrust fault exposures.

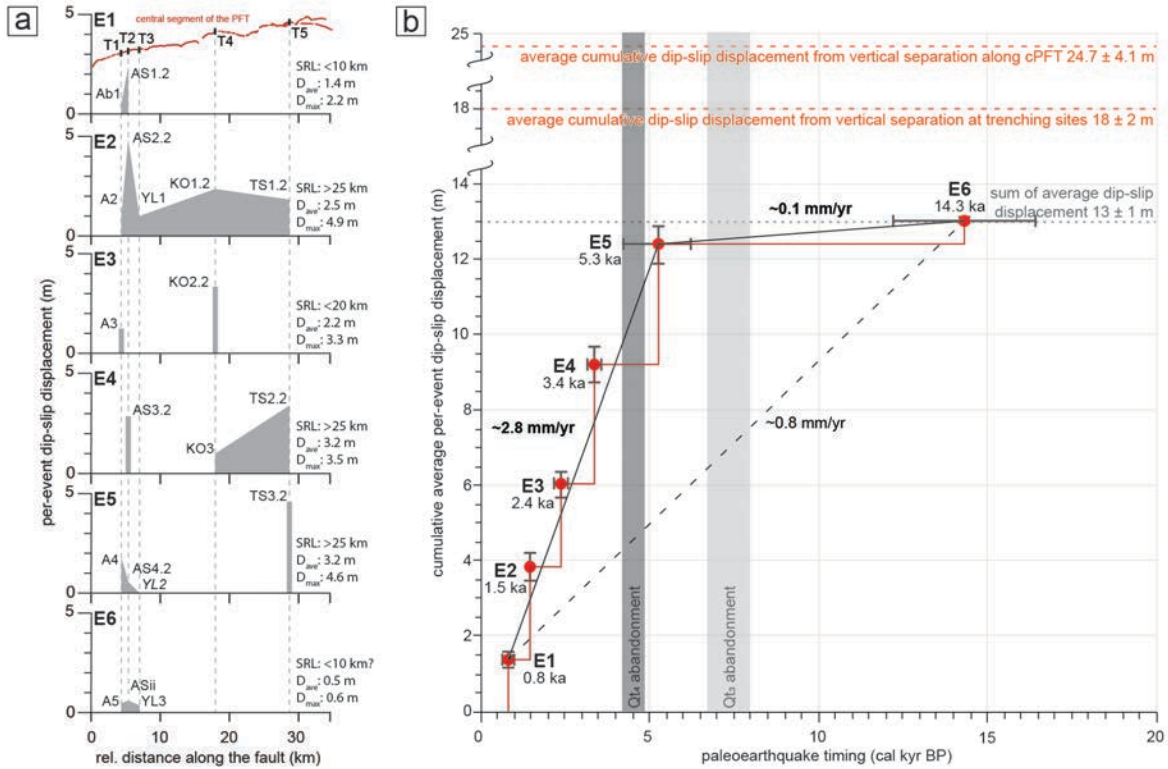


Figure 6.3 (a) Single per-event dip-slip displacements for each identified paleoearthquake at the trenching sites (Table 5.8). Surface rupture length (SRL) according to earthquake evidence along the central PFT. (b) Graphic integration of the Late Quaternary dip-slip rate along the central PFT. Relationship between cumulative average dip-slip displacement (from (a)) and age (Table 6.1) for each segment paleoearthquake.

Therefore, to provide a firm basis for the dip-slip rate calculations, I used the TanDEM-X-based VS estimates to re-calculate the associated accumulated dip-slip offsets along the cPFT assuming a thrust-dip angle of $21 \pm 3^\circ$ (averaged over all fault dips exposed in the trenches). However, as shown in other studies of reverse-fault scarps, the VS of the ground surface does not always reflect the actual fault throw (e.g., Kaneda et al., 2008), which is particularly true for older scarps that formed through multiple events (McCalpin & Carver, 2009) or where there is a profile asymmetry that likely leads to an over- or underestimated VS (e.g., at T2). To cross-check my VS estimates, I employ a second approach for total VS evaluation following the reverse-fault related parameters and resulting equation for parallel hanging wall and footwall ground surfaces $DS = VS \cos \alpha / \sin (\theta + \alpha)$; where DS is dip-slip displacement, a is the fan surface slope, and θ is the dip angle of the fault (Thompson et al., 2002; X. Yang et al., 2015). By

rearranging the equation, I used cumulative dip-slip displacements exposed in my trenches to calculate VS (Figure 6.4).

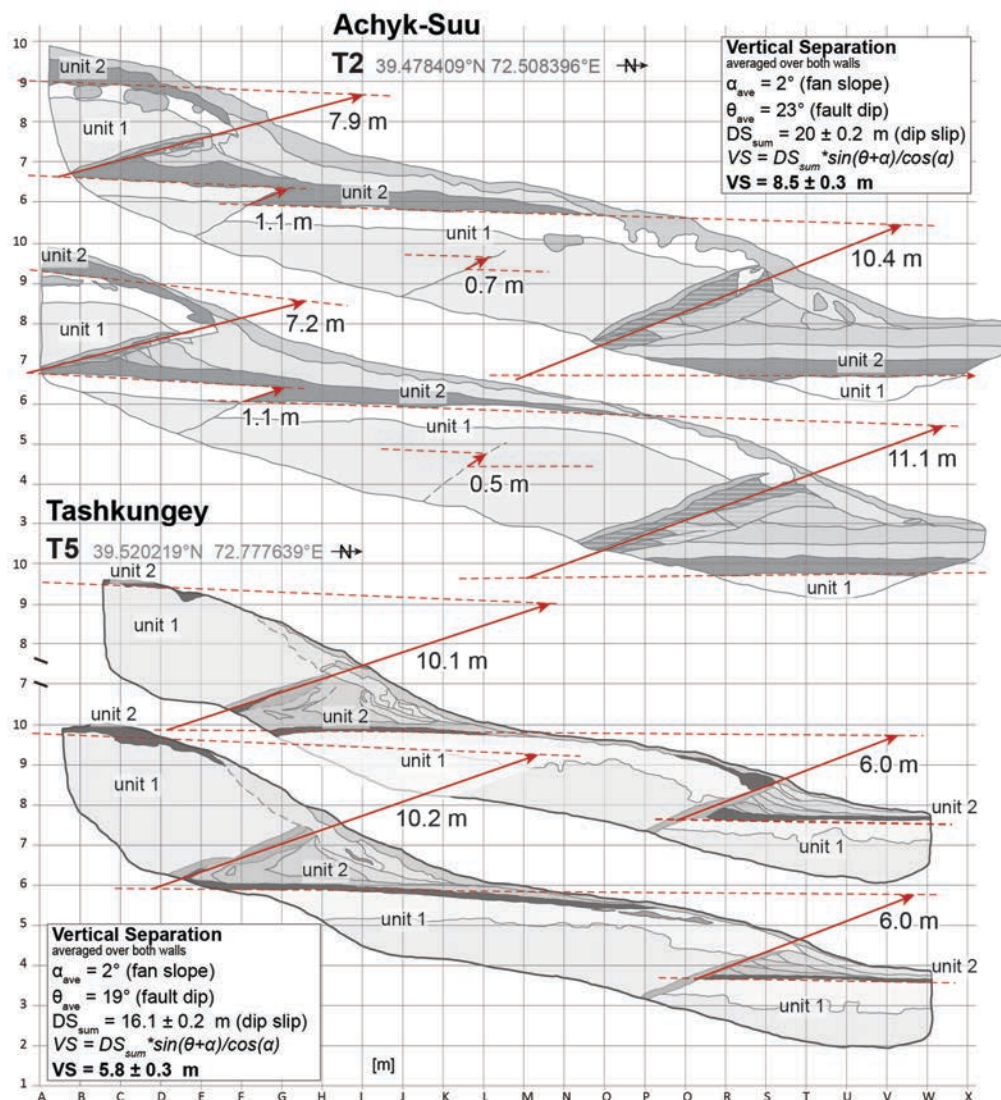


Figure 6.4 Near-field estimates for cumulative dip-slip displacement from the east and west walls in trenches T2 (Achyk-Suu) and T5 (Tashkungey). Stratigraphic marker is given by the contact between units 1 and 2 within the trench exposures. Corresponding vertical separation was calculated using the equation after Thompson et al. (2002) for parallel hanging wall and footwall surfaces.

In the subsurface of trenches T2 and T5 I used the contact between units 1 and 2 as a horizontal marker that can be laterally traced between the hanging wall, intermediate hanging wall, and footwall (Figure 6.4). Together with an average fault dip of $21 \pm 3^\circ$ exposed in the trenches and assuming a surface slope of $\sim 2^\circ$ I was able to estimate a cumulative net-amount of dip-slip motion at T2 and T5 which results in a VS of 8.5 ± 0.2 m and 5.8 ± 0.2 m, respectively (corresponding to profile P5 and P16; Table 6.2). The calculated VS of T5 coincides with the TanDEM-X-based VS of 6 m. In case of T2, the calculated VS within the trench is significantly larger than the one measured at the surface (8.5 m versus 5.2 m), but

better matches the along-strike distribution of VS (8-10 m) (Figure 6.2). In this case, I assume that possible differences in surface-process dynamics (e.g., enhanced lateral sediment transport) led to the apparent profile asymmetry at T2. In summary, I suggest that the TanDEM-X-based VS estimates in our study area are representative and can be used for further calculations.

Table 6.2 Summary of cumulative vertical separation and dip-slip displacement, and estimated dip-slip rate from west to east along the central PFT. See Chapter 4 for topographic profile locations.

Trenching Site	Source for Calculation	Vertical Separation ^a (m)	Cumulative Displacement ^b (m)	Dip-Slip Rate ^c (mm/yr)		
				max	min	
Achyk-Suu	T1	Profile P3	10.2 ± 0.2	26.0 ± 4.0	4.9 ± 1.8	1.8 ± 0.6
	T2	Profile P4	10.9 ± 0.5	27.8 ± 5.0	5.2 ± 2.0	1.9 ± 0.6
		Trench	8.5 ± 0.9	20.0 ± 4.0	3.8 ± 1.5	1.4 ± 0.5
Ylaisu	T3	Profile P5	5.2 ± 0.7	13.3 ± 3.5	2.5 ± 1.2	0.9 ± 0.4
		Profile P6	8.4 ± 0.7	21.5 ± 4.5	4.0 ± 1.7	1.5 ± 0.5
Komansu	T4	Profile P7	12.6 ± 0.4	32.3 ± 5.2	6.1 ± 2.2	2.3 ± 0.7
		Profile P11	5.1 ± 0.2	12.9 ± 2.3	2.4 ± 0.9	0.9 ± 0.3
Tashkuney	T5	Trench	5.8 ± 0.6	16.0 ± 3.0	3.0 ± 1.2	1.1 ± 0.4
		Profile P16	6.4 ± 0.5	16.4 ± 3.4	3.1 ± 1.3	1.1 ± 0.4
Max West		Profile P8	16.2 ± 0.2	41.5 ± 5.9	7.8 ± 2.7	2.9 ± 0.9
Max East		Profile P17	9.2 ± 0.2	23.6 ± 3.6	4.4 ± 1.6	1.6 ± 0.5
Average		All Profiles^d	9.6 ± 0.3	24.7 ± 4.1	4.7 ± 1.7	1.7 ± 0.5

^a Vertical separation modelled from TanDEM-X based topographic profiles (see Chapter 4).

^b Estimated from the VS with a fault dip of $21 \pm 3^\circ$.

^c Dip-slip rate calculations using 5.3 ± 1.1 ka and 14.3 ± 2.2 ka for max and min values, respectively.

^d Averaged over all vertical separation estimated from ground surface profiles (see Chapter 4).

The timing of paleoearthquakes varies along the segment between 14.3 ± 2.2 ka in the western (T1, T2, and T3) and 5.3 ± 1.1 ka in the central and eastern parts (T4 and T5), which hampers our ability to make a definite statement regarding fault initiation for the rate determination. Consequently, we bracket a minimum and maximum dip-slip rate using both ages, respectively. To emphasize the variations of the VS along the cPFT, I present selected profiles from and adjacent to the trenching sites for my calculations (Table 6.2). However, to be more cautious, I also use the average VS along the full length of the cPFT (9.6 ± 0.3 m), which corresponds to a cumulative dip-slip of 24.7 ± 4.1 m. To provide accurate estimates, I used the Python tool Slip Rate Calculator v0.1.3 (Styron, 2015), which uses age and offset PDFs to calculate the slip-rate PDF via Monte Carlo methods. For both offset and age, I used a normal distribution characterized by a mean and standard deviation. The final modeling yields an average minimum and maximum dip-slip rate of 1.7 ± 0.5 and 4.7 ± 1.7 mm/yr, respectively (Table 6.2; Figure 6.5). Using the maximum VS from the Syrinadjar River (Profile 8) results in 41.5 ± 5.9 m of cumulative dip-slip and a minimum and maximum dip-slip rate of 2.8 ± 0.8 and 7.8 ± 2.7 mm/yr, respectively (Table 6.2; Figure 6.5).

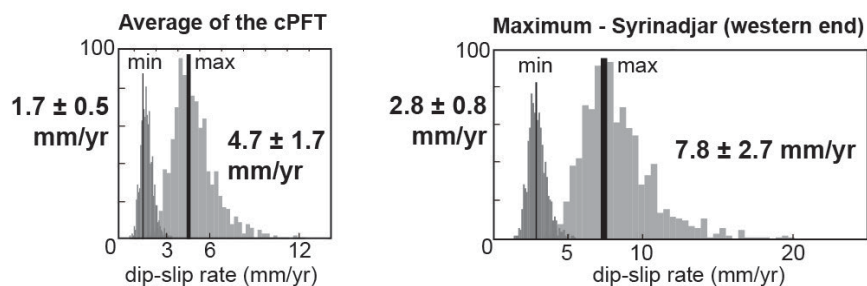


Figure 6.5 Dip-slip rate derived from vertical separation along the central PFT. Maximum dip-slip rate spans the time period since earthquake E5 (5.3 ± 1.1 ka) and minimum since E6 (14.3 ± 2.2 ka). See text for explanation.

6.3. Summary

A detailed analysis of the temporal overlaps of past earthquakes from several trenching sites along the central Pamir Frontal Thrust allowed a delineation of individual earthquakes along the segment length and helped defining at least five (possibly six) individual segment earthquakes, of which at least three may have activated the full length of the central segment during rupture. Combined with cumulative-offset measurements of associated landforms the data indicates a late Quaternary dip-slip rate of 4.7 mm/yr.

Chapter 7

Results IV: Earthquake geology of the 2008 M_w 6.6 Nura event, eastern Pamir-Tien Shan collision zone

In the previous chapters, I combined geomorphology and paleoseismology to estimate rupture extents, slip distributions during past earthquakes, and dip-slip deformation rates on geological timescales along the central sector of the Pamir Frontal Thrust. In this chapter, I systematically map and describe the surface rupture of the 2008 M_w 6.6 Nura earthquake in the eastern sector of the Pamir Frontal Thrust. In combination with an analysis of the geomorphic and structural geological aspects of this rupture, I aim at testing possible models to explain deformation processes within the Pamir-Tien Shan collision zone.

7.1. The 2008 M_w 6.6 Nura earthquake

The 2008 M_w 6.6 Nura earthquake rupture in the eastern Pamir initiated on October 5th at 15:52 (Greenwich time) at a hypocentral depth of ~3-4 km, 2-4 km south of the northern splay of the Pamir Frontal thrust (PFT_N) within the eastern continuation of the Pamir Thrust System (PTS) (Figure 7.1) (Sippl et al., 2014). Seismic shaking associated with this event reached distal areas including the Osh, Batken, Jalal-Abad and Naryn provinces in Kyrgyzstan, and border areas of Uzbekistan, Tadjikistan, and China (Kalmetieva et al., 2009). A point source deviatoric moment tensor determined from regional stations (i.e., Sippl et al., 2014) and a Global Centroid-Moment-Tensor (CMT) solution (<http://globalcmt.org>) records an almost pure reverse-faulting mechanism, with an ~east-west strike and 59° south-dipping fault plane. In contrast, an optimized fault model based on interferometric synthetic aperture radar (InSAR) measurements indicates deformation along a 80° south dipping PFT (Teshebaeva et al., 2014).

The main event caused a series of aftershocks with hypocentral maximum depths of 17 km. Sippl et al. (2014) divided these into five clusters based on the time of initiation and swarm location and with respect to the regional fault structures (Figure 7.1). Most of the aftershocks were located to the south of the main event following the E-W-striking structures of the PFT and the Trans Alai range, dominated by focal mechanisms indicating reverse faulting (red cluster; Figure 7.1). The Nura aftershocks include the two strongest events that apparently ruptured the same structure with magnitudes of M_w 5.2 and 5.4. A small cluster with reverse-fault mechanisms and a sub-vertical, east-striking rupture planes was initiated shortly after the main shock, presumably activating a splay of the PFT to the north (orange cluster; Figure 7.1). Approximately 20 km northwest and within the eastern terminus of the Alai intermontane basin, another small cluster was apparently triggered coseismically with respect to the main shock, but it was dominated by strike-slip faulting along northeast or northwest-striking fault planes (purple cluster; Figure 7.1).

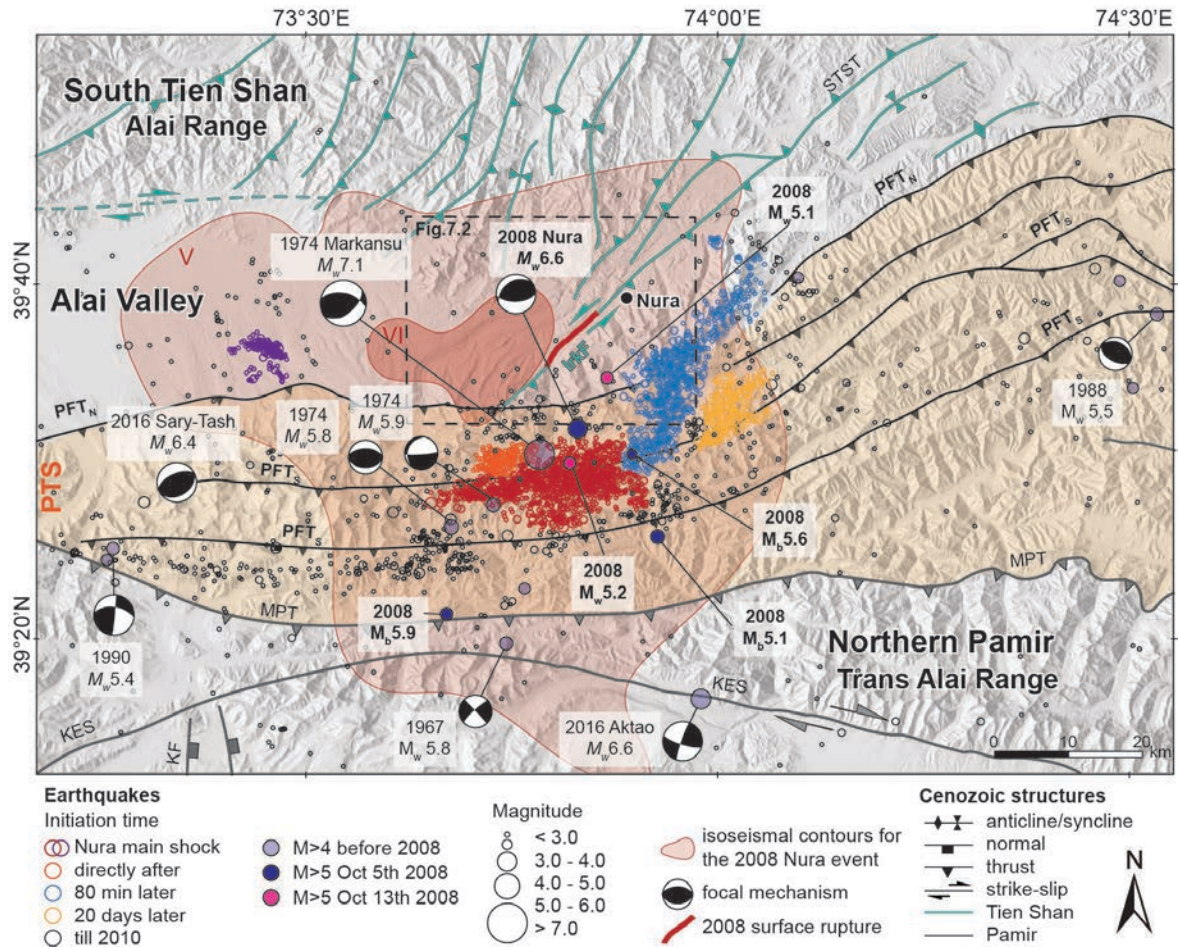


Figure 7.1 Overview of recent seismicity of the eastern part of the northern Pamir range front, the Alai Valley and the Pamir-Tien Shan collision zone with major fault structures and earthquake locations (see Figure 2.2, Chapter 2 for location). Colored circles indicate main shock and aftershock sequences related to the 2008 Nura earthquake from a regional network between 2008 and 2014 (Sippl et al., 2014). Black circles represent seismicity from the USGS earthquake catalogue between 1976 and 2021. Focal mechanisms are from the Global Centroid-Moment-Tensor catalog (Dziewonski et al., 1981; Ekström et al., 2012), Fan et al. (1994) and Sippl et al. (2014). Base map hillshade is a 30-m resolution NASA Shuttle Radar Topography Mission digital elevation model. KES = Kongur Extensional System, IrkF = Irkeshtam Fault, PTS = Pamir Thrust System, PFT = Pamir Frontal Thrust, MPT = Main Pamir, STST = South Tien Shan Thrust.

One distinct cluster of aftershocks occurred approximately 80 min after the main shock adjacent to, and at the eastern end of the main shock (red cluster). Seismicity of this cluster deviated toward the north-northeast and aligned with the faults of the southern Tien Shan north of the PFT (blue cluster; Figure 7.1). The earthquakes within the blue cluster appear to have ruptured shallower structures, with depths below < 10 km, and with fault planes dipping east to east-southeast, thus oblique with respect to the E-W-striking PFT faults. Sippl et al. (2014) distinguished three sub-parallel, *en echelon* and northeast-striking sectors of seismicity in this aftershock cluster. These *en echelon* clusters appear to follow the structural trend of faults in the southern sector of the Tien Shan in the north, but they cross topographic and structural trends of the PFT in the south. The fifth aftershock cluster was initiated about ~20 days after the main event and it was located east of the main shock (yellow cluster; Figure 7.1). The east-northeast-

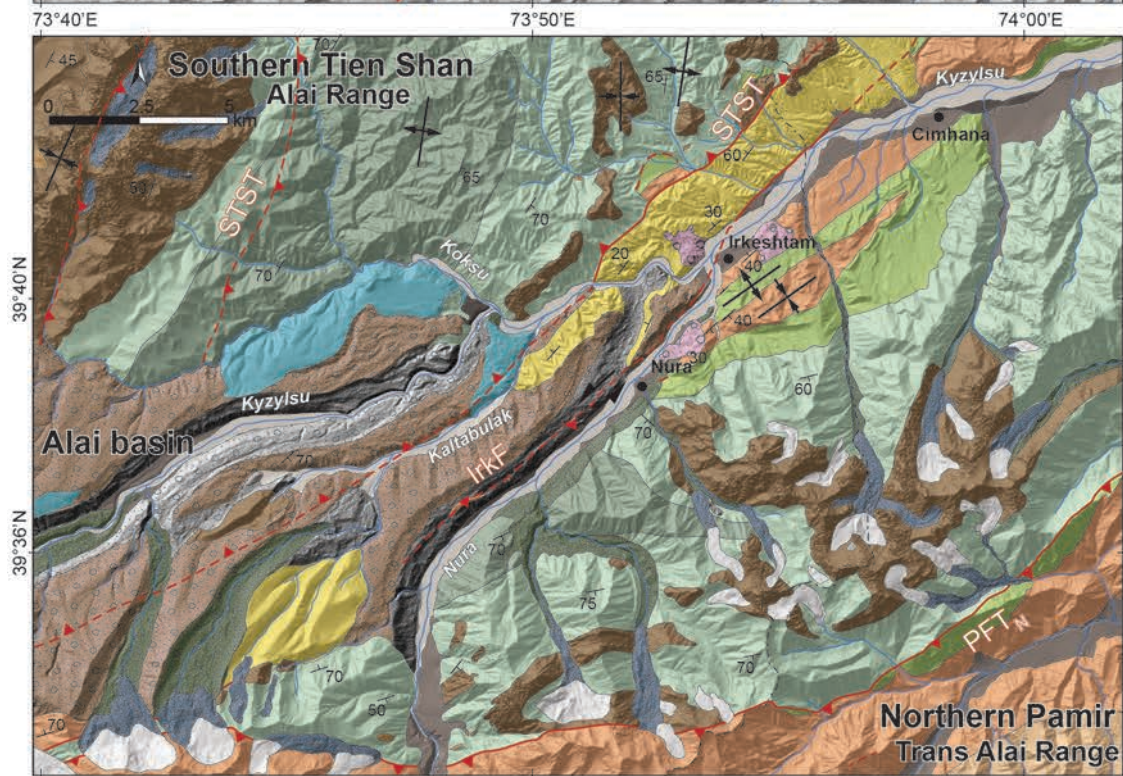
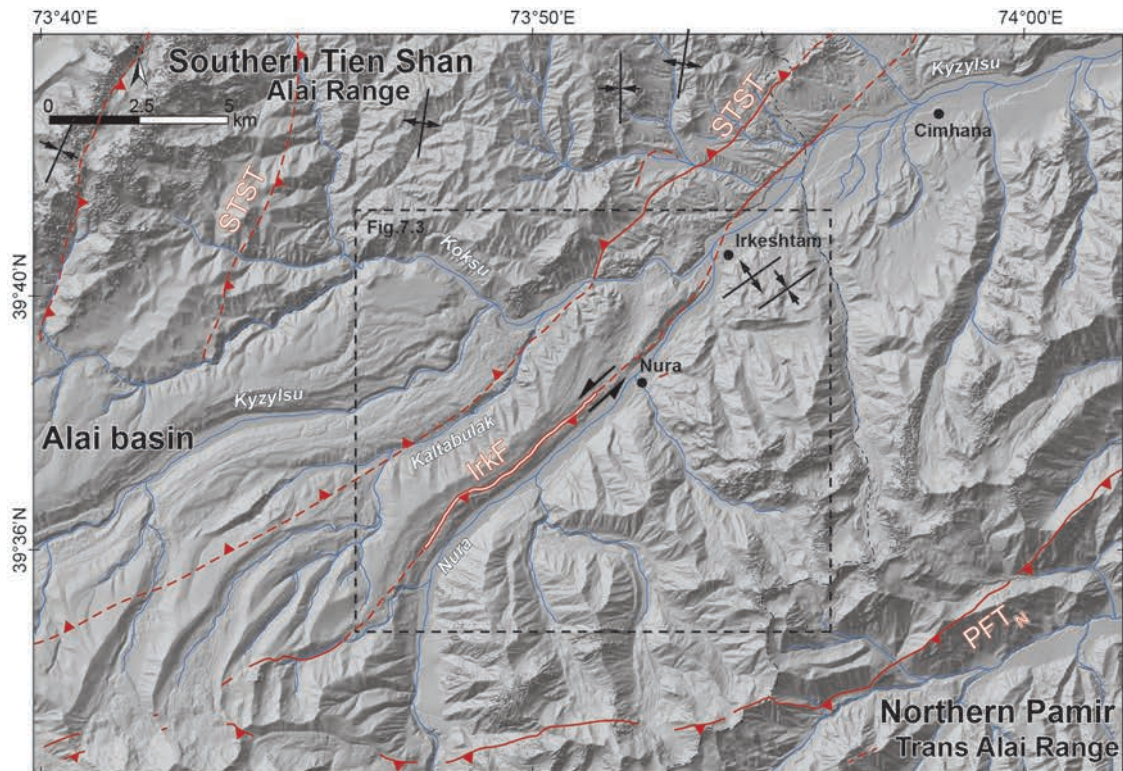
oriented sectors with thrust-reverse earthquakes within the yellow cluster appear to follow the local topography and the strike of the PFT that deviates slightly towards northeast (Sippl et al., 2014).

Despite the shallow depth and strength of the main shock, and the two strongest aftershocks, no surface rupture was initially reported along the structures of the PFT. However, the high-elevation landscape (>3000 m), glacial environments and snow cover hamper field-based or remote-sensing investigations in this area. InSAR measurements could not be sufficiently resolved along the PFT, due to these local limitations, but revealed a distinct signal of surface deformation north of the PFT, where no seismicity was recorded (Teshebaeva et al., 2014; Qiao et al., 2017). The InSAR-modelled surface deformation extends for a length of ~25 km northeast-southwest, following the sinistrally reverse Irkeshtam Fault (IrkF), which is obliquely oriented with respect to the PFT (Figure 7.1). An optimized fault model from Teshebaeva et al. (2014) defines the IrkF as a south-dipping fault with a change in dip from 37° to 44° from east to west, respectively. The slip was classified as having been associated with an oblique thrust-fault mechanism, with ~2 m of thrusting and ~1 m of left-lateral strike-slip offset. A combination of field (in 2012) and remote sensing observations along this deformation zone revealed a prominent 7-km-long surface rupture southwest of the village of Nura (Teshebaeva et al., 2014). The village of Nura was destroyed entirely, with 74 fatalities during this event (Kalmetieva et al., 2009). The surface rupture produced steep scarps, with vertical offsets of up to ~80 cm and evidence for left-lateral motion, which agrees with the kinematics of the deformation zone determined by InSAR-measurements (Teshebaeva et al., 2014). The surface rupture is well preserved and offers a valuable opportunity to document earthquake rupture behavior in this complex collisional tectonic setting. In this thesis the analysis of the fault zone follows the same transect of the rupture.

7.2. Geological and structural framework

The surface-rupture zone associated with the 2008 Nura earthquake is located within a structural transition of the collision between the Trans Alai range of the Northern Pamir and the Alai range of the southern Tien Shan (Teshebaeva et al., 2014; Sippl et al., 2014; Qiao et al., 2015). Here, the PTS juxtaposes folds and thrusts to its north that impinge on south-vergent structures of the Southern Tien Shan Thrust system (STST) (Figure 7.2).

To date, only few structural and tectono-geomorphic studies have been conducted along this structurally complex zone. Geological maps at a scale of 1:200,000 of the Kyrgyz Republic west of the Kyrgyz-Chinese border are available (Kozlov & Artemov, 1964), but access to the region is limited and under strict military control, affecting mobility (Yuzhong, 2003). Consequently, currently available interpretations of geological structures east of the Kyrgyz-Chinese border are based on first-order observations and often remain speculative (Sippl et al., 2014).



Explanation

Cretaceous limestones, claystones and gypsum	Upper Quaternary	Glacial till	glacier	thrust fault
Cretaceous red beds, conglomeratic sandstones	Miocene-Pliocene conglomerates (Baktry Fm.)	Qm ₄	landslide	normal fault
Jurassic sandstones, conglomerates and gypsum	Oligocene-Miocene (Massaget Fm.)	Qm ₃	Fluvial terraces	strike-slip fault
Devonian limestones	Paleocene limestone and gypsum	Qm ₂	Qt ₄	syncline
Silurian claystones, sandstones		Qm ₁	Qt ₃	anticline
		Country border	2008 surf. rupture	unconformity

Figure 7.2 Topographic and geologic overview of the Pamir-Tien Shan collision zone at the eastern end of the Alai Valley (see Figure 7.1 for map location). (a) Shaded relief map, derived from the TanDEM-X image (12 m resolution), with updated faults (red lines). Major rivers outlined in blue. (b) Updated geological map modified after Geological Map sheet J-43-II in the scale of 1:200,000 (Chong-Alai) (Kozlov & Artemov, 1964) and Sippl et al. (2014).

North of the imbricate PFT faults at $\sim 73^{\circ}55'E$, a sequence of folded Silurian-Devonian units related to the Tien Shan is exposed (compare cross section in Figure 7.3) and abuts folded lower Cretaceous-Paleogene strata at its northern margin. North of an anticline relict within this folded Cretaceous-Paleogene sequence, a northeast-trending exposure of Neogene conglomerates unconformably covers a syncline, which in turn, towards the northwest, is overthrust by folded Silurian-Devonian units of the Tien Shan (Figure 7.2). These north-northeast oriented fold-and-thrust structures along the eastern Alai range connect with mainly east-west oriented structures of the southern Tien Shan along the western and central Alai range. This spectacular change in strike may result from far-field wrenching and anticlockwise rotation along the dextral Talas-Ferghana Fault zone (see Figure 2.1; Chapter 2) (e.g., Bazhenov, 1993; Burtman et al., 1996; Sippl et al., 2014), in combination with differential deformation in this sector during the closure of the Alai Valley and possible out-of-sequence thrusting (e.g., Strecker et al., 2003).

Several streams from the Trans Alai range (Pamir) in the south and the Alai range (Tien Shan) in the north join the eastward-flowing Kyzylsu River in the vicinity of the rupture zone (Figure 7.2). It is important to note that this river has nothing to do with the river of the same name that drains the Alai Valley to the west (see Figure 2.1; Chapter 2). The Nura River, immediately to the south of the rupture zone, flows from south-north through the imbricate PFT folds and thrusts of the Trans Alai range; it changes its course to the northeast at $\sim 39^{\circ}35'N$, and eventually joins the Kyzylsu River. Along the northeast-flowing sector, the Nura River separates Paleozoic units from an extensive area of Paleogene sedimentary strata that are covered by Quaternary glacial tills; the tills are dissected by other north-flowing tributaries. Between the Nura and the Kyzylsu River (left tributary), Paleozoic and Neogene units are exposed in places, but a direct contact is not visible (Figure 7.2). Small, up to 100-meter-long outcrops of Paleogene gypsum occur along the northwestern slopes of the Nura river valley and at the inferred IrkF fault zone. From here the fault extends northeastward towards the unconformable contact between the folded Cretaceous-Paleogene and Neogene strata, and apparently bounds an anticline in the Paleozoic units (Figure 7.2). Based on the fault and outcrop relationships, Sippl et al. (2014) suggested that the IrkF constitutes a shallow-dipping thrust, which steepens farther southeast. North of and along the Kyzylsu tributary and at the junction with the Koksus River Jurassic gypsum is exposed and extends for several kilometers, with thicknesses reaching up to 200 m (Teshebaeva et al., 2014).

The glacial tills of the Nura region can be subdivided into four separate generations (Q_{m1-4}), as defined by Arrowsmith & Strecker (1999) and following the Nikonov et al. (1983) nomenclature. Similar to the Alai region, Q_{m1} can be well distinguished from $Q_{m2,3}$ based on less pronounced surface

roughness and more subdued topography (Arrowsmith & Strecker, 1999). The Qm₃ and Qm₂ tills, on the other hand, are more difficult to separate from each other; however, Qm₃ seems to be spatially less extensive and cuts into Qm₂. In the footwall of the Irkeshtam fault zone Qm₂ tills cut and overlie the Qm₁ deposits away from the Nura River in a northward-deflected direction, forming a ~100-m-deep valley (at ~39°39'N 73°50'E; Figure 7.2). Although no age control exists, based on the geomorphic and stratigraphic conditions it can be inferred that the relationship between the Qm₃ moraine deposits and associated Qt₃ terrace is comparable to that of moraine deposits in the Alai region (see Chapter 4), although their elevations might differ due to varying tectonic histories of the two regions. The youngest tills in the Nura region (Qm₄) are associated with the present-day glaciers in the upper-elevation sectors and comprise unvegetated, irregular surfaces that extend for up to ~1 km away from the glacial termini (Figure 7.2).

7.3. The Nura earthquake site

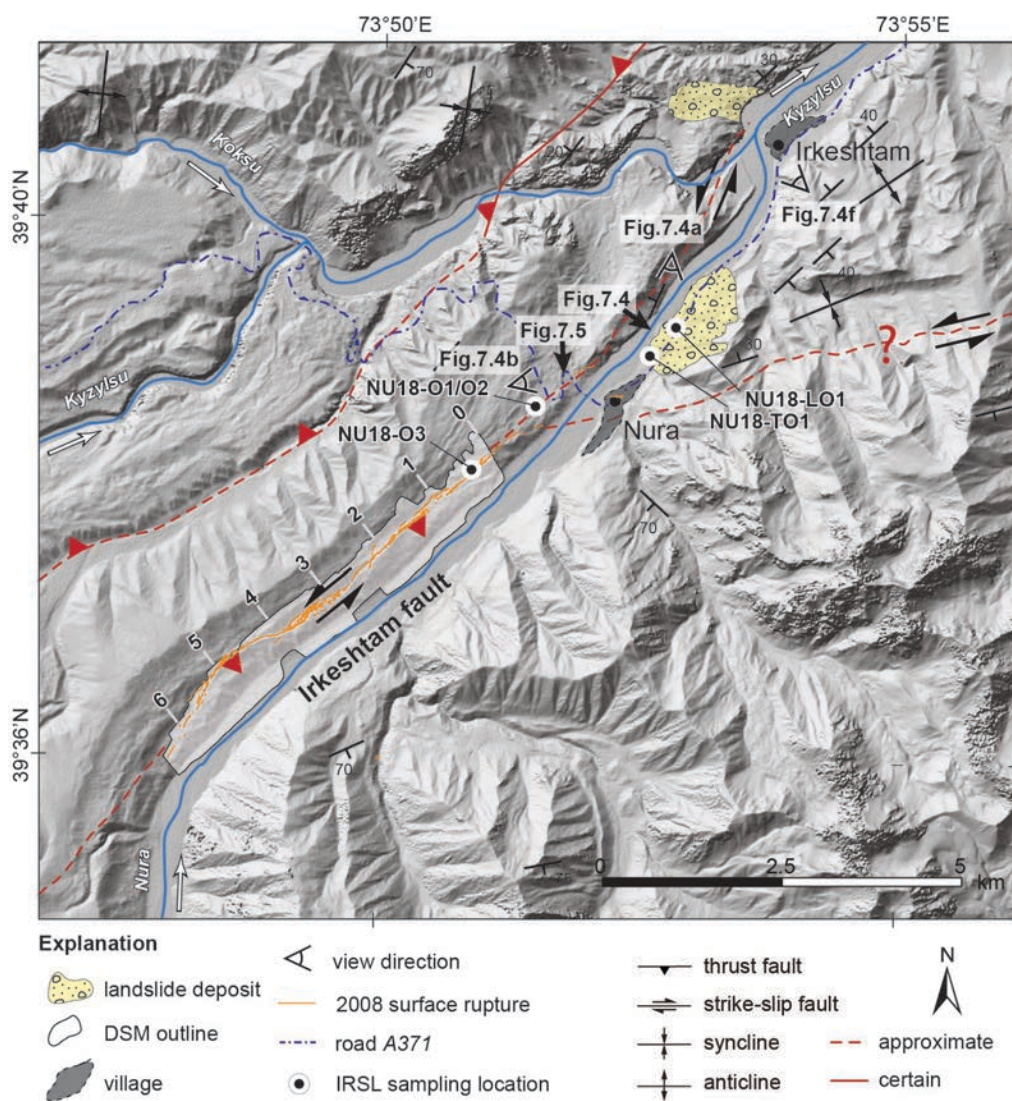


Figure 7.3 The Nura study site (see Figure 7.2 for map location). Surface-rupture extent of the 2008 Nura earthquake mapped in this study shown in orange. Major faults are drawn in red, dashed lines indicate inferred structures. Shaded polygon shows the extent of the digital surface model generated in this study using low-altitude aerial photographs from unmanned aircraft vehicles. Ticks show along-strike distance in kilometers. White arrows indicate direction of river flow. Base map is shaded relief image derived from 12 m TanDEM-X data.

7.3.1. Morphological and stratigraphic observations

The Nura study area comprises the extent of the surface rupture of the 2008 Nura earthquake on the northwestern river bank of the Nura River and the area of the Kyzylsu river junction in the northeast (Figure 7.3). To analyze the 2008 surface rupture, on-site observations and low-altitude aerial photographs were combined. Aerial photographs were obtained along the length of the surface break of the earthquake using unmanned aerial vehicles (UAV) to generate a high-resolution digital surface model (DSM) and mapping base (see following sections). The fault-zone geology and geomorphology were investigated at several locations along the *A371* road, which passes from the Alai Valley through the Nura village to China. According to reports from the residents, this road was built in 2005 and repaired in 2015.

The Nura village is located in the hanging wall of the IrkF and built on a fluvial terrace adjacent to lateral (presumably) Qm₃ moraine deposits that are inferred to correlate with Qm₃ (see also Figure 7.2). Northeast of the village a smooth free surface of the northern limb of a syncline in Paleogene rocks is exposed at the top of the southeastern river bank. Here, a series of landslide deposits covers the river terrace (Figure 7.3). The surface roughness of these deposits varies and therefore these could be divided into three different landslide generations: L1 to L3, from old to young (Figure 7.4). The landslide deposits are cut by the *A371* road; in the cross section along the road one can observe layered, fine-grained lake sediments that abut coarse, poorly sorted landslide deposits at the edge of landslide deposit L1, suggesting transitory lake formation along the Nura River during landslide-related (L1) valley impoundment. Farther southwest, in turn, the contact between landslide deposit L3 and the Nura terrace is exposed along the river cut (Figure 7.4). The IRSL dating of the paleo-lake (NU18-LO1) and terrace sediments (NU18-T1) yield an age of 12.0 ± 0.6 ka and 1.4 ± 0.1 ka, respectively (Figure 7.4; Table 7.1). Farther to the north, in the vicinity of the Kyzylsu river junction, northwest-dipping Neogene sediments are covered by another landslide deposit on the opposite side of the Irkeshtam village (Figure 7.3 and 7.4). Direct observations combined with surface geomorphology from ArcMap World Imagery Basemap and TanDEM-X images, suggest that the northern landslide deposits correspond to one mass-movement event. However, the age compared to the southern landslide deposits is not clear.

In the Kyrgyz national earthquake reviews after the 2008 Nura event, Abdrakhmatov et al. (2008) and Kalmetieva et al. (2009) reported on ruptures in the asphalt cover of the *A371* road crossing the Nura village and southeast and northwest of the bridge across the Nura River; these 5-cm-wide cracks

appeared every ~90 m along the road and smaller 1-cm-wide cracks were observed in between repeating every ~30 m (Abdrakhmatov et al., 2008). On the northwestern side of the bridge, repaired portions of the A371 were observed during the 2018 field campaign during our study. Here, the road cuts through the Qm₂ moraine deposits (compare Figure 7.2), and the cross section exposes a fault plane adjacent and subparallel to the repaired road sections (Figure 7.5).

The exposed Qm₂ moraine deposits contain up to several-meter-sized subangular to subrounded boulders and are covered by a layer of fine retransported loess. The thickness of the loess layer varies laterally between tens-of-centimeters and several meters; the moraine units are 20 to 30 m thick (Figure 7.5). At a location on the Qm₂ moraine further away from the road to the southwest (see Figure 7.3 for location), a thick > 2-m-loess layer was exposed in a former military trench. The IRSL dating of the retransported loess sediments (NU18-O1 and NU18-O2) yield ages of 3.4 ± 0.2 ka and 11.3 ± 0.5 ka, from top to bottom, respectively (Figure 7.5, Table 7.1). Farther southwest, where the contact between loess and moraine deposits could be established in another military trench (Figure 7.3; between 0 and 1 km of the DSM), a sample was taken from the moraine deposits; however, the IRSL dating of these (NU18-O3) could not be performed due to insufficient amount of grain size of the sample.

Table 7.1 Infrared Stimulated Luminescence ages (IRSL at 150°C). Concentration of dose-rate relevant elements (K, Th, and U), water content (W), dose rates (D), observed overdispersion (OD), equivalent dose (D_e). Samples run at the Institute of Earth and Environmental Sciences (University of Freiburg in Germany).

Sample Name ^a	Sample Type	Depth (cm)	W (%) ^b	K (%)	Th (ppm)	U (ppm)	D (Gy/ka)	Grain size (μm)
NU18-O1	tube	75	15±5	1.93±0.13	9.88±0.64	3.08±0.19	3.74±0.17	100-150
NU18-O2	tube	225	15±5	1.69±0.14	9.26±0.60	2.90±0.18	3.39±0.14	100-150
NU18-LO1	tube	383	15±5	1.56±0.13	6.21±0.41	1.93±0.13	2.81±0.13	100-150
NU18-TO1	tube	270	15±5	2.46±0.25	7.22±0.46	1.96±0.12	3.91±0.22	200-250

(continued)

Sample Name ^a	n ^c	OD	Model	D _e IRSL (Gy) ^d	D _e pIR-150 (Gy)	Age IRSL (kyr) ^e	Age pIR-150 (kyr)
NU18-O1	40/40	0.15/0.29	MAM/MAM	12.78±0.32	15.63±0.22	3.42±0.16	4.19±0.17
NU18-O2	40/40	0.03/0.02	CAM/CAM	38.49±0.25	53.75±0.46	11.3±0.5	15.8±0.7
NU18-LO1	40/40	0.06/0.06	CAM/CAM	33.68±0.38	46.91±0.54	12.0±0.6	16.7±0.8
NU18-TO1	40/40	0.07/0.11	CAM/MAM	5.44±0.06	6.29±0.09	1.39±0.08	1.61±0.09

^bWater content was estimated based on present day moisture and grain-size composition.

^cNumber of accepted aliquots passing internal recycling ratio criteria ($\geq 10\%$).

^dMean dose was calculated using either the Central Age Model (CAM) or the Minimum Age Model (MAM), depending on the statistical parameters of D_e distributions, such as overdispersion, skewness and kurtosis (cf. Galbraith & Roberts, 2012).

^eAges were calculated using ADELEv.2017 (Degering & Degering, 2020), using the results of high-resolution gamma spectrometry (cf. Preusser & Kasper, 2001).

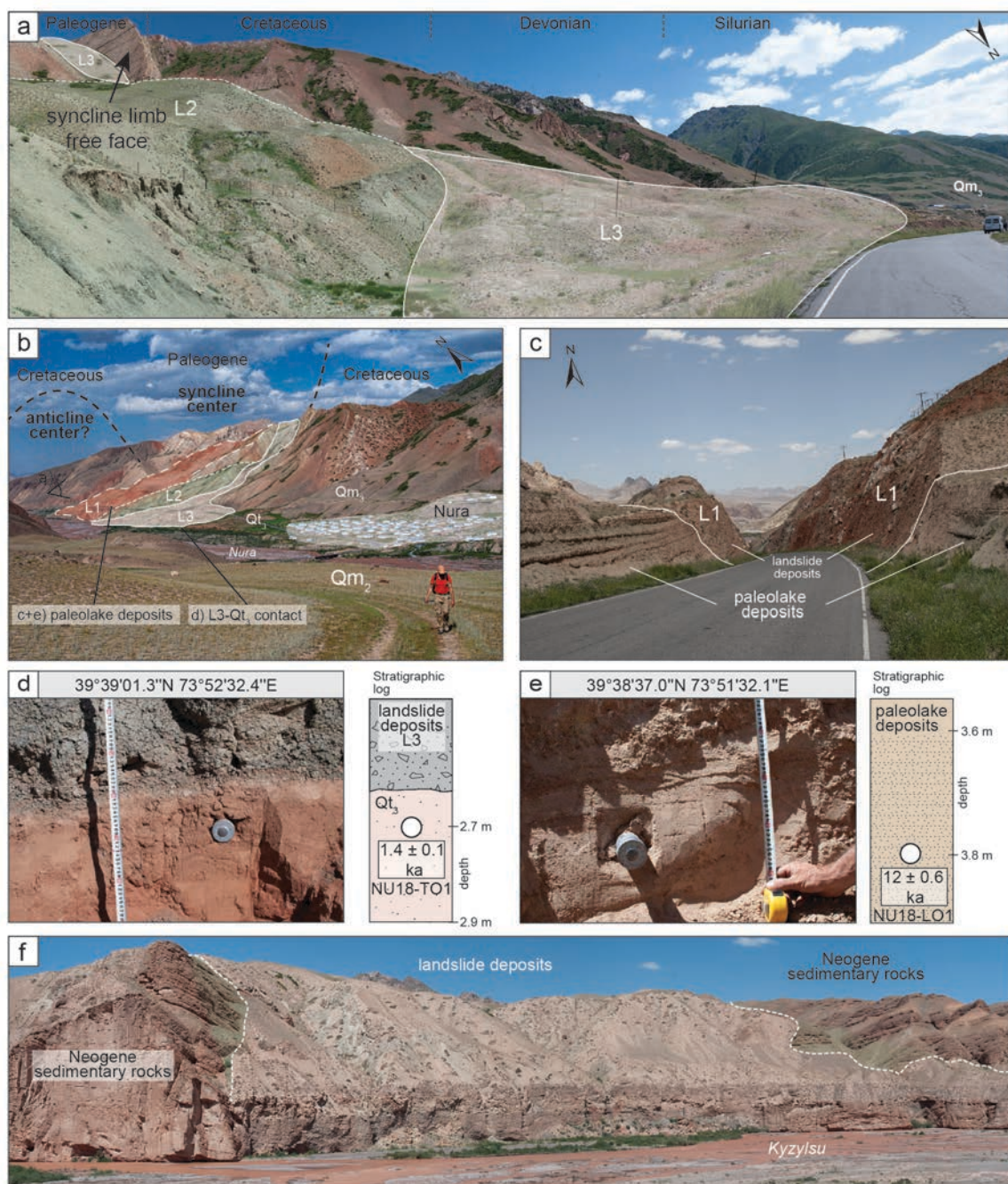


Figure 7.4 (a-c) Field views of three landslide-deposit generations and paleolake deposits along the eastern slope of the Nura river valley, northeast of the village of Nura. Note how the landslide deposits emerge from the open syncline structures of the folded Cretaceous-Paleogene units. (d-e) Stratigraphic relationships at two sites where samples were taken for luminescence analysis; see location in d). Paleolake sample was taken from the lowest exposed unit. See Figure 7.3 for viewpoint and sample location.

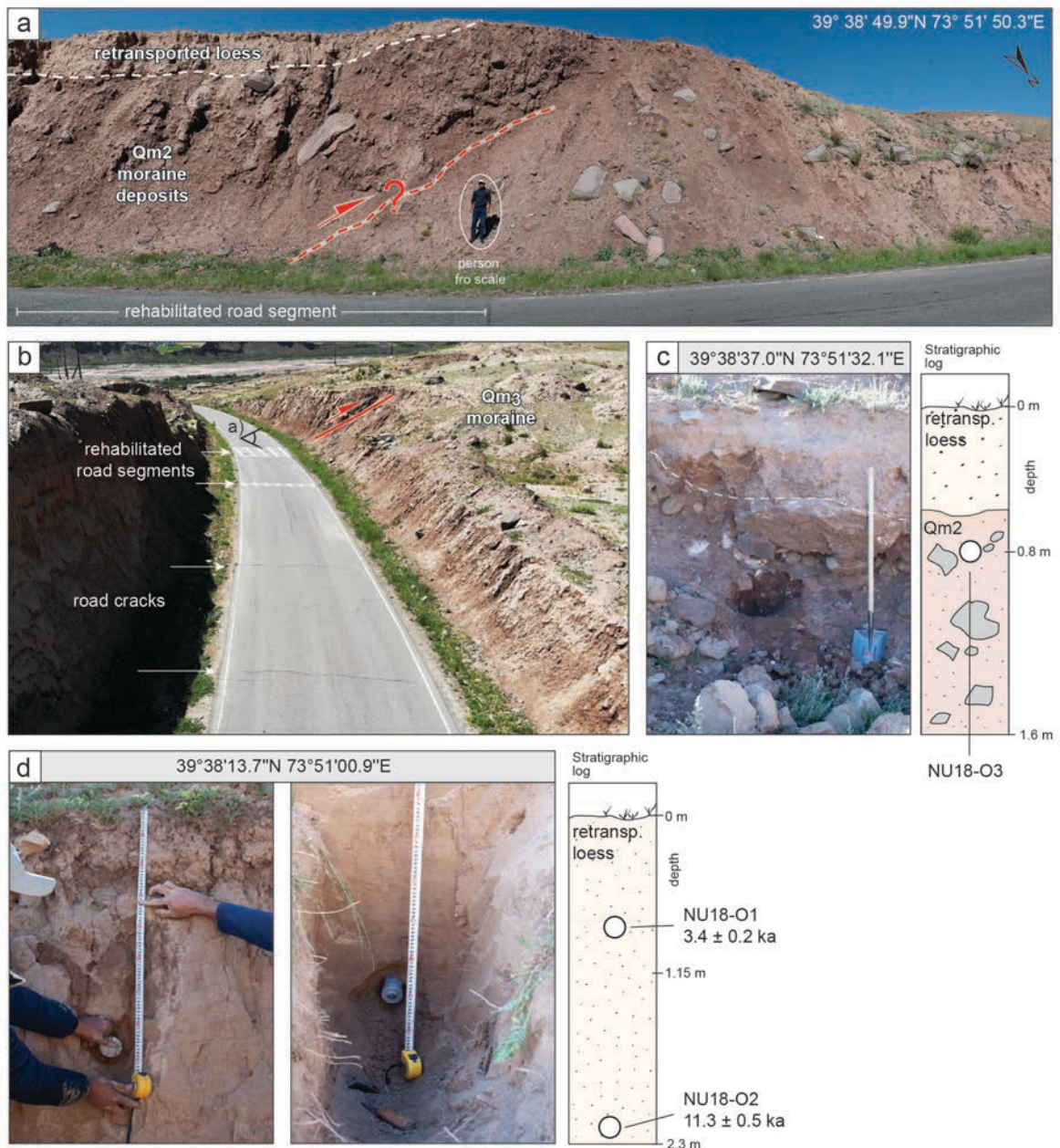


Figure 7.5 (a-b) Man-made cut through Qm₂ moraine deposits along the A371 road. Note rehabilitated road segments and cracks in asphalt subparallel to the inferred fault in (b). (c) View of Qm₃ stratigraphy. (d) Sampling site for luminescence analysis. See Figure 7.3 for viewpoint and sample location.

7.3.2. Digital surface model and data compilation

The UAV flight survey of ~8 km along strike of the 2008 Nura surface rupture covered an area of approximately ~5.5 km² (Figure 7.3). In total, 14,156 photographs and 10 videos were acquired, including 27 ground-control points (GCPs) georeferenced with dGNSS (see Chapter 3.2 for methodological details). Together, this survey resulted in eleven overlapping dense point clouds, orthomosaics, and digital surface models (DSM) with a resolution of 4-10 cm/px, and a georeferencing constraint of ~1-2 GCP/km² (Table 7.2). Three of the DSMs (set 9, 10 and 11) resulted in poorly georeferenced models due to an insufficient GCP distribution and were discarded for further analysis (Figure 7.6).

The DSM data and the computed topographic derivative maps (Figure 7.6) were used for mapping in ArcMap® at a fixed scale of 1:400. During the digital surface-break mapping three attributes were assigned to the rupture traces: an identification number, scarp-face direction, start/end point, length, strike and type (principal displacement zone (PDZ) or distributed). The “type” was assigned on the basis of trace continuity, length and/or vertical separation within the areas where the fault zone consists of multiple surface rupture splays. During fault trace mapping, surface breaks visible in the discarded DSMs (set 9, 10 and 11) were mapped and subsequently moved to the correct location relative to the overlapping georeferenced map. While this portion of the mapping will be considered for general discussion of the rupture extent and distribution, it will be excluded from all further calculations (Figure 7.6).

In addition to the DSM analysis, an extensive displacement-vector survey of the surface breaks was catalogued to provide a systematic documentation. The survey is subdivided into four 500- to 1000-m-long separated blocks (Figure 7.7). To record the exact locations of the ground observations for cartography and to trace selected surface breaks, dGNSS measurements were carried out. Displacement-vector measurements were taken every 10 m in each block. 119 field measurements include components of fault slip and sense of displacement derived from fault strike (fault azimuth), vertical offset, crack opening, the azimuth of the slip vector (opening direction) if a clear piercing point was available (see Appendix C, Table C1). I used ArcMap® to compile an interactive displacement-vector catalogue with measurement location, measurements details, and corresponding photographs. All collected data are archived and will be freely available from doi: 10.6084/m9.figshare.19534585.

Table 7.2 Data-acquisition summary of individual digital surface model (DSM) set areas along the 2008 Nura surface rupture. See Figure 7.7 for area location reference. Discarded DSMs (Set 9 to 11) marked in gray; see text for explanation.

Set ID	Area (km ²)	# of GCPs	# of photos	Length along strike(m)	Overlap with next set (m)	Mean Width (m)
1	3.27	4	1498	1330	360	670
2	2.88	5	1853	1010	440	860
3	3.01	3	2061	1200	400	650
4	2.12	3	1270	910	310	820
5	2.91	5	1284	1110	390	690
6	2.41	3	1988	970	200	850
7	1.90	3	1165	930	390	730
8	2.80	3	1853	1150	340	730
9	2.11	3	1230	1100	280	690
10	1.71	3	267	890	360	420
11	1.62	3	375	700	-	560

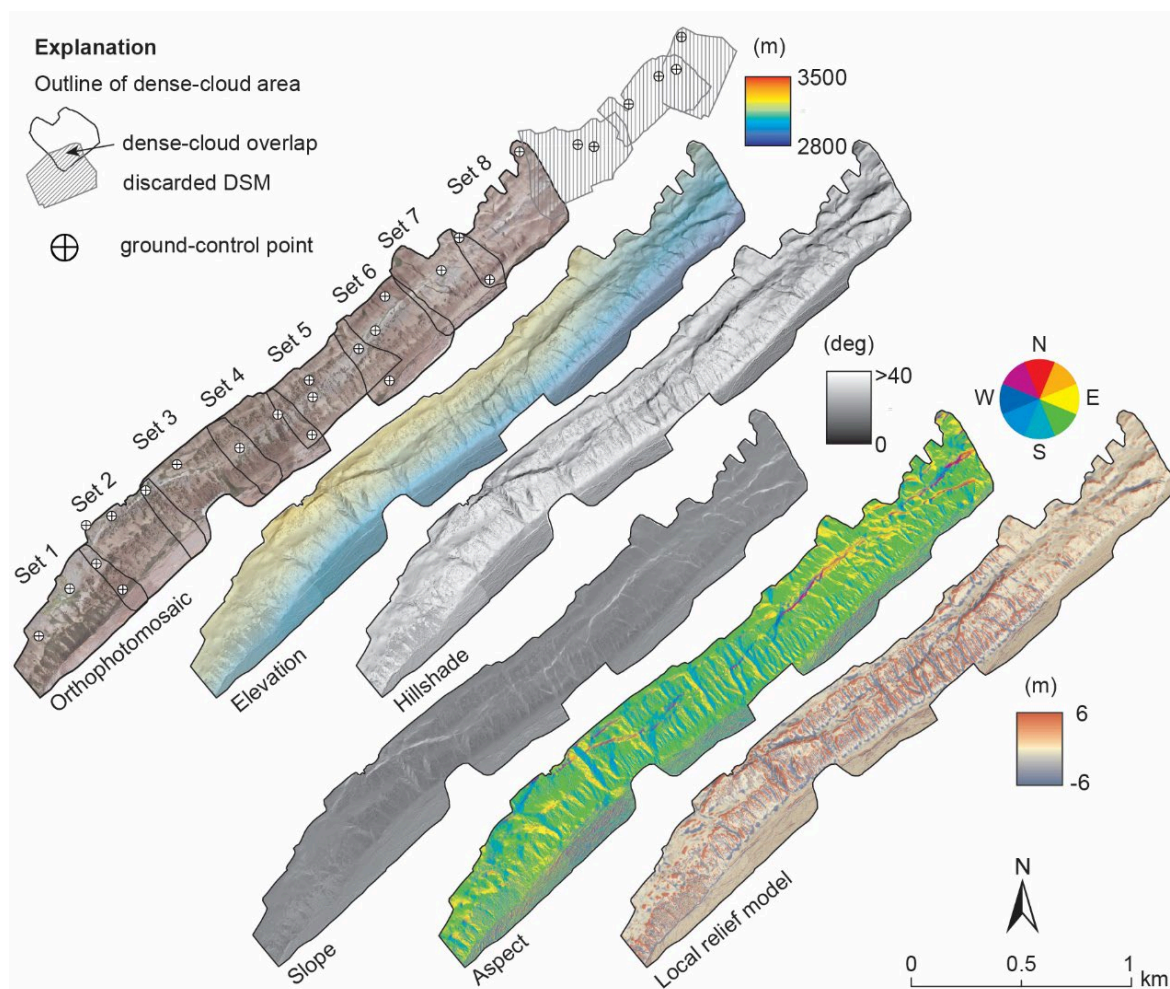


Figure 7.6 Different digital surface model (DSM) topographic derivative maps for the Nura earthquake site, to facilitate the identification of the fault zone, offsets, and landforms indicative of cumulative deformation. The model was generated from structure-from-motion and merged from eight single overlapping DSM sets (see Table 7.2). Raster data and orthomosaics are archived and will be freely available from OpenTopography.

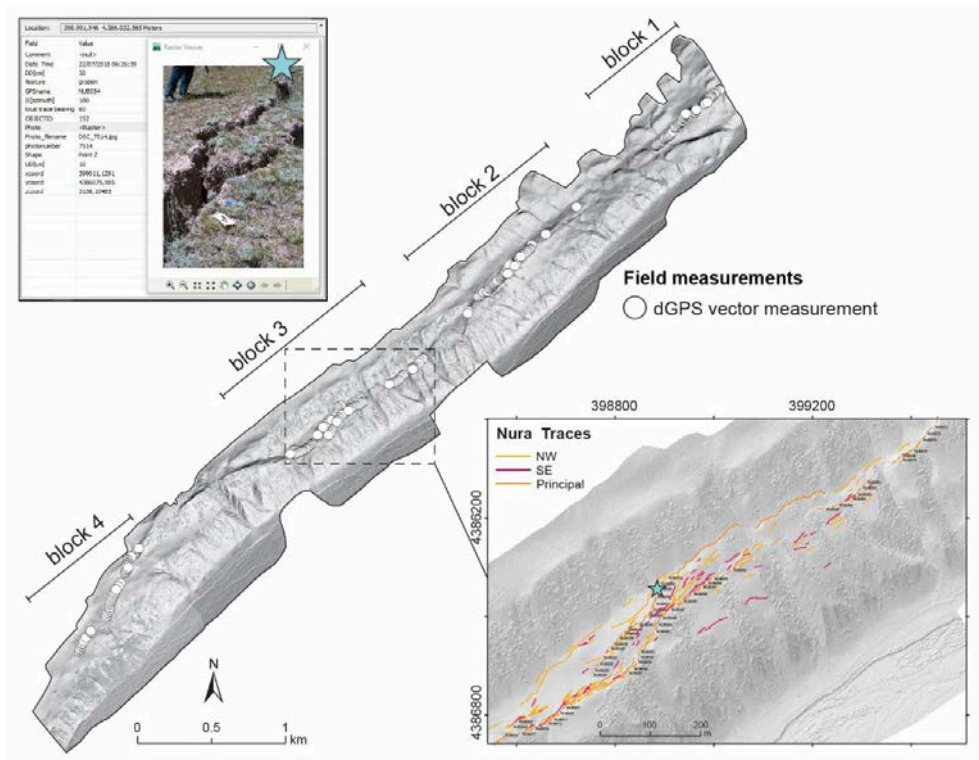


Figure 7.7 Distribution of the vector-survey blocks. Upper left: Example of one displacement-vector measurement on a hillshade map in ArcMap®. Location of characteristics is labeled by the corresponding observation ID. By clicking on the location mark (green star) with the identify cursor a pop-up window appears with summary-observation data and a link to the associated photograph. See Appendix C, Table C.1 for vector measurements.

7.4. The 2008 Nura earthquake surface rupture

In the following chapter, I describe the surface rupture of the Nura earthquake along strike by combining field observations and remotely sensed structural analysis.

7.4.1. Displacement-vector measurements and rupture-trace mapping

Field-based displacement-vector measurements were obtained at most pronounced surface offsets during the field campaign in 2018 (Figure 7.8; Appendix C, Table C1). In addition, I supply the spatially limited ground-deformation measurements acquired during the field campaign with those derived from high-resolution DSMs produced from UAV (Figure 7.8). The surface rupture mapped from DSMs has a length of ~ 6 km and follows an average trace with a bearing of 040. Poorly referenced DSMs excluded from further calculation (see above) show that the surface break, although less continuous, extends northeastward beyond the considered DSMs and our field measurements for another ~ 500 m along the trace and diverges eastward to ~ 080 for another ~ 300 m. Subparallel and following an apparent gap of ~ 800 m, another ~ 300 -m-long fracture cuts through moraine deposits of the western Nura river bank

(see Appendix C, Figure C2). Considering this, the observed extent of the surface rupture extends over a linear distance of ~ 8 km.

Within the 6-km-long section covered by well referenced DSMs (Figure 7.8), the majority of the surface breaks follow in the range between 040 and 060, with an opening direction between 090 and 100 (measured in the field), respectively. This relationship between strike and opening direction illustrates the left-lateral character of the sense of motion of the underlying fault that caused the rupture. However, the opening direction is represented by a sparse dataset, due to advanced soil erosion over the past ten years, which made measurements difficult, and in many cases impossible. Along strike in a southwesterly direction, the general ~ 040 trace of the fault zone changes into a westward direction of N080 at ~ 4 kilometers, continues upslope for approximately 500 m along strike, and returns back to a 040 orientation; this results in a right-step in the fault zone (between kilometers 3-4 and 4-5) of ~ 200 m (Figure 7.8).

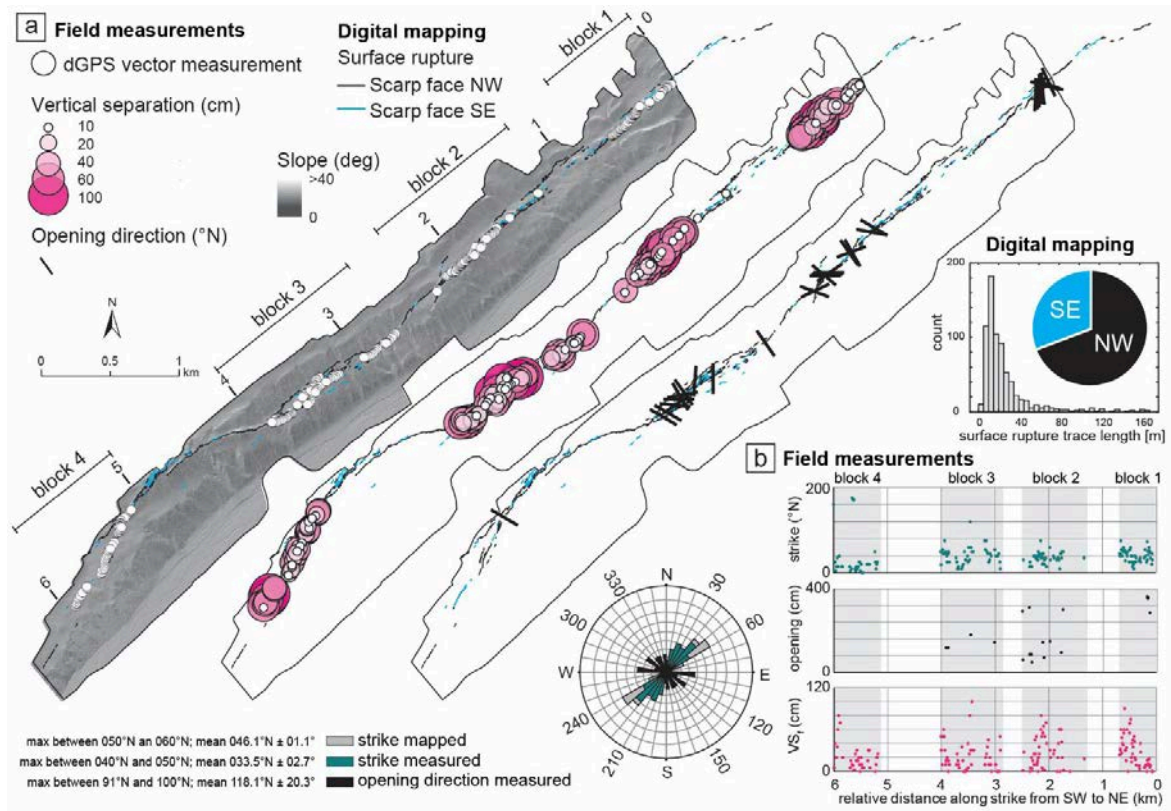


Figure 7.8 Characteristics of the 2008 Nura surface rupture. The base of this illustration is a slope-shade map (hillshade map overlain by slope map) derived from low-altitude unmanned aircraft vehicle (UAV) photography. Rupture trace from digital mapping. (a) From left to right: location of ground-based field measurements; ticks denote kilometer marks along the rupture zone covered by DSM; 0 is at the northeast. Circle size indicates amount of vertical separation in centimeters; line orientation represents opening direction from North. Rose diagram shows distribution of strike and opening direction of surface breaks. Histogram shows distribution of mapped rupture-trace length; inset chart shows ratio between southeast and northwest-facing scarps. (b) Distribution of strike, opening and vertical separation measurements obtained in the field.

At approximately 5 kilometers, the rupture trace bifurcates towards the south, with an orientation of 025 for approximately 1.5 km. Vertical separation measured in the field (VS_f) shows considerable scatter (0.1 to 1.0 m) and is asymmetrically distributed along strike. A peak in VS_f (0.3 to 0.9 m) occurs between block 1 and 2, and some outliers in block 3 and 4 (Figure 7.8). VS_f decreases steeply to the northeast, and more gently to the southwest.

The lateral extent of the fault zone could only be determined by remote fault-trace mapping. In total, I was able to trace 801 surface breaks, of which 70% are associated with a NW facing scarp. The longest continuous break was 195 m long (Figure 7.8). The distribution of the surface breaks, in some areas approximately 150 m wide, shows that most of the offsets measured in the field along single surface breaks only represent a lower bound of the overall displacements. This is especially the case for blocks 2 and 3. The measured offset values do not take into account possible distributed deformation and/or topographic flexure.

7.4.2. Surface breaks and local geomorphology

The observed surface rupture of the 2008 Nura earthquake ruptured lateral moraine deposits and affected the upslope topography with a northeast-southwest trace, southwest of the Nura village and along the northwestern slopes of the Nura river valley (Figure 7.3). The DSMs suggest a relationship between the local geomorphic conditions and the seismogenic surface rupture. Interestingly, the surface rupture from 2008 cuts through well-developed flexures with metric amplitudes that appear to represent older tectonic landforms (hereinafter referred to as such) indicative of earlier deformation (Figure 7.9). The remotely mapped rupture trace follows a 040 trace from kilometer 0 to 4 and then follows a northward-convex bend upslope at its southwestern end, which coincides with exposed Paleogene gypsum and mollusk-bearing limestone (kilometers 4-5; Figure 7.9).

7.4.3. Description and kinematic interpretation of the surface rupture

The Nura surface rupture can be divided into six deformation zones that have characteristic tectono-geomorphic and structural features: zone A (beyond kilometer 0, see Chapter 7.3.2 for explanation), zone B (kilometer 0 to 2), zone C (kilometer 2 to 3), zone D (kilometer 3 to 4), zone E (kilometer 4 to 5), zone F (kilometer 5 to 6) (Figure 7.9). These zones are not directly related to the “blocks” described above, which merely delineate the measurements made during the field campaign. The width of the rupture zone varies along strike and is as much as 150 m wide in the central part (kilometers 3-4, Figure 7.9). In the wider parts of the fault zone, I refer to the northwestern and southeastern fault zone boundary (edge), as NW-e and SE-e, respectively (see Figure 7.10 to Figure 7.16). In the following, these zones are presented and interpreted individually from the northeast to the southwest.

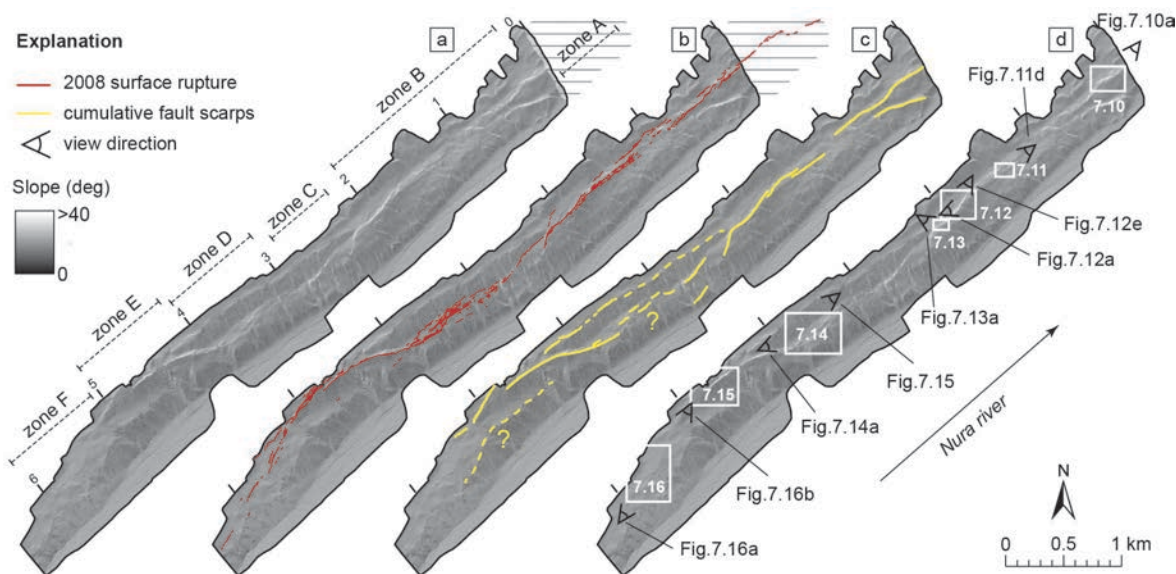


Figure 7.9 (a) Delineation of individual observation zones along the surface rupture (see text). Basemap is a slope-shade map (hillshade map overlain by slope map) of the Nura site derived from low-altitude unmanned aircraft vehicle (UAV) photography. Ticks denote kilometer marks along the rupture zone; 0 is at the northeast. (a) Surface-rupture traces of 2008 mapped in this study. Note how these align with older scarps of higher topography as outlined in (b). (c) Overview of the location and view direction of the associated DSM extracts and photographs in Figure 7.10 to Figure 7.16. See Appendix D, Figure D2 for high-resolution trace map.

Starting in zone A (beyond kilometer 0; Figure 7.9), the surface rupture follows a linear, 040 striking fault zone confined to a narrow band of discontinuous surface breaks that cut through a planar surface, only a few meters wide. The breaks exhibit little to no vertical offset and decimeter-wide horizontal opening, forming fissures that are several centimeters deep (*NU012*; Figure 7.10).

In zone B (starting at kilometer 0 of the DSM; Figure 7.9), the approximately 2-km-long part of the fault zone widens to ~100 m in its center, forming a narrow lens shape in map view. At the northeastern end of this zone the surface breaks along the SE-e of the lens cut mostly through the northwest-facing slopes of the older tectonic landforms (profiles P1 and P2; Figure 7.10). These breaks are dominated by *en echelon* ruptures with minor dextral components of motion (*NU100*; Figure 7.10). In the widest part of the lens (at ~1.5 kilometers; Figure 7.9), where the tectonic landforms are less pronounced, the SE-e widens and forms shallow grabens, ~50-cm-deep and up to ~30-m-wide; spatially, these coincide approximately with the highest part of the local relief (profiles P3 and P4; Figure 7.11). Here, these extensional structures along the SE-e are parallel to the NW-e of the lens. The surface breaks confining the NW-e of the lens were first discovered during digital mapping (Figure 7.11c). These are less pronounced, more discontinuous and cut topographically upslope tens of meters away and northwest from the surface breaks measured in field (blocks 1 and 2). The NW-e comprises predominantly faults with up to ~50 cm vertical offset and northwest-facing scarps (profile P5; Figure 7.11). At the southwestern end of zone B, the NW-e and SE-e seem to rejoin and the surface breaks coincide again with the tectonic landforms. Here, the breaks are more pronounced and continuous compared to those

described so far, forming extensional breaks in slope associated with collapsed scarp flanks along the northwest facing slopes of the tectonic landforms close to their crestal sectors (Figure 7.12a).

In zone C (kilometer 2-3; Figure 7.9), the surface breaks transition into less continuous, shorter *en echelon*-oriented surface cracks that cut through several meter-high landforms (profile P6; Figure 7.13). Within these zones of deformation broken boulders are offset dextrally (NU418; Figure 7.13), similar as observed at the beginning of zone B. The trace of the surface breaks that originates in zone B deviates from 040 to 010, following the tectonic landform, which dies out after ~130 m downslope towards the Nura River. Parallel, and approximately 300 m to the southwest, the surface breaks step over and cut through another 025 trending tectonic landform (Figure 7.9). Both structures are connected at the NW-e by a 040 trace of 2008 surface breaks, which offsets a planar slope surface by <50 cm, similar to the NW-e of zone B, where no unambiguously identifiable tectonic landforms are visible.

Farther southwest along trace in zone D, the fault zone widens forming another lens in map view. This lens is ~150-m-wide and 1000-m-long (kilometer 3-4; Figure 7.9), and it is the widest rupture zone along the 8-m-long surface rupture. In parts, farther downslope towards the Nura River, the SE-e of the lens comprises short, discontinuous ~50-cm-offsets with southeast-facing scarps (profile P8; Figure 7.14). In Zone D, the tectonic landforms are again less pronounced, similar to zone B. Numerous discontinuous surface breaks cut through the central area of the lens. However, in contrast to zone B here the breaks are oriented obliquely to the NW-e and SE-e of the zone (Figure 7.14). These surface breaks represent a series of near-vertical, sub-parallel and northwest-facing scarps with pronounced up to 1-m-high vertical offsets. These breaks deform the surface in a step-like pattern, are partly flanked by collapsed scarps and hanging-wall blocks (NUB033, NUB008; Figure 7.14); in places the scarps are part of up to 120-cm-deep fissures (NUB057; Figure 7.14). In the southwestern end of zone D, the topsoil layers are ripped open in a fan-like-manner over a bulged tectonic landform. Similar to zone B and C, the NW-e of zone D constitutes less pronounced, northwest-facing faults that offset a planar surface (profiles P7 and P8; Figure 7.14)

Zone E (kilometers 4-5; Figure 7.9) hosts the most pronounced tectonic landforms along the surface rupture, with cumulative offsets amounting to up to ~10 m (profile P9 and P10; Figure 7.15). Here, the rupture zone narrows to a several meters, deforms and offsets the north-facing slope of the tectonic landforms. Along the crest of these landforms steeply (60-80°) SE-dipping gypsiferous strata overlain by mollusk bearing limestone breccia crop out and seem to guide the surface rupture (Figure 7.15e and f).

The southwestern end of the Nura surface rupture bifurcates in zone F (kilometers 5-6; Figure 7.9). The northwestern splay was first discovered during digital mapping and could be traced for a length of approximately 400 m. Because the DSM terminates in this area, the nature of the continuation of the rupture beyond this point is uncertain. The splay to the south continues as a straight rupture for another ~1200 m (Figure 7.16). The northwest-facing surface breaks along this splay resemble those from zone A; they are less pronounced and more discontinuous, with gaps of tens to several hundreds of meters

(Figure 7.16). Approximately at kilometer 6 (Figure 7.9) the slope is offset by a 150-m-long and up to 80-cm-high, southeast-facing scarp (NUF030; Figure 7.16) that is associated with a spring. The surrounding area of ~80,000 m² comprises significantly denser vegetation cover and water availability, compared to the rest of the fault zone.

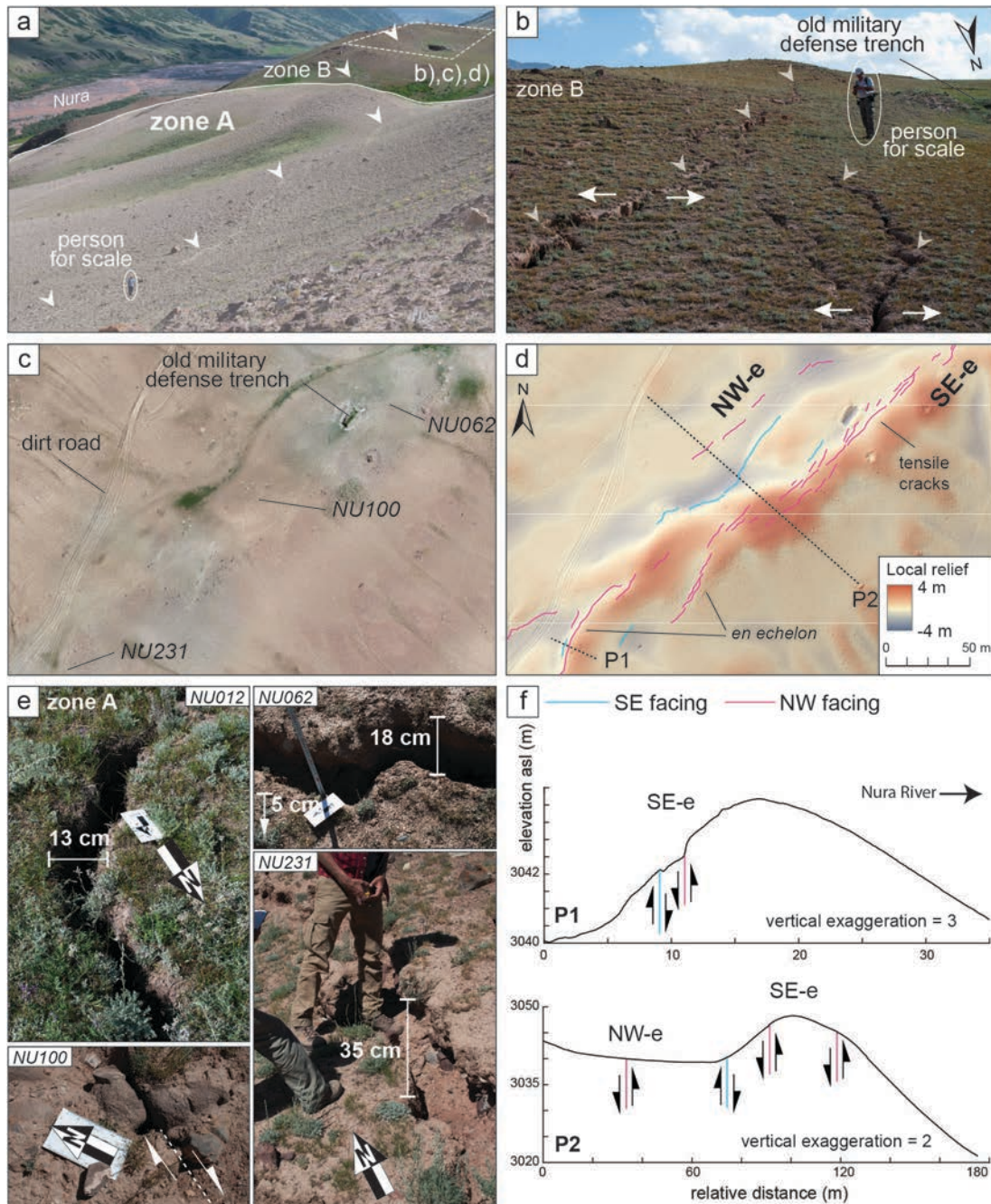


Figure 7.10 Zone A and northeastern end of zone B. See Figure 7.9 for locations and view directions. (a) Transition from zone A to B. (b) Fissures along the 2008 surface rupture. (c) Orthophoto of northeastern end of zone B generated from UAV. (d) Digital surface model overlay by a local-relief model and mapped surface-rupture traces. Dashed lines indicate topographic profile location. (e) Field photographs from surface-rupture trace measurements (see c for location and Table D1 in Appendix D). (f) Topographic profiles (location in d) extracted from DSM with inferred motion along the trace.

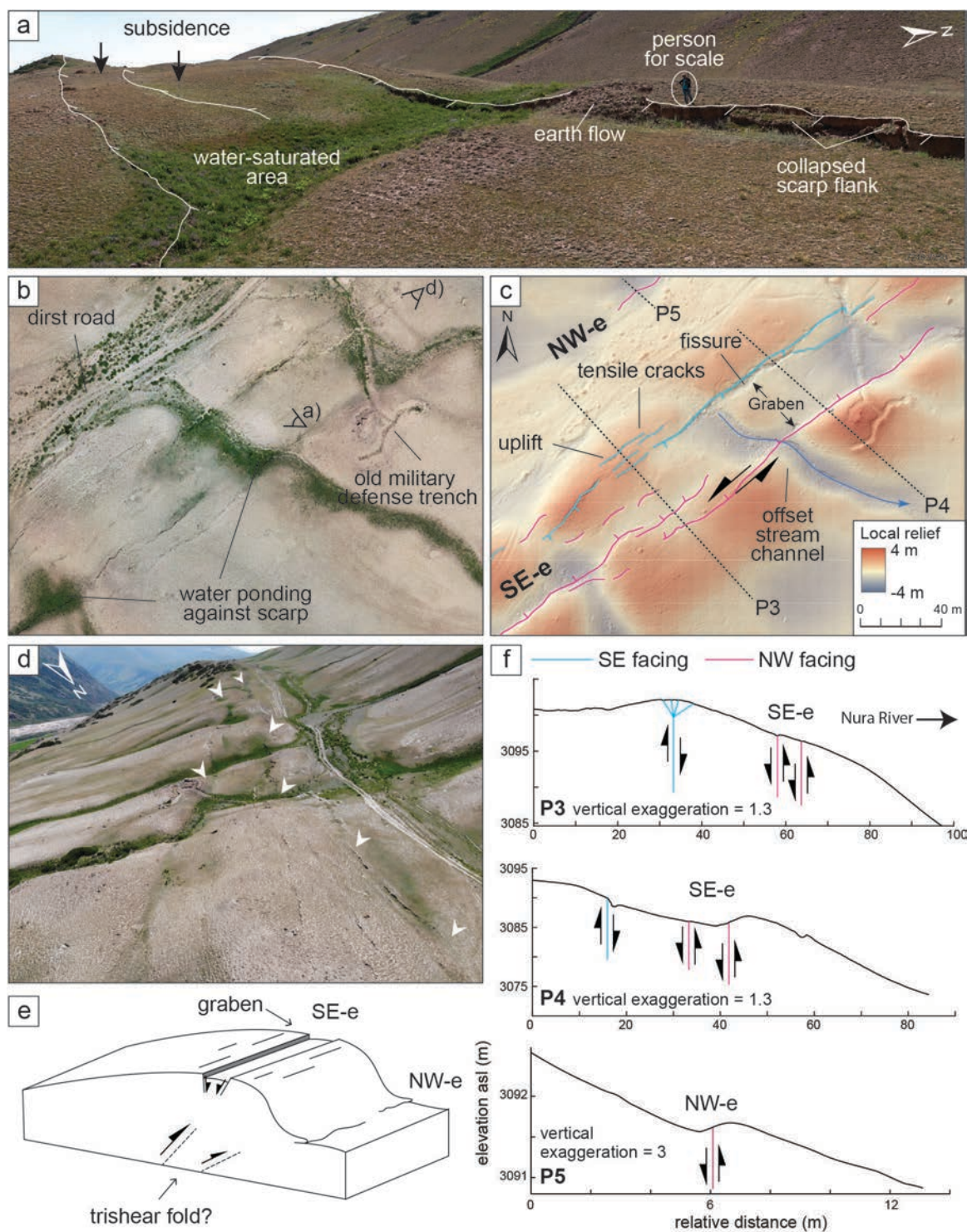


Figure 7.11 Central part of zone B. See Figure 7.9 for locations and view directions. (a) Graben at the crest of tectonic landform. (b) Orthophoto of central part of zone B generated from UAV. (c) Digital surface model overlain by a local-relief model and mapped surface-rupture traces. Dashed lines indicate topographic profile location. (d) Aerial photograph of 2008 surface rupture and resulting graben. (e) Sketch showing inferred structure of the surface-rupture zone. Modified after Philip & Meghraoui (1983). (f) Topographic profiles (location in c) extracted from DSM with inferred motion along the trace.

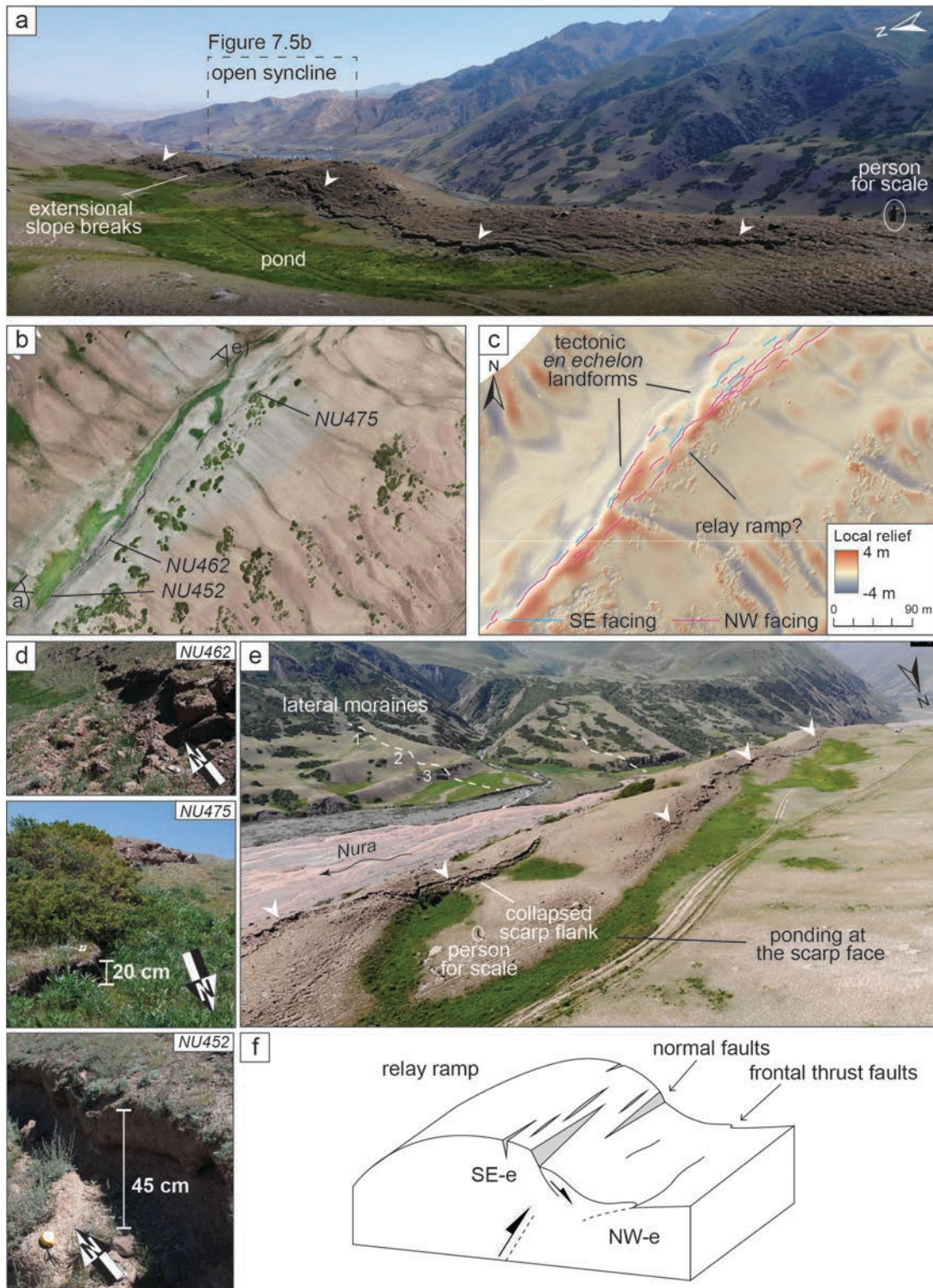


Figure 7.12 Southwestern end of zone B. See Figure 7.9 for locations and view directions. (a) Extensional slope breaks along tectonic landforms. (b) Orthophoto of southwestern end of zone B generated from UAV. (c) Digital surface model overlain by a local-relief model and mapped surface-rupture traces. (d) Field views of surface-rupture trace measurements (see b for location and Table D1 in Appendix D). (e) Aerial photograph of the 2008 surface rupture. (f) Sketch showing the inferred structure of the surface-rupture zone. Sketch modified after Philip & Meghraoui (1983).

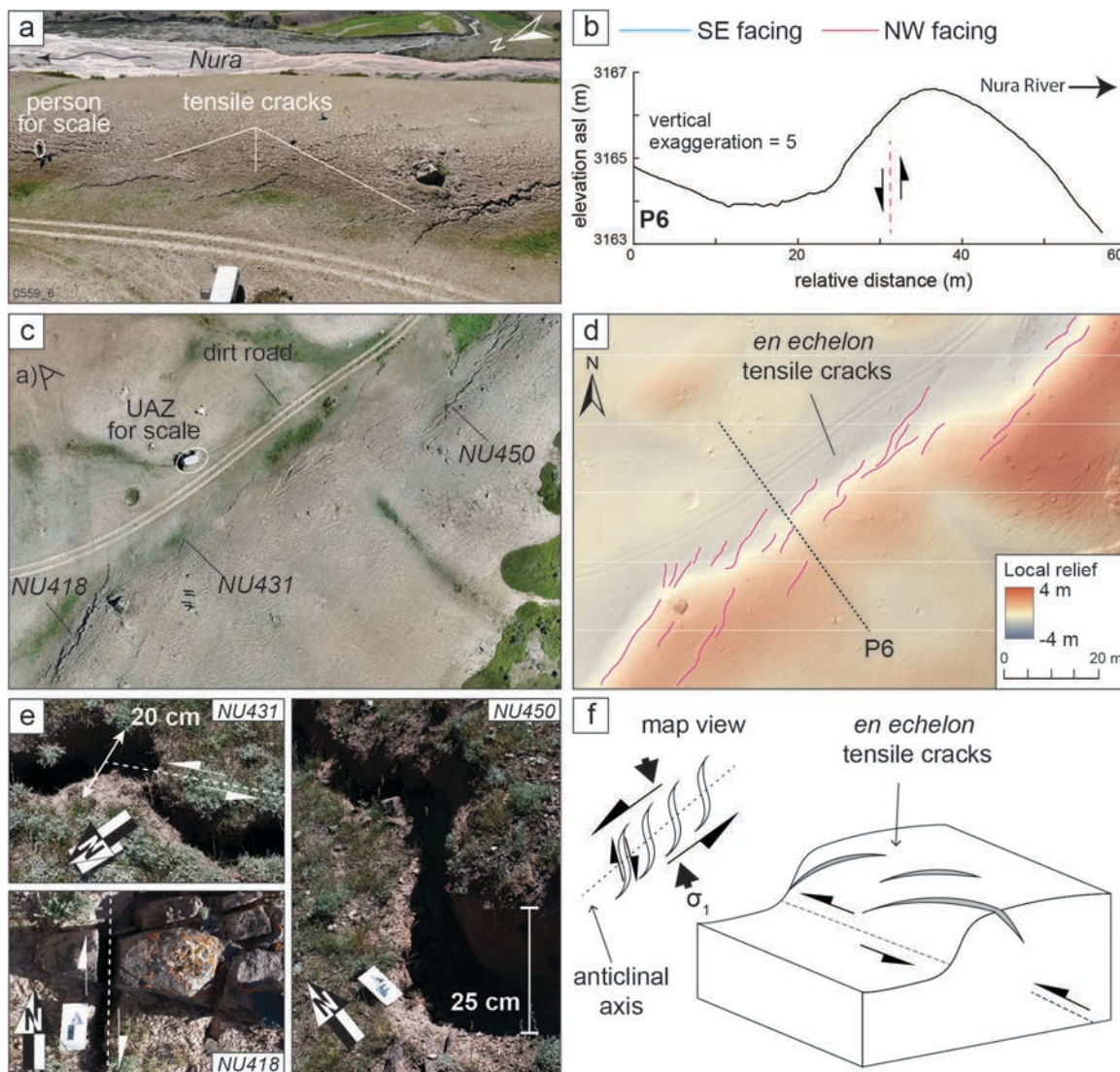


Figure 7.13 Northeastern end of zone C. See Figure 7.9 for locations and view directions. (a) Surface rupture of the Nura earthquake. (b) Topographic profile (location in d) extracted from DSM with inferred motion along the trace. (c) Orthophoto of northeastern end of zone C generated from UAV. (d) Digital surface model overlain by a local-relief model and mapped surface-rupture traces. Dashed lines indicate topographic profile location. (e) Field views from surface-rupture trace measurements (see b for location and Table D1 in Appendix D). (f) Sketch showing inferred structure of the surface-rupture zone. Modified after Philip & Meghraoui (1983).

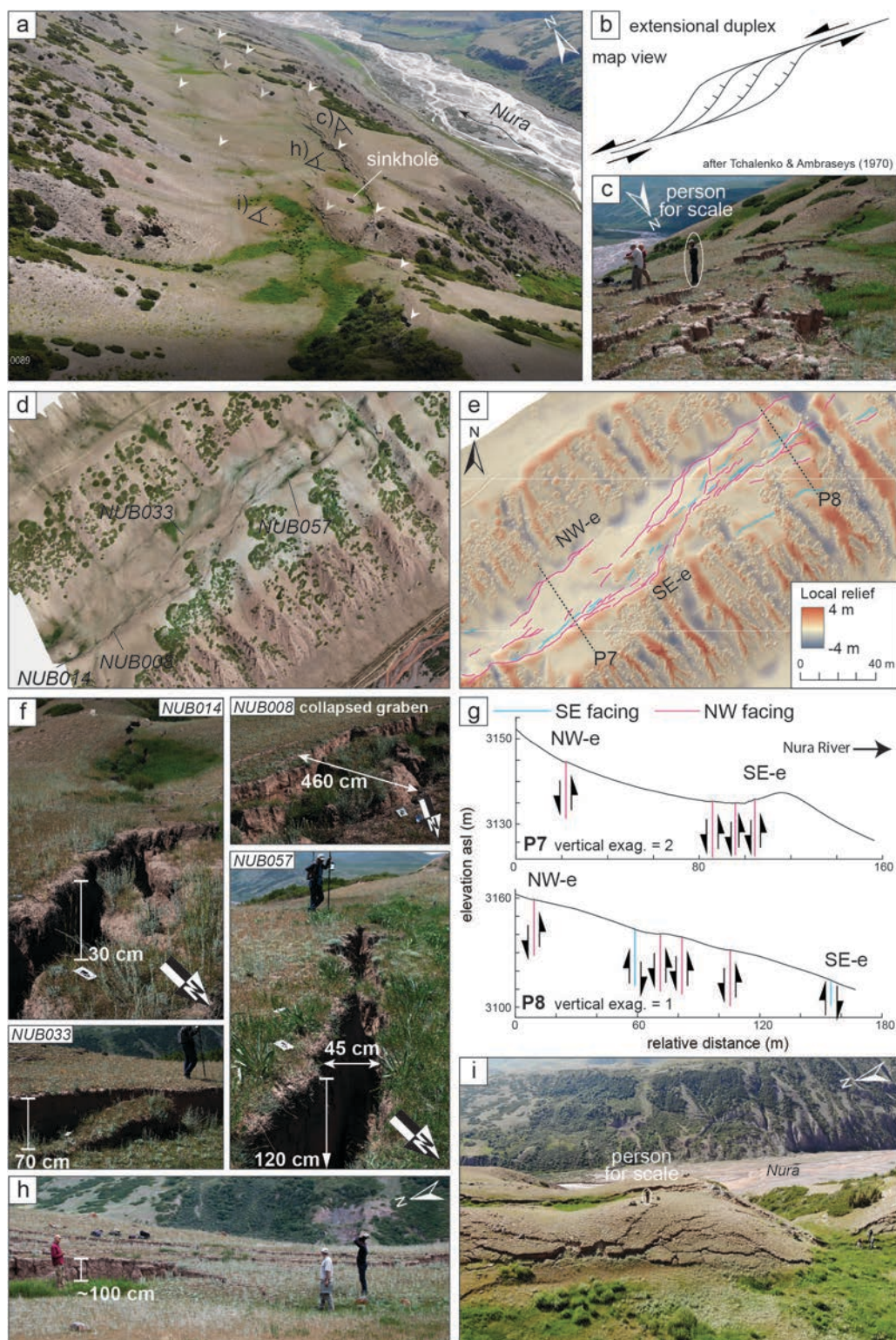


Figure 7.14 Zone D. See Figure 7.9 for locations and view directions. (a) Aerial photograph of the 2008 surface rupture. (b) Sketch showing the structure of the surface-rupture zone. (c) Complex fracturing along SE-e. (d) Orthophoto of zone D generated from UAV. (e) Digital surface model overlain by a local-relief model and mapped surface-rupture traces. Dashed lines indicate topographic profile location. (f) Field views of surface-rupture trace measurements (see (d) for location and Table D1 in Appendix D). (g) Topographic profiles (location in d) extracted from DSM with inferred motion along the trace. (h) Step-like trace pattern. (i) Fan-like extension pattern over tectonic landform.

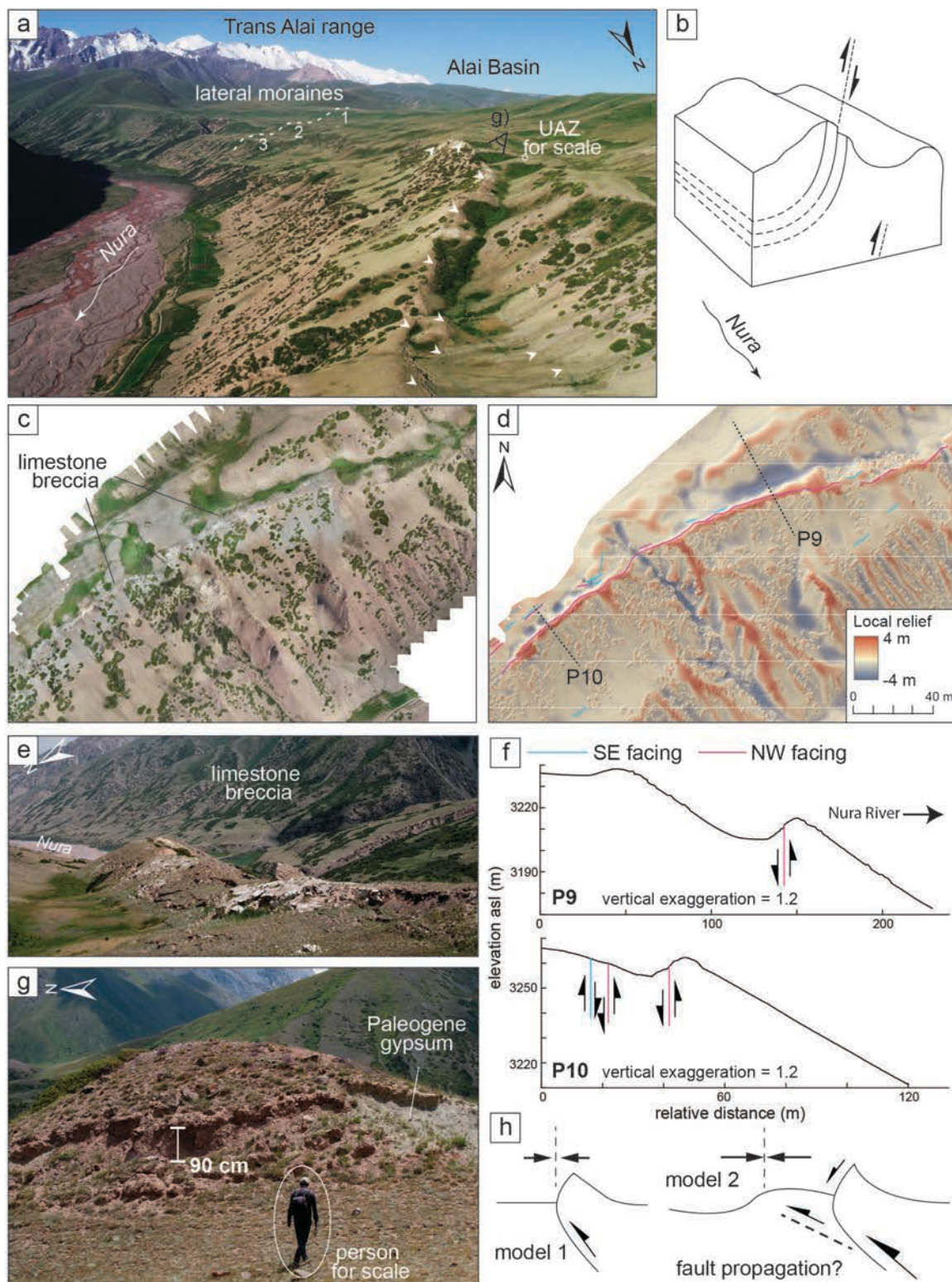


Figure 7.15 Zone E. See Figure 7.9 for locations and view directions. (a) Aerial photograph of distinct tectonic landform in zone E. (b) Sketch of the observed outcrop strata and inferred subsurface structural relation. (c) Orthophoto of zone E generated from UAV. (d) Digital surface model overlain by a local-relief model and mapped surface-rupture traces. Dashed lines indicate topographic profile location. (e) Limestone breccia along the crest of the tectonic landform. (f) Topographic profiles (location in d) extracted from DSM with inferred motion along the trace. (g) Extensional slope breaks along the tectonic landform. (h) Sketch of the structure of the surface rupture zone modified after Philip & Meghraoui (1983).

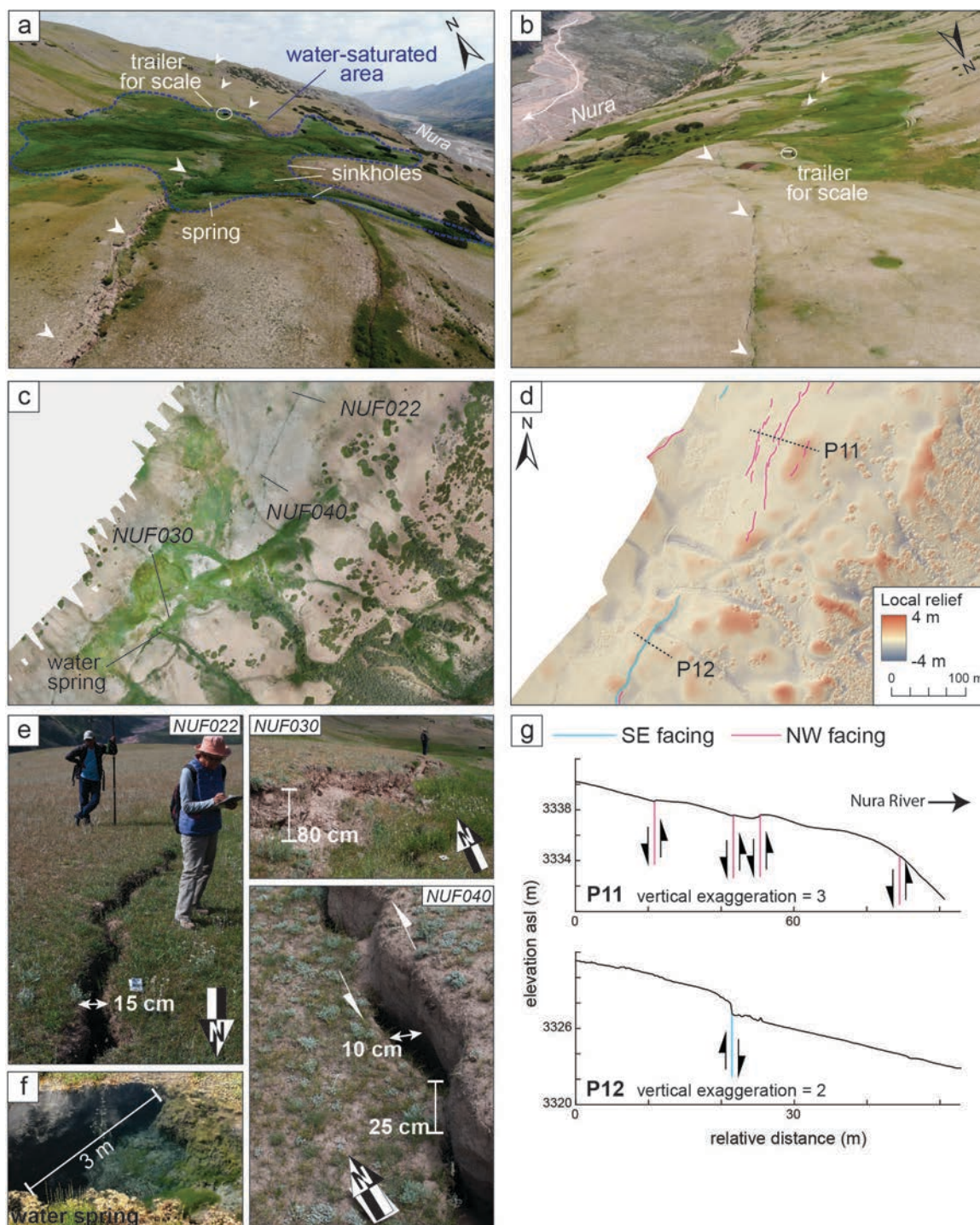


Figure 7.16 Zone F. See Figure 7.9 for locations and view directions. (a and b) Aerial photographs of the 2008 surface rupture form opposing viewing angles. (c) Orthophoto of zone F generated from UAV. (d) Digital surface model overlain by a local-relief model and mapped surface-rupture traces. Dashed lines indicate topographic profile location. (e) Field views of surface-rupture trace measurements (see c for location and Table D1 in Appendix D). (f) Spring situated along a SE-facing rupture trace. (g) Topographic profiles (traces in d) extracted from DSM with inferred motion along the trace.

7.4.4. Vertical separation

In Chapter 7.4.1, I reported on vertical offset values measured during the field campaign in 2018. I cautioned that these may not reflect the total amount of the vertical offset (net slip), especially in areas of previously undiscovered zones of distributed splay faulting (i.e., zones B and D). The topographic profiles presented in the previous chapter demonstrate in more detail the lateral distribution of surface offsets (profiles P1 to P12; Figure 7.10 to Figure 7.16). To provide a distribution of total vertical offset along the fault zone of the 2008 event, I use the DSMs to model individual vertical offsets along 50-m-spaced scarp-perpendicular topographic profiles, which can be added together subsequently to provide the associated net slip for each profile (Figure 7.17). Moreover, I tried to determine the cumulative offset of the apparent tectonic landforms, which show a clear relationship with the 2008 surface rupture.

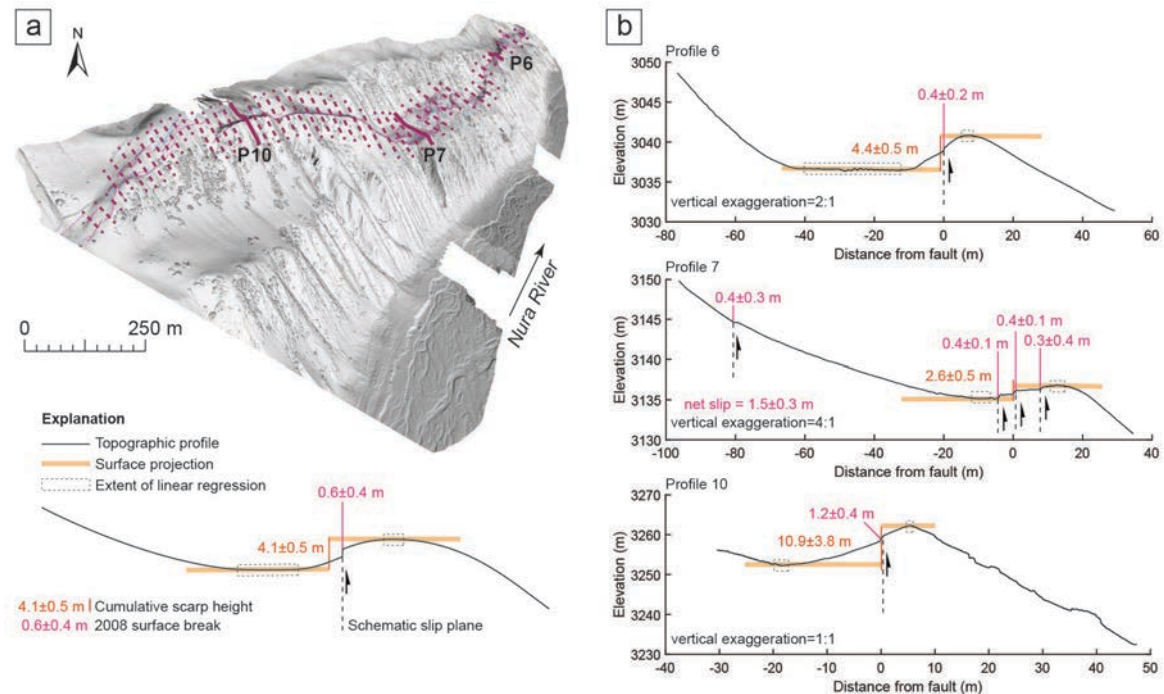


Figure 7.17 Selected topographic profiles along the 2008 Nura earthquake surface rupture. (a) Location of topographic profiles displayed on a shaded relief of the DSM visualized in 3-D. Dashed lines show schematic distribution of all 50-m-spaced topographic profiles. (b) A subset of vertical separation (VS) measurements along the 2008 surface breaks and modelled cumulative scarp heights along these sectors. Profile numbers refer to profiles examined in the previous Chapter 7.4.3.

Because faulting offsets and deforms the topography upslope, it is not entirely clear which section of the hanging wall and footwall represent the unfolded far-field surface. In particular, the step-like slope of the northern banks of the Nura River could represent the vestiges of several lateral moraine generations, such as those observed on the southeastern flanks of the river valley. Thus, the offset would be much less than if the slopes were assumed to have been without such “steps” prior to faulting and/or folding. Without further information, however, I only determine the approximate scarp height (Yang et al., 2015),

i.e., the offset between the planar surface of the “step” and the tip of the elevated tectonic landforms (Figure 7.17).

My analysis focused on the ~6-km-long section of the 2008 surface rupture that lies within the area of the DSMs presented above (see Figure 7.9). The distribution of the VS net slip along the NW-facing surface breaks range between 0.1 to 2.1 m (~0.5 to 3.3 m including uncertainties), and shows three apparent peaks; two in zone B (kilometers 0 to 1, and 1 to 2), and one in zones D and E (kilometers 3 to 5; Figure 7.18). The peak apexes increase from northeast to southwest, roughly proportional to the width of their almost uniformly distributed VS (Figure 7.18).

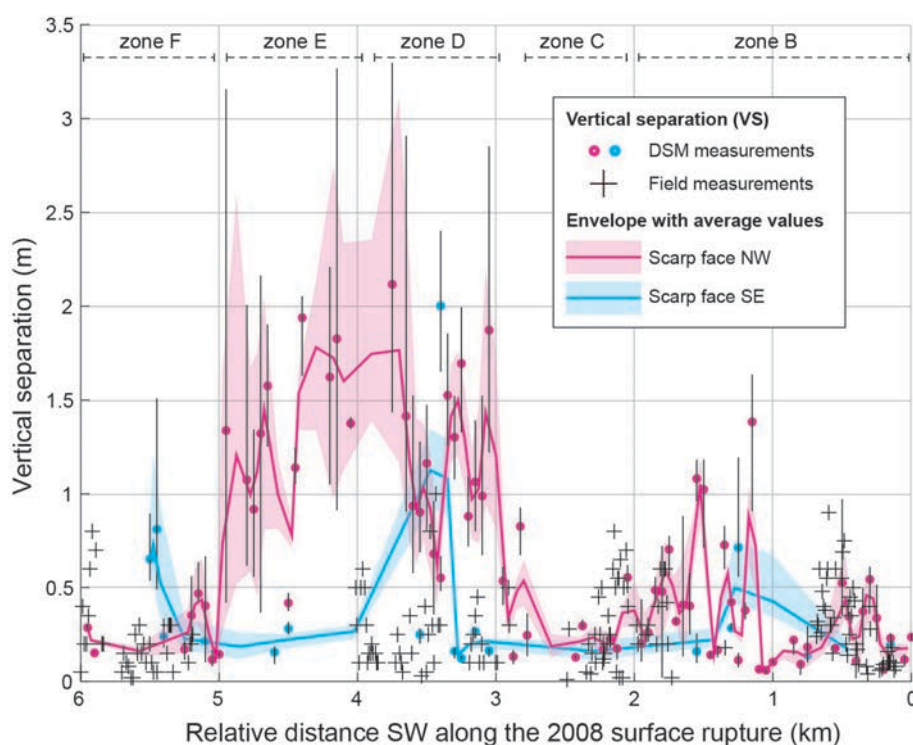


Figure 7.18 Vertical separation (VS) along the 2008 Nura earthquake surface rupture. The relative distance along the DSM is indicated (see Figure 7.9). Plotted are: remotely measured VS (pink and blue) compared to field measured VS (black crosses). Vertical lines indicate min-max VS range from multiple measurement iterations (see Chapter 3). Note that remotely measured VS represent the net slip calculated from all offsets along each topographic profile. Shaded areas show a moving average between neighboring points with an envelope of the corresponding minimum and maximum average value.

When comparing the remotely measured VS with the VS measurements from field, I note that the measurements in zones B, C and F agree well within the uncertainties. In contrast, in zone D where the fault-splay distribution is widest, the field measurements underestimate the remotely measured net slip by ~0.5-1.5 m (kilometers 3 to 4; Figure 7.18). Consequently, the overall geometry demonstrates a clearly asymmetric distribution towards southwest, which is in contrast to the previously assumed asymmetry to the northeast (see Chapter 7.4.1). The mean VS associated with the reverse faulting sense of motion

along the 6-km-long section of the 2008 rupture is 0.6 ± 0.2 m. Given the global fault-scaling relations (e.g., Wells & Coppersmith, 1994) for moment magnitude and surface rupture length or average displacement, a moment magnitude is obtained for the 2008 Nura event based on these surface rupture characteristics of M_w 6.0 and 6.6, respectively.

The observations in the previous chapters have already indicated that the 2008 surface rupture has an apparent relationship with the tectonic (cumulative) topographic landforms it ruptured. The examination of the scarp height of these presumed prehistoric fault scarps reveals a compound nature with the 2008 scarp. 56 scarp height measurements of the cumulative structures range from 0.4 to 9.8 m (Figure 7.19). Similar to the 2008 VS, the distribution of cumulative VS shows three distinct peaks, which appear to generally coincide with the peaks of the 2008 break. However, unlike the 2008 distributions, the maxima of the cumulative VS distribution peaks are approximately the same.

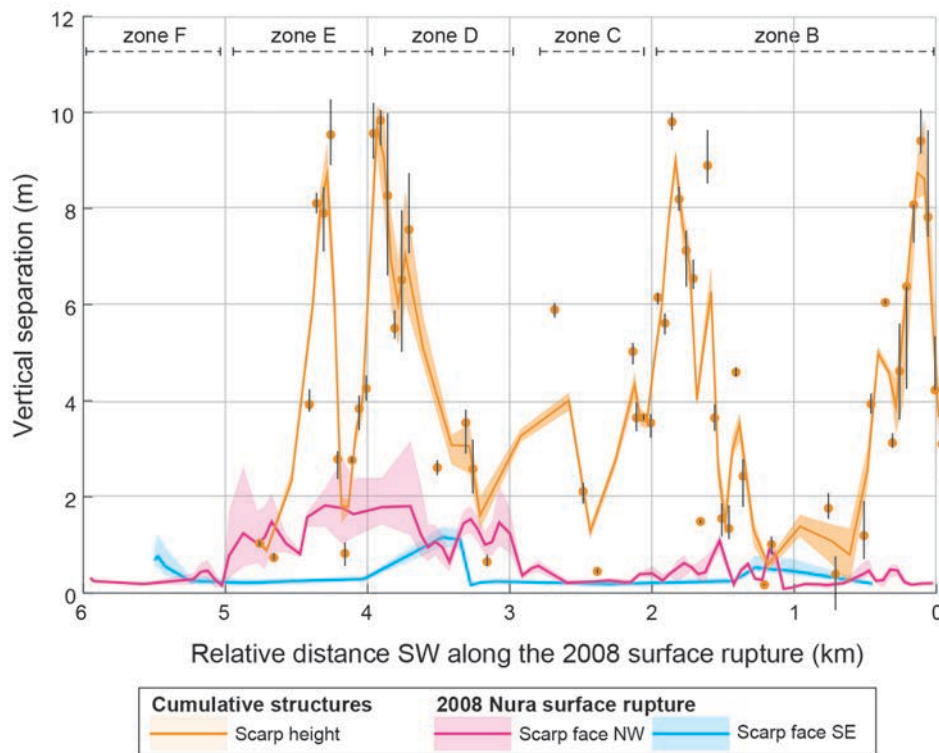


Figure 7.19 Comparison of the scarp-height distribution of old tectonic landforms with the net slip VS associated with the 2008 event surface rupture. Vertical lines indicate min-max VS range. Shaded areas show a moving average with a max/min envelope.

7.5. Possible secondary effects associated with the 2008 Nura surface rupture

During the field campaign and from remote DSM analyses along the 2008 Nura fault zone, fault-parallel sinkholes, ponded sediments on the footwall of the fault, and different types of mass-movement deposits were observed. The sinkholes are circular in map view ($\leq 20 \text{ m}^2$), the ponded areas correspond to sag ponds against the scarp and involve areas of $\leq 400 \text{ m}^2$, and the most extensive landslide deposits are several meter thick and cover areas of $\leq 13000 \text{ m}^2$ (Figure 7.20).

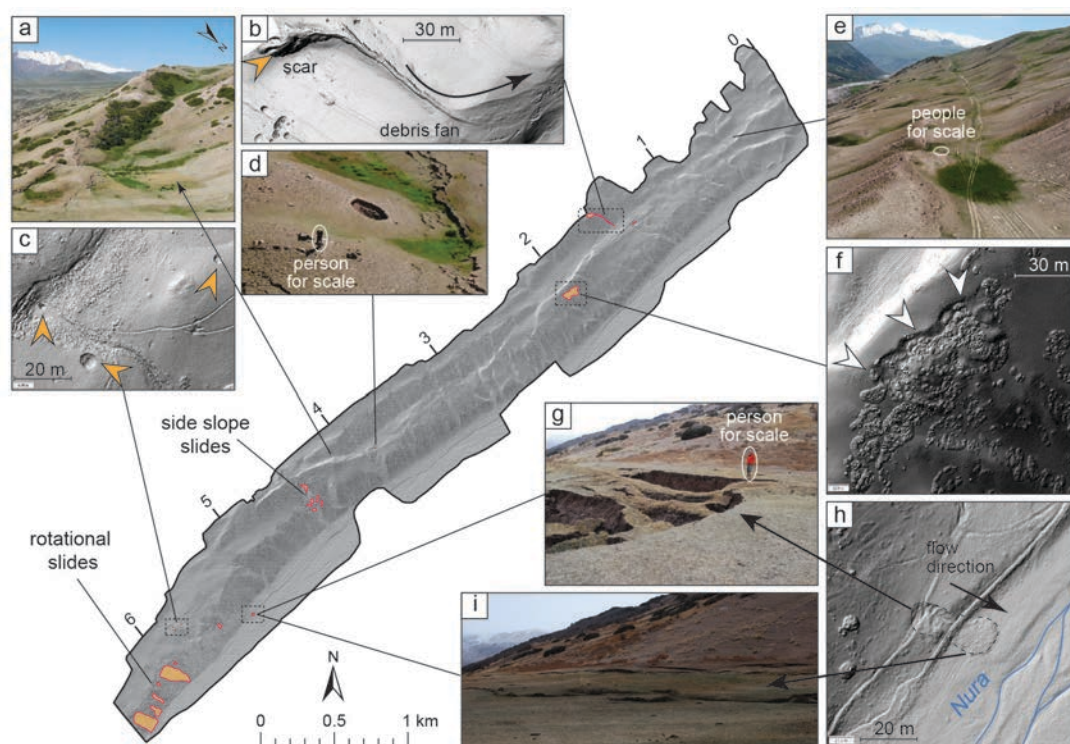


Figure 7.20 Secondary effects along the 2008 Nura earthquake surface rupture. Close-up images are from DSMs and UAV photographs: a) sag-pond formation in zone F; b) debris flow; c+d) sinkholes in zone E and F; e) sag-pond formation in zone B; f) slump slide; g-i) earthflow documented in 2010 after the 2008 earthquake. Photographs of the landslide head (g) and toe (i) sectors, kindly provided by B. Schurr (GFZ Potsdam).

Most landslides are situated topographically below the 2008 surface rupture in the high slope areas of the hanging wall of the IrkF, with an increased occurrence at the southwestern end and beyond the rupture zone (kilometer 6; Figure 7.20). Right at the surface rupture zone (kilometer 2; Figure 7.20) a rotational slump ($\sim 4500 \text{ m}^2$) was generated and directed toward the Nura River. Farther southwest, the slopes of a major (in regional context; see next section) stream channel that cuts through zone E (kilometer ~ 4.5 ; Figure 7.20), are associated with several slides that were generated along the valley flanks ($\sim 500\text{-}1000 \text{ m}^2$). One landslide ($\sim 500 \text{ m}^2$) was documented by B. Schurr (GFZ Potsdam) and colleagues during their field campaign in 2010; the slide is recognizable in the DSM of this study. It cuts through

the youngest terrace of the Nura River and its morphology resembles an earthflow with a fragmented surface at the head scarp and a toe area characterized by multiple lobes (kilometer \sim 5.5; Figure 7.20). Along the Nura River farther southwest a number of closely spaced rotational slides cut the lateral slopes of the river (kilometers 6-6.5; Figure 7.20).

Along the upper slopes (topographically above the rupture zone), within the footwall of the IrkF one \sim 350-m-long debris flow produced a debris fan, which appears deflected and banked against the rupture zone (kilometer \sim 1.5; Figure 7.20). In the footwall of the rupture zone, especially where the rupture zone is associated with old cumulative fault structures a noticeably increased vegetation density indicates sagpond formation against the scarp (e.g., kilometers 0.5 and 4-5; Figure 7.20). Within the footwall of the fault zone, numerous collapse sinkholes are observable (kilometers 3-6; Figure 7.20) and appear to be spatially related to the Paleogene gypsum strata.

The size of all of these features is sufficiently large to be recognized in freely available Google Maps satellite imagery (Image© 2022 Maxar Technologies). Importantly, the comparison of pre- and post-2008 imagery revealed that except for one landslide documented in 2010, the formation of all other features pre-dates the 2008 Nura earthquake.

7.6. Stream network analysis

The topographic slopes in the lateral moraine deposits are \sim 25° to 35° steep, with no major difference topographically below and above the fault zone. The slopes of the lower gradient “step” surfaces are typically $<$ 15°. The stream-channel network extracted from the DSMs of the Nura site reveal NW-SE-draining streams that join downslope with the SW-NE-flowing Nura River (Figure 7.21).

The stream channels draining the Nura site are relatively straight, closely spaced ($<$ 100 m) and barely branched. Their channel geometry and flow direction (derived using TopoToolBox; Schwanghart & Scherler, 2014) are closely related to the topography of the old cumulative fault structures. Most stream channels crossing the fault zone are disrupted, especially in the sectors where the cumulative structures are most pronounced. In these sectors, the streams in the upper drainage areas have a trellis pattern and are adjusted to the fault scarp by flowing at right angles and parallel to it. In the southwestern sector of the fault zone (beyond kilometer 5) knickpoints correlate with the “steps” in the lateral moraine deposits, whereas towards the northwest the knickpoints appear to be farther downslope, away from pronounced topographic steps (Figure 7.21), especially in areas where fluvial channels seem to be beheaded due to faulting or folding.

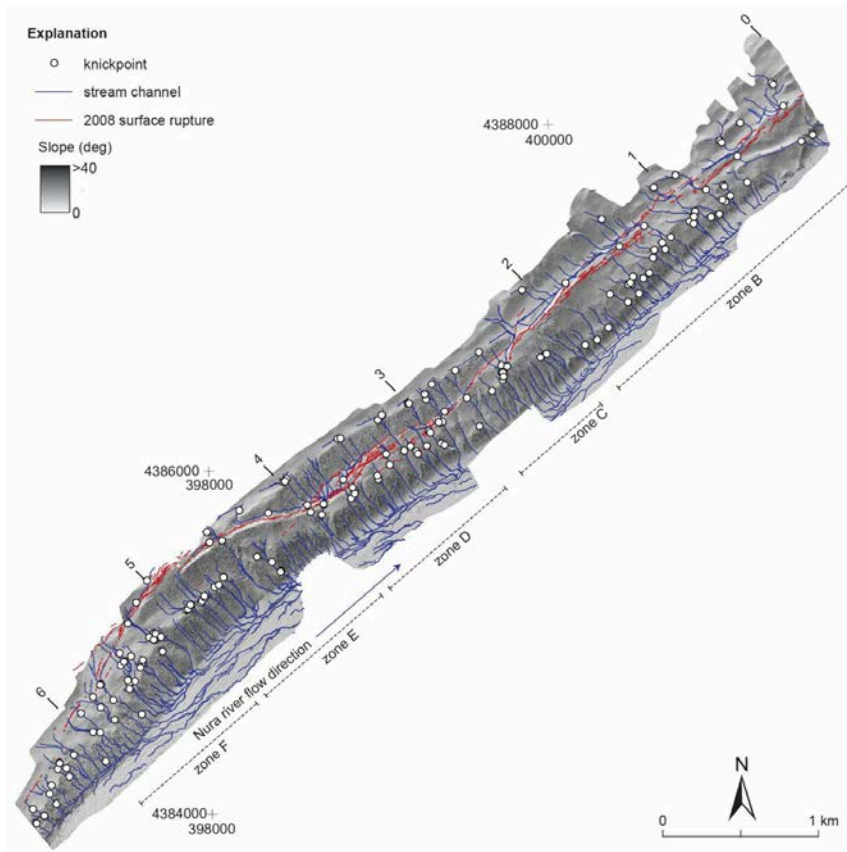


Figure 7.21 Stream-channel network and knickpoints (white circles) in the Irkeshtam fault-zone area along the 2008 surface rupture plotted on a shaded relief map. Tick marks denote kilometers along the rupture zone.

7.7. Summary

Surface breaks and ground-deformation effects from the 2008 Nura earthquake were mapped and documented locally in the field, and supplemented with more comprehensive data from aerial photographs and high-resolution geodetic digital surface model products. The combination of these observations and maps provides a substantial data set that allows detailed analysis of surface breaks and forms the basis for kinematic and seismotectonic interpretations for the fault in question, and the tectonic setting to which it belongs.

Chapter 8

Discussion and conclusions

This part of the thesis provides a multi-temporal description of the seismogenic behavior along a segmented mountain front in an active continental collision setting – the frontal sector of the Northern Pamir. Such tectonic settings are considered the most challenging in terms of seismogenic source zone and rupture-behavior characterization; thus, an understanding of the rupture mechanisms is fundamental for the assessment of seismotectonic segmentation in compressional environments. A geomorphic fault-zone study of tectonically active landforms combined with regional paleoseismology places constraints on the rupture behavior and seismogenic potential along the active Northern Pamir collision zone in southern Kyrgyzstan. This chapter discusses my results that are relevant for the kinematics and the overall impact of late Pleistocene to Holocene deformation along the leading edge of the Pamir orogen. I will also present implications that can be drawn from the correlation of long-term and present-day deformation characteristics in this region.

8.1. The central Pamir Frontal Thrust

8.1.1. Paleearthquake allocation and potential obstacles

In most terrestrial environments the reconstruction of a paleearthquake sequence relies on distinguishing between tectonic and depositional features in trench exposures. I emphasize that the stratigraphic and geomorphic nature of the faulted alluvial fans that cover fluvial deposits in my study area preserve important characteristics related to the accumulation of colluvium. In most cases within the alluvial fan, unit 2 constitutes the source material for the colluvial deposits that I identified in my exposures. Unit 2 is a thin (10–50 cm) layer composed of compacted fine to medium sand. The original fan slopes are $< 4^\circ$. If the age-thickness relationship of unit 2 is considered, the sedimentation rates in this area must be rather low. Mobilization of large amounts of debris from this unit during strong ground motion is thus not very likely in this environment. Considering the well-preserved, present-day surface of the Qt_3 terraces, I assume that extensive episodes of erosion have decreased during the last ~ 7.3 ka (see also Discussion below); neither do I consider the formation of the colluvial deposits to have been triggered by pronounced weathering or degradation related to storms or wet episodes (e.g., Rizza et al., 2019a). Instead, I relate colluvial strata observed in my study area (i.e., maximum thickness of 50 cm of mostly reworked silty sand) to surface faulting, scarp formation, and subsequent erosion and deposition. Consequently, I suggest that most of the colluvium represents weathered material generated by transport of scarp material from the new fault tip during the immediate postseismic interval of a ground-rupturing earthquake.

Reliable age models from past earthquakes require correct sampling of high-quality, datable material and rigorous interpretation of results. Typical targets for dating earthquakes in dip-slip fault exposures are colluvial-wedge deposits. These, however, are often prone to ambiguous age determinations, because (1) luminescence samples might be only partially bleached, and (2) in case of radiocarbon dating, inherited ages from reworked organic material might get incorporated into the deposits. As discussed above, in my trenches only a limited (base) part of the colluvial strata presumably results from co-seismic hanging-wall collapse, and only few of them seem to represent “pure” co-seismic colluvial wedges (i.e., T1-C3a and T5-Cb). I interpret that most of the colluvial deposits in the analyzed trenches result from processes described above and are similar to those that formed the top soil layers (TS) documented in the logs. Therefore, I assume that their deposition was rather slow and distributed through time, which allows sufficient bleaching of the materials.

Nevertheless, to avoid sampling of partially bleached material for IRSL dating, it has been recommended to sample the toe of the colluvial deposits (long transport distances) and not the materials immediately abutting the fault (short transport distances) (Gray et al., 2015). At trenching sites T1 and T3 only a limited portion of the toe was exposed, and at T5 the toes of different colluvial deposits merge with unit 2, thus, are not separable. Consequently, in these cases we were forced to sample the colluvial strata proximal to the fault, and collected the sample from the upper part of these colluvial deposits assuming a higher probability for interseismic deposition (see Discussion above), which then was used as maximum age for the subsequent event horizon. Finally, samples (T3: L2, L3, L4, L5, L6, L7; T5: L4e) that do reflect partial bleaching, as shown by a significant offset – more than two times higher – between the pIR and IRSL ages (Gray et al., 2015), were all retrieved from the fluvial deposits (unit 1) or deposits related to sediment-laden water columns (i.e., pond; unit 3). Such material may be associated with poor bleaching of luminescence signals due limited sunlight exposure and short residence times in riverbeds (e.g. Smedley et al., 2019; Ishii et al., 2022). Although the ages derived from these samples are generally consistent within their stratigraphic context and along the central sector of the Pamir Frontal Thrust (cPFT), and thus seem reliable, I cannot fully exclude a certain overestimation of their age range.

To reduce ambiguity of the IRSL ages, we also sampled organic material for radiocarbon dating. In case of trench T1, the ages are consistent and I am confident of the reliability of the results. In the case of trenches T2, T3 and T5, however, my radiocarbon samples (T2: Rb1e, R11e, R13e, R4e, R5e; T3: R2e; T5: R2e to R7e, R1n), yielded ages younger than those from IRSL. Because of additional chronological and stratigraphical inconsistency between these samples themselves, I have omitted these radiocarbon ages. Except for Rb1e (T2), all these samples contain only small amounts of charcoal, which may lead to erroneous dating. However, I suspect that the young ages result from either (1) poor sampling, where dark root fragments were erroneously classified as charcoal, (2) contamination due to downward penetration of younger roots or the influence of younger humic acids, or (3) bioturbation processes, where seasonal freeze-thaw phases or burrowing organisms within these units transported fine material

into the underlying units (e.g., Walker, 2005). The first suggestion may apply to material sampled below 50 cm depth, whereas the second and third issues apply to the material sampled at shallow depths of < 20 cm.

8.1.2. Completeness of the paleo-earthquake chronology along the central Pamir Frontal Thrust

My observations from five sites across different sectors of the cPFT provide new data on the effects of surface-rupturing paleoearthquakes with detailed slip histories. An overlap in earthquake timing based on observations from multiple trenches indicates extensive ruptures along the cPFT. My refined earthquake chronology documents six surface ruptures (E6–E1; old to young) since the late Pleistocene (<17 ka). Before I further address aspects of the seismogenic behavior along the cPFT, I assess the completeness of the modeled earthquake record. The temporal evidence is generally less well-constrained for events older than 3 ka. Lack of data is a common problem observed in paleoseismological studies (e.g., Nikonov, 1988; Nicol et al., 2016), which impacts the validity of the interpreted earthquake sequence. I compare my documented rupture evidence and associated timing with earthquake-related features (e.g., scarps, fissures, tension gashes) reported by Nikonov (1988) (Figure 8.1b and e). However, I caution that the chronology provided by Nikonov (1988) is partly based on lichenometry and the timing of the emplacement of mass-movement deposits is only inferred to have been seismically triggered.

My stratigraphic analysis did not reveal evidence for the A.D. 1978 M_w 6.6 Zaalai event in any of the trenches despite previous suggestions that ruptures partly propagated into the central segment during its aftershock sequence (Nikonov et al., 1983; Arrowsmith & Strecker, 1999). Instead, the MRE (E1) was dated to 0.8 ± 0.2 ka and was only visible at the western end of the cPFT (Figure 8.1), with strong evidence in trench T2. The penultimate event (E2) occurred at 1.5 ± 0.1 ka (Figure 8.1). The consistency and large number of rupture indicators for E2 in all five trenches, as well as the robustly modeled earthquake timing suggest a rupture extent of ≥ 35 km (full-segment length). Interestingly, three earthquake ages reported by Nikonov (1988) from the western and eastern transfer zones range from 1–2 ka, and thus overlap with the E2 event identified in this study (Figure 8.1). By including these observations, I infer a possible rupture extent of as much as ~ 65 km during E2. Event E3 (2.2 ± 0.2 ka) was modeled based on strong evidence and good timing in the intermediate Komansu site (T4), but weak evidence and ambiguous timing constraints from the westernmost trench T1. The E3 event overlaps with one earthquake age with a large uncertainty reported by Nikonov (1988). Consequently, the rupture extent of E3 is uncertain. This earthquake might have ruptured discontinuously and/or only a small portion of the cPFT (Figure 8.1).

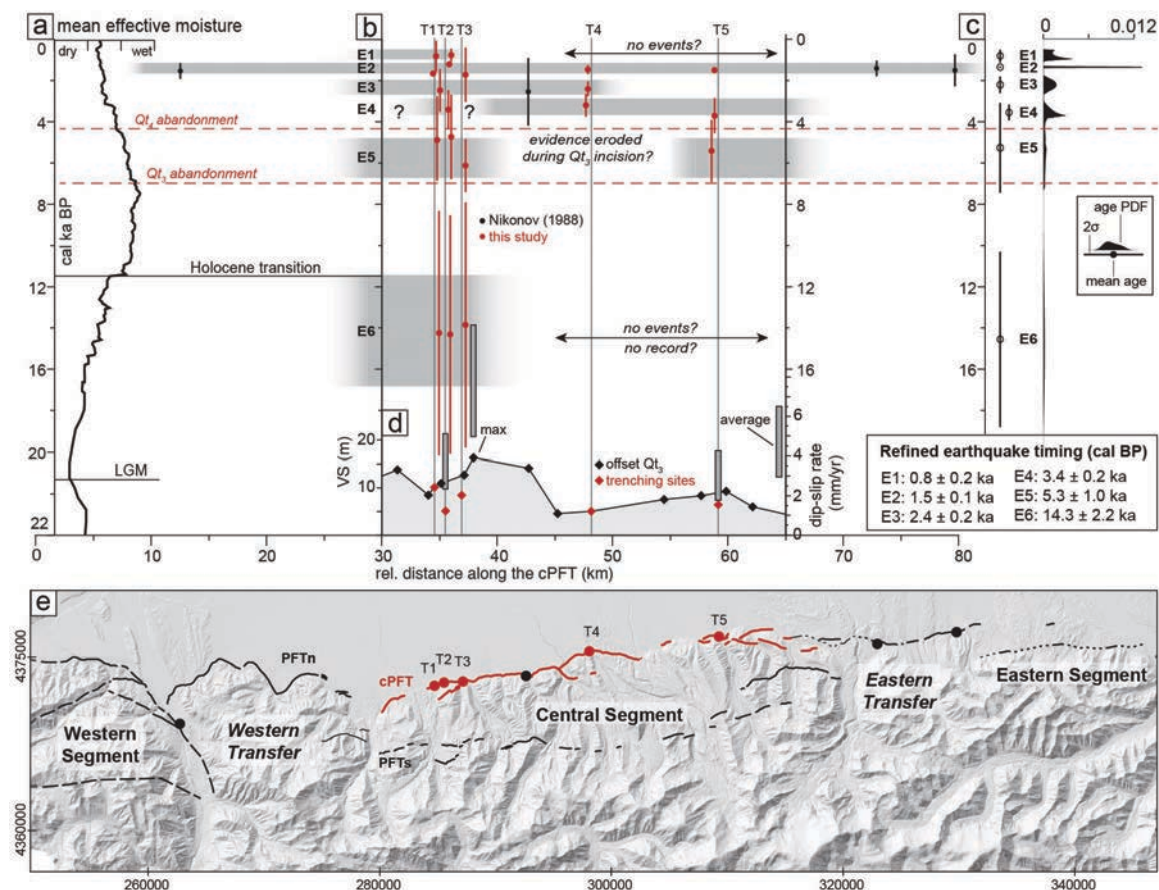


Figure 8.1 Summary of the paleoearthquake data for the PFT. (a) Mean effective moisture from Central Asia modified from Herzschuh (2006). (b) Correlation of modeled earthquake site PDFs (red filled circles $\pm 2\sigma$) from five trenching sites and selected earthquake ages from Nikonov (1988) (black circles $\pm 2\sigma$) along the PFT with locations in (e). Shaded areas in the background indicate the possible rupture extent of each earthquake along the fault. Vertical width represents the refined 1σ uncertainties of the product PDFs from (c) the central PFT earthquake model (black PDFs, with mean $\pm 2\sigma$) based on the correlation (see Figure 7). (d) Cumulative vertical separation from Chapter 4. Gray boxes show estimated Holocene (<6 ka) dip-slip rate from cumulative VS estimates from Achyk-Suu (T2), maximum, Tashkungey (T5) and average (from left to right). (e) Hillshade image based on TanDEM-X data. Red and black lines indicate the fault trace (solid) and approximate trace (dashed) of the cPFT and PFT_{N+S}, respectively. Black circles indicate locations of earthquake evidence from Nikonov (1988).

My interpretation regarding earthquake E4 (3.6 ± 0.2 ka) results from solid evidence in T2 and T5, weak evidence in T4, and overlapping earthquake PDFs from all three trenching sites (T2, T4, T5) spanning different sectors of the cPFT (Figure 8.1). I did not find evidence in either T1 or T3, despite their vicinity to T2. The relative age constraints and weak evidence in T1 and generally ambiguous earthquake indicators in T3 for events older than 2 ka, might result in an incomplete, less reliable earthquake chronology at these sites. In the case of E5 (5.3 ± 1.1 ka), with strong evidence from T2 and T5, weak evidence from T1 and T3, and missing evidence at the intermediate Komansu site (T4), I infer another possible discontinuous rupture extent. Considering the fact that trench T4 was excavated on the Qt₄ terrace surface (~ 4.5 ka; Figure 3), it is likely that any prior evidence was eroded during the incision of Qt₃ (<7.3 ka). In summary, I assume a segment-wide activation (~ 35 km) during earthquakes E4 and E5. Event E6 (14.6 ± 2.1 ka) presumably occurred during the formation of the Qt₃ terrace (20.1–7.3 ka).

For this event, I found only weak evidence at the western terminus of the cPFT (T1–T3) based on small stratigraphic offsets detected in fluvial terrace deposits (unit 1) with poor age control. A longer rupture extent during this event, however, cannot be ruled out because of the limited exposure of unit 1 in the other trenches.

A possible impediment to retrieving earthquake evidence older than 7 ka in the study area could be related to the effects of climatic conditions in the Pamir region during the Late Pleistocene to early Holocene. In a paleoclimate review for Central Asia, Herzschuh (2006) reported a major transition from dry climate conditions during the Last Glacial Maximum (LGM) at ~21 ka to wetter conditions and a peak in mean effective moisture at ~7.5 ka (Figure 8.1a). This period, which corresponds to the time of deposition of unit 1 and the aggradation of the Qt₃ terrace (20.1–7.3 ka), was characterized by deglaciation that was followed by minor glacial readvances starting at ~21 ka (e.g., Koppes et al., 2008; Röhringer et al., 2012). It therefore seems likely that the increased availability of meltwater during deglaciation caused substantial changes in fluvial dynamics and associated erosion and aggradation processes along the Pamir mountain front (e.g., Fuchs et al., 2013). These climate-driven complexities not only potentially explain the depositional gap (~13 kyr) between the formation of the fluvial terrace gravels of Qt₃ (unit 1) and terrace abandonment (post-dated by unit 2), but could also be a reason for the obliteration of geomorphic evidence of surface ruptures on fluvial channels during that time.

Consequently, if the trenching sites adjacent to active river channels (Ylaisu, T3; Komansu, T4; Tashkungey, T5) were indeed affected by increased glacio-fluvial dynamics that altered or removed evidence of surface ruptures, an incomplete chronology for earthquakes older than 7 ka is probable. However, because the chronology of the documented surface ruptures during E1 to E5 likely constitutes a complete record of strong surface-rupturing plaeoearthquakes over the past 7 kyr, I focus on this time period in my subsequent analysis.

8.1.3. Partial versus full-segment ruptures

Considering the earthquake correlation along the cPFT documented in this thesis, I suggest a 7-kyr-long history of seismogenic events that consisted of smaller, discontinuous ruptures (E1, E3) with lengths of < 20 km that partially broke the western end of the central segment. These were interspersed with more extensive, continuous ruptures (E4 and E5) that likely activated the entire length of the segment (~35 km) or even crossed its boundaries > 35 km (E2) (Figure 8.1). This apparent higher rupture frequency in the western half of the cPFT coincides with significantly larger scarp offsets (implying a greater dip-slip rate) in the west (Figure 8.1d).

If the estimated extent of earthquake evidence (equivalent to a surface rupture length, SRL) is compared with associated measured dip-slip displacements, it is possible to observe compatible scaling relationships for E2, E4, and E5, but discrepancies regarding the apparent partial ruptures associated

with E1 and E3 exist (following maximum displacement and rupture length scaling relations of Wells & Coppersmith [1994] and Manighetti et al. [2007]). In the latter cases (E1 and E3), the measured maximum dip-slip offset amount to several meters (2–3 m) and could imply SRLs of > 30 km instead of the inferred < 20 km. This discrepancy might be consistent with a common phenomenon observed in other thrust/reverse fault studies in Central Asia and elsewhere that revealed discontinuous surface-rupture traces that were shorter than expected, despite several meters of slip associated with major $M \geq 7$ earthquakes (e.g., Rockwell et al., 2013; Arrowsmith et al., 2017; Ainscoe et al., 2019; Grützner et al., 2019; Rimando et al., 2019). In this context, E1 and E3 might constitute ruptures with discontinuous surface breaks that potentially bypassed the remaining trenching sites. Another reason for such irregular surface displacement could be potentially complex interactions between faulting and additional folding of the hanging wall along the PFT thrusts (e.g., Baljinyam, 1993; Wang et al., 2020). Nevertheless, the significant dip-slip displacements suggest these ruptures were larger than what would be expected from the visible lateral extent of the surface rupture. This raises the question, as to whether or not the ruptures propagated into the neighboring western segment crossing geometric fault-trace discontinuities (see Discussion below) during a multi-segment rupture scenario (Rubin, 1996).

To estimate the seismic potential of the cPFT, I determine the seismic moment for a full-segment rupture as well as potential ruptures cascading into adjacent segments. The scalar seismic moment is $M_0 = \mu D_{ave} A$, where $\mu = 3 \cdot 10^{10}$ N/m² is the shear modulus for crustal faults (Hanks & Kanamori, 1979), D_{ave} is the average displacement, and A is the fault-plane area (length x width). The per-event dip-slip displacements associated with the documented events did not exceed 5 m; therefore, I generally exclude the possibility of megathrust paleo-events with $M_w > 8$ along the cPFT during the Holocene. However, the sparse number of dip-slip estimates and the complex nature of dip-slip may result in inaccurate (underestimated) values for D_{ave} . Since observed in all five trenches, $D_{ave-obs} = 2.5 \pm 0.5$ m for E2 is the most reliable estimate and was thus used for a seismic-moment calculation for full-segment ruptures. For comparison, I also used the minimum surface-rupture length (SRL) along the cPFT (lateral extent of earthquake evidence in trenches) and empirical self-consistent fault-scaling relationships for interplate dip-slip events (class II after Scholz et al., 1986) to estimate a robust D_{ave} by using the equation $\log(D_{ave-calc}) = -3.799 + 0.833 \log(SRL)$ (last updated by Leonard, 2010, 2014). To define fault width an average PFT fault dip of 30° was used (Nikonov et al., 1983; Burtman & Molnar, 1993; Arrowsmith & Strecker, 1999; Schurr et al., 2014) and a seismogenic depth of 15 km was assumed based on the depth range of instrumentally recorded large earthquakes in this region and the average-depth distribution of crustal seismicity associated with the PFT (e.g., Fan et al., 1994; Ekström et al., 2012; Sippl et al., 2013a, 2013b; Schurr et al., 2014).

For a full-segment rupture (~35 km; E4 and E5), I estimate a scaling-relationship derived $D_{ave-calc} = 1$ m and a total seismic moment release of $M_0 = 3.15 \cdot 10^{19}$ Nm, which is equivalent to a M_w 7.0 earthquake (with $M_w = 2/3 \log(M_0) - 6$). I infer a maximum extent of rupture of ~65 km (E2) assuming segment

interaction with the neighboring western and eastern transfer zones (Nikonov et al., 1983; Nikonov, 1988). In light of the relationship between the 1978 M_w 6.6 Zaalai earthquake main shock (equivalent to $M_0 = 0.71 \cdot 10^{19}$ Nm) and its strike-slip dominated aftershocks (Fan et al., 1994), with rupture-propagation patterns into the western transfer zone and the central segment (as reported by Nikonov et al., 1983), Arrowsmith & Strecker (1999) suggested that the ~ 15 -km-long western transfer zone can be categorized as a small, semi-independent rupture segment. If this is also assumed for the eastern transfer zone, a potential coupling of the segment-transfer zone during E2 with a $D_{\text{ave-calc}} = 1$ m for the cPFT, and 0.5 m the western and eastern transfer zone, respectively, yields a total seismic moment of $M_0 = 4.44 \cdot 10^{19}$ Nm, which is equivalent to a M_w 7.1 earthquake. If a surface rupture propagated farther west and broke through all four segments (i.e., eastern transfer, central, western transfer, and western) with similar average dip-slip displacements of ~ 0.5 – 1 m, the event would have been associated with a minimum seismic moment release of $M_0 = 7.12 \cdot 10^{19}$ Nm (M_w 7.2). Assuming the western and central segments were indeed joined by a breaching hard link (e.g., Arrowsmith and Strecker, 1999) and using observed displacements based on E2 ($D_{\text{ave-obs}} = 2.5$ m) a moment magnitude of $M_0 = 7.76 \cdot 10^{19}$ Nm (M_w 7.3) can be estimated for a 35-km-long rupture (central segment), $M_0 = 9.04 \cdot 10^{19}$ Nm (M_w 7.3) for the central segment and adjacent transfer zones (~ 65 km), and $M_0 = 11.70 \cdot 10^{19}$ Nm (M_w 7.4) during a propagation into the western segment (> 65 km). In summary, in light of the interpretation of full-segment length activation (≥ 35 km) during E5, E4, and E2, magnitudes of $M_w \geq 7$, but not larger than M_w 7.4 along the PFT_N and a mean recurrence interval of ~ 1.9 kyr for earthquakes, can be estimated.

Against the well-documented geomorphologically defined uplift pattern of the Qt₃ terrace within the central Trans-Alai Range (cPFT) versus the non-uniform distribution of fault-bounded terrace terminations at other mountain-front sectors (west and east of cPFT), Arrowsmith and Strecker (1999) suggested that the central segment of the PFT behaves independently. Measured vertical separation (VS) along the cPFT is asymmetric and increases in westward direction (Figure 8.1), pointing towards a mechanical interaction between neighboring faults as has been suggested by numerical analyses of such settings (e.g., Willemse, 1997; Bergen & Shaw, 2010). Reported rupture-propagation patterns during the 1978 M_w 6.6 Zaalai earthquake (Nikonov et al, 1983) emphasize the complexity of ruptures in the vicinity of segment boundaries along the cPFT and the potential segment interaction during ruptures. Willemse et al. (1996) suggested that such interaction can lead to significant slip-to-length ratio variations as well as off-center location of maximum slip, which could explain the seemingly partial ruptures in the western part of the cPFT (E1 and E3). More recent studies by Perrin et al., (2016a) furthermore show that the largest slip during an earthquake systematically occurs on one half of the fault (asymmetric), i.e., the most mature fault section. However, it is not clear if these partial ruptures represent the ends of longer ruptures which have overcome segment boundaries (Manighetti et al., 2005, 2007; Wesnousky, 2008). A full-segment-length activation with possible ruptures along adjacent segments could imply advanced fault maturity, which has important implications for future scenarios of fault segmentation. It cannot be ruled

out that a more mature, fully linked thrust fault connects the present-day western, western transfer zone, as well as the central and eastern transfer segments at depth and that this fault might be capable of generating events with $M_w \geq 7.2$.

Despite these caveats, the derived paleo-magnitude estimates for the past 7 ka do not exceed M_w 7.2 (or maximum M_w 7.4, if considering E2 measurements). Li et al. (2019) proposed similar maximum moment magnitudes of $M_w \leq 7.1$ for future earthquakes in the eastern half of the PFT in the Chinese Tarim Basin, but suggested much larger earthquakes for the PFT in the Alai Valley, an interpretation that is not supported by my local cPFT study. The notion of an extensive interface at depth along which even larger ruptures could occur is a simple, but reasonable suggestion when considering the substantial geologic and geophysical evidence for intracontinental subduction and large-scale convergence along the PTS (e.g., Burtman and Molnar, 1993). However, if this system is characterized by earthquakes with magnitudes $M_w \leq 7.4$, and megathrust events do not occur, then the Pamir mountain front may only represent a discontinuous, up-dip portion of an active continental subduction zone (e.g., Burtman and Molnar, 1993), where very large earthquakes ($M_w > 8$) would be expected. Instead, this area may indeed have reached a stage of continental collision with a decoupled subducting slab dominated by thin-skinned tectonics as suggested by other studies (Sobel et al., 2013; Sippl et al., 2013b; Kufner et al., 2016).

8.1.4. Holocene slip rate versus GNSS shortening rates

Considering the earthquake chronology since 7 ka (E5–E1) and the associated cumulative average dip-slip displacement of 24.7 ± 4.1 m, an average Holocene (since 5.3 ka) dip-slip rate for the cPFT of 4.7 ± 1.7 mm/yr can be estimated, which is equivalent to a horizontal shortening of 4.1 ± 1.5 mm/yr. This new estimate exceeds previous values of 2.0 to 2.5 mm/yr, but compares favorably with the suggested possible 4 mm/yr since 6 ka determined at the western end of the cPFT (Nikonov et al., 1983; Burtman & Molnar, 1993). Burtman and Molnar (1993) also estimated an approximate N–S convergence rate of ~ 3.5 mm/yr along the northern edge of the Pamir based on the relationship between the sum of seismic moment tensors from the AD 1963–1988 earthquake catalogue, an assumed representative shear modulus, and the estimated volume of the regional seismogenic layer (e.g., Kostrov, 1974). However, they suggested that this rate may be an underestimate due to the short time span represented in the earthquake data and the limited magnitude information. Alternatively, a Holocene dip-slip rate of ~ 6 mm/yr based on offset terraces at the Syrinadjar River, which crosses the central segment (Arrowsmith and Strecker, 1999), agrees within error with my dip-slip-rate point estimate of 7.8 ± 2.7 mm/yr since ~ 5.3 ka at the same location (Profile 8). However, considering the VS distribution along the cPFT, I infer that the VS at Syrinadjar represents the maximum VS (Figure 8.1), and that the associated slip is a local maximum along the cPFT rather than a minimum as suggested by Arrowsmith and Strecker (1999).

GNSS-derived horizontal surface velocities measured south of the PFT, across the northern Pamir plateau, show that the region is moving north-northwestward with respect to stable Eurasia at a rate of $\sim 20\text{--}25$ mm/yr (Zubovich et al., 2010, 2016; Ischuk et al., 2013; Metzger et al., 2020). Permanent GNSS stations north of the PFT, however, are moving northward at a rate of ~ 10 mm/yr (Figure 2.3). The resulting difference in horizontal surface velocities between the northern Pamir plateau and the Alai Valley is $\sim 10\text{--}15$ mm/yr. Thus, the revised Holocene shortening rate for the cPFT of ~ 4 mm/yr accounts for less than half of the difference in the geodetically-determined, north-south convergence rate measured across the PTS. This discrepancy may be related to a variety of factors that will be discussed in greater detail below in the context of my cPFT results, but also in relation to broader tectonic implications.

The detailed geomorphic and paleoseismic investigations carried out in this study provide strong evidence for fault partitioning both along and across the PTS. The distribution of cPFT scarps and associated structures suggests that the surface trace is discontinuous, with local back thrusts (south of T1, T2 and T3; at T4), bends (at the Minjar River), and more complex steps, and lateral fault splays (i.e., the eastern expansion of the cPFT; see Chapter 4 for more details). This along-strike structural diversity may result in coseismic and/or post-seismic offset accommodation across secondary fault branches, as has been observed in several studies that relate fault geometry to coseismic rupture propagation (Biasi & Wesnousky, 2016, 2017, 2021; Perrin et al., 2016). Furthermore, the analysis of high-resolution satellite imagery and TanDEM-X data performed in this study reveals the presence of pronounced fault scarps ~ 10 km south of the cPFT that displace Neogene conglomerates and Quaternary glacial and mass-movement deposits (PFTs, Figure 4.1). Nikonov (1988) also reported evidence of numerous earthquakes with ages younger than 10 ka along the PFTs. Local fault-trace diversion along the cPFT, potentially active PTS splay faults, off-fault deformation, fault partitioning, and active blind structures not accounted for may all contribute to regional deformation and thus may explain the discrepancy between geological and geodetic rates. Addressing these possibilities will require additional paleoseismic, geomorphologic, and geodetic investigations.

A recent study of folded river terraces in the active Qilian Shan Mountains along the northeastern margin of the Tibetan Plateau showed that shortening rates based on surface fault displacements may underestimate the total deformation because unrecognized folding in the range interior, changes in the dip of thrust faults at depth that are unaccounted for, and footwall underthrusting can accommodate a significant amount of regional shortening (Wang et al., 2020). Arrowsmith & Strecker (1999) showed that the geomorphic expression of the terrace surfaces, which extend parallel to and along the PFT, do not reveal folding and secondary fractures in the terrace profiles. However, their terrace profiles are less than 7-km-long and may only cover a minimum aperture of localized deformation at the Trans-Alai range front (i.e., the profiles were too short to capture recent deformation associated with potential folding or other PTS faults). More detailed work in the interior parts of the Trans Alai Range is required

to better quantify the effects of folding and the geometry of faults at depth on the shortening-rate estimates, including the documented rate discrepancy.

Another possible reason for the discrepancy relates to the observed geodetic surface velocity gradient from north to south across the PTS (Figure 2.3). Similar gradients are commonly observed across tectonically active mountain fronts including the Himalayas, the southern Bolivian Subandes, and Taiwan (e.g., Bilham et al., 1997; Hsu et al., 2003, 2009; Brooks et al., 2011; Weiss et al., 2016; Lindsey et al., 2018). These gradients are thought to represent the surface manifestation of slipping-to-locked transitions along an underlying décollement as well as the down-dip accumulation of elastic strain, which is released aseismically and/or incrementally by earthquakes that rupture the shallow portion of the décollement and overlying splay faults both within the mountain belt and at the orogenic wedge front (e.g., Brooks et al., 2011; Weiss et al., 2016). If this conceptual model is applied to the PTS, including the PFT shortening rate deficit, the implication is that strain release is not solely absorbed by the cPFT (PFT_N), but rather that it is shared by other PTS structures located farther south, particularly the southern PFT (PFT_S), and perhaps even the MPT. Both of these faults were previously thought to be inactive (e.g., Arrowsmith & Strecker, 1999; Sobel et al., 2013). As already suggested above, it can be assumed that the PFT_S and potentially other PTS structures such as the MPT as well as blind faults north of the PTS within the Alai Valley (Robinson et al., 2015) might accommodate some of the missing 10–15 mm/yr of shortening. Although beyond the scope of the current study, modeling of the geodetic data in the future would aid in determining the geometry and kinematics of an underlying décollement (e.g., Weiss et al., 2016; McFarland et al., 2017). This is an important next step towards understanding regional strain release and seismic hazard in this region. For example, the geodetic rates do not decrease to 0 mm/yr in the Alai Valley north of the PTS. This probably reflects the effects of the northward continuation of shortening in the Tien Shan and Fergana basin (Thompson et al., 2002; Rizza et al., 2019b). The distribution of shortening may thus indicate that the regional décollement is only partially locked and that slip can be transferred to blind faults within the Alai Valley and/or additional high-angle splay faults farther to the north in the southern Tien Shan (e.g., Burtman & Molnar, 1993). A completely different structural configuration might also be required to explain both the field-based and GNSS observations.

Due to predominantly dextral strike-slip focal mechanisms, comparably lower seismic moment release, and no significant thrust earthquakes along the central PTS during the past decades, Schurr et al. (2014) and Sippl et al. (2014) inferred either significant aseismic creep or fault locking with a long earthquake-recurrence interval. The results obtained in this study point towards the latter scenario, considering the estimated recurrence interval of ~1.9 kyr, combined with a clear indication of dip-slip thrust motion in the trench exposures, and no geomorphological observations along the cPFT that would support a dominant strike-slip component of motion. Based on these observations, I suggest that the PTS of the northern Pamir is underlain by a regional south-dipping décollement that is partially

locked. This is consistent with the model proposed by (Sippl et al., 2013b), where the upper and lower continental crust are separated by a décollement with the frontal ranges of the Pamir formed by ongoing northward propagation of deformation.

8.2. The 2008 M_w 6.6 Nura earthquake surface rupture

The 2008 M_w 6.6 Nura earthquake in southern Kyrgyzstan is the most recent seismogenic event that ruptured along the eastern continuation of the Pamir Thrust System (PTS), and which was associated with a surface rupture along the Irkeshtam Fault (IrkF), external and north of the PTS. Field work and new data on the surface rupture in this sector of the mountain range provides the unusual opportunity to study the seismogenic behavior of active faults in a poorly known collision-zone setting. Thus, one of the main motivations for this part of the study is to provide a detailed description of the principal surface rupture and secondary features along the IrkF in the context of the local geology and regional tectonic setting, in order to establish the source of deformation and a kinematic fault model.

8.2.1. Characteristics of the surface breaks and kinematic interpretation

My study of the earthquake geology of the Nura event focused on a ~6-km-long section of the surface rupture for which high-quality georeferenced digital surface models (DSM) generated from aerial photographs were available. However, poorly referenced DSMs excluded from further calculation (zone A; Figure 8.2) show that the surface break, although less continuous, extends northeastward beyond the considered DSMs and our field measurements for another ~2 km (see also Figure 7.8, Chapter 7). Following the immediate post-earthquake reports of Abdrakhmatov et al. (2008) and Kalmetieva et al. (2009), the northeastern termination of the surface rupture is compatible with observed fractures in the asphalt cover of the *A371* road passing through the Nura village on the opposite side of the river. Taken together, these observations result in a total surface rupture length (SRL) of ~8 km. Although the extent and propagation of the rupture remain uncertain, in light of a 25-km-long deformation zone inferred from InSAR modelling of the Nura site (Teshebaeva et al., 2014) it is likely that additional, discontinuous surface breaks with less offset developed toward the northeast, east and/or southwest.

The geometry of the observed surface breaks is complex, with a great variety of surficial deformation patterns along the ~6-km-section of the rupture zone. It was divided into six deformation zones based on characteristic tectono-geomorphic and structural features that change between zones A to E (Figure 8.2). In the following sections, I will briefly summarize the structural observations from each zone and compare these with superficial structures from historic earthquakes, in order to establish a relationship between deformation style and local geological features. To keep track of the spatial relationship between

observations are reminiscent of seismogenic surface ruptures reported during the 1980 M_s 7.3 El Asnam earthquake in Algeria, where local stress variations due to flexing of the hanging-wall anticlines result in bending-moment crestal grabens (Ouyed et al., 1981; Yielding et al., 1981; Ruegg et al., 1982; Philip & Meghraoui, 1983; Meghraoui et al., 1988).

Zone C's surface rupture style is a transition between zones B and D. Here, the surface breaks are less pronounced and confined to a narrower zone, but follow the topographic expression of old cumulative scarps that form an *en echelon* right-stepping pattern (kilometers 2 to 3; Figure 8.2). Also, similar to El Asnam the orientation of the *en echelon* step-overs is compatible with synthetic faults along sinistral strike-slip faults (e.g., Deng et al., 1986; Richard et al., 1991). The second step within zone C (south-westward) connects with zone D, where the narrow rupture zone splays open and forms a lens of synthetic fractures whose orientation remains subparallel to the fault scarps in zone C (kilometers 3 to 4; Figure 8.2). In map view zone D, resembles an extensional duplex resulting from left-lateral motion, similar to what was locally observed for instance after the 1968 M_w 7.1 Dasht-e Bayaz strike-slip earthquake in Iran (e.g., Tchalenko & Ambraseys, 1970). The lens-like zone is bounded by less prominent northwest facing thrusts at its northwestern edge (similar to zone B), and more discontinuous southeast-facing back (?) thrusts that cut the slopes below the main fault zone (southeastern edge). Together, such a fault array is indicative of a transpressional left-lateral shear zone, as has been observed in the Mesozoic Atacama fault system of Chile (e.g., Taylor et al., 1998; Cembrano et al., 2005) or along the Zagros collision zone (e.g., Harding, 1985; Mohajjel & Behyari, 2010).

Starting from zone D, Paleogene gypsum and limestone units are exposed in the stream channels that cut the overlying till northwest-southeast, topographically above and below the fault zone. In zone E, which hosts the highest, well-expressed cumulative landforms, the surface rupture tears the front (north-western) limb of these along $60 - 80^\circ$ SE-dipping gypsum layers and mollusk-bearing limestone breccias, which appear to have guided the deformation. The gypsum units outcrop again at the surface topographically below the fault zone with a $25^\circ - 30^\circ$ NW dipping bedding. Together, this resembles an asymmetric fold with an approximately north-west plunging fold axis (Figure 8.2). The steeply dipping bedding of the Paleogene units combined with the surface rupture cutting along high topography in this setting is reminiscent of the fault-zone geomorphology that was generated during flexural-slip faulting associated with the El Asnam earthquake rupture above an inferred blind thrust (Philip & Meghraoui, 1983).

The south-western termination of the surface rupture bifurcates and continues in parallel zones of discontinuous breaks and small offsets (zone F; Figure 8.2), similar to what was observed in zone A. In this zone surface rupture cuts through a densely vegetated area (at ~ 6 kilometers; Figure 8.2), where a several-meter-deep spring-fed pool with fast flowing water emanates from the fracture zone, and is surrounded by three sinkholes, similar to fault-line sinks in the central part of the Pamir (Strecker et al., 1995). The nature of this part of the fault zone indicates that water accumulates here and is forced

towards the surface due to subsurface barriers, such as faults or folded bedding planes (e.g., Jones & Deike, 1981). Combined with the inferred existence of a syncline in zone E, it may be assumed that its continuation extends into zone F, but is here still buried under the tills.

In summary, the surficial pattern of the rupture comprises extensional and reverse structures, as well as those associated with *en echelon* sinistral slip. The surface breaks occur in the tills along the Nura river bank, which overlie unconformably steeply south-dipping Paleogene sedimentary units along the SE dipping limb of a syncline, whose continuation is exposed to the north-east of the Nura village (see Figure 7.4; Chapter 7). Surficial fracturing and varying lateral distribution of the deformation along the rupture are likely caused by bed-parallel slip along these folded sedimentary layers, forming small scale (10s to 100s of m) secondary bending-moment and flexural-slip fault characteristics at the surface, depending on the thickness of the overlying till. In the zone where the till cover appears thinnest (where the underlying Paleogene units come to the surface), tectonic landforms and recent surface-rupture slip are most prominent, which may indicate characteristic fault-zone behavior likely related to a blind thrust beneath the folded Paleogene units (see Discussion below).

8.2.2. Seismogenic behavior of the Irkeshtam fault

The high-resolution documentation of the 2008 Nura surface rupture provides an excellent opportunity to assess scaling relationships between surface-rupture length (SRL), average displacement (D_{ave}), and maximum displacement (D_{max}) versus magnitude M_w global regressions, but also helps to put the single-event rupture into context with the cumulative landforms and develop an estimate for recurrence intervals along the IrkF. In the following I will consider 8 km for the SRL (see Discussion above).

Along the Nura earthquake surface rupture, the D_{ave} and D_{max} measured ten years after the 2008 rupture is $0.6 +0.2/-0.2$ m and $2.1 +1.2/-0.5$ m, respectively. The D_{max} estimate obtained in this study agrees with the dip-slip estimate of Teshebaeva et al.'s (2014) optimum fault model (up to 1.6 to 2 m). When placed into the context of regressions relating D_{ave} and D_{max} versus SRL (e.g., Wells & Coppersmith, 1994), my displacement measurements are relatively high compared to the SRL. Considering the regressions for relationships between D_{ave} and D_{max} , and M_w from an updated empirical scaling relationship for reverse mechanism established by Moss & Ross (2011) ($\log(D_{ave}) = 0.3244 * M_w - 2.2192$ and $\log(D_{max}) = 0.5102 * M_w - 3.1971$), a moment-magnitude range is obtained between M_w 5.8 to 6.7 and M_w 6.7 to 7.2, respectively. Teshebaeva et al. (2014) estimated for the IrkF a geodetic moment of $5.43 \cdot 10^{18}$ Nm, which corresponds to M_w 6.5; this is in agreement with my $M_w(D_{ave})$ estimate. The unrealistically high $M_w(D_{max})$ estimate could imply that (1) coseismic displacement was exceptionally high for the observed rupture length, and/or that (2) maximum fault-slip distribution was concentrated at shallow depth. In light of the detailed observations made at the Nura study site, I favor the first interpretation (1), because the maximum offsets are located in zones D and E where the presence of evaporitic rocks might have facilitated flexural-slip faulting along bedding planes of these units. This

interpretation is consistent with the brecciated gypsum layers exposed in the outcrops of these sectors of the rupture.

Teshebaeva et al. (2014) estimated a left-lateral fault offset between 1 and 1.3 m in the Nura rupture zone. The measurement of strike-slip offsets in my study was hampered by the advanced erosion of the surface breaks, and strike-slip offsets measured along few broken boulders only amounted to several-decimeters. This discrepancy between Teshebaeva's et al. and my own measurements could be explained by the fact that the local measurements (1) do not represent the net-strike-slip offset, which is probably distributed across multiple fault splays, and that these also (2) do not record off-fault deformation, which was integrated in Teshebaeva et al.'s (2014) fault model. Combined, however, these observations suggest the existence of a wider deformation zone away from the surface rupture, which is consistent with the deformation model proposed here.

To investigate the seismogenic character of the IrkF, it is important to place the 2008 surface rupture in the context of the evolution of cumulative structures that characterize the fault-zone geomorphology, fractures, and geochronology. Most of the 2008 surface breaks coincide with fault scarps that have modified the local topography of the Nura valley slopes. The offset distribution along both, the 2008 surface rupture as well as the inferred cumulative scarps are aligned (Figure 7.19; Chapter 7), indicating that more earthquakes with a similar style of surface ruptures must have taken place repeatedly in the past. If one were to divide the cumulative D_{ave} (4.64 m) by the 2008 D_{ave} (0.64 m), about seven earthquake ruptures similar to the Nura event in 2008 would be needed to generate the present-day cumulative fault-zone morphology.

To better constrain the age of the cumulative scarps, the regional tectonic setting of the Nura area must first be considered. The area is characterized by complete closure between the Pamir and Tien Shan, which caused the formation of a major drainage divide between the catchment areas of the present-day Kyzylsu rivers throughout the late Cenozoic (Pavlis, et al., 1997; Strecker, et al., 2003). The valley moraines cut by the Nura river of the eastern Kyzylsu catchment diverge at and along the IrkF, suggesting that activity of the IrkF fault most likely preceded the deposition of the associated moraine deposits. However, since much of the details of this history was probably erased by recurrent glacial activity and also tectonically overprinted, an unambiguous assessment of the fault activity can only be considered in the age range of deposits where deformation is preserved along the IrkF, i.e., in the Qm₂ moraine deposits. Geochronological control from the Nura site provides two important age estimates to constrain the time range when the cumulative scarps described above began to form. An IRSL sample from the re-transported loess covering the Qm₂ moraine deposits yields a minimum age of 11.3 ± 0.5 kyr. Farther northeast, on the opposite side of the Nura river, an IRSL age of 12.0 ± 0.6 kyr was determined from paleo-lake sediments observed north of the Nura village, associated with the oldest observed landslide (L1), which in turn may be related to activity along the IrkF. Taken together, and if the above interpretation of age relationships and the glacial depositional record is correct, the IRSL ages

provide a timespan of ~ 12 kyr for the last seven earthquakes, and thus a potential (minimum) recurrence time of ~ 1.7 kyr.

8.2.3. Deformation model of the Nura region in the context of prior investigations

Using InSAR (Teshebaeva et al., 2014) and seismological (Sippl et al., 2014) observations, deformation estimates and kinematic models have been proposed to relate the Nura mainshock along the PFT to the surface rupture along the IrkF. In the following paragraphs, I compare my findings in the context of these studies to discuss an updated deformation model.

The deformation model derived in this study is broadly consistent with the fault-kinematic model of oblique thrusting with a left-lateral strike-slip component of motion proposed by Teshebaeva et al. (2014). These authors concluded that oblique thrusting along the rupture zone of the Nura earthquake resulted from strain partitioning between the PFT_N and the IrkF, which likely share a common root and may form part of an imbricate north vergent thrust system. They suggested that the IrkF constitutes the integral part of an aseismic, moderately south dipping and several-kilometer-deep aseismic décollement controlled by mechanically weak Paleogene evaporites that are overthrust by folded Paleozoic units; they furthermore suggested that the presence of these evaporites accounts for the lack of aftershock seismicity along the IrkF. Consequently, these authors concluded that the IrkF was coseismically activated by the Nura main shock along the PFT_N, but that a significant part of the offset along the Nura surface breaks is due to post-seismic afterslip.

In contrast, Sippl et al. (2014) refuted the interpretation of coeval rupture, as their modeling of earthquake focal mechanisms of the Nura main shock sequence did not reveal any mechanism that could be associated with a “composite” mechanism of a coseismic rupture along these differently striking faults (i.e., the E-W striking PFT_N and the SE-NW striking IrkF). Instead, they pointed out an aftershock sequence ~ 10 km south-east from the IrkF (blue cluster; Figure 7.1 in Chapter 7), which was thought to be associated with the surface rupture along this fault. However, given the observations and modeling performed in my study, there is a significant disagreement between my modelled magnitude range of M_w 5.8 to 6.7 and the highest measured magnitude within the blue cluster of M_w 4.2 (Sippl et al., 2014), which is further difficult to associate with a ~ 8 -km-long surface rupture and an average ~ 1 -m-high offsets. Thus, the interpretation involving a direct connection with this aftershock sequence without afterslip – as well – is problematic. This level of offset rather implies that the surface rupture must be related to coseismic or triggered afterslip from the M_w 6.6 Nura main shock, as originally proposed by Teshebaeva et al. (2014).

In light of the previous studies and my own observations I propose the following scenario of deformation processes associated with the Nura earthquake. By inferring the existence of structural ramps at greater depths linked with detachments beneath the Chinese sector of the orogen (e.g., Bufe et al., 2017; Li et al., 2018, 2019; Scharer et al., 2004, 2006; Thompson et al., 2015; Thompson Jobe et al.,

2017), the existence of a deeply rooted fault that is associated with the IrkF zone and kinematically linked with the PFT in the south, is a reasonable assumption. However, due to a lack of data a more precise statement regarding the geometry of such a structure at depth cannot be defined in more detail. Nevertheless, the observations made in this study suggest that the IrkF is a secondary flexural-slip fault rather than a primary, deep-rooted fault plane, because (1) the IrkF is parallel to bedding within a synclinal limb of folded Paleogene sedimentary units that are steeply dipping to the south, whereas they are more gently inclined northward as can be seen on the lower slopes of the northern terrace risers of the Nura river valley, topographically below the surface rupture zone (Figure 8.3). Farther east the northern limb of the syncline (Paleogene units) forms an integral part of an adjacent anticline of Mesozoic strata (see Figure 7.2; Chapter 7). This setting is thus characterized by an asymmetric flexural-slip syncline in the Paleogene rocks whose origin is probably associated with a blind, north-vergent thrust at depth and possibly an additional thrust fault within the basement rocks farther south (Figure 8.3). (2) The recent Nura surface rupture has a close relationship with the flexural-slip fault and Quaternary deposits, which is here manifested in form of tectonic landforms that have developed within the moraine deposits overlying the flexural-slip faults.

In this context the faulted and folded Quaternary glacial deposits as well as the interstratal breccia layer in the Paleogene units underneath these landforms is also compatible with a north-vergent blind thrust that drives this deformation and that probably merges with other deep-seated thrust faults (Figure 8.3). Virtually identical relationships between growing flexural-slip folds, overlying deformed Quaternary deposits and landforms, and seismogenic blind thrusts at greater depth have been documented in other tectonically active regions as well (Yeats, 1986; Rockwell et al., 2013; Kaneko et al., 2015; T. Li et al., 2015a, 2015b, 2018; Arnous et al., 2020). It is therefore likely that such a scenario also presents a viable mechanism to explain the relationship between the energy release during the 2008 Nura earthquake at a depth of 3-4 km that caused strain transfer and coeval or slightly delayed flexural-slip faulting along mechanically weak Paleogene strata of the IrkF to the north.

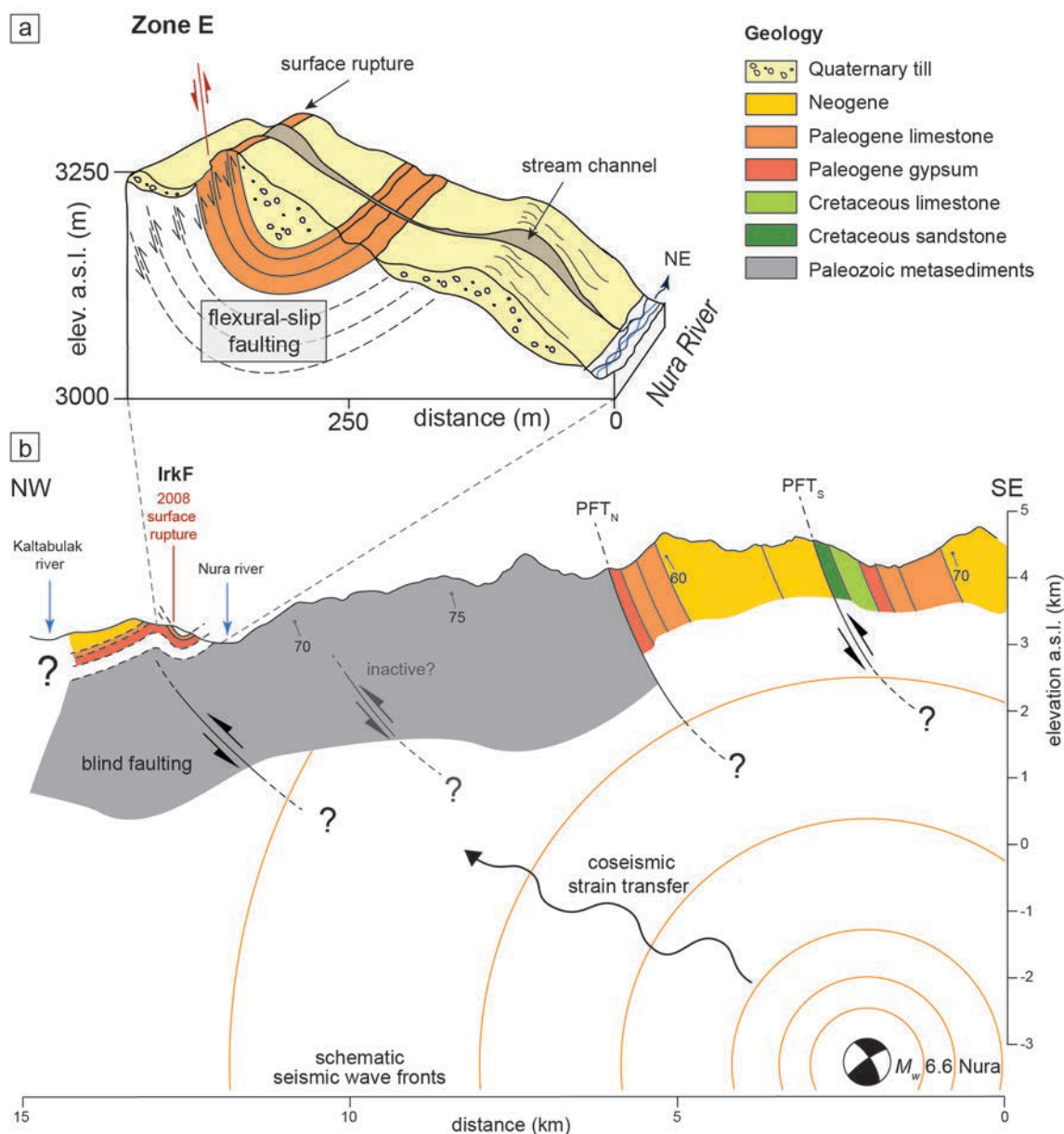


Figure 8.3 (a) Box diagram shows schematic subsurface relationships at the IrkF zone, illustrating folded Paleogene sedimentary units at zone E, and flexural-slip faulting along steeply dipping layers and approximate location of the surface slip (for location see Figure 8.2). Dips shown in sketch are based on field measurements; the geometry of the deformed Paleogene units in other sections of the fault zone can only be inferred and is not shown here. (b) Cross-sectional view with local topography across Pamir Frontal Thrust (PFT) and the Irkeshtam Fault zone (IrkF) at the Nura river synthesizing the inferred structural relationships. The focal mechanism represents the 2008 Nura main shock and is projected onto the profile plane. The precise geometry and continuation of the faults at depth is poorly constrained. In the subsurface of the IrkF zone, bedding of Paleogene folds is indicated by dashed lines.

8.3. Conclusions

The principal motivation of the dissertation was to examine the seismogenic behavior during ruptures along the segmented leading thrust front of the northern Pamir – the Pamir Frontal Thrust – by investigating surface ruptures on different timescales, from geological times to the present-day, and the role of this fault within the Pamir Thrust System and the structural framework of the Pamir-Tien Shan collision zone. The main outcomes of my dissertation are:

- New results from five paleoseismic trench excavations across the cPFT in the Pamir-Tien Shan continental collision zone of Central Asia reveal evidence for five surface-rupturing paleoearthquakes in this segment since ~ 7 ka, and possibly six events since ~ 16 ka. At least three of these events represent major $M_w \geq 7.2$ earthquakes that likely ruptured the full-segment length (~ 35 km) and possibly crossed segment boundaries (~ 65 km) with a recurrence interval of ~ 1.9 kyr. However, there were no indications for ruptures associated with megathrusts that may have exceeded $M_w > 8$.
- For two apparent partial segment ruptures affecting the western end of the cPFT, a discrepancy was observed between anomalously large amounts of dip-slip displacements (2–3 m) compared to a relatively short length (< 20 km) of the associated surface-rupture trace. This observation is compatible with major historic earthquakes in this region that did not produce significant surface ruptures. Combined with larger scarp offsets at the western end of the cPFT, this indicates that segment interaction has occurred in the past including complex (e.g., spillover and multi-segment) ruptures, which have important implications for assessing future seismogenic fault behavior and suggest the possibility of potentially larger-magnitude earthquakes in this region in the future.
- By combining geomorphic and paleoseismic data, I estimate an average dip-slip rate of 4.7 ± 1.7 mm/yr (equivalent to 4.1 ± 1.5 mm/yr horizontal shortening rate) for the past ~ 7 ka, and suggest that the shortening along the central PFT does not account for all of the present-day, geodetically derived shortening (10–15 mm/yr) across the northern Pamir. Rather, strain is likely released intermittently along additional, internal faults of the Pamir Thrust System and/or folds that have less pronounced geomorphic expressions than the central PFT.

- The fairly rapid decrease in GNSS-derived horizontal surface velocities across the mountain front suggest these structures may root within a partially locked regional décollement underlying the northern Pamir although additional modeling is required to better understand the associated fault geometry and kinematics and the potential influence on strain accumulation and release across the region.
- A detailed study of the surface rupture related to the 2008 M_w 6.6 Nura earthquake that occurred along the eastern continuation of the PFT revealed that the resulting deformation along the Irkeshtam fault to the north is a secondary, flexural-slip faulting phenomenon resulting from bedding-parallel slip along folded Paleogene strata; this deformation is likely related to slip along a blind thrust located at greater depths that was co-seismically triggered by strain transfer from the Nura earthquake hypocenter.
- The correlation between the recent rupture behavior and apparent cumulative tectonic landforms associated with the region of the Irkeshtam Fault implies a similar rupture behavior that has repeatedly contributed to the present state of tectonically influenced local topography. This suggests that ruptures similar to the 2008 Nura event must have recurred in the past every ~ 1.7 kyr.

The extensive research of my dissertation results in a paleoseismic database of the past ~ 16 kyr, which contributes to the understanding of the seismogenic behavior of the PFT, but also to that of segmented thrust-fault systems in active collisional settings. My observations underscore the importance of combining different methodological approaches in the geosciences, especially in structurally complex tectonic settings like the northern Pamir. Discrepancy between GNSS-derived present-day deformation rates and those from different geological archives in the central part, as well as the widespread distribution of the deformation due to earthquake triggered strain transfer in the eastern part reveals the complexity of this collision zone and calls for future studies involving multi-temporal and interdisciplinary approaches.

Bibliography

- Abdrakhmatov, K. E., Aldazhanov, S. A., Hager, B. H., Hamburger, M. W., Herring, T. A., Kalabaev, K. B., Makarov, V. I., Molnar, P., Panasyuk, S. V., Prilepin, M. T., Reilinger, R. E., Sadybakasov, I. S., Souter, B. J., Trapeznikov, Y. A., Tsurkov, V. Y., & Zubovich, A. V. (1996). Relatively recent construction of the Tien Shan inferred from GPS measurements of present-day crustal deformation rates. *Nature*, 384(6608), 450–453. <https://doi.org/10.1038/384450a0>
- Abdrakhmatov, K. E., Omuraliev, M., & Ormukov, C. (2008). Nura earthquake October 5, 2008 with $KP= 15.4$, $M_w= 6.7$, $I_0= 8$ (Kyrgyzstan) (*Izvestiya* (4); pp. 19–29).
- Ainscoe, E. A., Abdrakhmatov, K. E., Baikulov, S., Carr, A. S., Elliott, A. J., Grützner, C., & Walker, R. T. (2019). Variability in surface rupture between successive earthquakes on the Suusamyr Fault, Kyrgyz Tien Shan: Implications for palaeoseismology. *Geophysical Journal International*, 216(1), 703–725. <https://doi.org/10.1093/gji/ggy457>
- Aitken, M. J. (1998). *Introduction to optical dating: The dating of Quaternary sediments by the use of photon-stimulated luminescence*. Clarendon Press.
- Alfaro, P., Sánchez-Alzola, A., Martín-Rojas, I., García-Tortosa, F. J., Galindo-Zaldívar, J., Avilés, M., Garrido, A. C. L., de Galdeano, C. S., Ruano, P., Martínez-Moreno, F. J., Pedrera, A., Lacy, M. C., Borque, M. J., Medina-Cascales, I., & Gil, A. J. (2021). Geodetic fault slip rates on active faults in the Baza sub-Basin (SE Spain): Insights for seismic hazard assessment. *Journal of Geodynamics*, 144, 101815. <https://doi.org/10.1016/j.jog.2021.101815>
- Amidon, W. H., & Hynek, S. A. (2010). Exhumational history of the north central Pamir. *Tectonics*, 29(5). <https://doi.org/10.1029/2009TC002589>
- Anderson, J. G., Wesnousky, S. G., & Stirling, M. W. (1996). Earthquake size as a function of fault slip rate. *Bulletin of the Seismological Society of America*, 86(3), 683–690. <https://doi.org/10.1785/BSSA0860030683>
- Argus, D. F., Gordon, R. G., Heflin, M. B., Ma, C., Eanes, R. J., Willis, P., Peltier, W. R., & Owen, S. E. (2010). The angular velocities of the plates and the velocity of Earth's centre from space geodesy. *Geophysical Journal International*, 180(3), 913–960. <https://doi.org/10.1111/j.1365-246X.2009.04463.x>
- Arnous, A., Zeckra, M., Venerdini, A., Alvarado, P., Arrowsmith, R., Guillemoteau, J., Landgraf, A., Gutiérrez, A., & Strecker, M. R. (2020). Neotectonic Activity in the Low-Strain Broken Foreland (Santa Bárbara System) of the North-Western Argentinean Andes (26°S). *Lithosphere*, 2020(1), 8888588. <https://doi.org/10.2113/2020/8888588>
- Arrowsmith, J. R., Crosby, C. J., Korzhenkov, A. M., Mamyrov, E., Povolotskaya, I., Guralnik, B., & Landgraf, A. (2017). Surface rupture of the 1911 Kebin (Chon–Kemin) earthquake, Northern Tien Shan, Kyrgyzstan. *Geological Society, London, Special Publications*, 432(1), 233–253. <https://doi.org/10.1144/SP432.10>
- Arrowsmith, J. R., & Strecker, M. R. (1999). Seismotectonic range-front segmentation and mountain-belt growth in the Pamir-Alai region, Kyrgyzstan (India-Eurasia collision zone). *GSA Bulletin*, 111(11), 1665–1683. [https://doi.org/10.1130/0016-7606\(1999\)111<1665:SRFSAM>2.3.CO;2](https://doi.org/10.1130/0016-7606(1999)111<1665:SRFSAM>2.3.CO;2)
- Auclair, M., Lamothe, M., & Huot, S. (2003). Measurement of anomalous fading for feldspar IRSL using SAR. *Radiation Measurements*, 37(4), 487–492. [https://doi.org/10.1016/S1350-4487\(03\)00018-0](https://doi.org/10.1016/S1350-4487(03)00018-0)
- Baljinnyam, I. (1993). Ruptures of major earthquakes and active deformation in Mongolia and its surroundings. *Geological Society of America*.
- Bande, A., Sobel, E. R., Mikolaichuk, A., & Acosta, V. T. (2015). Talas–Fergana fault Cenozoic timing of deformation and its relation to Pamir indentation. *Geological Society, London, Special Publications*, 427(1), 295–311. <https://doi.org/10.1144/SP427.1>
- Bao, Z.-W., & Gao, Y. (2017). Crustal seismic anisotropy in the Tien Shan and adjacent areas. 60(4), 1359–1375. <https://doi.org/10.6038/cjg20170411>
- Bazhenov, M. L. (1993). Cretaceous paleomagnetism of the Fergana Basin and adjacent ranges, central Asia: Tectonic implications. *Tectonophysics*, 221(2), 251–267. [https://doi.org/10.1016/0040-1951\(93\)90335-H](https://doi.org/10.1016/0040-1951(93)90335-H)

- Bazhenov, M. L., & Burtman, V. S. (1982). The kinematics of the Pamir arc. *Geotectonics*, 16(4), 288–301.
- Bemis, S. P., Micklethwaite, S., Turner, D., James, M. R., Akciz, S., Thiele, S. T., & Bangash, H. A. (2014). Ground-based and UAV-Based photogrammetry: A multi-scale, high-resolution mapping tool for structural geology and paleoseismology. *Journal of Structural Geology*, 69, 163–178. <https://doi.org/10.1016/j.jsg.2014.10.007>
- Bergen, K. J., & Shaw, J. H. (2010). Displacement profiles and displacement-length scaling relationships of thrust faults constrained by seismic-reflection data. *GSA Bulletin*, 122(7–8), 1209–1219. <https://doi.org/10.1130/B26373.1>
- Berger, A., Jouanne, F., Hassani, R., & Mugnier, J. L. (2004). Modelling the spatial distribution of present-day deformation in Nepal: How cylindrical is the Main Himalayan Thrust in Nepal? *Geophysical Journal International*, 156(1), 94–114. <https://doi.org/10.1111/j.1365-246X.2004.02038.x>
- Bershaw, J., Garzzone, C. N., Schoenbohm, L., Gehrels, G., & Tao, L. (2012). Cenozoic evolution of the Pamir plateau based on stratigraphy, zircon provenance, and stable isotopes of foreland basin sediments at Oytay (Wuyitake) in the Tarim Basin (west China). *Journal of Asian Earth Sciences*, 44, 136–148. <https://doi.org/10.1016/j.jseas.2011.04.020>
- Biasi, G. P., & Weldon, R. J., II. (2009). San Andreas fault rupture scenarios from multiple paleoseismic records: Stringing pearls. *Bulletin of the Seismological Society of America*, 99(2A), 471–498. <https://doi.org/10.1785/0120080287>
- Biasi, G. P., & Wesnousky, S. G. (2016). Steps and gaps in ground ruptures: Empirical bounds on rupture propagation. *Bulletin of the Seismological Society of America*, 106(3), 1110–1124. <https://doi.org/10.1785/0120150175>
- Biasi, G. P., & Wesnousky, S. G. (2017). Bends and ends of surface ruptures. *Bulletin of the Seismological Society of America*, 107(6), 2543–2560. <https://doi.org/10.1785/0120160292>
- Biasi, G. P., & Wesnousky, S. G. (2021). Rupture passing probabilities at fault bends and steps, with application to rupture length probabilities for earthquake early warning. *Bulletin of the Seismological Society of America*, 111(4), 2235–2247. <https://doi.org/10.1785/0120200370>
- Bilham, R. (2019). Himalayan earthquakes: A review of historical seismicity and early 21st century slip potential. *Geological Society, London, Special Publications*, 483(1), 423–482. <https://doi.org/10.1144/SP483.16>
- Bilham, R., Larson, K., & Freymueller, J. (1997). GPS measurements of present-day convergence across the Nepal Himalaya. *Nature*, 386(6620), 61–64. <https://doi.org/10.1038/386061a0>
- Blayney, T., Najman, Y., Dupont-Nivet, G., Carter, A., Millar, I., Garzanti, E., Sobel, E. R., Rittner, M., Andò, S., Guo, Z., & Vezzoli, G. (2016). Indentation of the Pamirs with respect to the northern margin of Tibet: Constraints from the Tarim basin sedimentary record. *Tectonics*, 35(10), 2345–2369. <https://doi.org/10.1002/2016TC004222>
- Bloch, W., Metzger, S., Schurr, B. D., Yuan, X., Ratschbacher, L., Reuter, S., Xu, Q., Zhao, J., Murodkulov, S., & Oimuhhammadzoda, I. (2021, October 20). The 2015–2017 Pamir Earthquake Sequence: Fore-, Main-, and Aftershocks, Seismotectonics and Fault Interaction (world) [Preprint]. *Earth and Space Science Open Archive*; *Earth and Space Science Open Archive*. <http://www.essoar.org/doi/10.1002/essoar.10508392.1>
- Bollinger, L., Sapkota, S. N., Tapponnier, P., Klinger, Y., Rizza, M., Van der Woerd, J., Tiwari, D. R., Pandey, R., Bitri, A., & Bes de Berc, S. (2014). Estimating the return times of great Himalayan earthquakes in eastern Nepal: Evidence from the Patu and Bardibas strands of the Main Frontal Thrust. *Journal of Geophysical Research: Solid Earth*, 119(9), 7123–7163. <https://doi.org/10.1002/2014JB010970>
- Bronk Ramsey, C. (1995). Radiocarbon calibration and analysis of stratigraphy: The OxCal program. *Radiocarbon*, 37(2), 425–430. <https://doi.org/10.1017/S0033822200030903>
- Bronk Ramsey, C. (2001). Development of the radiocarbon calibration program. 43. <https://doi.org/10.1017/S0033822200038212>
- Bronk Ramsey, C. (2008). Deposition models for chronological records. *Quaternary Science Reviews*, 27(1), 42–60. <https://doi.org/10.1016/j.quascirev.2007.01.019>
- Bronk Ramsey, C. (2009). Bayesian analysis of radiocarbon dates. *Radiocarbon*, 51(1), 337–360. <https://doi.org/10.1017/S0033822200033865>

- Bronk Ramsey, C. (2017a). OxCal Program, Version 4.3. Oxford Radiocarbon Accelerator Unit: University of Oxford. Available at
- Bronk Ramsey, C. (2017b). Methods for summarizing radiocarbon datasets. *Radiocarbon*, 59(6), 1809–1833. <https://doi.org/10.1017/RDC.2017.108>
- Bronk Ramsey, C. (2021). OxCal 4.4. Available at: <https://c14.arch.ox.ac.uk/oxcal.html>
- Brooks, B. A., Bevis, M., Whipple, K., Ramon Arrowsmith, J., Foster, J., Zapata, T., Kendrick, E., Minaya, E., Echalar, A., Blanco, M., Euillades, P., Sandoval, M., & Smalley, R. J. (2011). Orogenic-wedge deformation and potential for great earthquakes in the central Andean backarc. *Nature Geoscience*, 4(6), 380–383. <https://doi.org/10.1038/ngeo1143>
- Bufe, A., Bekaert, D. P. S., Hussain, E., Bookhagen, B., Burbank, D. W., Thompson Jobe, J. A., Chen, J., Li, T., Liu, L., & Gan, W. (2017). Temporal changes in rock uplift rates of folds in the foreland of the Tian Shan and the Pamir and geodetic and geologic data. *Geophysical Research Letters*, 44(21), 10,977–10,987. <https://doi.org/10.1002/2017GL073627>
- Bull, W. B. (2007). *Tectonic Geomorphology of Mountains: A New Approach to Paleoseismology*. Blackwell Publishing. DOI:10.1002/9780470692318
- Burbank, D. W., & Anderson, R. S. (2011). *Tectonic Geomorphology*. John Wiley & Sons.
- Burgette, R. J., Hanson, A. M., Scharer, K. M., Rittenour, T. M., & McPhillips, D. (2020). Late Quaternary slip rate of the Central Sierra Madre fault, southern California: Implications for slip partitioning and earthquake hazard. *Earth and Planetary Science Letters*, 530, 115907. <https://doi.org/10.1016/j.epsl.2019.115907>
- Burtman, V. S. (1975). Structural geology of variscan Tien Shan, USSR. *Am. J. Sci*, 275, 157–186.
- Burtman, V. S. (2000). Cenozoic crustal shortening between the Pamir and Tien Shan and a reconstruction of the Pamir–Tien Shan transition zone for the Cretaceous and Palaeogene. *Tectonophysics*, 319(2), 69–92. [https://doi.org/10.1016/S0040-1951\(00\)00022-6](https://doi.org/10.1016/S0040-1951(00)00022-6)
- Burtman, V. S., & Molnar, P. H. (1993). Geological and geophysical evidence for deep subduction of continental crust beneath the Pamir. *Geological Society of America*.
- Burtman, V. S., Skobelev, S. F., & Molnar, P. (1996). Late Cenozoic slip on the Talas-Ferghana fault, the Tien Shan, central Asia. *GSA Bulletin*, 108(8), 1004–1021. [https://doi.org/10.1130/0016-7606\(1996\)108<1004:LCSOTT>2.3.CO;2](https://doi.org/10.1130/0016-7606(1996)108<1004:LCSOTT>2.3.CO;2)
- Cao, K., Wang, G.-C., van der Beek, P., Bernet, M., & Zhang, K.-X. (2013). Cenozoic thermo-tectonic evolution of the northeastern Pamir revealed by zircon and apatite fission-track thermochronology. *Tectonophysics*, 589, 17–32. <https://doi.org/10.1016/j.tecto.2012.12.038>
- Caputo, R., & Helly, B. (2008). The use of distinct disciplines to investigate past earthquakes. *Tectonophysics*, 453(1), 7–19. <https://doi.org/10.1016/j.tecto.2007.05.007>
- Cembrano, J., González, G., Arancibia, G., Ahumada, I., Olivares, V., & Herrera, V. (2005). Fault zone development and strain partitioning in an extensional strike-slip duplex: A case study from the Mesozoic Atacama fault system, Northern Chile. *Tectonophysics*, 400(1), 105–125. <https://doi.org/10.1016/j.tecto.2005.02.012>
- Cisternas, A., Philip, H., Bousquet, J. C., Cara, M., Deschamps, A., Dorbath, L., Dorbath, C., Haessler, H., Jimenez, E., Necessian, A., Rivera, L., Romanowicz, B., Gvishiani, A., Shebalin, N. V., Aptekman, I., Arefiev, S., Borisov, B. A., Gorshkov, A., Graizer, V., ... Tatevossian, R. (1989). The Spitak (Armenia) earthquake of 7 December 1988: Field observations, seismology and tectonics. *Nature*, 339(6227), 675–679. <https://doi.org/10.1038/339675a0>
- Council, N. R., Sciences, D. on E. and P., Applications, C. on P. S., Mathematics, and, Forum, G. R., & Committee, G. S. (1986). *Active Tectonics: Impact on Society*. National Academies Press.
- Coutand, I., Strecker, M. R., Arrowsmith, J. R., Hilley, G., Thiede, R. C., Korjenkov, A., & Omuraliev, M. (2002). Late Cenozoic tectonic development of the intramontane Alai Valley, (Pamir–Tien Shan region, central Asia): An example of intracontinental deformation due to the Indo–Eurasia collision. *Tectonics*, 21(6), 3-1-3–19. <https://doi.org/10.1029/2002TC001358>
- Cowgill, E. (2010). Cenozoic right-slip faulting along the eastern margin of the Pamir salient, northwestern China. *GSA Bulletin*, 122(1–2), 145–161. <https://doi.org/10.1130/B26520.1>

- Crone, A. J. (1988). Directions in paleoseismology. *Eos, Transactions American Geophysical Union*, 69(39), 881–882. <https://doi.org/10.1029/88EO01138>
- Czassny, B., Young, E. M., Arrowsmith, J. R., & Strecker, M. R. (1999). Stratigraphic and structural evidence of late Paleogene to early Neogene deformation in the southwestern Tien Shan, Pamir-Alai region, Kyrgyzstan. 80(46)(Fall Meeting Suppl.), F1016.
- Dal Zilio, L., van Dinther, Y., Gerya, T., & Avouac, J.-P. (2019). Bimodal seismicity in the Himalaya controlled by fault friction and geometry. *Nature Communications*, 10(1), 48. <https://doi.org/10.1038/s41467-018-07874-8>
- Dal Zilio, L., van Dinther, Y., Gerya, T. V., & Pranger, C. C. (2018). Seismic behaviour of mountain belts controlled by plate convergence rate. *Earth and Planetary Science Letters*, 482, 81–92. <https://doi.org/10.1016/j.epsl.2017.10.053>
- Davidzon, R. M., Kreidenkov, G. P., & Salibaev, G. K. (1982). Stratigraphy of Paleogene deposits of the Tadjik depression and adjacent territories. Tadjik Academy of Science, Dushanbe.
- Davis, K., Burbank, D. W., Fisher, D., Wallace, S., & Nobes, D. (2005). Thrust-fault growth and segment linkage in the active Ostler fault zone, New Zealand. *Journal of Structural Geology*, 27(8), 1528–1546. <https://doi.org/10.1016/j.jsg.2005.04.011>
- Davis, W. M. (1899). The geographical cycle. *The Geographical Journal*, 14(5), 481–504. <https://doi.org/10.2307/1774538>
- Degering, D., & Degering, A. (2020). Change is the only constant—Time-dependent dose rates in luminescence dating. *Quaternary Geochronology*, 58, 101074. <https://doi.org/10.1016/j.quageo.2020.101074>
- Deng, Q., Wu, D., Zhang, P., & Chen, S. (1986). Structure and deformational character of strike-slip fault zones. *Pure and Applied Geophysics*, 124(1), 203–223. <https://doi.org/10.1007/BF00875726>
- DePolo, C. M., Clark, D. G., Slemmons, D. B., & Ramelli, A. R. (1991). Historical surface faulting in the Basin and Range province, western North America: Implications for fault segmentation. *Journal of Structural Geology*, 13(2), 123–136. [https://doi.org/10.1016/0191-8141\(91\)90061-M](https://doi.org/10.1016/0191-8141(91)90061-M)
- Ducea, M. N., Lutkov, V., Minaev, V. T., Hacker, B., Ratschbacher, L., Luffi, P., Schwab, M., Gehrels, G. E., McWilliams, M., Vervoort, J., & Metcalf, J. (2003). Building the Pamirs: The view from the underside. *Geology*, 31(10), 849–852. <https://doi.org/10.1130/G19707.1>
- Duller, G. a. T. (2004). Luminescence dating of quaternary sediments: Recent advances. *Journal of Quaternary Science*, 19(2), 183–192. <https://doi.org/10.1002/jqs.809>
- Duller, G. a. T. (2008). Single-grain optical dating of Quaternary sediments: Why aliquot size matters in luminescence dating. *Boreas*, 37(4), 589–612. <https://doi.org/10.1111/j.1502-3885.2008.00051.x>
- DuRoss, C. B., Bunds, M. P., Gold, R. D., Briggs, R. W., Reitman, N. G., Personius, S. F., & Toké, N. A. (2019). Variable normal-fault rupture behavior, northern Lost River fault zone, Idaho, USA. *Geosphere*, 15(6), 1869–1892. <https://doi.org/10.1130/GES02096.1>
- DuRoss, C. B., Personius, S. F., Crone, A. J., Olig, S. S., & Lund, W. R. (2011). Integration of paleoseismic data from multiple sites to develop an objective earthquake chronology: Application to the Weber Segment of the Wasatch Fault Zone, Utah. *Bulletin of the Seismological Society of America*, 101(6), 2765–2781. <https://doi.org/10.1785/0120110102>
- Dziewonski, A. M., Chou, T.-A., & Woodhouse, J. H. (1981). Determination of earthquake source parameters from waveform data for studies of global and regional seismicity. *Journal of Geophysical Research: Solid Earth*, 86(B4), 2825–2852. <https://doi.org/10.1029/JB086iB04p02825>
- Ekström, G., Nettles, M., & Dziewoński, A. M. (2012). The global CMT project 2004–2010: Centroid-moment tensors for 13,017 earthquakes. *Physics of the Earth and Planetary Interiors*, 200–201, 1–9. <https://doi.org/10.1016/j.pepi.2012.04.002>
- Elliott, J. R., Nissen, E. K., England, P. C., Jackson, J. A., Lamb, S., Li, Z., Oehlers, M., & Parsons, B. (2012). Slip in the 2010–2011 Canterbury earthquakes, New Zealand. *Journal of Geophysical Research: Solid Earth*, 117(B3). <https://doi.org/10.1029/2011JB008868>
- Ellis, M. A., & Dunlap, W. J. (1988). Displacement variation along thrust faults: Implications for the development of large faults. *Journal of Structural Geology*, 10(2), 183–192. [https://doi.org/10.1016/0191-8141\(88\)90115-0](https://doi.org/10.1016/0191-8141(88)90115-0)

- Fan, G., Ni, J. F., & Wallace, T. C. (1994). Active tectonics of the Pamirs and Karakorum. *Journal of Geophysical Research: Solid Earth*, 99(B4), 7131–7160. <https://doi.org/10.1029/93JB02970>
- Forman, S. L. (2015). Luminescence dating in paleoseismology. *J Geophys Res*, 102, 8137–8157.
- Forman, S. L., Pierson, J., & Lepper, K. (2000). Luminescence Geochronology. In *Quaternary Geochronology* (pp. 157–176). American Geophysical Union (AGU). <https://doi.org/10.1029/RF004p0157>
- Freisleben, R. (2018). Tectonic geomorphology of the central Trans Alai piedmont, northern Pamir mountains, Kyrgyzstan [Master Thesis]. University of Potsdam.
- Fuchs, M. C., Gloaguen, R., & Pohl, E. (2013). Tectonic and climatic forcing on the Panj river system during the Quaternary. *International Journal of Earth Sciences*, 102(7), 1985–2003. <https://doi.org/10.1007/s00531-013-0916-2>
- Galbraith, R. F., & Roberts, R. G. (2012). Statistical aspects of equivalent dose and error calculation and display in OSL dating: An overview and some recommendations. *Quaternary Geochronology*, 11, 1–27. <https://doi.org/10.1016/j.quageo.2012.04.020>
- Gold, R. D., Reitman, N. G., Briggs, R. W., Barnhart, W. D., Hayes, G. P., & Wilson, E. (2015). On- and off-fault deformation associated with the September 2013 Mw 7.7 Balochistan earthquake: Implications for geologic slip rate measurements. *Tectonophysics*, 660, 65–78. <https://doi.org/10.1016/j.tecto.2015.08.019>
- Goodfriend, G. A., & Stipp, J. J. (1983). Limestone and the problem of radiocarbon dating of land-snail shell carbonate. *Geology*, 11(10), 575–577. [https://doi.org/10.1130/0091-7613\(1983\)11<575:LATPOR>2.0.CO;2](https://doi.org/10.1130/0091-7613(1983)11<575:LATPOR>2.0.CO;2)
- Gordon, R. G., & Stein, S. (1992). Global tectonics and space geodesy. *Science*. <https://doi.org/10.1126/science.256.5055.333>
- Gray, H. J., Mahan, S. A., Rittenour, T., Nelson, M., & Lund, W. R. (2015). Guide to luminescence dating techniques and their applications for paleoseismic research. *Proceedings Volume, Basin and Range Province Seismic Hazards Summit III Utah Geological Survey Miscellaneous Publication*, 15–5.
- Grützner, C., Campbell, G., Walker, R. t., Jackson, J., Mackenzie, D., Abdrakhmatov, K., & Mukambayev, A. (2019). Shortening accommodated by thrust and strike-slip Faults in the Ili Basin, northern Tien Shan. *Tectonics*, 38(7), 2255–2274. <https://doi.org/10.1029/2018TC005459>
- Grützner, C., Carson, E., Walker, R. T., Rhodes, E. J., Mukambayev, A., Mackenzie, D., Elliott, J. R., Campbell, G., & Abdrakhmatov, K. (2017). Assessing the activity of faults in continental interiors: Palaeoseismic insights from SE Kazakhstan. *Earth and Planetary Science Letters*, 459, 93–104. <https://doi.org/10.1016/j.epsl.2016.11.025>
- Hacker, B., Luffi, P., Lutkov, V., Minaev, V. T., Ratschbacher, L., Plank, T., Ducea, M. N., Patino, A., McWilliams, M., & Metcalf, J. (2005). Near-ultrahigh pressure processing of continental crust: Miocene crustal Xenoliths from the Pamir. *Journal of Petrology*, 46(8), 1661–1687. <https://doi.org/10.1093/petrology/egi030>
- Hamburger, M. W., Sarewitz, D. R., Pavlis, T. L., & Popandopulo, G. A. (1992). Structural and seismic evidence for intracontinental subduction in the Peter the First Range, Central Asia. *GSA Bulletin*, 104(4), 397–408. [https://doi.org/10.1130/0016-7606\(1992\)104<0397:SASEFI>2.3.CO;2](https://doi.org/10.1130/0016-7606(1992)104<0397:SASEFI>2.3.CO;2)
- Hanks, T. C., & Kanamori, H. (1979). A moment magnitude scale. *Journal of Geophysical Research: Solid Earth*, 84(B5), 2348–2350. <https://doi.org/10.1029/JB084iB05p02348>
- Hao, Y. C., & Zeng, X. L. (1984). Discussion of the Mesozoic-Cenozoic evolution of the western Tarim basin based on Foraminifera. *Chin. Micropaleonol. Bull*, 1, 1–4.
- Harding, T. P. (1985). Seismic characteristics and identification of negative flower structures, positive flower structures, and positive structural inversion. *AAPG Bulletin*, 69(4), 582–600. <https://doi.org/10.1306/AD462538-16F7-11D7-8645000102C1865D>
- Hayes, G. P., Smoczyk, G. M., Villaseñor, A. H., Furlong, K. P., & Benz, H. M. (2020). Seismicity of the Earth 1900–2018. In *Seismicity of the Earth 1900–2018* (USGS Numbered Series No. 3446; Scientific Investigations Map, Vol. 3446). U.S. Geological Survey. <https://doi.org/10.3133/sim3446>
- He, P., Hetland, E. A., Niemi, N. A., Wang, Q., Wen, Y., & Ding, K. (2018). The 2016 Mw 6.5 Nura earthquake in the Trans Alai range, northern Pamir: Possible rupture on a back-thrust fault constrained by Sentinel-1A radar interferometry. *Tectonophysics*, 749, 62–71. <https://doi.org/10.1016/j.tecto.2018.10.025>

- Herzschuh, U. (2006). Palaeo-moisture evolution in monsoonal Central Asia during the last 50,000 years. *Quaternary Science Reviews*, 25(1), 163–178. <https://doi.org/10.1016/j.quascirev.2005.02.006>
- Hsu, Y.-J., Avouac, J.-P., Yu, S.-B., Chang, C.-H., Wu, Y.-M., & Woessner, J. (2009). Spatio-temporal slip, and stress level on the faults within the Western Foothills of Taiwan: Implications for fault frictional properties. *Pure and Applied Geophysics*, 166(10), 1853–1884. <https://doi.org/10.1007/s00024-009-0510-5>
- Hsu, Y.-J., Simons, M., Yu, S.-B., Kuo, L.-C., & Chen, H.-Y. (2003). A two-dimensional dislocation model for interseismic deformation of the Taiwan mountain belt. *Earth and Planetary Science Letters*, 211(3), 287–294. [https://doi.org/10.1016/S0012-821X\(03\)00203-6](https://doi.org/10.1016/S0012-821X(03)00203-6)
- Huntley, D. J., Godfrey-Smith, D. I., & Thewalt, M. L. W. (1985). Optical dating of sediments. *Nature*, 313(5998), 105–107. <https://doi.org/10.1038/313105a0>
- Huntley, D. J., & Lamothe, M. (2001). Ubiquity of anomalous fading in K-feldspars and the measurement and correction for it in optical dating. *Canadian Journal of Earth Sciences*, 38(7), 1093–1106. <https://doi.org/10.1139/e01-013>
- Ischuk, A., Bendick, R., Rybin, A., Molnar, P., Khan, S. F., Kuzikov, S., Mohadjer, S., Saydullaev, U., Ilysova, Z., Schelochkov, G., & Zubovich, A. V. (2013). Kinematics of the Pamir and Hindu Kush regions from GPS geodesy. *Journal of Geophysical Research: Solid Earth*, 118(5), 2408–2416. <https://doi.org/10.1002/jgrb.50185>
- Ishii, Y., Takahashi, T., & Ito, K. (2022). Luminescence dating of cobbles from Pleistocene fluvial terrace deposits of the Ara River, Japan. *Quaternary Geochronology*, 67, 101228. <https://doi.org/10.1016/j.quageo.2021.101228>
- Jackson, J. A. (1980). Reactivation of basement faults and crustal shortening in orogenic belts. *Nature*, 283(5745), 343–346. <https://doi.org/10.1038/283343a0>
- Jackson, J. A., Molnar, P., Patton, H., & Fitch, T. (1979). Seismotectonic aspects of the Markansu Valley, Tadjikstan, earthquake of August 11, 1974. *Journal of Geophysical Research: Solid Earth*, 84(B11), 6157–6167. <https://doi.org/10.1029/JB084iB11p06157>
- Jara-Muñoz, J., Melnick, D., Brill, D., & Strecker, M. R. (2015). Segmentation of the 2010 Maule Chile earthquake rupture from a joint analysis of uplifted marine terraces and seismic-cycle deformation patterns. *Quaternary Science Reviews*, 113, 171–192. <https://doi.org/10.1016/j.quascirev.2015.01.005>
- Johnson, K., Nissen, E., & Lajoie, L. (2018). Surface rupture morphology and vertical slip distribution of the 1959 Mw 7.2 Hebgen Lake (Montana) earthquake from airborne lidar topography. *Journal of Geophysical Research: Solid Earth*, 123(9), 8229–8248. <https://doi.org/10.1029/2017JB015039>
- Johnson, K., Nissen, E., Saripalli, S., Arrowsmith, J. R., McGarey, P., Scharer, K., Williams, P., & Blisniuk, K. (2014). Rapid mapping of ultrafine fault zone topography with structure from motion. *Geosphere*, 10(5), 969–986. <https://doi.org/10.1130/GES01017.1>
- Jones, W. K., & Deike, G. H. (1981). A hydrogeologic study of the watershed of the National Fisheries Center at Leetown, West Virginia. *Environmental Data*, Frankford WV.
- Kalmetieva, Z. A., Mikolaichuk, A. V., Moldobekov, B. D., Meleshko, A. V., Jantaev, M. M., Zubovich, A. V., & Havenith, H. B. (2009). Atlas of earthquakes in Kyrgyzstan. In CAIAG, Bishkek (Vol. 76).
- Kamen, M. (1963). Early history of Carbon-14: Discovery of this supremely important tracer was expected in the physical sense but not in the chemical sense. *Science*. <https://doi.org/10.1126/SCIENCE.140.3567.584>
- Kaneda, H., Nakata, T., Tsutsumi, H., Kondo, H., Sugito, N., Awata, Y., Akhtar, S. S., Majid, A., Khattak, W., Awan, A. A., Yeats, R. S., Hussain, A., Ashraf, M., Wesnousky, S. G., & Kausar, A. B. (2008). Surface Rupture of the 2005 Kashmir, Pakistan, Earthquake and Its Active Tectonic Implications. *Bulletin of the Seismological Society of America*, 98(2), 521–557. <https://doi.org/10.1785/0120070073>
- Kaneko, Y., Hamling, I. J., Van Dissen, R. J., Motagh, M., & Samsonov, S. V. (2015). InSAR imaging of displacement on flexural-slip faults triggered by the 2013 Mw 6.6 Lake Grassmere earthquake, central New Zealand. *Geophysical Research Letters*, 42(3), 781–788. <https://doi.org/10.1002/2014GL062767>

- Karabacak, V., Ring, U., & Uysal, I. T. (2020). The off-fault deformation on the North Anatolian Fault zone and assessment of slip rate from carbonate veins. *Tectonophysics*, 795, 228633. <https://doi.org/10.1016/j.tecto.2020.228633>
- Kars, R. H., & Wallinga, J. (2009). IRSL dating of K-feldspars: Modelling natural dose response curves to deal with anomalous fading and trap competition. *Radiation Measurements*, 44(5), 594–599. <https://doi.org/10.1016/j.radmeas.2009.03.032>
- Koppes, M., Gillespie, A. R., Burke, R. M., Thompson, S. C., & Stone, J. (2008). Late Quaternary glaciation in the Kyrgyz Tien Shan. *Quaternary Science Reviews*, 27(7), 846–866. <https://doi.org/10.1016/j.quascirev.2008.01.009>
- Kostrov, V. V. (1974). Seismic moment and energy of earthquakes, and seismic flow of rock. *Izv. Acad. Sci. USSR Phys. Solid Earth, Engl. Transl.*, 1, 23–44.
- Kozlov, V. V., & Artemov, A. V. (1964). Geological map of Kyrgyzstan, scale 1:200,000, Alai Valley sheet J-43-II. All Union Geolog. TREST, Moscow.
- Krieger, G., Moreira, A., Fiedler, H., Hajnsek, I., Werner, M., Younis, M., & Zink, M. (2007). TanDEM-X: A satellite formation for high-resolution SAR interferometry. *IEEE Transactions on Geoscience and Remote Sensing*, 45(11), 3317–3341. <https://doi.org/10.1109/TGRS.2007.900693>
- Kufner, S.-K., Schurr, B., Haberland, C., Zhang, Y., Saul, J., Ischuk, A., & Oimahmadov, I. (2017). Zooming into the Hindu Kush slab break-off: A rare glimpse on the terminal stage of subduction. *Earth and Planetary Science Letters*, 461, 127–140. <https://doi.org/10.1016/j.epsl.2016.12.043>
- Kufner, S.-K., Schurr, B., Sippl, C., Yuan, X., Ratschbacher, L., Akbar, A. s/of M., Ischuk, A., Murodkulov, S., Schneider, F., Mechie, J., & Tilmann, F. (2016). Deep India meets deep Asia: Lithospheric indentation, delamination and break-off under Pamir and Hindu Kush (Central Asia). *Earth and Planetary Science Letters*, 435, 171–184. <https://doi.org/10.1016/j.epsl.2015.11.046>
- Kumar, S., Wesnousky, S. G., Rockwell, T. K., Briggs, R. W., Thakur, V. C., & Jayangondaperumal, R. (2006). Paleoseismic evidence of great surface rupture earthquakes along the Indian Himalaya. *Journal of Geophysical Research: Solid Earth*, 111(B3). <https://doi.org/10.1029/2004JB003309>
- Kyrgyz Geodetic and Cartographic Agency. (1978). Topographic map of Kyrgyzstan [Map]. Scientific and Technological Publishing House on Geology and the Earth's Interior (Gosgeoltechizdat).
- Lamothe, M., Auclair, M., Hamzaoui, C., & Huot, S. (2003). Towards a prediction of long-term anomalous fading of feldspar IRSL. *Radiation Measurements*, 37(4), 493–498. [https://doi.org/10.1016/S1350-4487\(03\)00016-7](https://doi.org/10.1016/S1350-4487(03)00016-7)
- Leith, W. (1982). Rock assemblages in central Asia and the evolution of the Southern Asian Margin. *Tectonics*, 1(3), 303–318. <https://doi.org/10.1029/TC001i003p00303>
- Leonard, M. (2010). Earthquake fault scaling: Self-consistent relating of rupture length, width, average displacement, and moment release. *Bulletin of the Seismological Society of America*, 100(5A), 1971–1988. <https://doi.org/10.1785/0120090189>
- Leonard, M. (2014). Self-consistent earthquake fault-scaling relations: Update and extension to stable continental strike-slip faults. *Bulletin of the Seismological Society of America*, 104(6), 2953–2965. <https://doi.org/10.1785/0120140087>
- Li, Q., Liu, M., & Stein, S. (2009). Spatiotemporal complexity of continental intraplate seismicity: Insights from geodynamic modeling and implications for seismic hazard estimation. *Bulletin of the Seismological Society of America*, 99(1), 52–60. <https://doi.org/10.1785/0120080005>
- Li, T., Chen, J., Thompson, J. A., Burbank, D. W., & Xiao, W. (2012). Equivalency of geologic and geodetic rates in contractional orogens: New insights from the Pamir Frontal Thrust. *Geophysical Research Letters*, 39(15). <https://doi.org/10.1029/2012GL051782>
- Li, T., Chen, J., Thompson, J. A., Burbank, D. W., & Yang, H. (2015a). Hinge-migrated fold-scarp model based on an analysis of bed geometry: A study from the Mingyaole anticline, southern foreland of Chinese Tian Shan. *Journal of Geophysical Research: Solid Earth*, 120(9), 6592–6613. <https://doi.org/10.1002/2015JB012102>
- Li, T., Chen, J., Thompson, J. A., Burbank, D. W., & Yang, X. (2013). Quantification of three-dimensional folding using fluvial terraces: A case study from the Mushi anticline, northern margin of the Chinese Pamir. *Journal of Geophysical Research: Solid Earth*, 118(8), 4628–4647. <https://doi.org/10.1002/jgrb.50316>

- Li, T., Chen, J., Thompson, J. A., Burbank, D. W., & Yang, X. (2015b). Active flexural-slip faulting: A study from the Pamir-Tian Shan convergent zone, NW China. *Journal of Geophysical Research: Solid Earth*, 120(6), 4359–4378. <https://doi.org/10.1002/2014JB011632>
- Li, T., Chen, J., Thompson Jobe, J. A., Burbank, D. W., Cheng, X., Xu, J., Li, Z., Zheng, W., & Zhang, P. (2018). Active bending-moment faulting: Geomorphic Expression, Controlling conditions, accommodation of fold deformation. *Tectonics*, 37(8), 2278–2306. <https://doi.org/10.1029/2018TC004982>
- Li, T., Chen, Z., Chen, J., Thompson Jobe, J. A., Burbank, D. W., Li, Z., He, X., Zheng, W., Zhang, P., & Zhang, B. (2019). Along-strike and downdip segmentation of the Pamir Frontal Thrust and its association with the 1985 Mw 6.9 Wuqia earthquake. *Journal of Geophysical Research: Solid Earth*, 124(9), 9890–9919. <https://doi.org/10.1029/2019JB017319>
- Li, T., Schoenbohm, L. M., Chen, J., Yuan, Z., Feng, W., Li, W., Xu, J., Owen, L. A., Sobel, E. R., Zhang, B., Zheng, W., & Zhang, P. (2019). Cumulative and coseismic (during the 2016 Mw 6.6 Aketao Earthquake) deformation of the dextral-slip Muji Fault, Northeastern Pamir Orogen. *Tectonics*, 38(11), 3975–3989. <https://doi.org/10.1029/2019TC005680>
- Li, W., Chen, Y., Yuan, X., Schurr, B., Mechie, J., Oimahmadov, I., & Fu, B. (2018). Continental lithospheric subduction and intermediate-depth seismicity: Constraints from S-wave velocity structures in the Pamir and Hindu Kush. *Earth and Planetary Science Letters*, 482, 478–489. <https://doi.org/10.1016/j.epsl.2017.11.031>
- Libby, W. F. (1961). Radiocarbon Dating. *Science*, 133(3453), 621–629.
- Lienkaemper, J. J., & Ramsey, C. B. (2009). OxCal: Versatile tool for developing paleoearthquake chronologies—A Primer. *Seismological Research Letters*, 80(3), 431–434. <https://doi.org/10.1785/gssrl.80.3.431>
- Lin, A. T., Yao, B., Hsu, S.-K., Liu, C.-S., & Huang, C.-Y. (2009). Tectonic features of the incipient arc-continent collision zone of Taiwan: Implications for seismicity. *Tectonophysics*, 479(1), 28–42. <https://doi.org/10.1016/j.tecto.2008.11.004>
- Lindsey, E. O., Almeida, R., Mallick, R., Hubbard, J., Bradley, K., Tsang, L. L. H., Liu, Y., Burgmann, R., & Hill, E. M. (2018). Structural control on downdip locking extent of the Himalayan megathrust. *Journal of Geophysical Research: Solid Earth*, 123(6), 5265–5278. <https://doi.org/10.1029/2018JB015868>
- Liu, Y., Xu, C., Li, Z., Wen, Y., & Forrest, D. (2011). Interseismic slip rate of the Garze–Yushu fault belt in the Tibetan Plateau from C-band InSAR observations between 2003 and 2010. *Advances in Space Research*, 48(12), 2005–2015. <https://doi.org/10.1016/j.asr.2011.08.020>
- Macaulay, E. A., Sobel, E. R., Mikolaichuk, A., Kohn, B., & Stuart, F. M. (2014). Cenozoic deformation and exhumation history of the Central Kyrgyz Tien Shan. *Tectonics*, 33(2), 135–165. <https://doi.org/10.1002/2013TC003376>
- Macaulay, E. A., Sobel, E. R., Mikolaichuk, A., Landgraf, A., Kohn, B., & Stuart, F. (2013). Thermochronologic insight into late Cenozoic deformation in the basement-cored Terskey Range, Kyrgyz Tien Shan. *Tectonics*, 32(3), 487–500. <https://doi.org/10.1002/tect.20040>
- Manighetti, I., Campillo, M., Bouley, S., & Cotton, F. (2007). Earthquake scaling, fault segmentation, and structural maturity. *Earth and Planetary Science Letters*, 253(3), 429–438. <https://doi.org/10.1016/j.epsl.2006.11.004>
- Manighetti, I., Campillo, M., Sammis, C., Mai, P. M., & King, G. (2005). Evidence for self-similar, triangular slip distributions on earthquakes: Implications for earthquake and fault mechanics. *Journal of Geophysical Research: Solid Earth*, 110(B5). <https://doi.org/10.1029/2004JB003174>
- Manighetti, I., Caulet, C., De Barros, L., Perrin, C., Cappa, F., & Gaudemer, Y. (2015). Generic along-strike segmentation of Afar normal faults, East Africa: Implications on fault growth and stress heterogeneity on seismogenic fault planes. *Geochemistry, Geophysics, Geosystems*, 16(2), 443–467. <https://doi.org/10.1002/2014GC005691>
- Mayer, L. (1986). Tectonic geomorphology of escarpments and mountain fronts. *Active Tectonics*, 7, 125–135.
- McCalpin, J. P. (2009). *Paleoseismology* (Vol. 95). Elsevier.
- McCalpin, J. P., & Carver, G. A. (2009). Paleoseismology—Chapter 5: Paleoseismology of compressional tectonic environments. In *International Geophysics* (Vol. 95, pp. 315–419). Academic Press. [https://doi.org/10.1016/S0074-6142\(09\)95005-7](https://doi.org/10.1016/S0074-6142(09)95005-7)

- McFarland, P. K., Bennett, R. A., Alvarado, P., & DeCelles, P. G. (2017). Rapid geodetic shortening across the Eastern Cordillera of NW Argentina observed by the Puna-Andes GPS array. *Journal of Geophysical Research: Solid Earth*, 122(10), 8600–8623. <https://doi.org/10.1002/2017JB014739>
- Mechie, J., Yuan, X., Schurr, B., Schneider, F., Sippl, C., Ratschbacher, L., Minaev, V., Gadoev, M., Oimahmadov, I., Abdybachaev, U., Moldobekov, B., Orunbaev, S., & Negmatullaev, S. (2012). Crustal and uppermost mantle velocity structure along a profile across the Pamir and southern Tien Shan as derived from project TIPAGE wide-angle seismic data. *Geophysical Journal International*, 188(2), 385–407. <https://doi.org/10.1111/j.1365-246X.2011.05278.x>
- Meghraoui, M., Philip, H., Albarede, F., & Cisternas, A. (1988). Trench investigations through the trace of the 1980 El Asnam thrust fault: Evidence for paleoseismicity. *Bulletin of the Seismological Society of America*, 78(2), 979–999. <https://doi.org/10.1785/BSSA0780020979>
- Melnick, D., Bookhagen, B., Strecker, M. R., & Echtler, H. P. (2009). Segmentation of megathrust rupture zones from fore-arc deformation patterns over hundreds to millions of years, Arauco peninsula, Chile. *Journal of Geophysical Research: Solid Earth*, 114(B1). <https://doi.org/10.1029/2008JB005788>
- Metzger, S., Ischuk, A., Deng, Z., Ratschbacher, L., Perry, M., Kufner, S.-K., Bendick, R., & Moreno, M. (2020). Dense GNSS profiles across the northwestern Tip of the India–Asia collision zone: Triggered slip and westward flow of the Peter the First Range, Pamir, into the Tajik depression. *Tectonics*, 39(2), e2019TC005797. <https://doi.org/10.1029/2019TC005797>
- Metzger, S., Schurr, B., Ratschbacher, L., Sudhaus, H., Kufner, S.-K., Schöne, T., Zhang, Y., Perry, M., & Bendick, R. (2017). The 2015 Mw7.2 Sarez strike-slip earthquake in the Pamir interior: Response to the underthrusting of India's Western promontory. *Tectonics*, 36(11), 2407–2421. <https://doi.org/10.1002/2017TC004581>
- Mirabella, F., Boccali, V., & Barchi, M. R. (2005). Segmentation and interaction of normal faults within the Colfiorito fault system (central Italy). *Geological Society, London, Special Publications*, 243(1), 25–36. <https://doi.org/10.1144/GSL.SP.2005.243.01.04>
- Mohadjer, S., Ehlers, T. A., Bendick, R., Stübner, K., & Strube, T. (2016). A Quaternary fault database for central Asia. *Natural Hazards and Earth System Sciences*, 16(2), 529–542. <https://doi.org/10.5194/nhess-16-529-2016>
- Mohadjer, S., Ehlers, T., Bendick, R., & Mutz, S. (2016). Comparison of GPS and Quaternary slip rates: Insights from a new Quaternary fault database for Central Asia. *EPSC2016-5963*.
- Mohajjel, M., & Behyari, M. (2010). Young transpressive positive flower structure along the Zagros collision zone, Nahavand area, west Iran. *New England Orogen 2010: Proceedings of a Conference Held at the University of New England, Armidale, New South Wales, Australia*, 242–251.
- Molnar, P. (1987). Active tectonics. *Eos, Transactions American Geophysical Union*, 68(12), 164–164. <https://doi.org/10.1029/EO068i012p00164-02>
- Molnar, P. (1988). Continental tectonics in the aftermath of plate tectonics. *Nature*, 335(6186), 131–137. <https://doi.org/10.1038/335131a0>
- Molnar, P., & Chen, W.-P. (1983). Seismicity and mountain building. *Symposium on Mountain Building*, pp. 41–56.
- Molnar, P., & Stock, J. M. (2009). Slowing of India's convergence with Eurasia since 20 Ma and its implications for Tibetan mantle dynamics. *Tectonics*, 28(3). <https://doi.org/10.1029/2008TC002271>
- Molnar, P., & Tapponnier, P. (1975). Cenozoic tectonics of Asia: Effects of a continental collision. *Science*, 189(4201), 419–426.
- Moss, R. E. S., & Ross, Z. E. (2011). Probabilistic fault displacement hazard analysis for reverse faults. *Bulletin of the Seismological Society of America*, 101(4), 1542–1553. <https://doi.org/10.1785/0120100248>
- Mugnier, J.-L., Gajurel, A., Huyghe, P., Jayangondaperumal, R., Jouanne, F., & Upreti, B. (2013). Structural interpretation of the great earthquakes of the last millennium in the central Himalaya. *Earth-Science Reviews*, 127, 30–47. <https://doi.org/10.1016/j.earscirev.2013.09.003>
- Mugnier, J.-L., Jouanne, F., Bhattarai, R., Cortes-Aranda, J., Gajurel, A., Leturmy, P., Robert, X., Upreti, B., & Vassallo, R. (2017). Segmentation of the Himalayan megathrust around the Gorkha earthquake (25 April 2015) in Nepal. *Journal of Asian Earth Sciences*, 141, 236–252. <https://doi.org/10.1016/j.jseaes.2017.01.015>

- Nicol, A., Van Dissen, R. J., Stirling, M. W., & Gerstenberger, M. C. (2016). Completeness of the paleoseismic active-fault record in New Zealand. *Seismological Research Letters*, 87(6), 1299–1310. <https://doi.org/10.1785/0220160088>
- Nikonov, A. A. (1988). Reconstruction of the main parameters of old large earthquakes in Soviet Central Asia using the paleoseismogeological method. *Tectonophysics*, 147(3), 297–312. [https://doi.org/10.1016/0040-1951\(88\)90191-6](https://doi.org/10.1016/0040-1951(88)90191-6)
- Nikonov, A. A., Vakov, A. V., & Veselov, I. A. (1983). Seismotectonics and earthquakes in the convergent zone between the Pamir and the Tien Shan. Moscow, Nauka.
- Nöth, L. (1932). Geologische Untersuchungen im nordwestlichen Pamirgebiet und mittleren Transalai. In Ficker, H.v., and Rickmers, W.R., eds., *Wissenschaftliche Ergebnisse der Alai-Pamir Expedition 1928, Part II*: Berlin, Reimer-Vohsen, 204 p. (in German).
- Novák, D. (2016). Local Relief Model (LRM) Toolbox for ArcGIS. <https://doi.org/10.13140/RG.2.2.13956.88961>
- Oskin, M., Perg, L., Blumentritt, D., Mukhopadhyay, S., & Iriondo, A. (2007). Slip rate of the Calico fault: Implications for geologic versus geodetic rate discrepancy in the Eastern California Shear Zone. *Journal of Geophysical Research: Solid Earth*, 112(B3). <https://doi.org/10.1029/2006JB004451>
- Ouyed, M., Meghraoui, M., Cisternas, A., Deschamps, A., Dorel, J., Frechet, J., Gaulon, R., Hatzfeld, D., & Philip, H. (1981). Seismotectonics of the El Asnam earthquake. *Nature*, 292(5818), 26–31. <https://doi.org/10.1038/292026a0>
- Papanikolaou, I. D., Roberts, G. P., & Michetti, A. M. (2005). Fault scarps and deformation rates in Lazio–Abruzzo, Central Italy: Comparison between geological fault slip-rate and GPS data. *Tectonophysics*, 408(1), 147–176. <https://doi.org/10.1016/j.tecto.2005.05.043>
- Patyniak, M., Landgraf, A., Dzhumabaeva, A., Abdrakhmatov, K., Rosenwinkel, S., Korup, O., Preusser, F., Fohlmeister, J., Arrowsmith, J. R., & Strecker, M. R. (2017). Paleoseismic record of three Holocene earthquakes rupturing the Issyk-Ata Fault near Bishkek, North Kyrgyzstan. *Bulletin of the Seismological Society of America*, 107(6), 2721–2737. <https://doi.org/10.1785/0120170083>
- Pavlis, G. L., & Das, S. (2000). The Pamir-Hindu Kush seismic zone as a strain marker for flow in the upper mantle. *Tectonics*, 19(1), 103–115. <https://doi.org/10.1029/1999TC900062>
- Perrin, C., Manighetti, I., Ampuero, J.-P., Cappa, F., & Gaudemer, Y. (2016). Location of largest earthquake slip and fast rupture controlled by along-strike change in fault structural maturity due to fault growth. *Journal of Geophysical Research: Solid Earth*, 121(5), 3666–3685. <https://doi.org/10.1002/2015JB012671>
- Perrin, C., Manighetti, I., & Gaudemer, Y. (2016). Off-fault tip splay networks: A genetic and generic property of faults indicative of their long-term propagation. *Comptes Rendus Geoscience*, 348(1), 52–60. <https://doi.org/10.1016/j.crte.2015.05.002>
- Personius, S. F., DuRoss, C. B., & Crone, A. J. (2012). Holocene behavior of the Brigham City Segment: Implications for forecasting the next large-magnitude earthquake on the Wasatch Fault Zone, Utah. *Bulletin of the Seismological Society of America*, 102(6), 2265–2281. <https://doi.org/10.1785/0120110214>
- Personius, S. F., & Mahan, S. A. (2005). Unusually low rates of slip on the Santa Rosa Range Fault Zone, Northern Nevada. *Bulletin of the Seismological Society of America*, 95(1), 319–333. <https://doi.org/10.1785/0120040001>
- Philibosian, B., & Meltzner, A. J. (2020). Segmentation and supercycles: A catalog of earthquake rupture patterns from the Sumatran Sunda Megathrust and other well-studied faults worldwide. *Quaternary Science Reviews*, 241, 106390. <https://doi.org/10.1016/j.quascirev.2020.106390>
- Philip, H., & Meghraoui, M. (1983). Structural analysis and interpretation of the surface deformations of the El Asnam Earthquake of October 10, 1980. *Tectonics*, 2(1), 17–49. <https://doi.org/10.1029/TC002i001p00017>
- Philip, H., Rogozhin, E., Cisternas, A., Bousquet, J. C., Borisov, B., & Karakhanian, A. (1992). The Armenian earthquake of 1988 December 7: Faulting and folding, neotectonics and palaeoseismicity. *Geophysical Journal International*, 110(1), 141–158. <https://doi.org/10.1111/j.1365-246X.1992.tb00718.x>
- Pigati, J. S., Quade, J., Shahanan, T. M., & Haynes, C. V. (2004). Radiocarbon dating of minute gastropods and new constraints on the timing of late Quaternary spring-discharge deposits in southern Arizona, USA.

- Palaeogeography, Palaeoclimatology, Palaeoecology, 204(1), 33–45. [https://doi.org/10.1016/S0031-0182\(03\)00710-7](https://doi.org/10.1016/S0031-0182(03)00710-7)
- Pigati, J. S., Rech, J. A., & Nekola, J. C. (2010). Radiocarbon dating of small terrestrial gastropod shells in North America. *Quaternary Geochronology*, 5(5), 519–532. <https://doi.org/10.1016/j.quageo.2010.01.001>
- Pirazzoli, P. A. (2019). Tectonics and neotectonics. In C. W. Finkl & C. Makowski (Eds.), *Encyclopedia of Coastal Science* (pp. 1680–1690). Springer International Publishing. https://doi.org/10.1007/978-3-319-93806-6_310
- Pojarkova, Z. N. (1969). Stratigraphy of Upper Cretaceous deposits of the southern Kirgizia. Ilim, Frunze.
- Preusser, F., Degering, D., Fuchs, M., Hilgers, A., Kadereit, A., Klasen, N., Krubetschek, M., Richter, D., & Spencer, J. Q. G. (2008). Luminescence dating: Basics, methods and applications. *E&G Quaternary Science Journal*, 57(1/2), 95–149. <https://doi.org/10.3285/eg.57.1-2.5>
- Preusser, F., & Kasper, H. U. (2001). Comparison of dose rate determination using high-resolution gamma spectrometry and inductively coupled plasma-mass spectrometry. *Ancient TL*, 19(1), 19–23.
- Preusser, F., Ramseyer, K., & Schlüchter, C. (2006). Characterisation of low OSL intensity quartz from the New Zealand Alps. *Radiation Measurements*, 41(7), 871–877. <https://doi.org/10.1016/j.radmeas.2006.04.019>
- Qiao, X., Wang, Q., Yang, S., Li, J., Zou, R., & Ding, K. (2015). The 2008 Nura Mw6.7 earthquake: A shallow rupture on the Main Pamir Thrust revealed by GPS and InSAR. *Geodesy and Geodynamics*, 6(2), 91–100. <https://doi.org/10.1016/j.geog.2015.01.005>
- Qiao, X., Yu, P., Nie, Z., Li, J., Wang, X., Kuzikov, S. I., Wang, Q., & Yang, S. (2017). The crustal deformation revealed by GPS and InSAR in the northwest corner of the Tarim Basin, northwestern China. *Pure and Applied Geophysics*, 174(3), 1405–1423. <https://doi.org/10.1007/s00024-017-1473-6>
- Razvalyaev, L. T., Protasevich, & Evdokimova, E. A. (1964). Geological map of Kyrgyzstan, scale 1:200,000, Alai Valley sheet J-43-I. All Union Geolog. TREST, Moscow.
- Reigber, Ch., Michel, G. W., Galas, R., Angermann, D., Klotz, J., Chen, J. Y., Papschev, A., Arslanov, R., Tzurkov, V. E., & Ishanov, M. C. (2001). New space geodetic constraints on the distribution of deformation in Central Asia. *Earth and Planetary Science Letters*, 191(1), 157–165. [https://doi.org/10.1016/S0012-821X\(01\)00414-9](https://doi.org/10.1016/S0012-821X(01)00414-9)
- Reimer, P. J., Austin, W. E. N., Bard, E., Bayliss, A., Blackwell, P. G., Ramsey, C. B., Butzin, M., Cheng, H., Edwards, R. L., Friedrich, M., Grootes, P. M., Guilderson, T. P., Hajdas, I., Heaton, T. J., Hogg, A. G., Hughen, K. A., Kromer, B., Manning, S. W., Muscheler, R., ... Talamo, S. (2020). The IntCal20 northern hemisphere radiocarbon age calibration curve (0–55 cal kBP). *Radiocarbon*, 62(4), 725–757. <https://doi.org/10.1017/RDC.2020.41>
- Reimer, P. J., Bard, E., Bayliss, A., Beck, J. W., Blackwell, P. G., Ramsey, C. B., Buck, C. E., Cheng, H., Edwards, R. L., & Friedrich, M. (2013). IntCal13 and Marine13 radiocarbon age calibration curves 0–50,000 years cal BP. *Radiocarbon*, 55(4), 1869–1887.
- Reitman, N. G., Bennett, S. E. K., Gold, R. D., Briggs, R. W., & DuRoss, C. B. (2015). High-Resolution Trench Photomosaics from Image-Based Modeling: Workflow and Error Analysis. *Bulletin of the Seismological Society of America*, 105(5), 2354–2366. <https://doi.org/10.1785/0120150041>
- Reznichenko, N. V., Andrews, G. R., Geater, R. E., & Strom, A. (2017). Multiple origins of large hummock deposits in Alai Valley, Northern Pamir: Implications for palaeoclimate reconstructions. *Geomorphology*, 285, 347–362. <https://doi.org/10.1016/j.geomorph.2017.02.019>
- RGI Consortium. (2017). Randolph Glacier Inventory – A dataset of global glacier outlines: Version 6.0: Technical Report [Digital Media]. Global Land Ice Measurements from Space. <http://www.glims.org/RGI/randolph60.html>
- Rhodes, E. J. (2011). Optically stimulated luminescence dating of sediments over the past 200,000 years. *Annual Review of Earth and Planetary Sciences*, 39(1), 461–488. <https://doi.org/10.1146/annurev-earth-040610-133425>
- Richard, P., Mocquet, B., & Cobbold, P. R. (1991). Experiments on simultaneous faulting and folding above a basement wrench fault. *Tectonophysics*, 188(1), 133–141. [https://doi.org/10.1016/0040-1951\(91\)90319-N](https://doi.org/10.1016/0040-1951(91)90319-N)
- Rimando, J. M., Aurelio, M. A., Dianala, J. D. B., Taguibao, K. J. L., Agustin, K. M. C., Berador, A. E. G., & Vasquez, A. A. (2019). Coseismic ground rupture of the 15 October 2013 magnitude (Mw) 7.2 Bohol

- earthquake, Bohol Island, Central Philippines. *Tectonics*, 38(8), 2558–2580. <https://doi.org/10.1029/2019TC005503>
- Rizza, M., Abdrakhmatov, K., Walker, R., Braucher, R., Guillou, V., Carr, A. S., Campbell, G., McKenzie, D., Jackson, J., Aumaitre, G., Bourlès, D. L., & Keddadouche, K. (2019). Rate of slip from multiple Quaternary dating methods and paleoseismic investigations along the Talas-Fergana Fault: Tectonic implications for the Tien Shan range. *Tectonics*, 38(7), 2477–2505. <https://doi.org/10.1029/2018TC005188>
- Rizza, M., Bollinger, L., Sapkota, S. N., Tapponnier, P., Klinger, Y., Karakaş, Ç., Kali, E., Etchebes, M., Tiwari, D. R., Siwakoti, I., Bitri, A., & Bes de Berc, S. (2019). Post earthquake aggradation processes to hide surface ruptures in thrust systems: The M8.3, 1934, Bihar-Nepal earthquake ruptures at Charnath Khola (Eastern Nepal). *Journal of Geophysical Research: Solid Earth*, 124(8), 9182–9207. <https://doi.org/10.1029/2018JB016376>
- Rizzoli, P., Martone, M., Gonzalez, C., Wecklich, C., Borla Tridon, D., Bräutigam, B., Bachmann, M., Schulze, D., Fritz, T., Huber, M., Wessel, B., Krieger, G., Zink, M., & Moreira, A. (2017). Generation and performance assessment of the global TanDEM-X digital elevation model. *ISPRS Journal of Photogrammetry and Remote Sensing*, 132, 119–139. <https://doi.org/10.1016/j.isprsjprs.2017.08.008>
- Robinson, A. C., Yin, A., Manning, C. E., Harrison, T. M., Zhang, S.-H., & Wang, X.-F. (2004). Tectonic evolution of the northeastern Pamir: Constraints from the northern portion of the Cenozoic Kongur Shan extensional system, western China. *GSA Bulletin*, 116(7–8), 953–973. <https://doi.org/10.1130/B25375.1>
- Robinson, T. R., Davies, T. R., Reznichenko, N. V., & De Pascale, G. P. (2015). The extremely long-runout Komansu rock avalanche in the Trans Alai range, Pamir Mountains, southern Kyrgyzstan. *Landslides*, 12(3), 523–535.
- Rockwell, T. K., Ragona, D. E., Meigs, A. J., Owen, L. A., Costa, C. H., & Ahumada, E. A. (2013). Inferring a thrust-related earthquake history from secondary faulting: A long rupture record of La Laja Fault, San Juan, Argentina. *Bulletin of the Seismological Society of America*, 104(1), 269–284. <https://doi.org/10.1785/0120110080>
- Röhringer, I., Zech, R., Abramowski, U., Sosin, P., Aldahan, A., Kubik, P. W., Zöller, L., & Zech, W. (2012). The late Pleistocene glaciation in the Bogchigir Valleys (Pamir, Tajikistan) based on ¹⁰Be surface exposure dating. *Quaternary Research*, 78(3), 590–597. <https://doi.org/10.1016/j.yqres.2012.09.002>
- Rubin, C. M. (1996). Systematic underestimation of earthquake magnitudes from large intracontinental reverse faults: Historical ruptures break across segment boundaries. *Geology*, 24(11), 989–992. [https://doi.org/10.1130/0091-7613\(1996\)024<0989:SUEMF>2.3.CO;2](https://doi.org/10.1130/0091-7613(1996)024<0989:SUEMF>2.3.CO;2)
- Ruegg, J. C., Kasser, M., Tarantola, A., Lepine, J. C., & Chouikrat, B. (1982). Deformations associated with the El Asnam earthquake of 10 October 1980: Geodetic determination of vertical and horizontal movements. *Bulletin of the Seismological Society of America*, 72(6A), 2227–2244. <https://doi.org/10.1785/BSSA07206A2227>
- Sanz de Galdeano, C., López Casado, C., Delgado, J., & Peinado, M. A. (1995). Shallow seismicity and active faults in the Betic Cordillera. A preliminary approach to seismic sources associated with specific faults. *Tectonophysics*, 248(3), 293–302. [https://doi.org/10.1016/0040-1951\(94\)00279-I](https://doi.org/10.1016/0040-1951(94)00279-I)
- Scharer, K. M., Burbank, D. W., Chen, J., & Weldon, R. J., II. (2006). Kinematic models of fluvial terraces over active detachment folds: Constraints on the growth mechanism of the Kashi-Atushi fold system, Chinese Tian Shan. *GSA Bulletin*, 118(7–8), 1006–1021. <https://doi.org/10.1130/B25835.1>
- Scharer, K. M., Burbank, D. W., Chen, J., Weldon, R. J., Rubin, C., Zhao, R., & Shen, J. (2004). Detachment folding in the Southwestern Tian Shan–Tarim foreland, China: Shortening estimates and rates. *Journal of Structural Geology*, 26(11), 2119–2137. <https://doi.org/10.1016/j.jsg.2004.02.016>
- Scharer, K. M., Weldon, R. J., II, Fumal, T. E., & Biasi, G. P. (2007). Paleoseismicity on the Southern San Andreas Fault, Wrightwood, California, 3000 to 1500 b.c.: A New Method for Evaluating Paleoseismic Evidence and Earthquake Horizons. *Bulletin of the Seismological Society of America*, 97(4), 1054–1093. <https://doi.org/10.1785/0120060137>
- Schmidt, J., Hacker, B. R., Ratschbacher, L., Stübner, K., Stearns, M., Kylander-Clark, A., Cottle, J. M., Alexander, A., Webb, G., Gehrels, G., & Minaev, V. (2011). Cenozoic deep crust in the Pamir. *Earth and Planetary Science Letters*, 312(3), 411–421. <https://doi.org/10.1016/j.epsl.2011.10.034>

- Schneider, F. M., Yuan, X., Schurr, B., Mechie, J., Sippl, C., Haberland, C., Minaev, V., Oimahmadov, I., Gadoev, M., Radjabov, N., Abdybachev, U., Orunbaev, S., & Negmatullaev, S. (2013). Seismic imaging of subducting continental lower crust beneath the Pamir. *Earth and Planetary Science Letters*, 375, 101–112. <https://doi.org/10.1016/j.epsl.2013.05.015>
- Scholz, C. H., Aviles, C. A., & Wesnousky, S. G. (1986). Scaling differences between large interplate and intraplate earthquakes. *Bulletin of the Seismological Society of America*, 76(1), 65–70. <https://doi.org/10.1785/BSSA0760010065>
- Scholz, C. H., & Gupta, A. (2000). Fault interactions and seismic hazard. *Journal of Geodynamics*, 29(3), 459–467. [https://doi.org/10.1016/S0264-3707\(99\)00040-X](https://doi.org/10.1016/S0264-3707(99)00040-X)
- Schulte, S. M., & Mooney, W. D. (2005). An updated global earthquake catalogue for stable continental regions: Reassessing the correlation with ancient rifts. *Geophysical Journal International*, 161(3), 707–721. <https://doi.org/10.1111/j.1365-246X.2005.02554.x>
- Schurr, B., Ratschbacher, L., Sippl, C., Gloaguen, R., Yuan, X., & Mechie, J. (2014). Seismotectonics of the Pamir. *Tectonics*, 33(8), 1501–1518. <https://doi.org/10.1002/2014TC003576>
- Schwab, M., Ratschbacher, L., Siebel, W., McWilliams, M., Minaev, V., Lutkov, V., Chen, F., Stanek, K., Nelson, B., Frisch, W., & Wooden, J. L. (2004). Assembly of the Pamirs: Age and origin of magmatic belts from the southern Tien Shan to the southern Pamirs and their relation to Tibet. *Tectonics*, 23(4). <https://doi.org/10.1029/2003TC001583>
- Schwanghart, W., & Scherler, D. (2014). Short Communication: TopoToolbox 2 – MATLAB-based software for topographic analysis and modeling in Earth surface sciences. *Earth Surface Dynamics*, 2(1), 1–7. <https://doi.org/10.5194/esurf-2-1-2014>
- Schwartz, D. P., & Coppersmith, K. J. (1984). Fault behavior and characteristic earthquakes: Examples from the Wasatch and San Andreas Fault Zones. *Journal of Geophysical Research: Solid Earth*, 89(B7), 5681–5698. <https://doi.org/10.1029/JB089iB07p05681>
- Seeber, L., Armbruster, J. G., & Quittmeyer, R. C. (1981). Seismicity and continental subduction in the Himalayan Arc. In *Zagros Hindu Kush Himalaya Geodynamic Evolution* (pp. 215–242). American Geophysical Union (AGU). <https://doi.org/10.1029/GD003p0215>
- Sippl, C., Ratschbacher, L., Schurr, B., Krumbiegel, C., Rui, H., Pingren, L., & Abdybachev, U. (2014). The 2008 Nura earthquake sequence at the Pamir-Tian Shan collision zone, southern Kyrgyzstan. *Tectonics*, 33(12), 2382–2399. <https://doi.org/10.1002/2014TC003705>
- Sippl, C., Schurr, B., Tynpel, J., Angiboust, S., Mechie, J., Yuan, X., Schneider, F. M., Sobolev, S. V., Ratschbacher, L., & Haberland, C. (2013). Deep burial of Asian continental crust beneath the Pamir imaged with local earthquake tomography. *Earth and Planetary Science Letters*, 384, 165–177. <https://doi.org/10.1016/j.epsl.2013.10.013>
- Sippl, C., Schurr, B., Yuan, X., Mechie, J., Schneider, F. M., Gadoev, M., Orunbaev, S., Oimahmadov, I., Haberland, C., Abdybachev, U., Minaev, V., Negmatullaev, S., & Radjabov, N. (2013). Geometry of the Pamir-Hindu Kush intermediate-depth earthquake zone from local seismic data. *Journal of Geophysical Research: Solid Earth*, 118(4), 1438–1457. <https://doi.org/10.1002/jgrb.50128>
- Smedley, R. K., Buylaert, J.-P., & Újvári, G. (2019). Comparing the accuracy and precision of luminescence ages for partially-bleached sediments using single grains of K-feldspar and quartz. *Quaternary Geochronology*, 53, 101007. <https://doi.org/10.1016/j.quageo.2019.101007>
- Sobel, E. R., Chen, J., Schoenbohm, L. M., Thiede, R., Stockli, D. F., Sudo, M., & Strecker, M. R. (2013). Oceanic-style subduction controls late Cenozoic deformation of the Northern Pamir orogen. *Earth and Planetary Science Letters*, 363, 204–218. <https://doi.org/10.1016/j.epsl.2012.12.009>
- Sobel, E. R., & Dumitru, T. A. (1997). Thrusting and exhumation around the margins of the western Tarim basin during the India-Asia collision. *Journal of Geophysical Research: Solid Earth*, 102(B3), 5043–5063. <https://doi.org/10.1029/96JB03267>
- Sobel, E. R., Schoenbohm, L. M., Chen, J., Thiede, R., Stockli, D. F., Sudo, M., & Strecker, M. R. (2011). Late Miocene–Pliocene deceleration of dextral slip between Pamir and Tarim: Implications for Pamir orogenesis. *Earth and Planetary Science Letters*, 304(3), 369–378. <https://doi.org/10.1016/j.epsl.2011.02.012>

- Spooner, N. A. (1994). The anomalous fading of infrared-stimulated luminescence from feldspars. *Radiation Measurements*, 23(2), 625–632. [https://doi.org/10.1016/1350-4487\(94\)90111-2](https://doi.org/10.1016/1350-4487(94)90111-2)
- Stein, S., Liu, M., Calais, E., & Li, Q. (2009). Mid-continent earthquakes as a complex system. *Seismological Research Letters*, 80(4), 551–553.
- Stewart, I., & Hancock, P. (1994). Neotectonics. In P. Hancock (Ed.), *Continental Deformation* (pp. 370–409). Pergamon Press.
- Strecker, M. R., Frisch, W., Hamburger, M. W., Ratschbacher, L., Semiletkin, S., Zamoruyev, A., & Sturchio, N. (1995). Quaternary deformation in the Eastern Pamirs, Tadjikistan and Kyrgyzstan. *Tectonics*, 14(5), 1061–1079. <https://doi.org/10.1029/95TC00927>
- Strecker, M. R., Hilley, G. E., Arrowsmith, J. R., & Coutand, I. (2003). Differential structural and geomorphic mountain-front evolution in an active continental collision zone: The northwest Pamir, southern Kyrgyzstan. *GSA Bulletin*, 115(2), 166–181. [https://doi.org/10.1130/0016-7606\(2003\)115<0166:DSAGMF>2.0.CO;2](https://doi.org/10.1130/0016-7606(2003)115<0166:DSAGMF>2.0.CO;2)
- Stuiver, M., Braziunas, T. F., Becker, B., & Kromer, B. (1991). Climatic, solar, oceanic, and geomagnetic influences on Late-glacial and Holocene atmospheric $^{14}\text{C}/^{12}\text{C}$ change. *Quaternary Research*, 35(1), 1–24. [https://doi.org/10.1016/0033-5894\(91\)90091-I](https://doi.org/10.1016/0033-5894(91)90091-I)
- Styron, R. (2015). Slip-rate calculator. https://github.com/cossatot/slip_rate_calculator
- Styron, R., & Pagani, M. (2020). The GEM Global Active Faults Database. *Earthquake Spectra*, 36(1_suppl), 160–180. <https://doi.org/10.1177/8755293020944182>
- Sun, J., Xiao, W., Windley, B. F., Ji, W., Fu, B., Wang, J., & Jin, C. (2016). Provenance change of sediment input in the northeastern foreland of Pamir related to collision of the Indian Plate with the Kohistan-Ladakh arc at around 47 Ma. *Tectonics*, 35(2), 315–338. <https://doi.org/10.1002/2015TC003974>
- Tapponnier, P., Mattauer, M., Proust, F., & Cassaigneau, C. (1981). Mesozoic ophiolites, sutures, and large-scale tectonic movements in Afghanistan. *Earth and Planetary Science Letters*, 52(2), 355–371. [https://doi.org/10.1016/0012-821X\(81\)90189-8](https://doi.org/10.1016/0012-821X(81)90189-8)
- Tapponnier, P., & Molnar, P. (1979). Active faulting and Cenozoic tectonics of the Tien Shan, Mongolia, and Baykal Regions. *Journal of Geophysical Research: Solid Earth*, 84(B7), 3425–3459. <https://doi.org/10.1029/JB084iB07p03425>
- Tapponnier, P., Peltzer, G., & Armijo, R. (1986). On the mechanics of the collision between India and Asia. *Geological Society, London, Special Publications*, 19(1), 113–157. <https://doi.org/10.1144/GSL.SP.1986.019.01.07>
- Tatar, M., Hatzfeld, D., & Ghafory-Ashtiani, M. (2004). Tectonics of the Central Zagros (Iran) deduced from microearthquake seismicity. *Geophysical Journal International*, 156(2), 255–266. <https://doi.org/10.1111/j.1365-246X.2003.02145.x>
- Taylor, G. K., Grocott, J., Pope, A., & Randall, D. E. (1998). Mesozoic fault systems, deformation and fault block rotation in the Andean forearc: A crustal scale strike-slip duplex in the Coastal Cordillera of northern Chile. *Tectonophysics*, 299(1), 93–109. [https://doi.org/10.1016/S0040-1951\(98\)00200-5](https://doi.org/10.1016/S0040-1951(98)00200-5)
- Tchalenko, J. S., & Ambraseys, N. N. (1970). Structural analysis of the Dasht-e Bayaz (Iran) earthquake fractures. *GSA Bulletin*, 81(1), 41–60. [https://doi.org/10.1130/0016-7606\(1970\)81\[41:SAOTDB\]2.0.CO;2](https://doi.org/10.1130/0016-7606(1970)81[41:SAOTDB]2.0.CO;2)
- Teshebaeva, K., Sudhaus, H., Echter, H., Schurr, B., & Roessner, S. (2014). Strain partitioning at the eastern Pamir-Alai revealed through SAR data analysis of the 2008 Nura earthquake. *Geophysical Journal International*, 198(2), 760–774. <https://doi.org/10.1093/gji/ggu158>
- Thatcher, W. (2009). How the continents deform: The evidence from tectonic geodesy. *Annual Review of Earth and Planetary Sciences*, 37(1), 237–262. <https://doi.org/10.1146/annurev.earth.031208.100035>
- Thompson, J. A., Burbank, D. W., Li, T., Chen, J., & Bookhagen, B. (2015). Late Miocene northward propagation of the northeast Pamir thrust system, northwest China. *Tectonics*, 34(3), 510–534. <https://doi.org/10.1002/2014TC003690>
- Thompson, J. A., Li, T., Bookhagen, B., Chen, J., & Burbank, D. (2018). Dating growth strata and basin fill by combining $^{26}\text{Al}/^{10}\text{Be}$ burial dating and magnetostratigraphy: Constraining active deformation in the Pamir–Tian Shan convergence zone, NW China. *Lithosphere*, 10(6), 806–828. <https://doi.org/10.1130/L727.1>

- Thompson Jobe, J. A., Li, T., Chen, J., Burbank, D. W., & Bufe, A. (2017). Quaternary tectonic evolution of the Pamir-Tian Shan convergence zone, Northwest China. *Tectonics*, 36(12), 2748–2776. <https://doi.org/10.1002/2017TC004541>
- Thompson, S. C., Weldon, R. J., Rubin, C. M., Abdrakhmatov, K., Molnar, P., & Berger, G. W. (2002a). Late Quaternary slip rates across the central Tien Shan, Kyrgyzstan, central Asia. *Journal of Geophysical Research: Solid Earth*, 107(B9), ETG 7-1-ETG 7-32. <https://doi.org/10.1029/2001JB000596>
- Thompson, S. C., Weldon, R. J., Rubin, C. M., Abdrakhmatov, K., Molnar, P., & Berger, G. W. (2002b). Late Quaternary slip rates across the central Tien Shan, Kyrgyzstan, central Asia. *Journal of Geophysical Research: Solid Earth*, 107(B9), EGT 7-1. <https://doi.org/10.1029/2001jb000596>
- Trumbore, S. E. (2000). Radiocarbon Geochronology. In *Quaternary Geochronology* (pp. 41–60). American Geophysical Union (AGU). <https://doi.org/10.1029/RF004p0041>
- Vassallo, R., Mugnier, J.-L., Jomard, H., Cortès Aranda, J., Malik, M. A., Jouanne, F., & Buoncristiani, J.-F. (2020). Recurrence of large paleo-earthquakes in Kashmir Himalaya seismic gap (Riasi area, India). *Journal of Asian Earth Sciences*, 201, 104505. <https://doi.org/10.1016/j.jseaes.2020.104505>
- Walker, M. (2005). *Quaternary Dating Methods*. John Wiley and Sons.
- Walker, R. T., Wegmann, K. W., Bayasgalan, A., Carson, R. J., Elliott, J., Fox, M., Nissen, E., Sloan, R. A., Williams, J. M., & Wright, E. (2015). The Egin Davaa prehistoric rupture, central Mongolia: A large magnitude normal faulting earthquake on a reactivated fault with little cumulative slip located in a slowly deforming intraplate setting. *Geological Society, London, Special Publications*, 432(1), 187–212. <https://doi.org/10.1144/SP432.4>
- Wallace, R. E. (1981). Active faults, paleoseismology, and earthquake hazards in the Western United States. In *Earthquake Prediction* (pp. 209–216). American Geophysical Union (AGU). <https://doi.org/10.1029/ME004p0209>
- Wang, Y., Oskin, M. E., Zhang, H., Li, Y., Hu, X., & Lei, J. (2020). Deducing crustal-scale reverse-fault geometry and slip distribution from folded river terraces, Qilian Shan, China. *Tectonics*, 39(1), e2019TC005901. <https://doi.org/10.1029/2019TC005901>
- Weber, G. E., & Cotton, W. R. (1981). Geologic investigation of recurrence intervals and recency of faulting along the San Gregorio fault zone, San Mateo County, California. In *Geologic investigation of recurrence intervals and recency of faulting along the San Gregorio fault zone, San Mateo County, California* (USGS Numbered Series No. 81–263; Open-File Report, Vols. 81–263). U.S. Geological Survey. <https://doi.org/10.3133/ofr81263>
- Weiss, J. R., Brooks, B. A., Foster, J. H., Bevis, M., Echalar, A., Caccamise, D., Heck, J., Kendrick, E., Ahlgren, K., Raleigh, D., Smalley Jr., R., & Vergani, G. (2016). Isolating active orogenic wedge deformation in the southern Subandes of Bolivia. *Journal of Geophysical Research: Solid Earth*, 121(8), 6192–6218. <https://doi.org/10.1002/2016JB013145>
- Wells, D. L., & Coppersmith, K. J. (1994). New empirical relationships among magnitude, rupture length, rupture width, rupture area, and surface displacement. *Bulletin of the Seismological Society of America*, 84(4), 974–1002. <https://doi.org/10.1785/BSSA0840040974>
- Wesnousky, S. G. (2006). Predicting the endpoints of earthquake ruptures. *Nature*, 444(7117), 358–360. <https://doi.org/10.1038/nature05275>
- Wesnousky, S. G. (2008). Displacement and geometrical characteristics of earthquake surface ruptures: Issues and implications for seismic-hazard analysis and the process of earthquake rupture. *Bulletin of the Seismological Society of America*, 98(4), 1609–1632. <https://doi.org/10.1785/0120070111>
- Wesnousky, S. G., Kumahara, Y., Chamlagain, D., Pierce, I. K., Karki, A., & Gautam, D. (2017). Geological observations on large earthquakes along the Himalayan frontal fault near Kathmandu, Nepal. *Earth and Planetary Science Letters*, 457, 366–375. <https://doi.org/10.1016/j.epsl.2016.10.006>
- Willemse, E. J. M. (1997). Segmented normal faults: Correspondence between three-dimensional mechanical models and field data. *Journal of Geophysical Research: Solid Earth*, 102(B1), 675–692. <https://doi.org/10.1029/96JB01651>
- Willemse, E. J. M., Pollard, D. D., & Aydin, A. (1996). Three-dimensional analyses of slip distributions on normal fault arrays with consequences for fault scaling. *Journal of Structural Geology*, 18(2), 295–309. [https://doi.org/10.1016/S0191-8141\(96\)80051-4](https://doi.org/10.1016/S0191-8141(96)80051-4)

- Wintle, A. G. (1973). Anomalous fading of thermo-luminescence in mineral samples. *Nature*, 245(5421), 143–144. <https://doi.org/10.1038/245143a0>
- Xiong, W., Qiao, X., Liu, G., Chen, W., & Nie, Z. (2019). Coulomb stress evolution along the Kongur Extensional System since 1895 and present seismic hazard. *Geodesy and Geodynamics*, 10(1), 1–9. <https://doi.org/10.1016/j.geog.2018.11.007>
- Yang, S., Li, J., & Wang, Q. (2008). The deformation pattern and fault rate in the Tianshan Mountains inferred from GPS observations. *Science in China Series D: Earth Sciences*, 51(8), 1064–1080.
- Yang, X., Li, W., & Qin, Z. (2015a). Calculation of reverse-fault-related parameters using topographic profiles and fault bedding. *Geodesy and Geodynamics*, 6(2), 106–112. <https://doi.org/10.1016/j.geog.2014.09.002>
- Yang, X., Li, W., & Qin, Z. (2015b). Calculation of reverse-fault-related parameters using topographic profiles and fault bedding. *Geodesy and Geodynamics*, 6(2), 106–112. <https://doi.org/10.1016/j.geog.2014.09.002>
- Yeats, R. S. (1986). Active faults related to folding. *Active Tectonics*, 63–79.
- Yeats, R. S., & Prentice, C. S. (1996). Introduction to special section: Paleoseismology. *Journal of Geophysical Research: Solid Earth*, 101(B3), 5847–5853. <https://doi.org/10.1029/95JB03134>
- Yeats, R. S., Sieh, K. E., & Allen, C. R. (1997). *The Geology of Earthquakes*. Oxford University Press.
- Yielding, G., Jackson, J. A., King, G. C. P., Sinvhal, H., Vita-Finzi, C., & Wood, R. M. (1981). Relations between surface deformation, fault geometry, seismicity, and rupture characteristics during the El Asnam (Algeria) earthquake of 10 October 1980. *Earth and Planetary Science Letters*, 56, 287–304. [https://doi.org/10.1016/0012-821X\(81\)90135-7](https://doi.org/10.1016/0012-821X(81)90135-7)
- Youngs, R. R., & Coppersmith, K. J. (1985). Implications of fault slip rates and earthquake recurrence models to probabilistic seismic hazard estimates. *Bulletin of the Seismological Society of America*, 75(4), 939–964. <https://doi.org/10.1785/BSSA0750040939>
- Yuzhong, X. (2003). *地名中的新疆 (Xinjiang)*. 新疆人民出版社.
- Zhao, Y., Grujic, D., Baruah, S., Drukpa, D., Elkadi, J., Hetényi, G., King, G. E., Mildon, Z. K., Nepal, N., & Welte, C. (2021). Paleoseismological Findings at a New Trench Indicate the 1714 M8.1 Earthquake Ruptured the Main Frontal Thrust Over all the Bhutan Himalaya. *Frontiers in Earth Science*, 9. <https://www.frontiersin.org/article/10.3389/feart.2021.689457>
- Zhou, Y., He, J., Oimahmadov, I., Gadoev, M., Pan, Z., Wang, W., Abdulov, S., & Rajabov, N. (2016). Present-day crustal motion around the Pamir Plateau from GPS measurements. *Gondwana Research*, 35, 144–154. <https://doi.org/10.1016/j.gr.2016.03.011>
- Zubovich, A., Schöne, T., Metzger, S., Mosienko, O., Mukhamediev, Sh., Sharshebaev, A., & Zech, C. (2016). Tectonic interaction between the Pamir and Tien Shan observed by GPS. *Tectonics*, 35(2), 283–292. <https://doi.org/10.1002/2015TC004055>
- Zubovich, A., Wang, X., Scherba, Y. G., Schelochkov, G. G., Reilinger, R., Reigber, C., Mosienko, O. I., Molnar, P., Michajljow, W., Makarov, V. I., Li, J., Kuzikov, S. I., Herring, T. A., Hamburger, M. W., Hager, B. H., Dang, Y., Bragin, V. D., & Beisenbaev, R. T. (2010). GPS velocity field for the Tien Shan and surrounding regions. *Tectonics*, 29(6). <https://doi.org/10.1029/2010TC002772>

Appendix A: Supplementary material for Chapter 4

A1 Additional information on scarp fit and vertical separation

Method for scarp fit and vertical separation from Monte Carlo sampling, through linear regression of GPS points of upper and lower fan slope, and their intersection with the fault where the scarp gradient is the steepest.

Script provided by John Elliott (last update January 2019). Email: j.elliott@leeds.ac.uk

Used in following published papers:

Grützner, C., Carson, E., Walker, R. T., Rhodes, E. J., Mukambayev, A., Mackenzie, D., Elliott, J. R., Campbell, G., & Abdrakhmatov, K. (2017). Assessing the activity of faults in continental interiors: Palaeoseismic insights from SE Kazakhstan. *Earth and Planetary Science Letters*, 459, 93–104. <https://doi.org/10.1016/j.epsl.2016.11.025>

Walker, R. T., Wegmann, K. W., Bayasgalan, A., Carson, R. J., Elliott, J., Fox, M., Nissen, E., Sloan, R. A., Williams, J. M., & Wright, E. (2015). The Egiin Davaa prehistoric rupture, central Mongolia: A large magnitude normal faulting earthquake on a reactivated fault with little cumulative slip located in a slowly deforming intraplate setting. *Geological Society, London, Special Publications*, 432(1), 187–212. <https://doi.org/10.1144/SP432.4>

Method based on following papers:

Colman, S. M., & Watson, K. (1983). Ages Estimated from a Diffusion Equation Model for Scarp Degradation. *Science*, 221(4607), 263–265. <https://doi.org/10.1126/science.221.4607.263>

Hanks, T. C. (2000). The Age of Scarplike Landforms From Diffusion-Equation Analysis. In *Quaternary Geochronology* (pp. 313–338). American Geophysical Union (AGU). <https://doi.org/10.1029/RF004p0313>

Hanks, T. C., & Andrews, D. J. (1989). Effect of far-field slope on morphologic dating of scarplike landforms. *Journal of Geophysical Research: Solid Earth*, 94(B1), 565–573. <https://doi.org/10.1029/JB094iB01p00565>

Spelz, R. M., Fletcher, J. M., Owen, L. A., & Caffee, M. W. (2008). Quaternary alluvial-fan development, climate and morphologic dating of fault scarps in Laguna Salada, Baja California, Mexico. *Geomorphology*, 102(3), 578–594. <https://doi.org/10.1016/j.geomorph.2008.06.001>

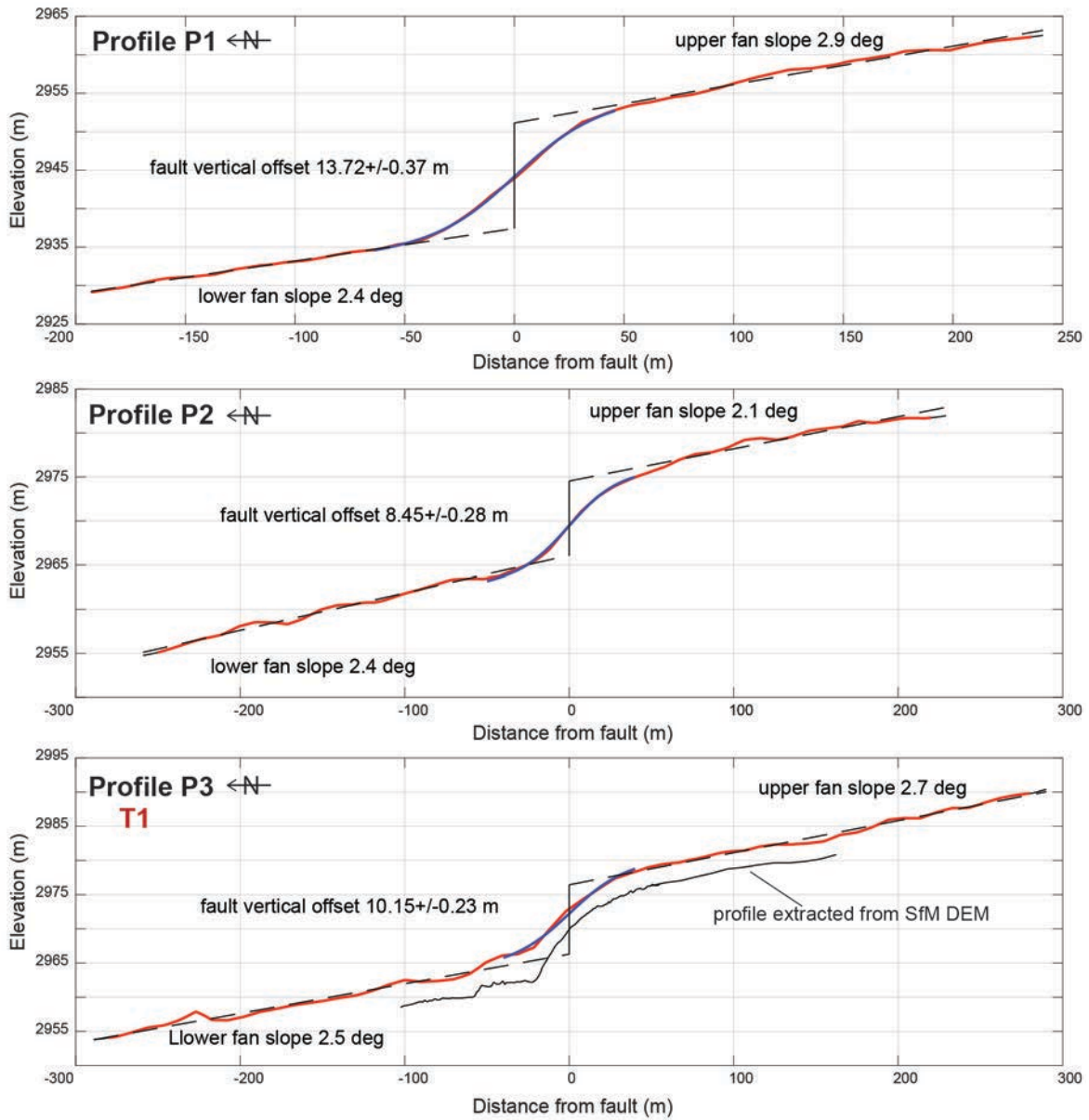


Figure A1 Scarp perpendicular TanDEM-X based topographic profiles along the cPFT and vertical separation estimates. The extent of the footwall, hanging wall, and fault-scarp face surfaces is based upon linear inversion through upper and lower slopes (and misfit to slopes). Scarp slope fit (blue) to profile (red) with estimated lower/upper fan slope and vertical separation (black). At profile P3, P5, P6 and P16 (trench T1, T2, T3 and T5) additional topographic profiles from 0.5-m-resolution Structure-from-Motion (SfM) digital surface models (DSM) are added for correlation.

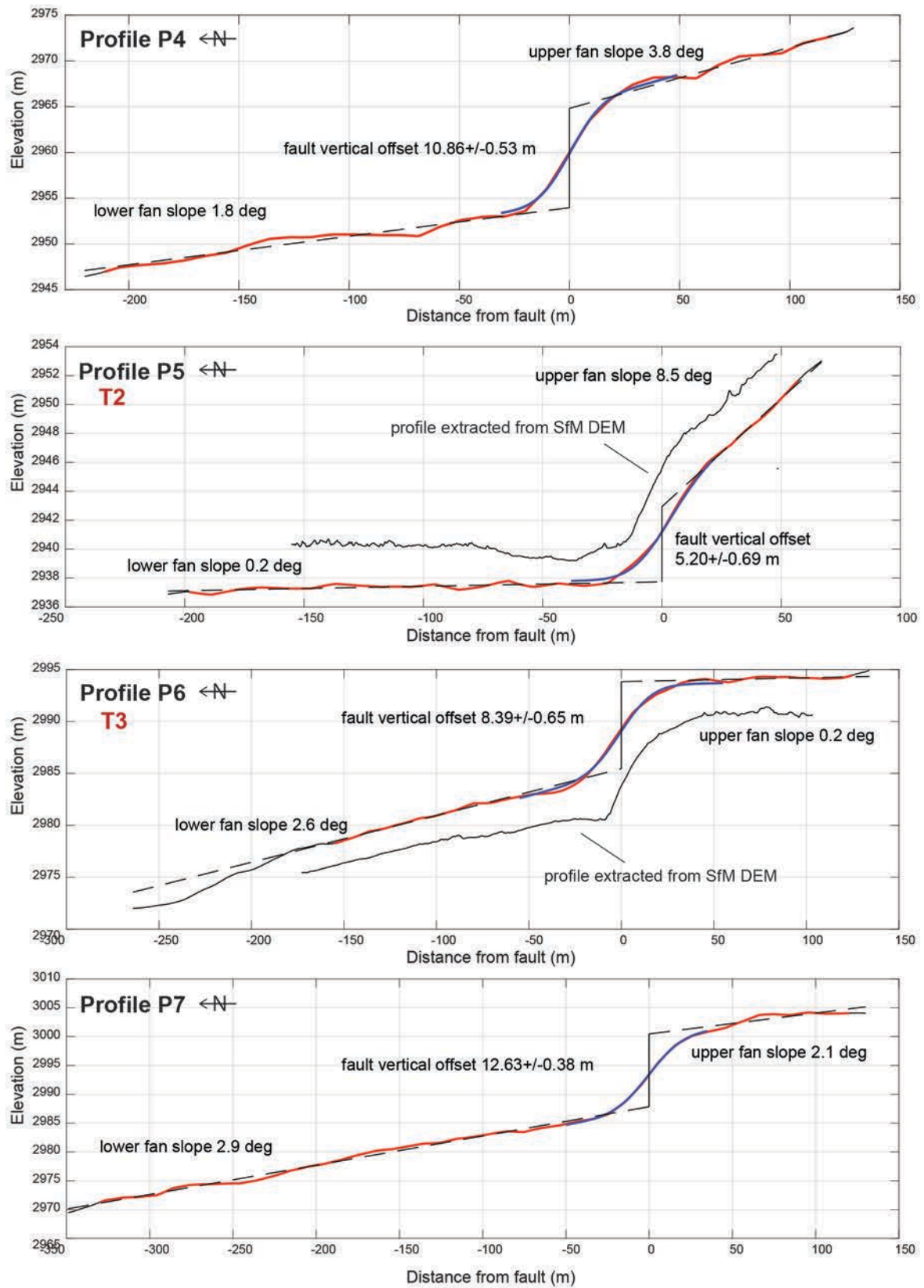


Figure A1 (continued)

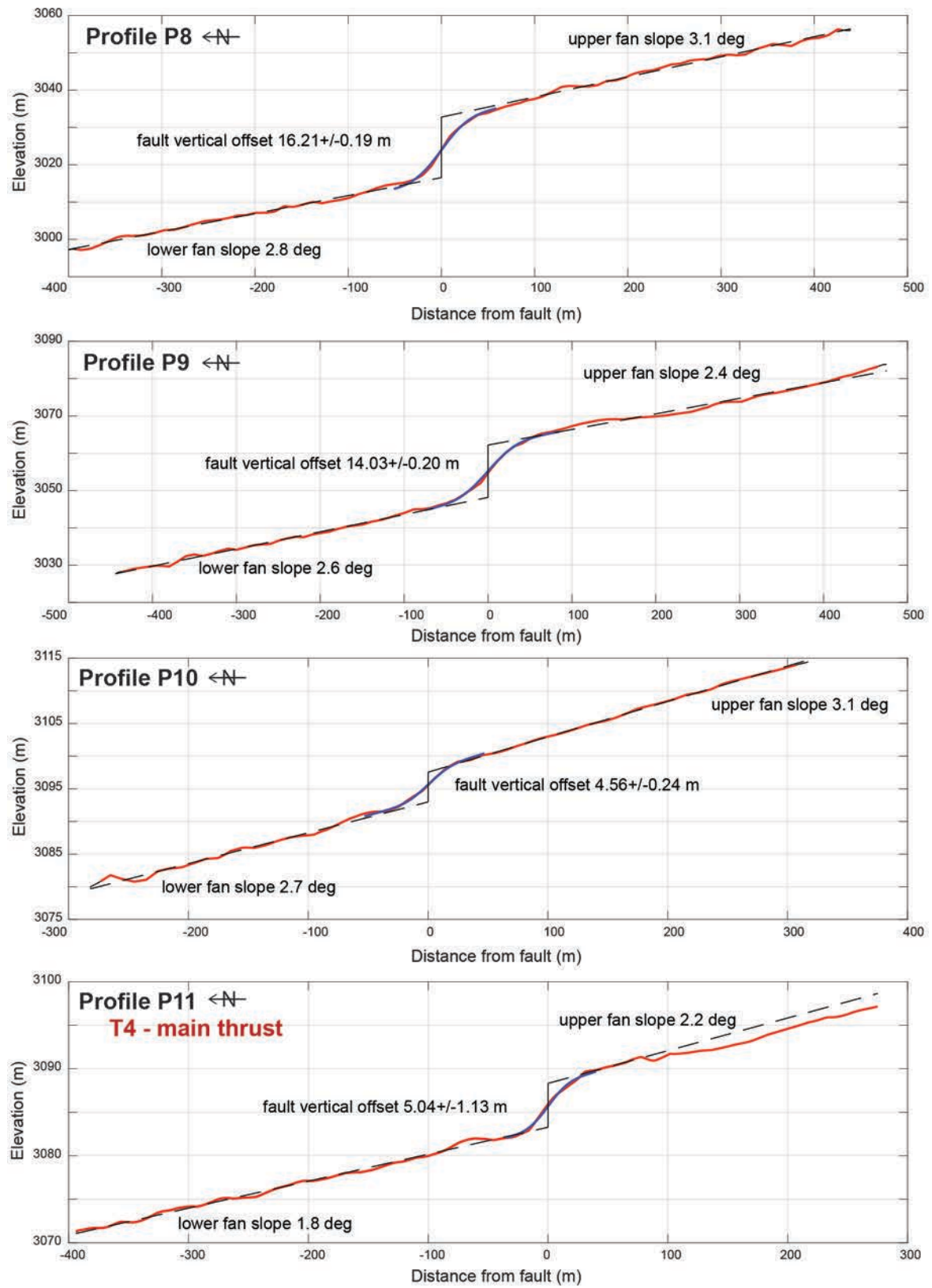


Figure A1 (continued)

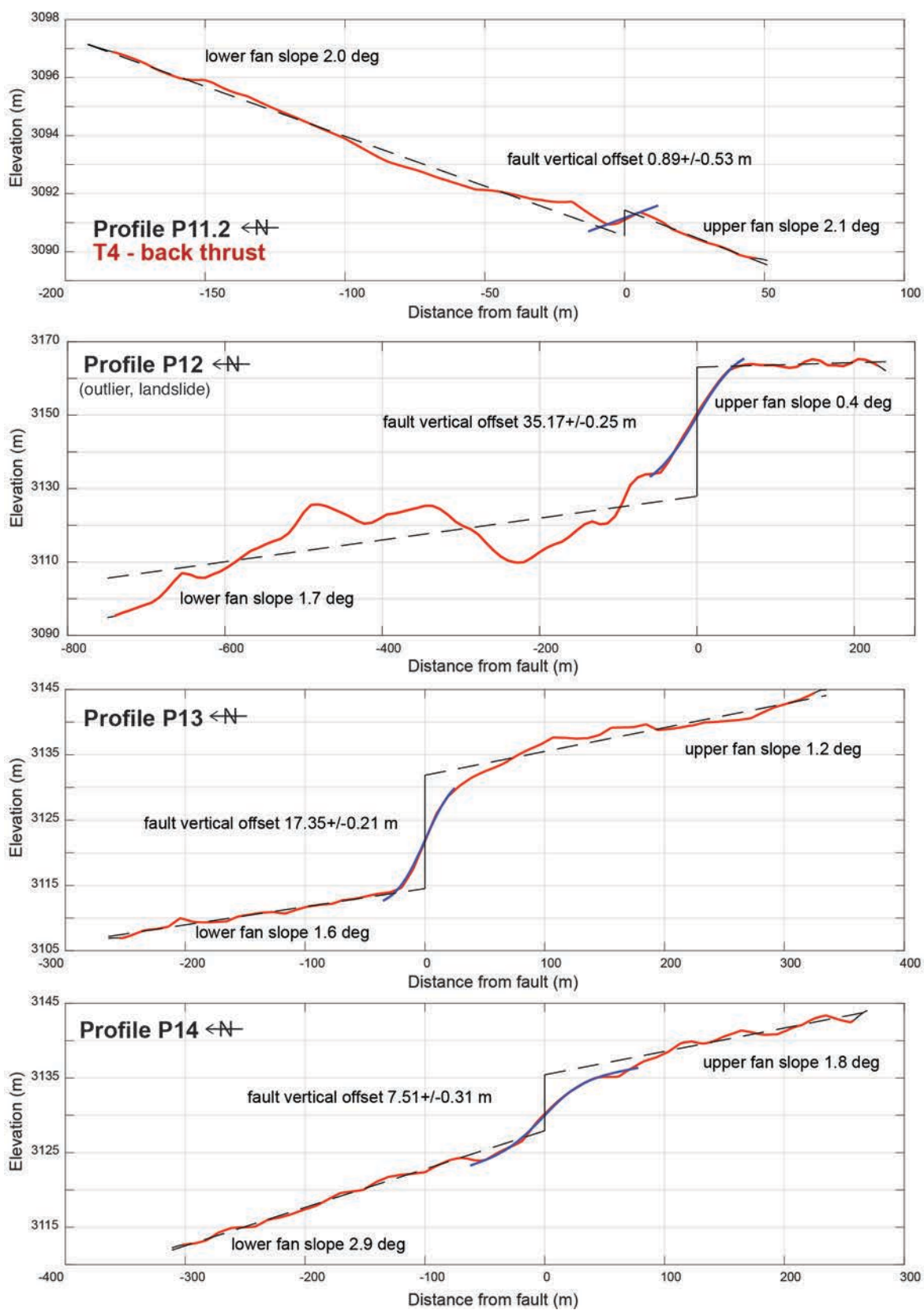


Figure A1 (continued)

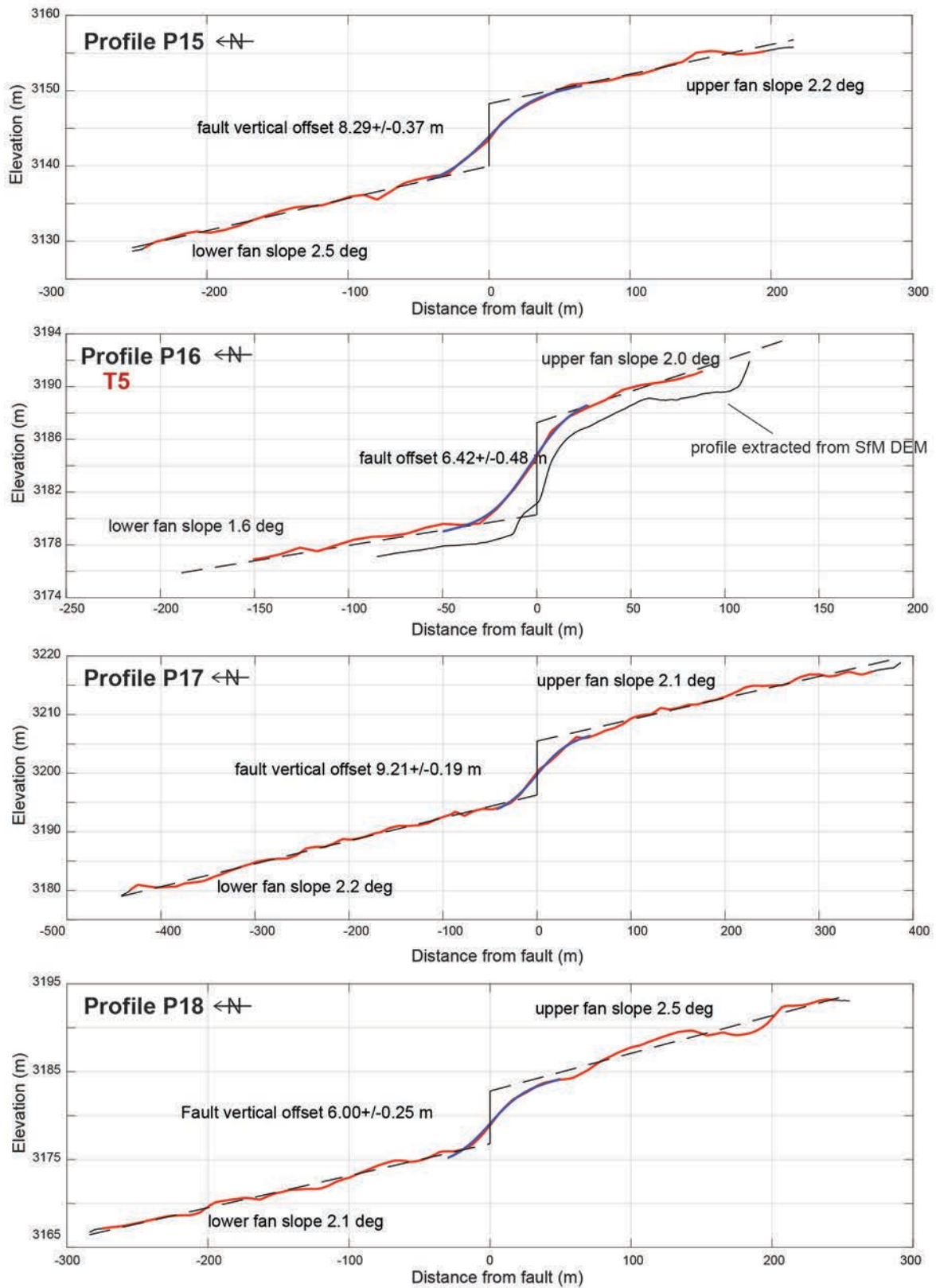


Figure A1 (continued)

Appendix B: Supplementary material for Chapter 5

B1 Additional information on sample preparation and measurement protocol for IRSL dating

This study (text provided by Frank Preusser):

“After chemical cleaning (20% HCl, 30% H₂O₂), a K-feldspar fraction was enriched using heavy liquid separation ($\delta < 2.58 \text{ g/cm}^3$). For measurements on a Freiberg Instruments Lexsyg Smart device (Richter et al., 2015), the dried material was fixed on stainless steel discs using a 1 mm stamp of silicon oil. Similar to other studies in active mountain belts (Preusser et al., 2006), the quartz grains investigated here have a low luminescence sensitivity. Consequently, feldspar measured using the single aliquot regenerative dose protocol. This includes preheating at 180°C followed by the measurement of Infrared Stimulated Luminescence (IRSL) at 50°C and a subsequent stimulation at 150°C, the so-called post-IR IRSL (pIR) measurement. A Schott BG39 and a AHF BrightLine HC 414/46 were used as detection filters. The procedure was verified by dose recovery tests on selected samples. Usually 40 aliquots have been measured of which the majority passed the usual rejection criteria (recycling, recuperation <10%). Mean dose was calculated using either the Central Age Model (CAM) or the Minimum Age Model (MAM), depending on the statistical parameters of D_e distributions, such as overdispersion, skewness and kurtosis (cf. Galbraith & Roberts, 2012). In storage tests, we observed little if any signal loss (<1 g/decade), which imply the absence of fading in the samples investigated. Ages were calculated using ADELEv.2017 (Degering & Degering, 2020), using the results of high-resolution gamma spectrometry (cf. Preusser & Kasper, 2001).”

Study campaign in 1999 (text provided by Steve Forman):

“The samples collected in 1999 were processed in the same year by S. Forman at the Luminescence Dating Research Laboratory at the University of Illinois in Chicago. The luminescence analyses were completed on the 4-11 μm poly-mineral fraction. The resultant blue emission is isolated by 5-58 and GG400 Corning filters and measured by a standard photomultiplier tube. The total bleach–multiple aliquot additive dose (MAAD) method was used with the residual response level defined by 2-hour sunlight exposure. An exponential or linear fit were used to model the additive dose response with the interpolation to the residual level < 20% of the highest applied beta dose. The equivalent dose was calculated for 3 to 90 seconds after initial exposure to infrared excitation ($880 \pm 80 \text{ nm}$). The precision of analysis is very good, with dispersion in additive dose response usually $\leq 10\%$. Dose rate estimate was calculated from alpha counting to determine U and Th content (assuming secular equilibrium) and elemental analyses to provide for K component. Moisture contents were assumed to be $10 \pm 3 \%$ in the final age calculation.”

B2 Additional information on high-resolution photomosaics from trench exposures along the central Pamir Frontal Thrust

Digital high-resolution files of all trench exposures are available at figshare (<https://doi.org/10.6084/m9.figshare.16670902.v2>)



Figure B1 Uninterpreted high-resolution photomosaic of the east (mirrored) trench wall from trench T1 compiled in Agisoft Photoscan from 289 photos/wall.



Figure B2 Uninterpreted high-resolution photomosaic of both trench walls from trench T2 compiled in Agisoft Photoscan from 564 (west) and 728 (east) photos/wall.



Figure B3 Uninterpreted high-resolution photomosaic of both trench walls from trench T3 compiled in Agisoft Photoscan from 360 (west) and 488 (east) photos/wall.

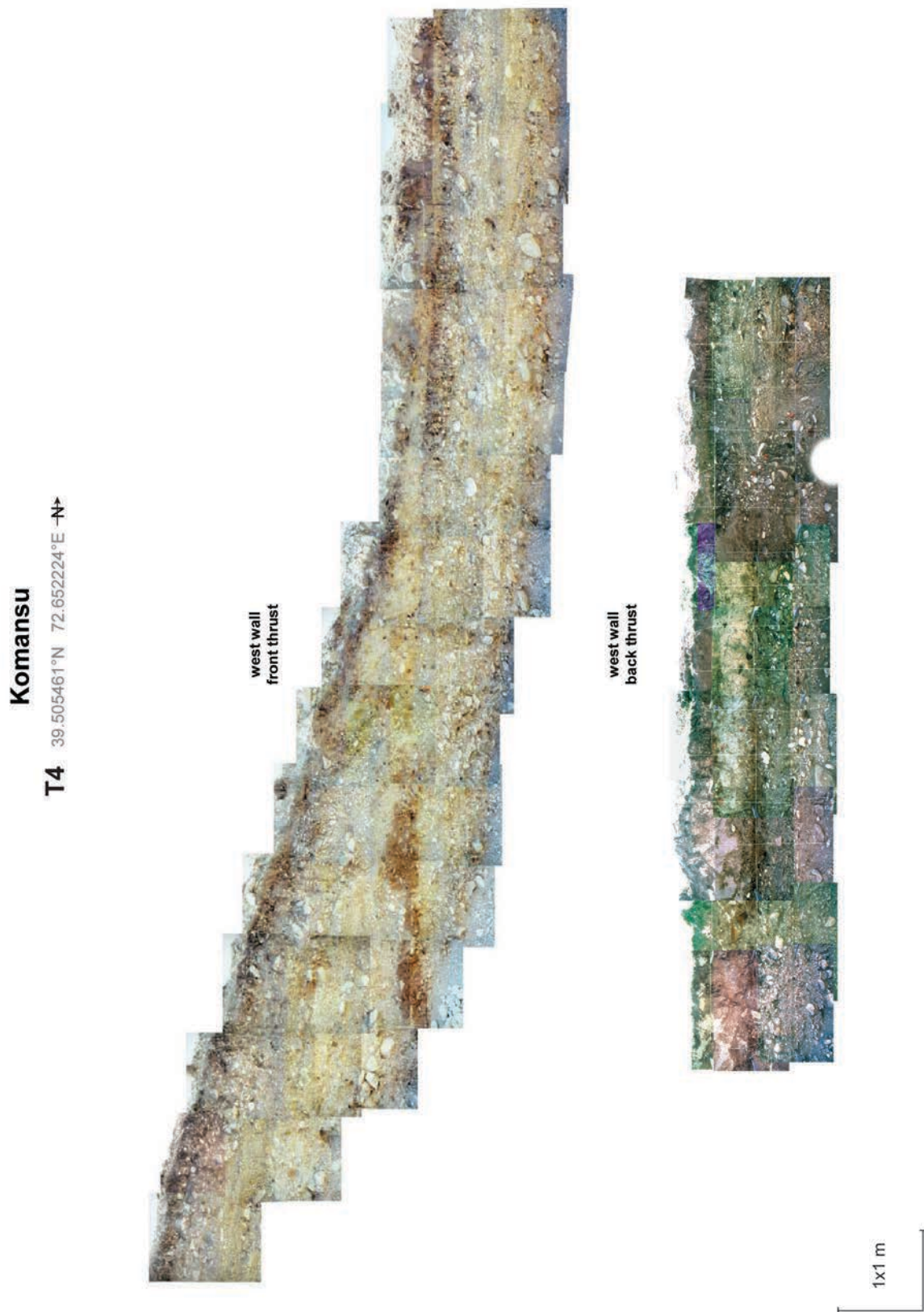


Figure B4 Uninterpreted photomosaic of both trench walls from trench T4 compiled with an image processing software in 1999 from 69 (front) and 38 (back) analog photos/wall.



Figure B5 Uninterpreted high-resolution photomosaic of both trench walls from trench T5 compiled in Agisoft Photoscan from 529 (west) and 563 (east) photos/wall.

B3 Additional information on OxCal modeling for trenches T1 to T5

Code B1: OxCal model trench T1, Achyk-Suu

```

Plot ()
{
  Sequence("Achyk-Suu T1")
  {
    Boundary("start sequence");
    Phase("Unit1 - fluvial gravel deposition")
    {
      C_Combine("Unit1 ages from T2, T3 and T5")
      {
        C_Date("T3-L7", -22582, 2700);
        C_Date("T2-L4e", -20983, 3510);
        C_Date("T3-L2", -19282, 1300);
        C_Date("T5-L4e", -19082, 1100);
        C_Date("T3-L6", -15882, 1100);
      };
    };
    Zero_Boundary("pre A5");
    Boundary("EQ A5");
    Zero_Boundary("post A5");
    Phase("Unit2 - terrace abandonment Qt3")
    {
      Combine("Unit2 ages from T2 and pits from HW of terraces")
      {
        C_Combine("IRSL")
        {
          C_Date("TR-Syn", -4832, 360);
          C_Date("T2-L2e", -4793, 860);
          C_Date("TR-Tsh", -4192, 280);
          C_Date("T2-L5e", -3753, 550);
        };
        R_Combine("14C")
        {
          R_Date("T2-Rs4w", 7070, 40);
          R_Date("T2-Rs1e", 6800, 50);
          R_Date("T2-Rs2e", 5030, 40);
        };
      };
    };
    Phase("Unit3; relative age")
    {
      };
    Zero_Boundary("pre A4");
    Boundary("EQ A4");
    Zero_Boundary("post A4");
    Phase("C1; relative age")
    {
      };
    Phase("Unit4; relative age")
    {
      };
    Boundary("EQ A3");
    Phase("C2")
    {
      C_Date("T1-L3", -13, 200);
      R_Date("T1-R2", 1840, 30);
    };
    Boundary("EQ A2");
    Phase("C3a; relative age")
    {
      };
    Phase("C3b")
    {
      C_Date("T1-L5", 297, 140);
      R_Date("T1-Rb2", 1595, 30);
    };
    Boundary("EQ Ab1");
    Phase("TS")
    {
      R_Date("T1-Rb1", 225, 35);
      R_Date("T1-R1", 130, 30);
    };
    Boundary("end sequence");
  };
};

```

Code B2: OxCal model trench T2, fault zone F1, F2, F3, F4, Achyk-Suu

```

Plot()
{
  Sequence("Achyk-Suu T2 - F1, F2, F3, F4")
  {
    Boundary("start sequence");
    Phase("Unit1 - fluvial gravel deposition")
    {
      C_Combine("Unit1 ages from T2, T3 and T5")
      {
        C_Date("T3-L7", -22582, 2700);
        C_Date("T2-L4e", -20983, 3510);
        C_Date("T3-L2", -19282, 1300);
        C_Date("T5-L4e", -19082, 1100);
        C_Date("T3-L6", -15882, 1100);
      };
    };
    Zero_Boundary("pre AS5");
    Boundary("EQ AS5; F2");
    Zero_Boundary("post AS5");
    Phase("Unit2 - terrace abandonment Qt3")
    {
      Combine("Unit2 ages from T2 and pits from HW of terraces")
      {
        C_Combine("IRSL")
        {
          C_Date("TR-Syn", -4832, 360);
          C_Date("T2-L2e", -4793, 860);
          C_Date("TR-Tsh", -4192, 280);
          C_Date("T2-L5e", -3753, 550);
        };
        R_Combine("14C")
        {
          R_Date("T2-Rs4w", 7070, 40);
          R_Date("T2-Rs1e", 6800, 50);
          R_Date("T2-Rs2e", 5030, 40);
        };
      };
    };
    Boundary("EQ AS4; F1, F3, F4");
    Phase("Unit3 - Pond")
    {
      R_Date("T2-R1e", 3560, 35);
      R_Date("T2-R3e", 3500, 40);
    };
    Boundary("EQ AS3; F1, F4");
    Zero_Boundary("post AS3");
    Phase("C1 and Cb; relative age")
    {
      Phase("Unit4 Post-Pond")
      {
        R_Date("T2-R7e", 1845, 35);
        R_Date("T2-R6e", 1495, 30);
      };
    };
    Boundary("EQ AS2; F1, F4");
    Phase("C2 and Cc")
    {
      //R_Date("T2-R8e; C2 inherited from unit 4", 1490, 40);
      R_Date("T2-R10e; Cc", 1210, 30);
      R_Date("T2-R2w; C2", 1195, 30);
      R_Date("T2-R1w; C2", 1145, 30);
      R_Date("T2-Rb1w; C2", 1130, 30);
      R_Date("T2-R9e; Cc", 840, 140);
      //R_Date("T2-Rble; Cc poor sampling", 114, 30);
    };
    Boundary("EQ AS1");
    Phase("C3; relative age")
    {
      //R_Date("T2-R6w; inherited from C2", 1215, 30)
      //R_Date("T2-R5w; inherited from C2", 1145, 30);
    };
    Phase("Burrow formation, loosen upper exposed unit 1 (iHW)")
    {
      //R_Date("T2-Rb3w", 575, 30);
      //R_Date("T2-R10w", 260, 60);
      //R_Date("T2-R8w; modern", 0, 0);
    };
    Phase("TS")
    {
      R_Date("T2-Rb2w", 495, 30);
      R_Date("T2-R7w", 310, 30);
      R_Date("T2-R5e", 215, 30);
      R_Date("T2-Rb4e", 155, 30);
      R_Date("T2-R4e", 50, 30);
    };
    Boundary("end sequence");
  };
};

```


Code B3: OxCal model trench T3, Ylaisu

```

Plot()
{
Sequence("Ylaisuu T3 - F1, F1b, F2, F3")
{
Boundary("start sequence");
Phase("Unit1 - fluvial gravel deposition")
{
C_Combine("Unit1 ages from T2, T3 and T5")
{
C_Date("T3-L7", -22582, 2700);
C_Date("T2-L4e", -20983, 3510);
C_Date("T3-L2", -19282, 1300);
C_Date("T5-L4e", -19082, 1100);
C_Date("T3-L6", -15882, 1100);
};
};
Zero_Boundary("pre YL3");
Boundary("EQ YL3 - Oblique slip F3 and thrust F2");
Zero_Boundary("post YL3");
Phase("Unit2 - terrace abandonment Qt3")
{
Combine("Unit2 ages from T2 and pits from HW of terraces")
{
C_Combine("IRSL")
{
C_Date("TR-Syn", -4832, 360);
C_Date("T2-L2e", -4793, 860);
C_Date("TR-Tsh", -4192, 280);
C_Date("T2-L5e", -3753, 550);
};
R_Combine("14C")
{
R_Date("T2-Rs4w", 7070, 40);
R_Date("T2-Rs1e", 6800, 50);
R_Date("T2-Rs2e", 5030, 40);
};
};
};
Boundary("EQ YL2 - F1");
Phase("unit3 - Pond")
{
R_Date("T3-R3w", 4550, 15);
C_Date("T3-L5e", -2182, 370);
C_Date("T3-L4e", -1602, 390);
R_Date("T3-R1e", 3095, 15);
R_Date("T3-R1w", 2795, 15);
//R_Date("T3-R4w", 2455, 15);
};
Boundary("EQ YL1 - F1 Fb");
Phase("unit3 - younger stage")
{
//C_Date("T3-L3e", -6662, 500);
R_Date("T3-Rb1w", 890, 30);
R_Date("T3-R5w", 330, 15);
R_Date("T3-R2e", 170, 20);
};
Phase("TS")
{
//R_Date("T3-Rb2; modern", 0, 0);
};
Boundary("end sequence");
};
};
};

```

Code B4: OxCal model trench T4, main thrust F1 and back thrust Fb, Komansu

```

Plot()
{
  Sequence("Komansu T4 - Front and Back Thrust")
  {
    Boundary("start sequence");
    Phase("Unit1 - fluvial gravel deposition")
    {
      C_Combine("Unit1 ages from T2, T3 and T5")
      {
        C_Date("T3-L7", -22582, 2700);
        C_Date("T2-L4e", -20983, 3510);
        C_Date("T3-L2", -19282, 1300);
        C_Date("T5-L4e", -19082, 1100);
        C_Date("T3-L6", -15882, 1100);
      };
    };
    Phase("Unit2 - terrace abandonment Qt3")
    {
      Combine("Unit2 ages from T2 and pits from HW of terraces")
      {
        C_Combine("IRSL")
        {
          C_Date("TR-Syn", -4832, 360);
          C_Date("T2-L2e", -4793, 860);
          C_Date("TR-Tsh", -4192, 280);
          C_Date("T2-L5e", -3753, 550);
        };
        R_Combine("14C")
        {
          R_Date("T2-Rs4w", 7070, 40);
          R_Date("T2-Rs1e", 6800, 50);
          R_Date("T2-Rs2e", 5030, 40);
        };
      };
    };
    Phase("Unit2b - terrace abandonment Qt4")
    {
      C_Date("TR-Tsh2", -2441, 180);
      C_Date("T4-L1b", -1673, 160);
    };
    Boundary("EQ K03 - F1");
    Phase("Unit2b - top")
    {
      //C_Date("T4-L7; outlier", -8121, 720);
      C_Date("T4-L3", -1201, 220);
      R_Date("T4-R1b", 2470, 40);
    };
    Boundary("EQ K02 - F1, Fb1");
    Zero_Boundary("model K02 closer to unit2b");
    Phase("unit3")
    {
      C_Date("T4-L3b", 129, 140);
      R_Date("T4-R2b", 1900, 60);
    };
    Phase("C1")
    {
      //C_Date("T4-L5; probably not reset", -1201, 260);
      C_Date("T4-L4", 489, 100);
    };
    Boundary("EQ K01 - F1, Fb2");
    Phase("C2")
    {
      C_Date("T4-L2", 569, 100);
    };
    Phase("TS")
    {
      C_Date("T4-L2b", 897, 90);
    };
    Boundary("end sequence");
  };
};

```

Code B5: OxCal model trench T5, fault zone F1, F2, Tashkungey

```

Plot()
{
  Sequence("Teshkungey T5 - F1 and F2")
  {
    Boundary("start sequence");
    Phase("Unit1 - fluvial gravel deposition")
    {
      C_Combine("Unit1 ages from T2, T3 and T5")
      {
        C_Date("T3-L7", -22582, 2700);
        C_Date("T2-L4e", -20983, 3510);
        C_Date("T3-L2", -19282, 1300);
        C_Date("T5-L4e", -19082, 1100);
        C_Date("T3-L6", -15882, 1100);
      };
    };
    Phase("Unit2 - terrace abandonment Qt3")
    {
      Combine("Unit2 ages from T2 and pits from HW of terraces")
      {
        R_Combine("14C")
        {
          R_Date("T2-Rs4w", 7070, 40);
          R_Date("T2-Rs1e", 6800, 50);
          R_Date("T2-Rs2e", 5030, 40);
        };
        C_Combine("IRSL")
        {
          C_Date("TR-Syn", -4832, 360);
          C_Date("T2-L2e", -4793, 860);
          C_Date("TR-Tsh", -4192, 280);
          C_Date("T2-L5e", -3753, 550);
        };
      };
    };
    Boundary("EQ TS3 - F1, F2");
    Phase("C1 and Ca-relative age")
    {
      C_Date("T5-L1e", -2772, 350);
      //R_Date("T5-R4e", 1085, 50);
      C_Date("T5-L3e", -2432, 280);
      //R_Date("T5-R1w", 90, 15);
    };
    Boundary("EQ TS2 - F1, F2");
    Phase("C2 and Cb")
    {
      C_Date("T5-L5e; Cb", -1761, 440);
      C_Date("T5-L6e; C2", -1042, 140);
      R_Date("T5-Rb2w; C2", 2590, 30);
      C_Date("T5-L2e; C2", -232, 140);
    };
    Phase("PS")
    {
      C_Date("T5-L1w", -12, 130);
      R_Date("T5-Rb1e", 1975, 30);
      R_Date("T5-R9e", 1645, 15);
    };
    Boundary("EQ TS1 - F1, F2");
    Phase("C3 and Cc")
    {
      R_Date("T5-Rb1w; Cc", 1645, 30);
      //R_Date("T5-R8e; C3", 350, 15);
      //R_Date("T5-R6e; C3", 285, 15);
    };
    Phase("TS")
    {
      R_Date("T5-R10e", 805, 15);
      R_Date("T5-R11e", 260, 15);
    };
  };
};

```

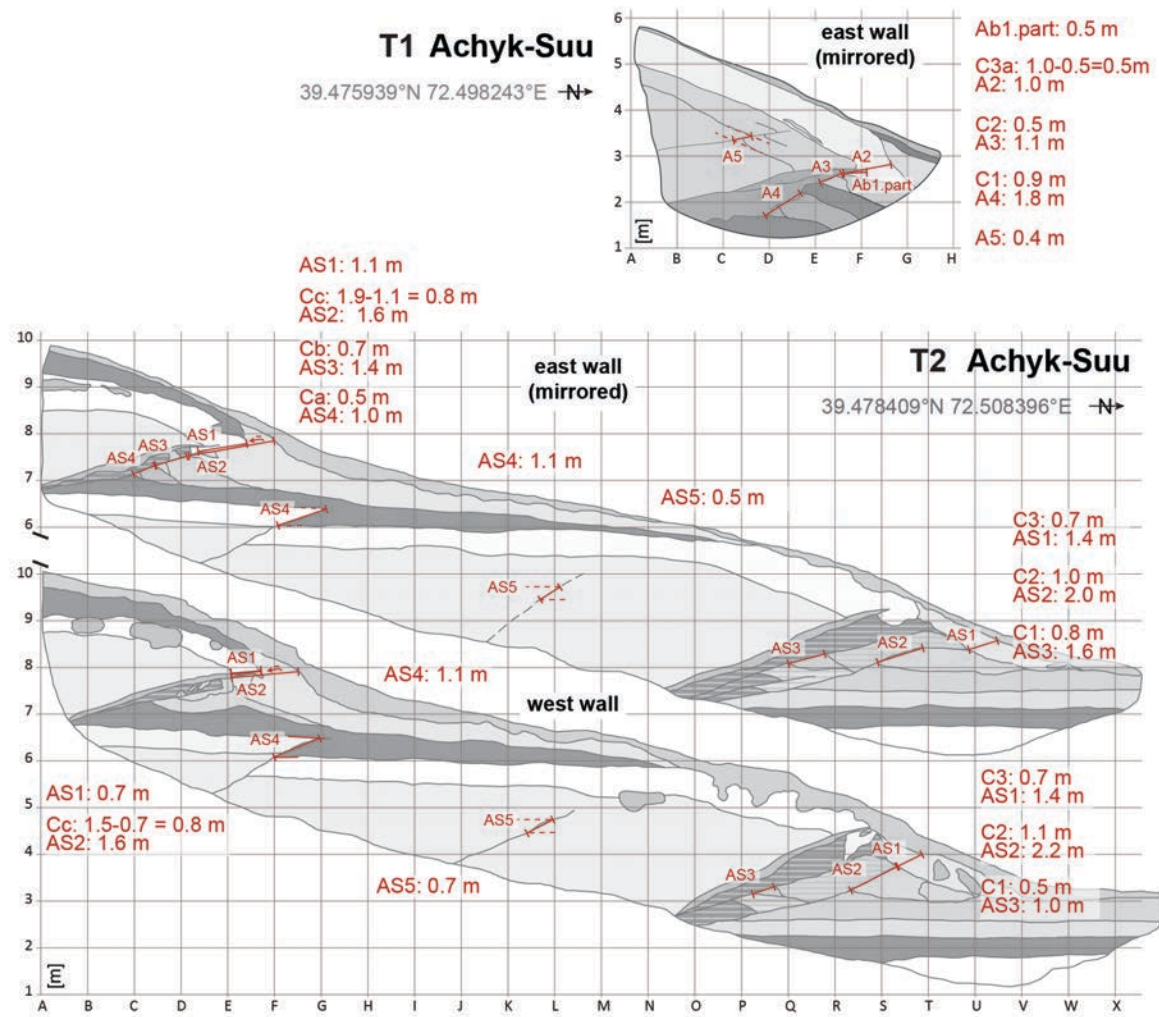


Figure B6 Per-event dip-slip measurements from the trench wall exposures. When measured along the fault-proximal cut edge of paleoearthquake related colluvium the true net slip is assumed to be twice the measured amount (see Chapter 5 for explanation)

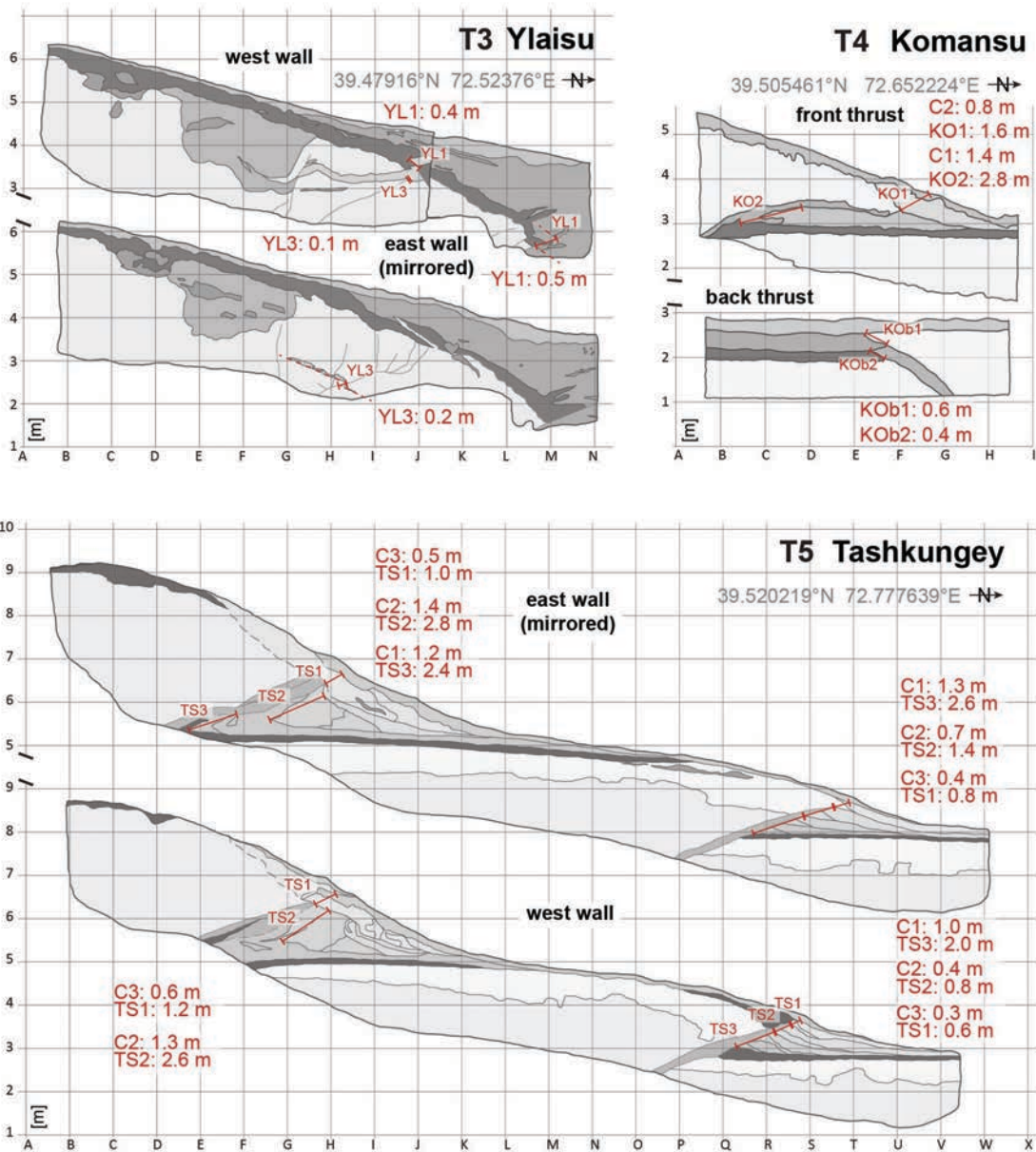


Figure B6 (continued)

Appendix C: Supplementary material for Chapter 7

Table C1 Measurements and information for the displacement vector along the 2008 Nura surface rupture, compiled in 2018. The corresponding interactive KMZ file with linked imagery is available at figshare (<https://doi.org/10.6084/m9.figshare.19534585>)

GPS name	feature	Photo ID	DD [cm]	II [azimuth]	UD [cm]	local trace bearing	Comment	xcoord	ycoord	zcoord
NU007	graben	7156	10	0	0	30	fracture ave. str. 030, (Graben-12), 10-40-10	401407.8	4388161.8	3026.3
NU012	fissure	7157	13	15(155)	0	45		401404.2	4388158.8	3027.5
NU017	fissure	7159	13	21(290)	0	20		401404.3	4388154.2	3029.1
NU039	fissure	7160	11	285	8	35		401380.7	4388143	3034.9
NU054	fissure	7161	12	0	6	48	*if Azimuth 0 --> no lateral movement	401373.4	4388133	3036.492
NU063	fissure	7163	11	0	10	52		401369.5	4388130	3037.083
NU062	subsidence	7162	13	0	18	60		401364.2	4388125	3038.076
NU072	fissure	7164	9	355	10	52		401355.2	4388116	3039.755
NU073	fissure	7165	15	350	11	42		401349.4	4388109	3041.16
NU082	fissure	7167-68	22	358	10	50		401345.4	4388111	3040.642
NU083	graben	7169	12	0	16	30	slope increase of topo	401340.9	4388105	3041.759
NU074	fissure	7166	8	10	10	74		401342.8	4388103	3042.725
NU084	fissure	7170	15	0	0	25		401335.8	4388098	3044.168
NU107	fissure	7175	8	0	9	40	Photto --> Bleistiftspitze -> N	401327.5	4388079	3046.195
NU108	fissure	7176	8	2	7	55		401322.3	4388074	3047.076
NU100	broken clast	7171-74	117	002	6	35		401307.1	4388062	3049.161
NU127	graben	7188	68	0	28	25		401251.2	4388027	3050.051
NU126	graben	7184+86	30	0	40	35		401248.1	4388021	3049.192
NU125	graben	7183	30	0	4	30		401241.9	4388010	3046.577
NU124	fissure	7182	12	0	8	28		401238.3	4388003	3044.942
NU236	graben	7243	4	0	9	35		401180.4	4387999	3047.609
NU235	graben	7242	5	0	17	25		401174.5	4387993	3046.511
NU234	graben	7241	10	0	20	40		401169.6	4387984	3045.529
NU233	graben	7240	67	0	43	25		401164.5	4387975	3045.487
NU232	graben	7239	17	0	50	10		401160.2	4387965	3044.669
NU231	graben	7238	33	0	35	20		401157.1	4387953	3044.226
NU230	graben	7237	66	0	45	15		401154.6	4387945	3044.305
NU229	graben	7236	65	0	25	40		401150.5	4387941	3043.618
NU228	graben	7235	50	0	40	25		401143.7	4387935	3042.44
NU227	graben	7234	12	0	14	40		401139.1	4387937	3041.084
NU226	graben	7233	17	0	20	40		401134	4387929	3041.002
NU224	graben	7232	140	0	75	60		401125.4	4387920	3041.775

GPS name	feature	Photo ID	DD [cm]	II [azimuth]	UD [cm]	local trace bearing	Comment	xcoord	ycoord	zcoord
NU223	graben	7231	73	0	69	55		401115.6	4387914	3041.093
NU222	graben	7230	60	0	55	25		401109.5	4387907	3041.086
NU221	fissure	7229	0	0	0	50	diffuse degraded --> no other meas.	401096.2	4387883	3041.005
NU220	graben	7228	85	0	60	40		401087.7	4387870	3041.064
NU219	graben	7227	112	0	34	45		401080	4387862	3039.923
NU218	fissure + graben	7226	42	0	15	50		401072.8	4387856	3039.597
NU217	fissure	7225	46	0	30	28		401065.3	4387850	3040.227
NU216	fissure	7224	45	0	30	50		401058.9	4387851	3040.634
NU215	graben	7223	224	0	90	54		401048.9	4387844	3038.509
NU214	graben	7222	118	0	60	50		401042.6	4387839	3036.986
NU186	fissure	7212-14	40	0	55	60		401037.4	4387835	3038.806
NU185	graben	7211	112	0	38	50		401031.9	4387827	3041.729
NU184	graben	7210	155	0	40	40		401023.8	4387817	3042.059
NU183	graben	7208+09	180	0	48	55		401016.2	4387811	3041.835
NU182	strike of fissure	7207	12	0	26	55		401010.3	4387806	3041.657
NU181	strike of fissure	7203-06	30	0	60	75		401000	4387801	3041.599
NU180	strike of fissure	7202	18	0	30	45		400992.7	4387796	3042.097
NU179	strike of fissure	7200-01	10	0	32	40		400987.8	4387792	3043.32
NU178	strike of fissure	7199	52	0	24	45		400983.7	4387787	3043.983
NU238	graben	7245	130	0	18	35	18((40N))	400460	4387384	3082.535
NU242	fissure	7259	0		0			400258.9	4387207	3115.525
NU243	broken clast	7261+62	10	300	2	50		400165	4387136	3135.41
NU475	graben	7319-20	8	0	20	50		400155.7	4387111	3136.276
NU476	graben	7321	20	100	42	35	fissure 1m deep	400150.2	4387107	3137.756
NU477	graben	7322	20	0	60	45		400141.4	4387099	3143.081
NU478	graben	7323	50	0	60	45	scarp start to diffuse + broken block	400133.3	4387093	3146.941
NU479	graben	7324	0	0	0	10	very diffuse	400126.1	4387085	3149.224
NU480	graben	7325	20	0	60	30		400114.1	4387075	3149.258
NU481	graben	7326	15	0	40	35		400101.8	4387067	3148.972
NU482	graben	7332-36	20	0	20	35		400092.9	4387059	3148.89
NU474	big graben	7318	0	0	0	30	subsidence, extension	400083.7	4387049	3148.755
NU473	graben	7314	70	0	40	15		400018.9	4387006	3152.353
NU472	graben	7313	0	0	70	35		400012.8	4386995	3152.953
NU471	feature	7312	0	0	50	30	big graben structure	400007.1	4386977	3155.536
NU470	broken clast	7308	2	75	2	20		400003.3	4386971	3154.732
NU469	fissure	7307	60	0	65	45		399995.7	4386957	3157.106
NU468	broken clast	7306	0.5	145	2	35		399990.8	4386953	3156.446

GPS name	feature	Photo ID	DD [cm]	II [azimuth]	UD [cm]	local trace bearing	Comment	xcoord	ycoord	zcoord
NU467	graben	7305	80	0	55	22		399986.7	4386949	3155.837
NU466	graben	7304	80	0	55	20	washed and diffused	399983.4	4386942	3155.942
NU465	graben	7303	22	0	5	45		399977.9	4386934	3156.771
NU464	graben	7302	100	0	50	40		399971.5	4386930	3157.065
NU463	graben	7297-99	0	0	80	35		399965.3	4386924	3158.555
NU462	graben	7294-96	0	0	60	75	big open collapsed zone	399960	4386917	3159.145
NU461	graben	7293	0	0	25	45	diffused?	399941.4	4386900	3158.336
NU460	graben	7292	20	0	35	40	washed and diffused	399934.9	4386895	3157.117
NU459	graben	7291	15	0	20	50		399928.1	4386889	3156.564
NU458	fissure	7290	15	0	0	30		399920.7	4386884	3155.17
NU457	fissure	7287-89	16	0	15	30		399915.5	4386878	3155.555
NU456	graben	7286	20	0	12	35		399914.1	4386872	3157.213
NU455	graben	7285	60	0	10	40		399907.4	4386866	3157.604
NU454	graben	7284	0	0	50	35	washed and diffused	399901.5	4386862	3157.777
NU453	graben	7283	20	0	25	35		399893.6	4386855	3158.49
NU452	graben	7282	50	0	45	40		399887	4386845	3160.353
NU451	slope breaking	7281	15	0	10	40		399875.3	4386829	3163.881
NU450	slope break	7280	30	0	25	40		399871.7	4386824	3164.816
NU449	fissure	7279	10	55	15	-5		399849.1	4386824	3162.721
NU444	fissure	7277	10	90	4	15		399844.1	4386818	3163.281
NU439	graben	7276	10	90	20	15		399833.3	4386807	3164.831
NU434	fissure	7275	10	90	5	25		399818.3	4386799	3164.858
NU431	fissure	7274	20	310	0	15		399810.7	4386795	3164.725
NU418	broken clast	7270	11	65	28	30		399747.2	4386698	3157.175
NU419	broken clast	7272	6	290	1	-	also start point	399743.4	4386683	3154.557
NUB071	graben	7546	10	0	30	10		399449.1	4386389	3125.658
NUB072	graben	7547	30	0	50	25		399446.1	4386384	3124.528
NUB073	graben	7548	0	0	0	45	washed and diffused	399430.7	4386370	3124.509
NUB074	graben	7549	0	0	0	40	washed and diffused	399421.6	4386357	3120.764
NUB075	graben	7550	0	0	0	40	washed and diffused	399403.8	4386336	3119.401
NUB076	graben	7551	35	0	10	40	collapsed rock	399392.3	4386324	3120.556
NUB078	broken clast	7553	12	145	10	55		399381.2	4386317	3118.741
NUB060	fissure	7535	10	0	0	40		399319.8	4386280	3115.597
NUB061	graben	7536	5	0	10	45		399309.4	4386272	3116.381
NUB062	graben	7537	10	0	20	30		399299.9	4386260	3117.031
NUB063	graben	7538	30	0	10	25		399290.1	4386247	3116.913
NUB064	graben	7539	10	0	45	45		399279	4386239	3117.12
NUB065	graben	7540	10	0	35	50	in channel	399265.2	4386231	3115.568
NUB066	graben	7541	20	0	25	75		399251.9	4386225	3118.57

GPS name	feature	Photo ID	DD [cm]	II [azimuth]	UD [cm]	local trace bearing	Comment	xcoord	ycoord	zcoord
NUB067	graben	7542	40	0	20	55	collapsed down slope	399236.8	4386222	3122.868
NUB068	graben	7543	15	0	10	75		399225.1	4386217	3125.878
NUB051	graben	7511	5	0	30	50		399048	4386100	3137.951
NUB052	graben	7512	40	0	30	50		399036.9	4386094	3138.496
NUB053	graben	7513	170	0	100	50		399023.3	4386083	3137.724
NUB054	graben	7514	30	180	10	60		399011.1	4386076	3138.105
NUB055	graben	7515	10	0	30	120		398998.9	4386076	3140.038
NUB056	graben	7516-17	0	0	80	30		398986.4	4386067	3141.786
NUB057	graben	7518	45	0	25	60	deep 120cm	398976.3	4386059	3142.696
NUB058	graben	7519	10	0	5	25		398965.9	4386050	3143.201
NUB059	graben	7520	5	0	40	40		398957	4386046	3143.818
NUB045	graben	7505	20	0	3	30		398936.5	4386031	3145.754
NUB046	graben	7506	0	0	0	30	washed and collapsed	398923.7	4386022	3146.328
NUB047	graben	7507	0	0	0	50	collapsed	398911.5	4386014	3147.149
NUB048	fissure	7508	15	0	0	20		398894.9	4385997	3147.658
NUB049	graben	7509	5	0	15	15		398885.3	4385983	3147.3
NUB050	graben	7510	40	0	35	10		398881.1	4385970	3145.537
NUB027	graben	7487	15	0	5	10		398850.5	4385928	3138.755
NUB028	graben	7488	20	0	10	15		398848.7	4385918	3138.899
NUB029	graben	7489	50	0	15	10		398844.6	4385907	3138.077
NUB030	graben	7490	30	0	25	25		398836.2	4385894	3136.292
NUB031	graben	7491	15	0	10	35		398825.6	4385885	3134.464
NUB005	graben	7465	15	0	10	25		398714.4	4385823	3134.897
NUB006	graben	7466	6	120	10	50		398706.8	4385819	3134.493
NUB007	graben	7467	10	0	15	45	deep - 90cm	398699	4385815	3134.134
NUB008	graben	7468	0	0	0	45	collapsed graben 137cm (deep), open 460cm	398691.3	4385811	3133.616
NUB009	graben	7469	22	0	15	25	perpendicular -> NU-AUT-379	398686.8	4385803	3133.061
NUB010	graben	7470	10	0	20	40	offset meas. in Ramons book	398680.2	4385796	3132.151
NUB011	graben	7471	7	120	15	45		398674.5	4385791	3131.563
NUB012	graben	7472	50	0	15	50		398662.4	4385783	3130.559
NUB013	graben	7473	15	0	10	45		398655.1	4385779	3130.844
NUB014	graben	7474	25	0	30	75		398646.6	4385775	3131.099
NUB015	graben	7475	20	0	50	45		398635.8	4385773	3130.965
NUB016	graben	7476	50	0	60	45		398622.7	4385766	3131.485
NUB017	graben	7477	40	0	50	55		398609.4	4385762	3135.175
NUB018	graben	7478	20	0	10	50	washed and diffused	398598.4	4385759	3137.226
NUB019	graben	7479	20	0	30	18		398582.3	4385761	3133.624
NUB020	graben	7480	25	0	50	50		398573.7	4385759	3132.479
NUF006	graben	7559	10	0	25	25		397575.5	4385136	3229.41

GPS name	feature	Photo ID	DD [cm]	II [azimuth]	UD [cm]	local trace bearing	Comment	xcoord	ycoord	zcoord
NUF005	graben	7558	5	0	20	20		397570.4	4385129	3226.931
NUF004	graben	7557	10	0	20	10		397564.9	4385118	3223.865
NUF003	graben	7556	15	0	10	25		397558.3	4385109	3220.213
NUF002	fissure	7555	10	0	0	50		397550	4385100	3217.365
NUF018	graben	7575	5	0	5	20	washed and diffused	397505.7	4385013	3213.603
NUF017	graben	7574	10	0	30	20		397500.7	4385000	3212.337
NUF016	graben	7573	20	0	30	20		397495.4	4384994	3211.65
NUF015	graben	7572	15	0	30	20		397490.1	4384984	3209.371
NUF014	graben	7571	10	0	15	20		397484.8	4384974	3206.578
NUF020	graben	7576	3	0	5	0		397453.7	4384909	3197.021
NUF022	graben	7578	15	0	5	0		397441.5	4384887	3196.492
NUF021	graben	7577	5	0	10	20		397435.5	4384875	3195.721
NUF047	graben	7607	10	0	20	5		397426.7	4384864	3195.658
NUF046	fissure	7606	20	0	0	25		397420.4	4384850	3195.384
NUF045	graben	7605	10	0	10	25		397414.4	4384839	3195.087
NUF044	graben	7604	15	0	20	15		397408.2	4384824	3194.181
NUF043	graben	7603	15	0	15	10		397401.7	4384810	3192.532
NUF042	graben	7602	5	0	30	15		397394.8	4384797	3190.458
NUF041	graben	7601	10	0	15	5	diffused	397388.6	4384784	3188.361
NUF040	graben	7600	10	0	25	10	move slope related	397385.2	4384768	3185.415
NUF039	graben	7599	15	0	2	170		397384.4	4384752	3183.377
NUF038	graben	7598	15	0	2	170		397383.9	4384738	3182.025
NUF037	graben	7597	5	0	8	175		397382.3	4384721	3180.095
NUF036	graben	7596	5	0	10	10		397369.9	4384711	3179.861
NUF035	graben	7595	5	0	15	5		397364.2	4384691	3179.228
NUF034	graben	7594	10	0	5	15		397359.3	4384680	3178.841
NUF033	graben	7593	10	0	20	15		397260	4384592	3178.063
NUF032	graben	7592	20	0	20	15	very diffused	397259.6	4384581	3176.894
NUF031	graben	7591	140	0	70	40	more collapsed + bigger offset, spring place big graben	397229.1	4384549	3179.087
NUF030	graben	7590	160	0	80	15		397215.4	4384527	3179.942
NUF029	graben	7589	30	0	60	35		397207.7	4384512	3178.343
NUF028	graben	7588	15	0	35	15	very diffused	397201	4384503	3176.91
NUF027	graben	7587	5	0	20	5		397198.5	4384489	3173.788
NUF026	graben	7586	20	0	20	25		397189.7	4384476	3174.074
NUF025	graben	7585	10	0	40	5		397184	4384465	3172.047
NUF024	graben	7584	15	0	5	160		397182.8	4384452	3169.73

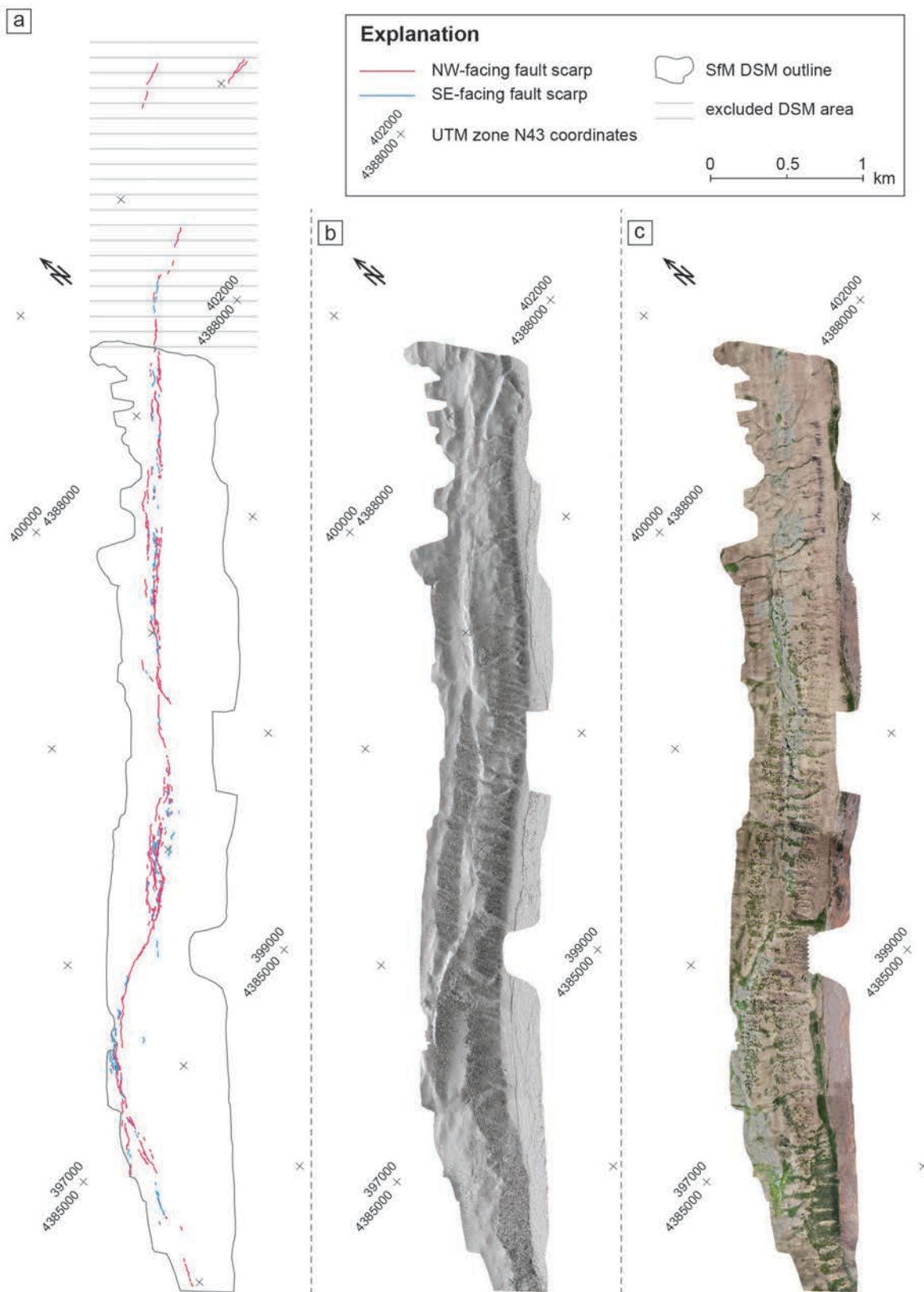


Figure C1 High-resolution digital surface models (DSM) generated from unmanned aerial photographs from the Nura site. (a) Remotely mapped surface rupture trace and outline of DSM. (b) Shaded relief map of the DSM. (c) Orthomosaic of the DSM. Shapefile and raster data sets available at figshare (<https://doi.org/10.6084/m9.figshare.19534585>)